Purdue University
Purdue e-Pubs

Open Access Theses | Theses and Dissertations

8-2016

Laboratory Characterization of Ohio Gold Frac Sand

Maria Gabriela Alvarado Calle
Purdue University

Follow this and additional works at: https://docs.lib.purdue.edu/open_access_theses

 Part of the Civil Engineering Commons

Recommended Citation
Alvarado Calle, Maria Gabriela, "Laboratory Characterization of Ohio Gold Frac Sand" (2016). *Open Access Theses*. 919.
https://docs.lib.purdue.edu/open_access_theses/919

This document has been made available through Purdue e-Pubs, a service of the Purdue University Libraries. Please contact epubs@purdue.edu for additional information.

Graduate School Form
30 Updated 12/26/2015

PURDUE UNIVERSITY
GRADUATE SCHOOL
Thesis/Dissertation Acceptance

This is to certify that the thesis/dissertation prepared

By Maria Gabriela Alvarado Calle

Entitled

LABORATORY CHARACTERIZATION OF OHIO GOLD FRAC SAND

For the degree of Master of Science in Civil Engineering

Is approved by the final examining committee:

Monica Prezzi
Co-chair

Rodrigo Salgado
Co-chair

Ghadir Haikal

To the best of my knowledge and as understood by the student in the Thesis/Dissertation Agreement, Publication Delay, and Certification Disclaimer (Graduate School Form 32), this thesis/dissertation adheres to the provisions of Purdue University's "Policy of Integrity in Research" and the use of copyright material.

Approved by Major Professor(s): Monica Prezzi
Rodrigo Salgado

Approved by: Dulcy M. Abraham 7/28/2016
Head of the Departmental Graduate Program Date

LABORATORY CHARACTERIZATION OF OHIO GOLD FRAC SAND

A Thesis

Submitted to the Faculty

of

Purdue University

by

Maria Gabriela Alvarado Calle

In Partial Fulfillment of the

Requirements for the Degree

of

Master of Science in Civil Engineering

August 2016

Purdue University

West Lafayette, Indiana

To my mom, I love you so much.

ACKNOWLEDGEMENTS

I would like to thank to Professor Monica Prezzi and Professor Rodrigo Salgado for opening me the doors and providing me the opportunity to be part of the Master program at Purdue University.

Many thanks to my major professor, Professor Monica Prezzi for your positive encouragement and guidance along this research work. All her advice and comments for the development of this thesis were really appreciated.

I would like to thank to my colleague Eshan Ganju for his valuable support and dedication along the experimental work of this thesis.

I am very thankful with the Ecuadorian government for the financial support to complete my Master program.

I am very grateful with all my friends at Purdue, I will always keep good memories of you.

Thanks to William Schmidt for his collaboration during the experimental work in the geotechnical laboratory at Purdue University.

Thanks to the Brazil Scientific Mobility Program students, whose collaboration was fundamental part for the culmination of this thesis.

Thanks to my family and friends for the continuous encouragement and emotional support to complete this goal

Special thanks to my beloved mom, Mariana Calle, for her continuous support, and unconditional love.

And above all, thanks to God, He was my strength on my weakness moments.

TABLE OF CONTENTS

Page

ACKNOWLEDGEMENTS iii

TABLE OF CONTENTS v

LIST OF TABLES xii

LIST OF FIGURES xv

LIST OF ABBREVIATIONS xxxi

LIST OF SYMBOLS xxxii

ABSTRACT xxxviii

CHAPTER 1. INTRODUCTION 1

1.1 Problem statement 1

1.2 Research objectives and approach 2

1.3 Organization of the thesis 3

CHAPTER 2. OVERVIEW OF SOIL CHARACTERIZATION AND PARTICLE CRUSHING 5

2.1 Laboratory testing 5

2.2 Index properties of soils 5

2.3 Mineralogy of soils 8

2.4 Examination of particle morphology 11

2.4.1 Image processing tools 15

2.4.2 Further studies for particle morphology characterization 15
2.5 Strength testing of soils 18
2.6 Particle crushing characterization 22
2.6.1 Main factors that affect particle crushing 23
2.6.1.1 Particle-size distribution 23
2.6.1.2 Particle shape 24
2.6.1.3 Effective confining stress and effective stress path 25
2.6.1.4 Void ratio 26
2.6.1.5 Particle hardness 27
2.6.2 Particle damage mechanisms 28
2.6.3 Particle crushing during compression 29
2.6.4 Particle crushing during shearing 32
2.6.4.1 Shear band formation 33
2.6.5 Quantification of particle crushing 35
2.6.5.1 Breakage potential 35
2.6.5.2 Total breakage 37
2.6.5.3 Relative breakage 38
CHAPTER 3. EXPERIMENTAL PROGRAM 41
3.1 Index properties 41
3.1.1 Specific gravity test 41
3.1.1.1 Equipment 43
3.1.1.2 Sample preparation 44
3.1.1.3 Calibration of pycnometers 44

3.1.1.4 Specific gravity test setup 44
3.1.2 Minimum and maximum relative density test 44
3.1.2.1 Equipment 47
3.1.2.2 Sample preparation 47
3.1.2.3 Minimum density test setup 47
3.1.2.4 Maximum density test setup 48
3.1.3 Grain size analysis 49
3.1.3.1 Equipment 50
3.1.3.2 Sample preparation 50
3.1.3.3 Sieve analysis test setup 51
3.1.3.4 Sedimentation analysis test setup 53
3.2 Particle mineralogy study 55
3.2.1 X-Ray diffraction test 55
3.2.1.1 Equipment 56
3.2.1.2 Sample preparation 56
3.2.1.3 XRD test setup 57
3.3 Particle morphology analysis 57
3.3.1 Light microscope and image processing 57
3.3.1.1 Equipment 57
3.3.1.2 Sample preparation 58
3.3.1.3 Microscope analysis setup 58
3.3.1.4 Image processing tool setup 59
3.4 Strength tests 60

3.4.1 Direct shear test 60
3.4.1.1 Equipment 60
3.4.1.2 Sample preparation 61
3.4.1.3 Direct shear test setup 61
3.4.2 Ring shear tests 65
3.4.2.1 Equipment 65
3.4.2.2 Sample preparation 66
3.4.2.3 Ring shear test setup 66
3.5 Particle characterization after loading 69
3.5.1 One-dimensional compression tests 69
3.5.1.1 Equipment 70
3.5.1.2 Load cell calibration 71
3.5.1.3 LVDT calibration 72
3.5.1.4 Calibration of the load frame 72
3.5.1.5 Sample preparation 73
3.5.1.6 One-dimensional compression test setup 74
3.5.2 Ring shear tests 77
3.5.2.1 Equipment 77
3.5.2.2 Sand sample preparation 78
3.5.2.3 Ring shear test setup 78
CHAPTER 4. TEST RESULTS 79
4.1 Specific gravity 79
4.2 Minimum density 80

4.3 Maximum density 81

4.4 Grain-size distribution 82

4.4.1 Soil classification 84

4.5 Mineralogy results 85

4.6 Morphology analyses 86

4.7 Direct shear peak and critical-state friction angles 90

4.8 Ring shear peak and critical-state friction angles 94

4.9 One-dimensional compression test results 99

4.9.1 Particle breakage parameters of Ohio Gold Frac sand after one-dimensional compression tests 107

4.9.2 Particle size evolution after one-dimensional compression tests 115

4.9.3 Particle morphology evaluation after one-dimensional compression tests.. 119

4.10 Ring shear test results 129

4.10.1 Shear band formation in the ring shear tests 130

4.10.2 Stress-displacement response 132

4.10.2.1 Ring shear tests performed on a dense (D_R=86%) sample with a normal stress of 100 kPa and shear displacement of 20 meters. 132

4.10.2.2 Ring shear test performed on a loose sample (D_R=36%) with a normal stress of 200 kPa and shear displacement of 20 meters. 136

4.10.2.3 Ring shear test performed on a dense sample (D_R=87.4%) with a normal stress of 300 kPa and shear displacement of 2 meters. 139

4.10.2.4 Ring shear tests performed on dense samples (relative density ranging from 80.8 to 86.1%) with a normal stress of 400 kPa and shear displacement of 1, 2, 4, 6 and 7 meters. 142

4.10.3 Breakage parameters for Ohio Gold Frac sand after the ring shear tests .. 147

4.10.4 Particle size evolution in ring shear tests 157

4.10.5 Minimum and maximum void ratios of the crushed sand in the shear band formed in the ring shear tests. 161

4.10.6 Particle morphology evolution after the ring shear tests performed on Ohio Gold Frac sand. 164

CHAPTER 5. CONCLUSIONS 176

5.1 Index properties of Ohio Gold Frac sand 176

5.2 Mineralogy and morphology properties of Ohio Gold Frac sand 177

5.3 Shear strength response 177

5.4 Particle crushing analyses during one-dimensional compression tests 178

5.4.1 Morphology evolution after one-dimensional compression tests 179

5.5 Particle crushing analyses after ring shear tests 180

5.5.1 Particle breakage quantification after large shear displacement tests 181

5.5.2 Minimum and maximum void ratio after ring shear tests 182

5.5.3 Particle morphology evolution after large shear displacements tests 183

LIST OF REFERENCES 185

APPENDICES

Appendix A Calibrations 193

a. Load cell calibration 193

b. LVDT calibration 195

c. Pycnometer calibration 199

Appendix B Calculations 201

a. Minimum and maximum void ratios 201

b. Direct shear test 202

c. Ring shear test 203

d. One-dimensional compression test 204

e. Hydrometer 205

f. Breakage potential 206

Appendix C Morphology parameters 207

a. One-dimensional compression test 207

b. Ring shear tests 213

LIST OF TABLES

Table Page

Table 2.1 Specific gravity values for different types of sands. 6

Table 2.2 USCS Particle size boundaries (modified after Germaine and Germaine 2009).8

Table 4.1 Specific gravity of Ohio Gold Frac sand (Pycnometer E). 79

Table 4.2 Specific gravity of Ohio Gold Frac sand (Pycnometer H)..... 80

Table 4.3 Minimum density of Ohio Gold Frac sand (funnel method). 81

Table 4.4 Maximum density of Ohio Gold Frac sand (vibratory table method). 82

Table 4.5 Particle size distribution data for Ohio Gold Frac sand. 83

Table 4.6 Soil composition of Ohio Gold Frac sand. 84

Table 4.7 Particle parameters of Ohio Gold Frac sand. 84

Table 4.8 Interplanar spacing for the first eight peaks of the X-ray diffraction test on Ohio Gold Frac sand. 85

Table 4.9 Parameters obtained after the processing of a digital image of OGF sand. 88

Table 4.10 Load schedule for one-dimensional compression tests performed on Ohio Gold Frac sand. 99

Table 4.11 Matrix test table for one-dimensional compression tests performed on Ohio Gold Frac sand. 100

Table 4.12 Void ratio change with normal stress for one-dimensional compression tests performed for 10 hours. 100

Table Page

Table 4.13 Void ratio change with normal stress for one-dimensional compression tests performed for 5 days. 103

Table 4.14 Void ratio change with normal stress for one-dimensional compression tests performed for a period of 10 days..... 105

Table 4.15 Initial breakage potential B_{p0}, final breakage potential B_{pf}, total breakage B_t, and relative breakage B_r obtained after one-dimensional compression tests on Ohio Gold Frac sand (D> 0.001 mm). 110

Table 4.16 Initial breakage potential B_{p0}, final breakage potential B_{pf}, total breakage B_t, and relative breakage B_r obtained after one-dimensional compression tests on Ohio Gold Frac sand (D> 0.075 mm). 110

Table 4.17 Gradation parameters of Ohio Gold Frac sand before and after performing one-dimensional compression tests..... 116

Table 4.18 Global particle morphology parameters after one-dimensional compression tests. 120

Table 4.19 Ring shear tests performed on Ohio Gold Frac sand. 130

Table 4.20 Shear band thickness obtained after the ring shear tests performed on Ohio Gold Frac sand. 131

Table 4.21 Breakage parameters for Ohio Gold Frac sand before and after ring shear tests (D> 0.001mm). 149

Table 4.22 Breakage parameters for Ohio Gold Frac sand before and after ring shear tests (D> 0.075mm). 149

Table Page

Table 4.23 Rate of crushing of Ohio Gold Frac for ring shear test performed with normal stress of 400 kPa (D> 0.001 mm). 156

Table 4.24 Rate of crushing of Ohio Gold Frac for ring shear test performed with normal stress of 400 kPa (D> 0.075mm). 157

Table 4.25 Gradation parameters for Ohio Gold Frac sand before and after ring shear testing. 158

Table 4.26 Minimum and maximum void ratios of the sand from the shear band after ring shear tests (these ratios were determined using reconstituted sand mixtures). 163

Table 4.27 Morphology parameters of the original and crushed Ohio Gold Frac sand.. 164

LIST OF FIGURES

Figure Page

Figure 2.1 X-Ray diffraction pattern (modified after Mitchell and Soga 2005)..... 10

Figure 2.2 Definition of roundness (modified after Wadell 1932). 12

Figure 2.3 Roundness and sphericity chart (modified after Krumbein and Sloss 1963). . 13

Figure 2.4 Fourier series method for particle analysis (modified after Kaye 1982)..... 16

Figure 2.5 Various segment lengths *r* applied to two different profiles (modified after Cox and Budhu 2008)..... 17

Figure 2.6 Log-log plot between the segment r and the number of segments N (modified after Cox and Budhu 2008)..... 18

Figure 2.7. Schematic of a typical direct shear test equipment (modified after Das 2013). 19

Figure 2.8 Typical shear stress versus horizontal shear displacement curves for dense, medium and loose sand specimens (modified after Das 2013)..... 20

Figure 2.9 Schematic of the stress-strain curves from drained triaxial compression tests carried out o three identical samples with differernt confining stresses: (a) $q=\sigma'_1-\sigma'_3$ versus axial strain ε_a; (b) principal effective stress ratio σ'_1/σ'_3 versus axial strain ε_a (modified after Salgado 2008). 21

Figure 2.10 Schematic diagram of the RSR-150 residual ring shear testing equipment. . 22

Figure Page

Figure 2.11 Definition of coordination number: (a) high coordination number; (b) low coordination number. 23

Figure 2.12 Soil gradation: (a) well-graded soil; (b) poorly-graded soil. 24

Figure 2.13 Particle shape: (a) angular particle; (b) rounded particle. 25

Figure 2.14 Phase diagram of the distinct phases separated by three layers (modified after Salgado 2008). 27

Figure 2.15 Void ratio: (a) small void ratio (dense soil); (b) high void ratio (loose soil). 27

Figure 2.16 Levels of particle breakage (modified after Daouadji et al. 2009). 29

Figure 2.17 Grain size distribution curves for Ottawa sand before and after 1D compression tests (modified after Hagerty 1993). 31

Figure 2.18 Shear band evolution on sand column during ring shear tests: (i) before the shear test; (a) before shear localization; (b) initiation of shear localization around 6 mm of shear displacement; (c) – (d) evolution of the shear band with shear displacement (modified after Sadrekarimi and Olson 2010). 34

Figure 2.19 Area BCAB defined as breakage potential of the initial grading (modified after Hardin 1985). 36

Figure 2.20 Description of total breakage (modified after Hardin 1993). 37

Figure 2.21 Total breakage (modified after Lee and Farhoomand 1967). 38

Figure 2.22 Relative breakage (modified after Lee and Farhoomand 1967). 39

Figure 2.23 Levels of particle breakage (modified after Daouadji et al. 2009). 40

Figure 3.1 Equipment used to obtain the specific gravity of Ohio Gold Frac sand. 43

Figure Page

Figure 3.2 Equipment employed for the determination of: (a) minimum density and (b) maximum density for Ohio Gold Frac sand. 48

Figure 3.3 Equipment employed for the grain size distribution: (a) sedimentation analysis (b) sieve analysis for Ohio Gold Frac sand. 51

Figure 3.4 Equipment employed to perform the X-Ray diffraction test on Ohio Gold Frac sand. 56

Figure 3.5 Equipment used to study the morphology of Ohio Gold Frac sand. 58

Figure 3.6 Arrangement of twenty particles under the microscope. 59

Figure 3.7 Direct shear equipment employed to obtain the peak and critical-state friction angles of Ohio Gold Frac sand 61

Figure 3.8 Illustration of the change of the area of the sample during shearing. 64

Figure 3.9 Ring shear equipment used to obtain the peak friction angle and critical-state friction angle of Ohio Gold Frac sand. 66

Figure 3.10 Steps followed to analyze particle crushing and morphology after performing one-dimensional compression tests on Ohio Gold Frac sand. 70

Figure 3.11 Load-frame system used to perform one-dimensional compression tests on Ohio Gold Frac sand. 71

Figure 3.12 LVDT calibration device. 72

Figure 3.13 Load frame calibration before performing one-dimensional compression tests on Ohio Gold Frac sand. 73

Figure Page

Figure 3.14 Ohio Gold Frac sand after one-dimensional compression test: left dish shows the material collected from sieve #200 and pan; and the right dish shows the material collected from sieve #20 to sieve #100. 76

Figure 3.15 Steps followed to study particle crushing and morphology after performing ring shear tests on Ohio Gold Frac sand. 77

Figure 4.1 Particle size distribution of Ohio Gold Frac sand. 83

Figure 4.2 X-ray diffraction pattern for Ohio Gold Frac sand. 86

Figure 4.3 Random selection of Ohio Gold Frac sand particles from various gradations: (a) Sieve #20 (mesh opening size = 0.841 mm); (b) Sieve #40 (mesh opening size = 0.420 mm); (c) Sieve #60 (mesh opening size= 0.250 mm); and (d) Sieve #100 (mesh opening size = 0.149 mm). 87

Figure 4.4 Digital image of OGF sand processed by the ImajeJ software. 88

Figure 4.5 Results obtained after the processing of the OGF sand digital images: (a) morphology parameters obtained per each sieve; (b) average of the morphology parameters for all the sieves. 89

Figure 4.6 Shear stress versus horizontal displacement curves (direct shear test, σ_N= 25 kPa, 50 kPa, and 100 kPa, D_R=85%). 91

Figure 4.7 Vertical displacement versus horizontal displacement curves (direct shear test, σ_N= 25 kPa, 50 kPa, and 100 kPa, D_R=85%). 91

Figure 4.8 Direct-shear peak and critical-state friction angles for tests performed with normal stresses of 25 kPa, 50 kPa and 100 kPa in dense OGF sand samples (D_R= 85%).93

Figure 4.9 Direct shear critical-state envelope for Ohio Gold Frac sand. 93

Figure Page

Figure 4.10 Grain size distribution curves of Ohio Gold Frac sand before and after performing direct shear tests on dense samples (D_R= 85%) with normal stresses of 25 kPa, 50 kPa and 100 kPa. 94

Figure 4.11. Shear stress versus shear displacement curves (ring shear test, σ_N= 25 kPa, 50 kPa, and 100 kPa, D_R=80%, 80.4% and 81.3%). 95

Figure 4.12. Vertical displacement versus shear displacement (ring shear test, σ_N= 25 kPa, 50 kPa, and 100 kPa; D_R=80%, 80.4% and 81.3% respectively). 95

Figure 4.13 Ring shear peak and critical-state friction angle for different confining stresses of 25 kPa, 50 kPa and 100 kPa in dense samples (D_R=80%, 80.4% and 81.3%). 97

Figure 4.14 Ring shear critical-state strength envelope for Ohio Gold Frac sand. 97

Figure 4.15. Grain size distribution curves of Ohio Gold Frac sand before and after performing ring shear tests on dense samples (D_R=80%, 80.4% and 81.3%) of Ohio Gold Frac sand with normal stresses of 25 kPa, 50 kPa and 100 kPa. 98

Figure 4.16 Void ratio versus normal stress (log scale) curves for one-dimensional compression tests performed on Ohio Gold Frac sand for 10 hours (maximum σ_N = 24 MPa). 101

Figure 4.17 Void ratio versus normal (linear scale) stress curves for one-dimensional compression tests performed on Ohio Gold Frac sand for 10 hours (maximum σ_N = 24 MPa). 102

Figure 4.18 Void ratio versus normal stress (log scale) curves for one-dimensional compression tests performed on Ohio Gold Frac sand for 5 days (maximum σ_N = 24 MPa). 103

Figure Page

Figure 4.19 Void ratio versus normal stress (linear scale) curves for one-dimensional compression tests performed on Ohio Gold Frac sand for 5 days (maximum σ_N = 24 MPa). 104

Figure 4.20. Void ratio versus normal stress (log scale) curves for one-dimensional compression tests performed on Ohio Gold Frac sand during 10 days (σ_N= 24 MPa).. .. 105

Figure 4.21 Void ratio versus normal (linear scale) stress curves for one-dimensional compression tests performed on Ohio Gold Frac sand for 10 days (maximum σ_N = 24 MPa). 106

Figure 4.22. Grain size distribution curves for Ohio Gold Frac sand before and after performing one-dimensional compression tests for a period of 10 hours with normal stresses of up to 24 MPa. 107

Figure 4.23. Grain size distribution curves for Ohio Gold Frac sand before and after performing one-dimensional compression tests for a period of 5 days with normal stresses of up to 24 MPa..... 108

Figure 4.24. Grain size distribution curves for Ohio Gold Frac sand before and after performing one-dimensional compression tests for a period of 10 days with normal stresses of up to 24 MPa..... 109

Figure 4.25. Initial breakage potential B_{p0} for Ohio Gold Frac sand. 111

Figure 4.26. Breakage parameters for the test performed on a loose sample (D_R=35%) of Ohio Gold Frac during 10 hours with normal stresses of up to 24 MPa. 111

Figure 4.27. Breakage parameters for the test performed on a dense sample (D_R=85%) of Ohio Gold Frac during 10 hours with normal stresses of up to 24 MPa. 112

Figure Page

Figure 4.28. Breakage parameter values for the test performed on a loose sample (D_R=35%) of Ohio Gold Frac during 5 days with normal stresses of up to 24 MPa..... 112

Figure 4.29. Breakage parameter values for the test performed on a dense sample (D_R=85%) of Ohio Gold Frac during 5 days with normal stresses of up to 24 MPa..... 113

Figure 4.30. Breakage parameter values for the test performed on a loose sample (D_R=35%) of Ohio Gold Frac during 10 days with normal stresses of up to 24 MPa..... 113

Figure 4.31. Breakage parameter values for the test performed on a dense sample (D_R=85%) of Ohio Gold Frac during 10 days with normal stresses of up to 24 MPa..... 114

Figure 4.32. Relative breakage evolution for the Ohio Gold Frac sand after performing one-dimensional compression tests for 10 hours and 10 days. 115

Figure 4.33 Particle diameter evolution after performing one-dimensional compression tests on loose samples (D_R=35%) of Ohio Gold Frac sand during 10 hours, 5 days and 10 days. 117

Figure 4.34 Particle diameter evolution after performing one-dimensional compression tests on dense samples (D_R=85%) of Ohio Gold Frac sand during 10 hours, 5 days and 10 days. 117

Figure 4.35 Coefficient of uniformity evolution after performing one-dimensional compression tests on dense samples (D_R=85%) of Ohio Gold Frac sand during 10 hours, 5 days and 10 days. 118

Figure 4.36 Coefficient of curvature evolution after performing one-dimensional compression tests on dense samples (D_R=85%) of Ohio Gold Frac sand during 10 hours, 5 days and 10 days. 118

Figure Page

Figure 4.37 Microscope image of the particles retained on sieves # 20, # 40, # 60 and #100 after performing one-dimensional compression tests on Ohio Gold Frac sand. 119

Figure 4.38 Sand particle morphology parameters after 1D compression test of a loose sample (D_R= 35%) to normal stresses of up to 24 MPa during 10 hours. 122

Figure 4.39 Comparison between the global particle morphology parameters obtained before and after a one-dimensional compression test on a loose (DR=35%) sand sample tested with normal stresses of up to 24 MPa during 10 hours. 123

Figure 4.40 Sand particle morphology parameters after 1D compression test of a dense sample (D_R= 85%) to normal stresses of up to 24 MPa during 10 hours. 123

Figure 4.41 Comparison between the global particle morphology parameters obtained before and after a one-dimensional compression test on a dense (D_R= 85%) sand sample tested with normal stresses of up to 24 MPa during 10 hours. 124

Figure 4.42 Sand particle morphology parameters after 1D compression test of a loose sample (D_R= 35%) to normal stresses of up to 24 MPa during 5 days. 124

Figure 4.43 Comparison between the global particle morphology parameters obtained before and after a one-dimensional compression test on a loose (D_R=35%) sand sample tested with normal stresses of up to 24 MPa during 10 days. 125

Figure 4.44 Sand particle morphology parameters after 1D compression test of a dense sample (D_R= 85%) to normal stresses of up to 24 MPa during 5 days. 125

Figure 4.45 Comparison between the global particle morphology parameters obtained before and after a one-dimensional compression test on a dense (D_R=85%) sand sample tested with normal stresses of up to 24 MPa during 10 days. 126

Figure Page

Figure 4.46 Sand particle morphology parameters after 1D compression test of a loose sample (D_R= 35%) to normal stresses of up to 24 MPa during 10 days. 126

Figure 4.47 Comparison between the global particle morphology parameters obtained before and after a one-dimensional compression test on a loose (D_R=35%) sand sample tested with normal stresses of up to 24 MPa during 10 days. 127

Figure 4.48 Sand particle morphology parameters after 1D compression test of a dense sample (D_R= 85%) to normal stresses of up to 24 MPa during 10 days. 127

Figure 4.49 Comparison between the global particle morphology parameters obtained before and after a one-dimensional compression test on a dense (D_R=85%) sand sample tested with normal stresses of up to 24 MPa during 10 days. 128

Figure 4.50 Global sand particle morphology parameters versus time after performing one-dimensional compressional tests on loose samples (D_R=35%) with normal stresses of up to 24 MPa during 10 hours, 5 days and 10 days. 128

Figure 4.51 Global sand particle morphology parameters versus time after performing one-dimensional compressional tests on dense samples (D_R=85%) with normal stresses of up to 24 MPa during 10 hours, 5 days and 10 days. 129

Figure 4.52 Shear band formation in Ohio Gold Frac sand after performing a ring shear test on a dense sample (D_R= 81.4%) with a normal stress of 400 kPa and shear displacement of 4 meters: (a) uniform shear band; (b) shear band thickness; and (c) particle damage within the shear band. 131

Figure Page

Figure 4.53 Shear stress and vertical displacement versus shear displacement curves for a ring shear test performed on a dense sample (D_R= 86%) of Ohio Gold Frac with a normal stress of 100 kPa and shear displacement of 20 m..... 134

Figure 4.54 Mobilized friction angle for a ring shear test performed on a dense sample (D_R= 86%) of Ohio Gold Frac with a normal stress of 100 kPa and shear displacement of 20 m. 134

Figure 4.55 Mobilized friction angle and vertical displacement versus shear displacement curves for a ring shear test performed on a dense sample (D_R=86%) of OGF sand with a normal stress of 100 kPa and shear displacement of 20 m: (a) shear displacement from 0 to 0.1 m; (b) shear displacement from 18 to 2 m. 135

Figure 4.56 Shear stress and vertical displacement versus shear displacement curves for a ring shear test performed on a loose sample (D_R=36%) of Ohio Gold Frac with a normal stress of 200 kPa and shear displacement of 20 m..... 137

Figure 4.57 Mobilized friction angle for a ring shear test performed on a loose sample (D_R=36%) of Ohio Gold Frac with a normal stress of 200 kPa and shear displacement of 20 m. 138

Figure 4.58 Mobilized friction angle and vertical displacement versus shear displacement curves for a ring shear test performed on a dense sample (D_R=86%) of OGF sand with a normal stress of 200 kPa and shear displacement of 20 m: (a) shear displacement from 0 to 0.1 m; (b) shear displacement from 10 to 12 m. 139

Figure Page

Figure 4.59 Shear stress and vertical displacement versus shear displacement curves for a ring shear test performed on a dense sample (D_R=87.4%) of Ohio Gold Frac with a normal stress of 300 kPa and shear displacement of 2 m..... 140

Figure 4.60 Mobilized friction angle and vertical displacement versus shear displacement curves for a ring shear test performed on a dense sample (D_R= 87.4%) of OGF sand with a normal stress of 300 kPa and shear displacement of 2 m: (a) shear displacement from 0 to 0.1 m; (b) shear displacement from 0 to 0.5 m. 141

Figure 4.61 Shear stress and vertical displacement versus shear displacement curves for ring shear tests performed on three dense samples (D_R=85.7% and 86.1%) of Ohio Gold Frac with a normal stress of 400 kPa and shear displacements of 1, 2 and 7 m. 143

Figure 4.62 Mobilized friction angle and vertical displacement versus shear displacement curves for ring shear tests performed on three dense samples (D_R=85.7% and 86.1%) of Ohio Gold Frac with a normal stress of 400 kPa and shear displacements of 1, 2 and 7 m. 144

Figure 4.63 Mobilized friction angle and vertical displacement versus shear displacement curves (for the first 100mm of shear displacement) for ring shear tests performed on three dense samples (D_R=85.7% and 86.1%) of Ohio Gold Frac with a normal stress of 400 kPa and shear displacements of 1, 2 and 7 m. 144

Figure 4.64 Shear stress and vertical displacement versus shear displacement curves for ring shear tests performed on dense samples (D_R=80.8% and 81.4%) of Ohio Gold Frac with a normal stress of 400 kPa and shear displacements of 4 and 6 m. 146

Figure Page

Figure 4.65 Mobilized friction angle and vertical displacement versus shear displacement curves for ring shear tests performed on dense samples (D_R=80.8% and 81.4%) of Ohio Gold Frac with a normal stress of 400 kPa and shear displacements of 4 and 6 m. 146

Figure 4.66 Mobilized friction angle and vertical displacement versus shear displacement curves (during the first 100mm) for ring shear tests performed on dense samples (D_R=80.8% and 81.4%) of Ohio Gold Frac with a normal stress of 400 kPa and shear displacements of 4 and 6 m. 147

Figure 4.67 Particle size distribution curves obtained for Ohio Gold Frac sand before and after performing ring shear tests with different normal stresses and shear displacements. 148

Figure 4.68 Initial breakage potential (B_{p0}) of Ohio Gold Frac sand before the ring shear tests. 150

Figure 4.69 Total breakage (B_t) for the test performed on a dense sample (D_R=86%) of Ohio Gold Frac sand with a normal stress of 100 kPa and shear displacement of 20 m. 152

Figure 4.70 Total breakage (B_t) for the test performed on a loose sample (D_R=36%) of Ohio Gold Frac sand with a normal stress of 200 kPa and shear displacement of 20 m. 152

Figure 4.71 Total breakage (B_t) for the test performed on a dense sample (D_R=87.4%) of Ohio Gold Frac sand with a normal stress of 300 kPa and shear displacement of 2 m. . 153

Figure 4.72 Total breakage (B_t) for the test performed on a dense sample (D_R=85.7%) of Ohio Gold Frac sand with a normal stress of 400 kPa and shear displacement of 1m. .. 153

Figure 4.73 Total breakage (B_t) for the test performed on a dense sample (D_R=86.1%) of Ohio Gold Frac sand with a normal stress of 400 kPa and shear displacement of 2m. .. 154

Figure Page

Figure 4.74 Total breakage (B_t) for the test performed on a dense sample (D_R=81.4%) of Ohio Gold Frac sand with a normal stress of 400 kPa and shear displacement of 4 m.. 154

Figure 4.75 Total breakage (B_t) for the test performed on a dense sample (D_R=80.8%) of Ohio Gold Frac sand with a normal stress of 400 kPa and shear displacement of 6 m.. 155

Figure 4.76 Total breakage (B_t) for the test performed on a dense sample (D_R=86.1%) of Ohio Gold Frac sand with a normal stress of 400 kPa and shear displacement of 7 m.. 155

Figure 4.77 Relative breakage parameter evolution for the ring shear tests performed on Ohio Gold Frac sand with a normal stress of 400 kPa and with shear displacements of 1, 2, 4, 6, and 7 m..... 157

Figure 4.78 Particle diameter evolution in the shear band for ring shear tests performed on Ohio Gold Frac sand with a normal stress of 400 kPa and shear displacements of 1, 2, 4, 6 and 7 m..... 159

Figure 4.79 Coefficient of uniformity evolution in the shear band for the ring shear tests performed on Ohio Gold Frac sand with a normal stress of 400 kPa and with shear displacements of 1, 2, 4, 6, and 7m..... 160

Figure 4.80 Coefficient of curvature evolution for the ring shear tests performed on Ohio Gold Frac sand with a normal stress of 400 kPa and shear displacements of 1, 2, 4, 6, and 7 meters..... 161

Figure 4.81 Minimum and maximum void ratio evolution for the Ohio Gold Frac sand in the shear band formed in ring shear tests performed with a normal stress of 400 kPa and shear displacements of 1, 2, 4, 6, and 7 meters..... 163

Figure Page

Figure 4.82 Sand particle morphology parameters before and after performing a ring shear test on a dense sample (D_R=86%) with a normal stress of 100 kPa and shear displacement of 20 m. 167

Figure 4.83 Comparison between the global particle morphology parameters obtained before and after performing a ring shear test on a dense sand sample (D_R=86%) with a normal stress of 100 kPa and shear displacement of 20 m. 168

Figure 4.84 Sand particle morphology parameters before and after performing a ring shear test on a loose sample (D_R=36%) with a normal stress of 200 kPa and shear displacement of 20 m. 168

Figure 4.85 Comparison between the global particle morphology parameters obtained before and after performing a ring shear test on a loose sand sample (D_R=36%) with a normal stress of 200 kPa and shear displacement of 20 m. 169

Figure 4.86 Sand particle morphology parameters before and after performing a ring shear test on a dense sample (D_R=87.4%) with a normal stress of 300 kPa and shear displacement of 2 m. 169

Figure 4.87 Comparison between the global particle morphology parameters obtained before and after performing a ring shear test on a dense sand sample (D_R=87.4%) with a normal stress of 300 kPa and shear displacement of 2 m. 170

Figure 4.88 Sand particle morphology parameters before and after performing a ring shear test on a dense sample (D_R=85.7%) with a normal stress of 400 kPa and shear displacement of 1 m. 170

Figure Page

Figure 4.89 Comparison between the global particle morphology parameters obtained before and after performing a ring shear test on a dense sand sample (D_R=85.7%) with a normal stress of 400 kPa and shear displacement of 1 m. 171

Figure 4.90 Sand particle morphology parameters before and after performing a ring shear test of a dense sample (D_R=86.1%) with a normal stress of 400 kPa and shear displacement of 2 m. 171

Figure 4.91 Comparison between the global particle morphology parameters obtained before and after performing a ring shear test on a dense sand sample (D_R=86.1%) with a normal stress of 400 kPa and shear displacement of 2 m. 172

Figure 4.92 Sand particle morphology parameters before and after performing a ring shear test of a dense sample (D_R=81.4%) with a normal stress of 400 kPa and shear displacement of 4 m. 172

Figure 4.93 Comparison between the global particle morphology parameters obtained before and after performing a ring shear test on a dense sand sample (D_R=81.4%) with a normal stress of 400 kPa and shear displacement of 4 m. 173

Figure 4.94 Sand particle morphology parameters before and after performing a ring shear test of a dense sample (D_R=80.8%) with a normal stress of 400 kPa and shear displacement of 6 m. 173

Figure 4.95 Comparison between the global particle morphology parameters obtained before and after performing a ring shear test on a dense sand sample (D_R=80.8%) with a normal stress of 400 kPa and shear displacement of 6 m. 174

Figure Page

Figure 4.96 Sand particle morphology parameters before and after performing a ring shear test of a dense sample (D_R=86.1%) with a normal stress of 400 kPa and shear displacement of 7 m. 174

Figure 4.97 Comparison between the global particle morphology parameters obtained before and after performing a ring shear test on a dense sand sample (D_R=85%) with a normal stress of 400 kPa and shear displacement of 7 m. 175

Figure 4.98 Global sand particle morphology parameters versus shear displacement curves for the ring sheart tests performed with a normal stress equal to 400 kPa and shear displacement equal to 1, 2, 4, 6 and 7 m. 175

LIST OF ABBREVIATIONS

AR	Aspect Ratio
ASTM	American Society for Testing and Materials
DAQ	Data Acquisition System
DEM	Discrete Element Method
DIC	Digital Image Correlation
GSD	Grain Size Distribution
LM	Light Microscope
LVDT	Linear Variable Differential Transformer
NGI	Norwegian Geotechnical Institute
NIH	National Institute of Health
NGI	Norwegian Geotechnical Institute
OGF	Ohio Gold Frac
PSD	Particle Size Distribution
SEM	Scanning Electron Microscope
SP	Poorly Graded Sand
USCS	Unified Soil Classification System

LIST OF SYMBOLS

a	Correction factor for the percent finer calculation
A_0	Initial area
A_p	Projected area of the particle
$Area$	cross-sectional particle area
A_{ST}	Corrected area at the direct shear test
b_p	Potential for breakage of a given size portion
b_{p0}	Potential for breakage before the crushing
b_{pl}	Potential for breakage after the crushing
B_i	Fourier coefficients
B_r	Relative breakage parameter
B_p	Breakage potential
B_t	Total breakage
c	Cohesive intercept
C	Constant and the fractal dimension
Cal_{factor}	Calibration factor
C_i	Fourier coefficients
Cu	Coefficient of uniformity
Cc	Coefficient of curvature

C_T	Temperature correction
d	Distancing between parallel atomic planes
D	Particle diameter
D_{1DC}	Diameter of the oedometer container
D_f	Differential of percent passing divided by 100
D_R	Relative density
D_{R1DC}	Relative density of the sand sample
D_{RRST}	Relative density of the sand sample at the ring shear test
D_{RST}	Relative density of the sand sample at the direct shear test
D_{RSTi}	Inner diameter of the ring shear box
D_{RSTo}	Outer diameter of the ring shear box
D_{ST}	Diameter of the container at the direct shear test
D_{10}	Particle diameter according to 10 percent finer by dry mass in the GSDC
D_{30}	Particle diameter according to 30 percent finer by dry mass in the GSDC
D_{50}	Particle diameter according to 50 percent finer by dry mass in the GSDC
D_{60}	Particle diameter according to 60 percent finer by dry mass in the GSDC
e	Void ratio
e_{1DC}	Void ratio of the sand sample
e_{max}	Maximum void ratio
e_{min}	Minimum void ratio
e_{RST}	Void ratio of the sand sample at the ring shear test
e_{ST}	Void ratio of the sand sample at the direct shear test
Excitation	Input voltage at which the LVDT works

F	Correction factor
g	Acceleration of the gravity
G_s	Specific gravity
$G_{s,t}$	Specific gravity of soil solids at the test temperature
H_{1DC}	Height of the oedometer container
H_{RST}	Height of the ring shear box
H_{ST}	Height of the shear box container at the direct shear test
k	Temperature coefficient from the standard tables
k_H	Constant for the particle diameter calculation
L	Length of the particle profile
L_H	Hydrometer depth
L_{major}	Major axis of the particle (Feret)
L_{minor}	Minor axis of the particle (Feret)
M_m	Mass of the mold without the collar
M_{ms_max}	Mass of mold with soil for maximum density test
M_{ms_min}	Mass of mold with soil for minimum density test
M_p	Average mass of the dry pycnometer at calibration temperature
$M_{retsoil}$	Mass of retained sand
M_s	Mass of the oven dry soil solids
M_{s1DC}	Height of the oedometer container
M_{SH}	Mass of the dry soil in the hydrometer test
M_{sieve}	Mass of the clean empty sieve
$M_{sieve+sand}$	Mass of the sieve with the retained soil

M_{sRST}	Height of the ring shear box container
M_{sSA}	Initial soil mass
M_{sST}	Height of the shear box container at the direct shear test
$M_{pw,c}$	Mass of the pycnometer and water at the calibration temperature
$M_{pw,t}$	Mass of the pycnometer and water at the test temperature
n	Number of wave lengths
N	Number of segments
P	Projected perimeter
Pa	Atmospheric pressure
$Perimeter$	Perimeter of the particle
P_{SH}	Percent finer
r_i	Radius of curvature of grain corners
R	Radius of the largest inscribed sphere
R_c	Rate of crushing
R_C	Radius of the circumscribed circle
R_{Corr}	Corrected hydrometer reading
R_{CorrF}	Final corrected hydrometer reading
R_H	Hydrometer reading
R_I	Radius of inscribed circle
R_{LVDT}	Lecture of the vertical LVDT at the direct shear test
R_{MC}	Meniscus correction reading
R_p	Radio of the particle in polar coordinates
R_{ST}	Lecture in length units at the direct shear test

R_{ZC}	Zero correction lecture from the hydrometer
S	Shear stress
t	Time
v_0	initial voltage at which the DAQ starts to record the data
v_i	input voltage at which the LVDT works
V	Total volume
V_{1DC}	Volume of the oedometer container
V_m	Volume of the mold
V_p	Pycnometer calibrated volume
V_{RST}	Volume of the ring shear box
V_s	Volume of solids
V_{s1DC}	Diameter of the oedometer container
V_{sRST}	Diameter of the ring shear box container
V_{sST}	Diameter of the container at the direct shear test
V_{ST}	Volume of the shear box container at the direct shear test
V_v	Volume of voids
$Zero$	Initial voltage at which the DAQ starts to record the data
γ_{d1DC}	Dry unit weight of the sand sample used in one-dimensional compressional test
γ_{dRST}	Dry unit weight of the sand sample used in the ring shear test
γ_{dST}	Dry unit weight of the sand sample used in the direct shear test
γ_w	Specific weight of water
Δh	Horizontal displacement

ΔB_r	Variation of relative breakage
Δu	Variation of shear displacement
θ	Angle at which the X-Rays of wavelength λ strikes a crustal
θ_F	Phase angle
λ	Wavelength
μ	Viscosity of fluid
ρ_d	Dry mass density
ρ_{max}	Maximum mass density
ρ_{min}	Minimum mass density
ρ_s	Mass density of solids
ρ_f	Mass density of fluid
ρ_w	Density of the water
$\rho_{w,c}$	Mass density of water at the calibration temperature
$\rho_{w,t}$	Mass density of water at the test temperature
σ'	Effective normal stress
σ_N	Normal stress
v	Terminal velocity
ϕ	Friction angle of the soil
τ	Shear stress
$\%S_{finer}$	Percentage of soil finer
$\%S_{retained}$	Percentage of soil retained

ABSTRACT

Alvarado C., Maria G. M.S.C.E., Purdue University, August 2016. Laboratory Characterization of Ohio Gold Frac Sand. Major Professor: Monica Prezzi.

The mechanical response of sand depends on state variables (such as density, stress state and fabric) and intrinsic variables (such as particle size distribution and particle shape). The mechanical response of sand is also a function of sand crushability. Recent research studying the cone penetration process in a unique digital image correlation (DIC) chamber is underway at Purdue University. The test sand is Ohio Gold Frac sand, which meets criteria regarding particle size and gradation related to elimination of chamber boundary and scale effects.

The mechanical behavior of this sand can be simulated by a suitable constitutive model, such as the Purdue Sand Model (PSM). In order to calibrate the constitutive model, a number of laboratory tests are required. This thesis describes some of these tests, which include determination of index properties, particle mineralogy and morphology, one-dimensional compression tests, direct shear and ring shear tests.

Ohio Gold Frac sand is classified as a clean, poorly-graded silica sand (99% of silica content). Additionally, the minimum and maximum void ratios are equal to 0.59 and 0.81, respectively. The critical-state direct shear friction angle is 35º, while the critical-state ring shear friction angle is 31.3º.

Particle crushing was observed in one-dimensional compression tests, ring shear tests as well as in cone penetration tests. In order to understand the degree of particle crushing and the process by which it happens, the evolution of particle gradation and morphology of Ohio Gold Frac sand was assessed both before and after one-dimensional compression and ring shear tests. One-dimensional compression tests were performed to a maximum load of 74 kN (24 MPa); crushing for loose and dense samples of Ohio Gold Frac sand intensified at normal stresses of 9 MPa and 10 MPa, respectively.

Ring shear tests were performed on Ohio Gold Frac sand with normal stresses of 100 kPa, 200 kPa, 300 kPa and 400 kPa and shear displacements ranging from 1 to 20 m. Cycles of contraction and dilation followed by stages of stabilization due to particle crushing were observed in all the tests. The results indicated that particle damage within the shear band (with a thickness of about 6 mm) increased with increasing normal stresses and shear displacements. The fines content of the sand in the shear band increased to 5% after the ring shear test performed with a normal stress of 400 kPa and 7 m of shear displacement.

The main particle damage mechanisms that affected the gradation of Ohio Gold Frac sand after loading were abrasion and shearing off of asperities of large particles and splitting of the small particles, which produced an increment of the fines content of the sand, without affecting the maximum particle size.

CHAPTER 1. INTRODUCTION

1.1 Problem statement

Generally, soil forms through the processes of weathering and erosion, which transform rock into sediment. Also, other processes contribute to soil formation, such as: transportation, deposition and post-deposition. For instance, transportation processes affect the surface texture of particles, while deposition processes affect the grain arrangement and grain size of soils.

Traditional soil mechanics is divided into two main soil types: sands and clays. However, there are marked differences in the response of these two soils due to particle size, hydraulic conductivity, and volume change behavior. Soil deformation during loading, in the presence or absence of pore fluid, can be classified as: 1) elastic deformation at small strains; 2) inelastic or irrecoverable deformation due to particle rearrangement, crushing and sliding.

In recent years, many geotechnical problems have been solved using advanced constitutive models that need to be calibrated with experimental data. Constitutive models provide a mathematical representation of the soil response to loading. Therefore, constitutive models need appropriate and reliable parameters obtained from soil testing at the element level to simulate soil response under different loading conditions in boundary-value problems.

The focus of this thesis is the laboratory characterization of Ohio Gold Frac sand, which is a sand mined from the Sharon conglomerate formation at the Thompson Plant in Ohio. According to Arshad et al. (2014), Ohio Gold Frac sand is classified as poorly-graded sand (SP) and is composed of 99 % of silica. Generally, silica sand particles have different shapes, such as angular, sub-angular, sub-rounded, rounded, and well-rounded. According to Arshad et al. (2014), Ohio Gold Frac sand has sub-angular particles.

Arshad et al. (2014) performed cone penetration tests on Ohio Gold Frac sand samples prepared in a digital image correlation (DIC) chamber. Ohio Gold Frac sand was selected because it met with all the ideal characteristics of particle size and gradation. At present, underway research is using the same (DIC) chamber and testing Ohio Gold Frac sand with different type of piles and test setups.

Constitutive models can be calibrated to simulate the behavior of Ohio Gold Frac sand under different conditions of loading; therefore, it is necessary to perform a series of laboratory tests, such as one-dimensional compression tests and ring shear tests, where special attention is given to particle crushing.

1.2 Research objectives and approach

The main objective of this thesis is to determine all the properties of Ohio Gold Frac sand and to understand its response to loading. The thesis is divided into four parts. The first part focuses on the determination of all the index properties of Ohio Gold Frac sand; the second part aims at determining its mineralogical and morphological characteristics; the third part involves the assessment of the strength characteristics of the sand, and finally, the fourth part considers the crushability of the sand caused by

compression and shearing, and assesses particle morphology and particle size evolution due to crushing. The systematic experimental program on Ohio Gold Frac sand consisted of evaluating the following:

- Index properties (specific gravity, gradation and minimum and maximum densities);
- Particle mineralogy (X-ray diffraction test);
- One-dimensional compression behavior (one-dimensional compression tests performed with normal stresses of up to 24 MPa);
- Shear strength in the absence of particle crushing (direct shear and ring shear tests performed with normal stresses smaller than 100 kPa);
- Shear strength evolution with particle crushing (ring shear tests performed with normal stresses greater than 100 kPa);
- Particle morphology characteristics (microscope image analyses before and after particle crushing due to one-dimensional compression and also due to compression and shearing combined).

1.3 Organization of the thesis

The thesis is organized in five chapters: (1) a brief introduction of the problem studied; (2) a literature review of the characterization methods used for sands; (3) the testing methods used to study Ohio Gold Frac sand; (4) presentation and analyses of the test results, and (5) conclusions. The content of each of the five chapters is briefly explained in the following paragraphs.

Chapter 1 explains the importance of experimental tests on soils and the motivation of the present research, the scope and objectives of the thesis.

Chapter 2 reviews the literature on laboratory characterization of sands, including particle morphology characterization and crushing of sands.

Chapter 3 explains and summarizes all the methods followed in the experimental work conducted for this thesis. All the American Society for Testing and Materials (ASTM) standards and procedures are explained in detail.

Chapter 4 presents the results of the experimental tests performed to evaluate the index properties and the strength and crushability characteristics of Ohio Gold Frac sand, considering particle gradation and morphology evolution with loading.

Chapter 5 summarizes the important conclusions and lessons learned from the test results.

CHAPTER 2. OVERVIEW OF SOIL CHARACTERIZATION AND PARTICLE CRUSHING

2.1 Laboratory testing

In the laboratory, a soil sample to be tested is treated as a point in the soil mass, subjected to a stress state (Saada and Townsend 1981). To characterize the nature of soils, it is necessary to follow standard test methods. The present work follows the ASTM International Standards, which include descriptions of the equipment and test procedures followed in the characterization Ohio Gold Frac sand.

There are many soil testing methods that can be used to characterize soils. Some factors to be considered when undertaking an experimental testing program are the initial state of the samples (sample density and fabric and initial stress state) and loading paths. Also, the adequate calibration of load cells, LVDTs and other sensors is necessary to obtain correct results. The experimental program is detailed in Chapter 3.

2.2 Index properties of soils

In order to characterize and classify a soil, first it is necessary to determine its index properties, such as specific gravity, maximum and minimum densities, and particle size distribution. Table 2.1 shows specific gravity values for different types of sands.

Table 2.1 Specific gravity values for different types of sands.

Nomination	Specific Gravity	Reference
Ottawa 20/40 sand	2.63	Sadrekarimi and Olson (2009)
Mississippi River sand	2.65	Sadrekarimi and Olson (2009)
Illinois River sand	2.63	Sadrekarimi and Olson (2009)
Virginia Beach sand	2.65	Karimpour and Lade (2010)
Pumice sand	2	Liu, Orense, and Pender (2015)
Toyoura sand	2.64	Liu, Orense, and Pender (2015)

The relative density of a sand is determined from its maximum and minimum void ratios, which, in turn, depend on the gradation and shape of the sand particles. Particle-size distribution analyses are done for all geotechnical materials, with particle size ranging from very large particles (boulders or cobbles) to small particles (silts or clays). According to the Unified Soil Classification System (USCS), which is standardized by ASTM D2487-06, first, soils are divided into three major categories: (1) coarse-grained soils, where more than 50% of the soil is retained on the #200 sieve (0.075mm), (2) fine-grained soils, where more than 50% passes the #200 sieve, and (3) highly organic soils, such as peat and muck.

The first major category has two subdivisions: 1) gravel, if 50% or more of the soil is retained over the sieve #4 (4.25mm) or 2) sand, if 50 % or more passes the sieve #4 (4.25mm). If the gravel contains less than 5% of fines, it is described as a clean gravel, but if the percentage of fines surpasses 12%, then it is classified as gravel with fines. In the case of sand, if its fines content is less than 5%, then it is classified as clean sand, but if the percentage of fines exceeds 12%, it is classified as sand with fines. Also, the coefficient of

uniformity C_u and the coefficient of curvature C_c (dimensionless parameters) are parameters that are used to classify coarse-grained soils as well graded or poorly graded. These parameters are defined as:

$$C_u = \frac{D_{60}}{D_{10}} \tag{2.1}$$

$$C_c = \frac{\left(D_{30}\right)^2}{D_{60} \times D_{10}} \tag{2.2}$$

where

D_{10}= particle diameter in the GSDC for which 10% of the sample is finer by weight

D_{30}= particle diameter in the GSDC for which 30% of the sample is finer by weight

D_{60}= particle diameter in the GSDC for which 60% of the sample is finer by weight

A gravel can be classified as well graded, if the coefficient of uniformity C_u is greater than 4 and the coefficient of curvature C_c is between 1 and 3; both of these criteria have to be met at the same time. Otherwise, the gravel is classified as poorly graded. For a sand to be classified as a well-graded sand, both the C_u has to be greater than 6 and the C_c has to be between 1 and 3; if not, then the sand is classified as a poorly-graded sand.

The liquid limit, which is the water content at which clayey soils change from plastic to liquid, plays an important role on the classification of fine-grained soils. These soils are classified as: (1) silts and clays, when the liquid limit is equal to or less than 50%, and (2) silts and clays, when the liquid limit is greater than 50%. Also, silts and clays can be further classified as organic or inorganic soil depending on their content of organic matter. ASTM D2487-06 provides all the criteria used for soil classification. Table 2.2 shows the particle size boundaries according to the size of the soil particles.

Table 2.2 USCS Particle size boundaries (modified after Germaine and Germaine 2009).

	Sieve Size		Grain Size (mm)		
Soil Component	Lower Bound	Upper Bound	Lower Bound	Upper Bound	Separation Technique
Boulders	0.75 in.	--	300	--	Manual Measurement
Cobbles	3 in.	12 in.	75	300	
Gravel			75		Mechanical Sieving
Coarse	0.75 in.	3 in.	19	75	
Fine	#4	0.75 in.	4.75	19	
Sand					
Coarse	#10	#4	2	4.75	
Medium	#40	#10	0.425	2	
Fine	#200	#40	0.075	0.425	
Fines	--	#200		0.075	Sedimentation

Furthermore, there are many techniques for soil classification and identification based on new technologies, software and equipment (light microscope, Scanning Electron Microscope (SEM), Matlab tools, and image processing software).

2.3 Mineralogy of soils

As part of the study of soils, the knowledge of particle mineralogy is important. According to Mitchell and Soga (2005), particle mineralogy is the main parameter that governs particle size and shape and the overall properties of soils. Clay minerals tend to have platy, needle or tubular shape, whereas non-clay minerals usually have bulky particles. It has been determined that the mineral in coarse-grained soils establishes their hardness and resistance to physical and chemical breakdown (Mitchell and Soga 2005). For example, sands that are constituted by carbonate minerals are weaker than sands formed by quartz minerals.

As mentioned previously, soil is the product of weathering of former rocks or soils; therefore, the dominant minerals in soils are present in them due to the following reasons: (1) they are very plenty in the source material, (2) they are not affected by weathering, and (3) they are product of weathering. For example, the mineral quartz has a tetrahedral structure, which has strong stability, without cleavage planes and, therefore, it has high hardness. On the other hand, feldspar has cleavage planes and moderate hardness, and, therefore, it breaks easily. Another important mineral is mica, which has a sheet structure and gives soils high compressibility.

According to Mitchell and Soga (2005), X-ray diffraction is often used to study fine-grained soil minerals and their crystal structure. X-rays with wavelengths of 1 Å are of the same order as the spacing d of atomic planes of crystals. Figure 2.1 explains the basis for crystal identification. An X-ray diffraction pattern is composed of a set of reflections with different intensities at different values of 2θ, where every reflection refers to an element of the soil sample. The typical wavelength used for X-ray diffraction tests is Cu-Kalpha radiation (wavelength equal to 1.54 Å).

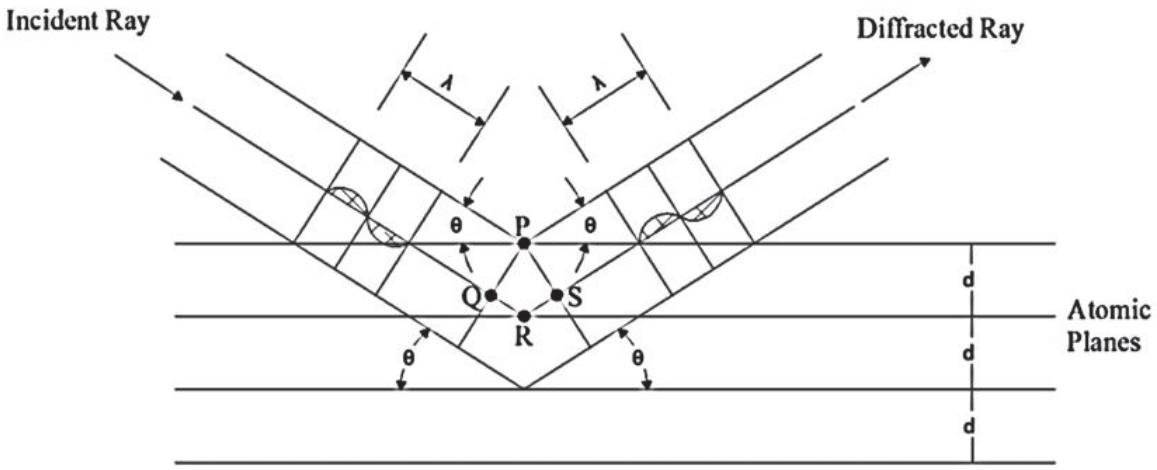

Figure 2.1 X-Ray diffraction pattern (modified after Mitchell and Soga 2005).

As can be seen in Figure 2.1, $QR = RS$ and $RS = d\sin\theta$. According to Bragg's law, the X-ray wavelength is related to distance between parallel atomic planes in a crystal by:

$$n\lambda = 2d\sin\theta \tag{2.3}$$

where

n = positive integer number

λ = wavelength of incident X-rays

d = distance between parallel atomic planes of a crystal

θ = angle at which the X-rays of wavelength λ strikes a crystal

Using Equation (2.3), the distance d can be determined for different values of the angle θ; therefore, the minerals present in a soil can be determined by comparison with X-ray diffraction patterns of known minerals.

2.4 Examination of particle morphology

Particle morphology is a result of soil formation history (weathering, transportation and sedimentation processes) and particle mineralogy. Generally, clay minerals are the product of weathering in wet environments and their evolution as minerals is due to thermal and chemical processes. On the other hand, sand minerals evolve through mechanical and chemical processes. In general terms, smaller particles (particle diameter 50 – 400 μm) tend to have less flaws than larger particles (particle diameter > 400 μm); therefore, smaller particles tend to fail by cleavage, producing new particles with platy shapes, while larger particles tend to have brittle fracturing characteristics (Cho et al. 2006).

Particle morphology plays a role in the mechanical response of soils. The shear strength and deformation response of frictional materials depend on both confining stress and density. Dilative response depends on inter-particle friction, and particle interlocking and arrangement (Cox and Budhu 2008). Particle morphology and surface texture affect soil particle arrangement and interlocking. Additionally, other parameters depend on particle morphology. Sands with angular particles have greater maximum and minimum void ratios, higher critical-state friction angles and higher compressibility than sands with rounded particles (Muszynski and Vitton 2012).

Wadell (1932) introduced the terms sphericity and roundness to characterize the morphology of particles. Sphericity is defined as the ratio between the radius R_I of an inscribed circle to the radius R_C of a circumscribed circle:

$$Sphericity = \frac{R_I}{R_C} \tag{2.4}$$

Figure 2.2 shows the definition of roundness according to Wadell (1932). Roundness is defined as the ratio of the average radius r_i of curvature of grain corners to the radius R of the largest inscribed sphere (where n is the number of grain corners)

$$Roundness = \frac{\sum_{i=1}^{n} \frac{r_i}{R}}{n} \tag{2.5}$$

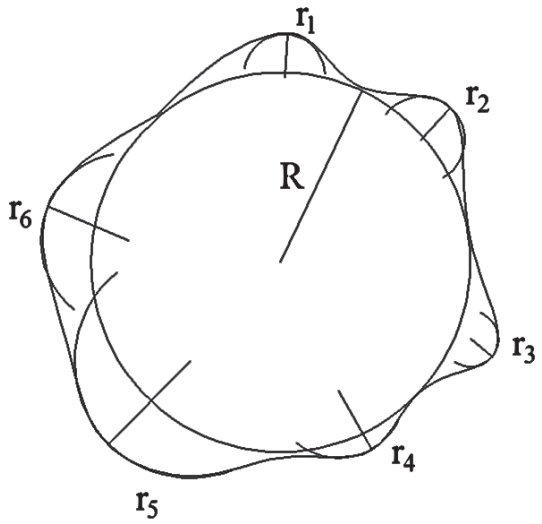

Figure 2.2 Definition of roundness (modified after Wadell 1932).

Traditionally, the sphericity and roundness parameters have been determined by visual comparison of soil particles with those in standard charts. Figure 2.3 shows the Krumbein and Sloss (1963) chart. The roundness parameter indicates whether the edges of a particle are rounded or angular, while the sphericity parameter indicates whether the particles are spherical or elongated.

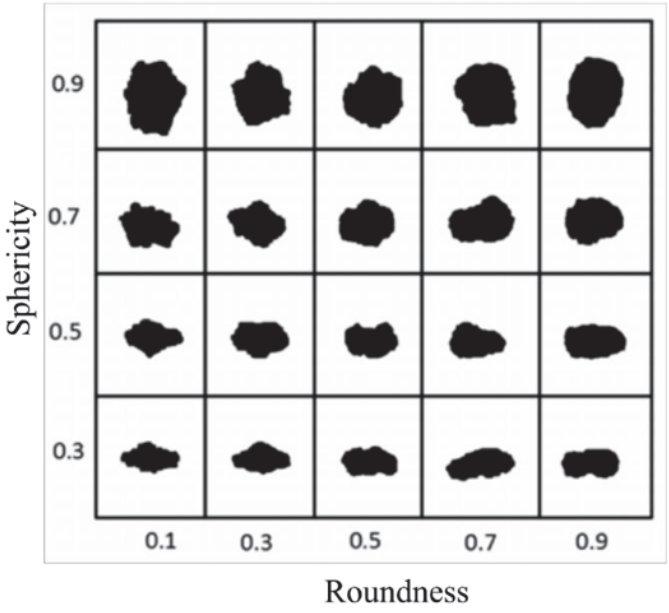

Figure 2.3 Roundness and sphericity chart (modified after Krumbein and Sloss 1963).

There is no standard methodology to study particle morphology. According to Mitchell and Soga (2005), particle morphology is dependent on the scale of the particle and the methodology employed. For example, sophisticated microscopes, such as the Scanning Electron Microscope (SEM), provide a very good appreciation of the roughness of even small particles, while a light microscope (LM), may just provide the profile of a particle. Lastly, new technologies have been developed to study the morphology of particles by analyzing digital images. ImageJ (Rasband 2004), which is a software developed by the National Institute of Health (NIH) for public use, is a Java based image-processing tool that is used to process and analyze microscope images.

The shape characterization through the use of image-processing tools has innumerable advantages over the traditional visual characterization. The morphology characterization is more precise because it studies more number of particles. Also, the

results are less subjective and the processing is less tedious Altuhafi et al. (2012). Additionally, with the automation of the digital image analysis algorithms the morphology analysis can be quickly processed.

According to Cox and Budhu (2008), with the development of new computer software, morphology parameters can be easily defined with mathematical equations. Roundness, aspect ratio *AR* and circularity *C* are defined by:

$$Roundness = \frac{4 \times A}{\pi \times L_{major}^{\ 2}} \tag{2.6}$$

$$AR = \frac{L_{major}}{L_{\min or}} \tag{2.7}$$

$$C = \frac{4 \times \pi \times A}{Perimeter^2} \tag{2.8}$$

where

L_{major}= major axis of a particle (Feret)

L_{minor}= minor axis of a particle (Feret)

Area= cross-sectional particle area

Perimeter= perimeter of the particle

The sphericity parameter quantifies the similitude between a particle and a sphere. Altuhafi et al. (2012), using the QICPIC imaging system, defined the sphericity parameter as:

$$S = \frac{2\sqrt{\pi A_p}}{P} \tag{2.9}$$

where

A_p = projected area of the particle

P = projected perimeter

In this thesis, the above defined particle morphology parameters are calculated for Ohio Gold Frac sand before and after particle crushing.

2.4.1 Image processing tools

The new morphology processing techniques require digital images. For this purpose, SEM (Scanning Electron Microscope) or LM (light microscope) are the most used devices to obtain digital images by means of a charge-couple camera. The camera is mounted on the optical path of the microscope. Additionally, image-processing tools are used to assess particle morphology. In addition to ImajeJ, Scion Image is another image-processing tool developed by Scion Corporation; both softwares are free to download. For more information of these software refer to: http://rsb.info.nih.gov/ij/ and http://scion-image.software.informer.com/ .

2.4.2 Further studies for particle morphology characterization

New definitions have been introduced using Fourier series, Fourier descriptors and fractal dimension (Cox and Budhu, 2008) for particle shape characterization. The Fourier series technique measures the radius at every selected angle evenly distributed between 0 and 360 degrees, in that way, the outline of a particle is expanded, as shown in Figure 2.4.

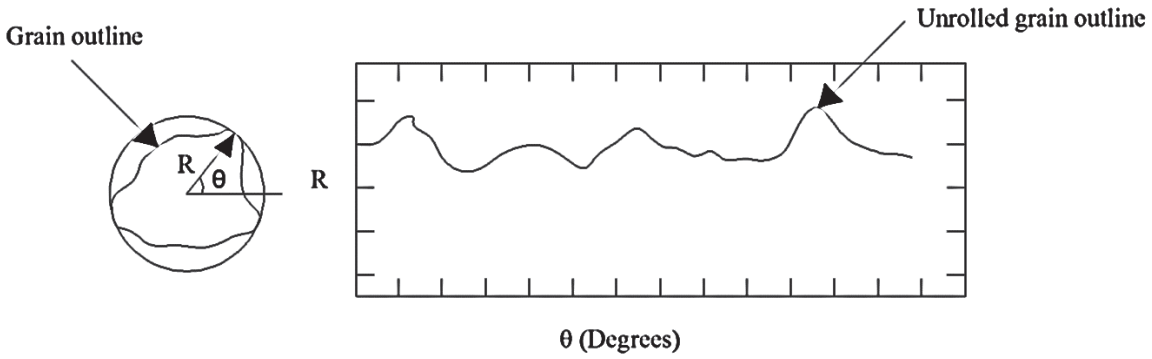

Figure 2.4 Fourier series method for particle analysis (modified after Kaye 1982).

According to Santamarina et al. (2001), the Fourier descriptors in two dimensions are given by:

$$R_p\left(\theta_F\right) = A_0 + \sum_{i=1}^{m} B_i \cos\left(i\theta_F\right) + \sum_{i=1}^{m} C_i \sin\left(i\theta_F\right) \tag{2.10}$$

where

θ_F= phase angle

R_p= Radio of the particle in polar coordinates

B_i , C_i= Fourier coefficients

The first two terms in Equation (2.10) describe the sphericity of the particle; higher terms describe roundness, and very higher terms, describe the roughness (Santamarina et al. 2001).

With respect to the fractal dimension, it is used to measure the roughness of a particle and it is expressed by:

$$\log L = \log C + \left(1 - D\right)\log r \tag{2.11}$$

where

L= length of the particle profile

C= fitting coefficient

D= fractal dimension

R= segment length

The typical method to define the fractal dimension is the divider method (Vallejo 1995). Figure 2.5 shows two particle profiles with a particular segment length *r* along the entire boundary. The number of segments *N* is counted to determine the total length *L* of the particle profile. Figure 2.6 shows the relationship for the fractal dimension between the segment length *r* and the number of segments *N*. According to Cox and Budhu (2008), it is important to correctly choose the segment length *r* to get a reliable length of the outline of the grain.

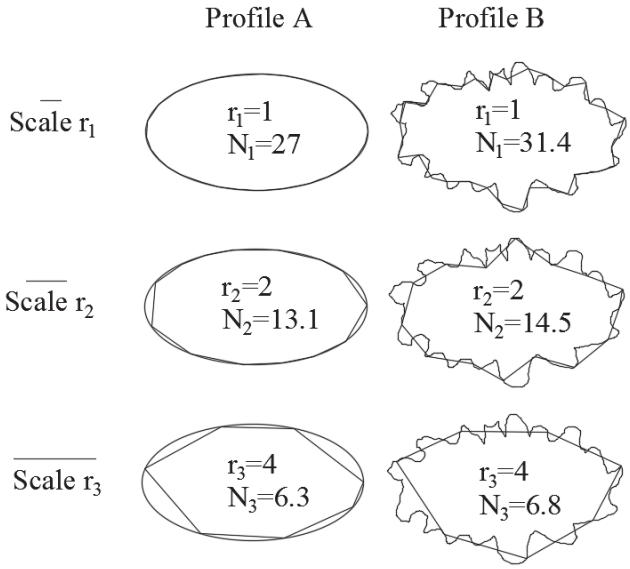

Figure 2.5 Various segment lengths *r* applied to two different profiles (modified after Cox and Budhu 2008).

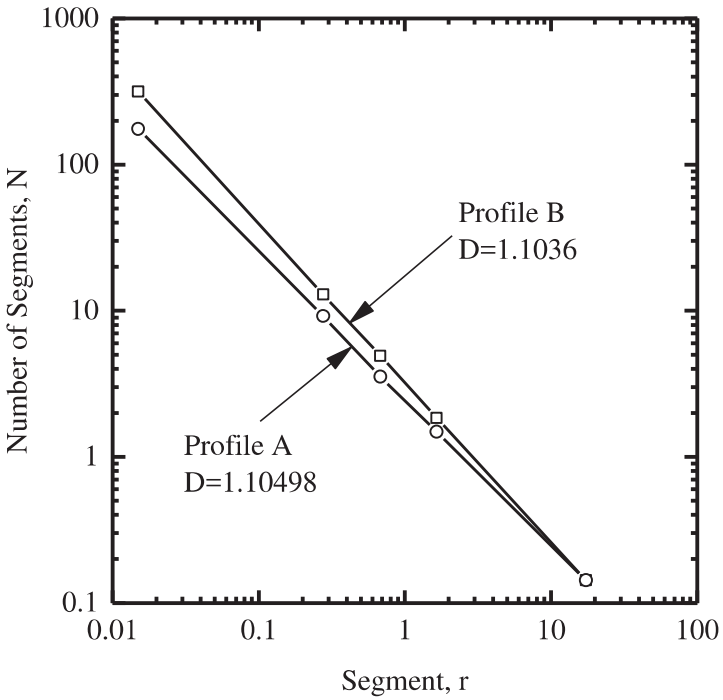

Figure 2.6 Log-log plot between the segment r and the number of segments N (modified after Cox and Budhu 2008).

2.5 Strength testing of soils

To quantify the shear strength of soils, the Mohr-Coulomb strength criterion is often used:

$$s = c + \sigma' \tan\phi \tag{2.12}$$

where

s = shear stress (kPa)

c = cohesive intercept

σ' = effective normal stress (kPa)

ϕ = friction angle of the soil

The main objective of the shear tests is to obtain the shear force and volume change of the material that is sheared (Germaine and Germaine 2009). Figure 2.7 shows a typical schematic of shear tests.

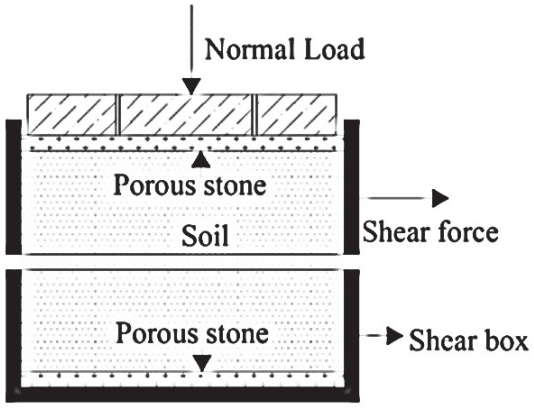

Figure 2.7. Schematic of a typical direct shear test equipment (modified after Das 2013).

Figure 2.8 shows the typical response observed for direct shear tests performed on soils with different densities. Soil response depends on the density of the soil sample and the magnitude of the normal stress applied. Generally, dense and medium dense sand samples show a well-defined peak in the shear-displacement curve. On the other hand, loose samples show a shear-displacement curve with no peak. The peak friction angle of the sand (due to dilative response) corresponds to the peak in the shear-deformation curve. The critical-state friction angle corresponds to the stage at which the shear stress (see Figure 2.8) and vertical deformation approach a plateau as the horizontal shear displacement increases.

Figure 2.9(a) and Figure 2.9(b) show the stress-strain curves of drained triaxial compression tests performed with different confining stresses. Figure 2.9(a) shows that

there is a reduction of the peak friction angle with increase in the confining stress. After the peak is reached by each sample, a plateau develops with increasing strain, indicating that critical state was reached. Also, the peak shear strength is observed at different values of axial strain ε_a. Figure 2.9(b) shows the same results, but in terms of principal effective stress ratio $\sigma'_1/\ \sigma'_3$ (note that as the normal stress on a sample increases, dilatancy is suppressed and peak strength is no longer observed).

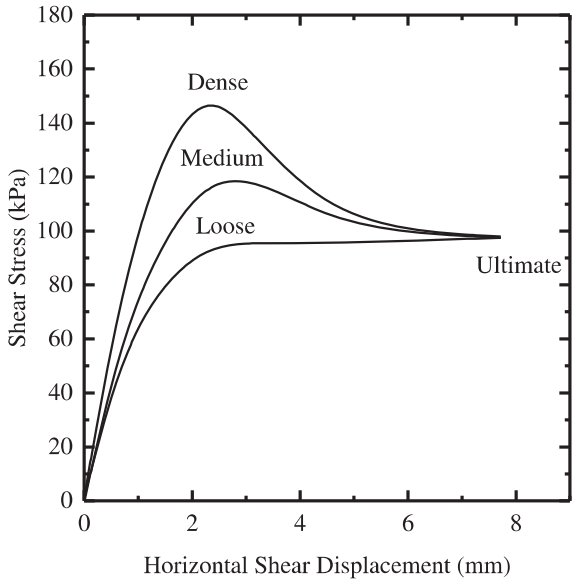

Figure 2.8 Typical shear stress versus horizontal shear displacement curves for dense, medium and loose sand specimens (modified after Das 2013).

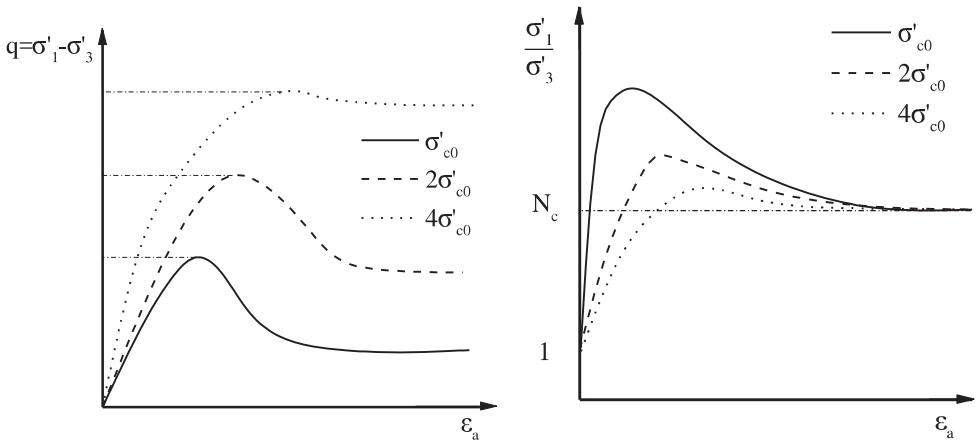

(a) (b)

Figure 2.9 Schematic of the stress-strain curves from drained triaxial compression tests carried out o three identical samples with differernt confining stresses: (a) $q= \sigma'_1 - \sigma'_3$ versus axial strain ε_a; (b) principal effective stress ratio σ'_1/σ'_3 versus axial strain ε_a (modified after Salgado 2008).

The ring shear test is used to investigate the behavior of soil at large displacements. The first ring shear equipment was developed jointly by the Norwegian Geotechnical Institute (NGI) and Imperial College. A shearing zone develops in the horizontal plane created by the boundary between the upper and lower ring (Terzaghi et al. 1996).

According to Sadrekarimi and Olson (2010), the ring shear equipment has many advantages in comparison with the direct shear equipment. Some of these advantages are: a) unlimited shear displacements; b) shearing on depositional planes; c) continuous rotation of the orientations of the principal stresses, and d) constant cross-sectional area during shearing. Figure 2.10 shows a schematic of the ring shear test equipment.

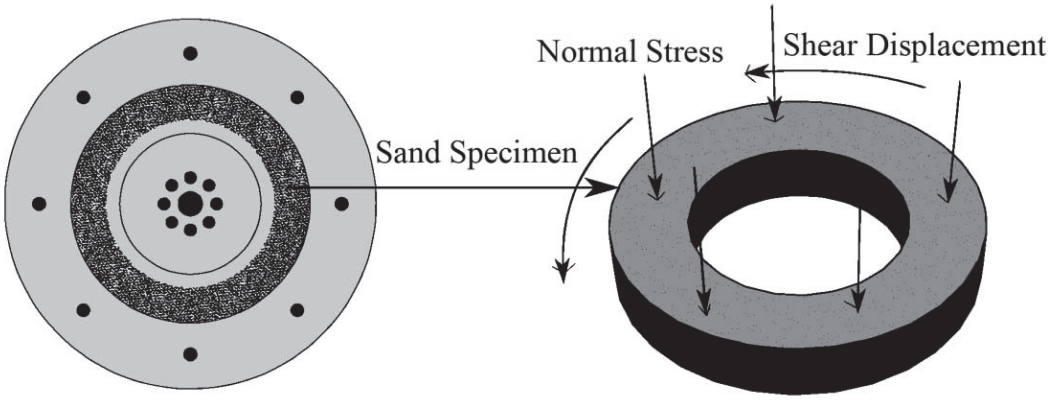

Figure 2.10 Schematic diagram of the RSR-150 residual ring shear testing equipment.

2.6 Particle crushing characterization

Particle breakage or crushing occurs when the applied stresses surpass the strength of the soil particles (Lade et al. 1996). According to Hardin (1985), the stress-strain response of a soil is influenced by the stage at which crushing or particle breakage happens in the course of loading and deformation. One-dimensional compression or isotropic compression produce particle breakage and volume reduction. In the case of triaxial compression or simple shear tests, both tests produce breakage of particles or crushing at inter-particle contacts, reducing the dilative response of soil. The amount of particle crushing that takes place in an element of soil subjected depends on the: (1) particle-size distribution, (2) particle shape, (3) particle hardness, (4) confining stress and loading path; and (5) sample density (Hardin 1985).

2.6.1 Main factors that affect particle crushing

2.6.1.1 Particle-size distribution

According to Hardin (1985), in general, particle crushing increases with the size of the particles because the contact stresses increase with particle size and because large particles tend to have more flaws than small particles. However, if larger particles are surrounded by smaller particles, and thus have a high coordination number (the coordination number is defined as the number of particles neighboring any given particle), contact stresses are reduced, implying also a reduction in particle damage. Accordingly, well-graded soils are less susceptible to particle crushing than poorly-graded soils (Lee and Farhoomand 1967). Figure 2.11 shows the definition of coordination number and Figure 2.12 shows a well-graded soil and a poorly-graded soil.

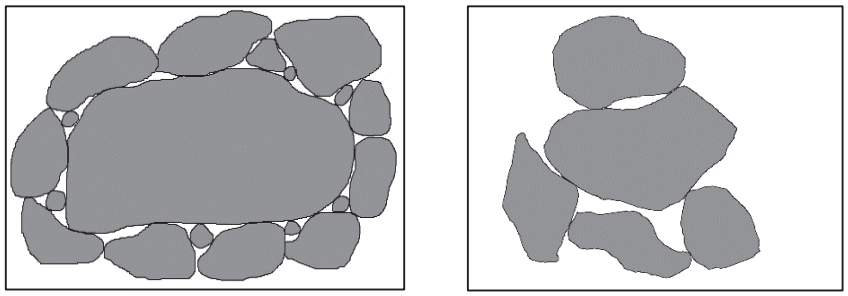

(a) (b)

Figure 2.11 Definition of coordination number: (a) high coordination number; (b) low coordination number.

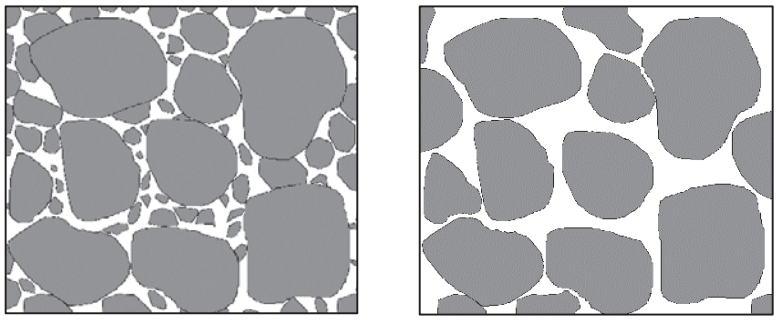

(a) (b)

Figure 2.12 Soil gradation: (a) well-graded soil; (b) poorly-graded soil.

As particle crushing progresses, the amount of fines presents in a soil increases, thereby increasing the coordination number of the large particles and reducing their susceptibility to additional crushing. Large particles tend to have more contact points with small particles, which, on the other hand, tend to have progressively lower coordination number (as there are fewer smaller particles surrounding the small particles), and thus small particles tend to become more easily crushed as crushing progresses (Mitchell and Soga 2005).

2.6.1.2 Particle shape

Another factor that contributes to particle crushing is particle shape. Angular particles are more susceptible to crushing because of the stress concentration on their asperities and angularities. Also, as angular particles are more elongated than rounded or sub-rounded particles, stresses can concentrate on their thinnest dimension, splitting them apart (Lade et al. 1996).

Lee and Farhoomad (1967) carried out anisotropic and isotropic triaxial compression tests on sands with rounded and angular particles; their study showed that the angular sand was more compressible and underwent more particle crushing than the rounded sand. The initial sand gradation (before particle crushing) had 2% of the particles finer than 1mm of particle size diameter, and, after particle crushing, this value increased to 10%. Figure 2.13 shows a schematic drawing of angular and rounded particle shapes.

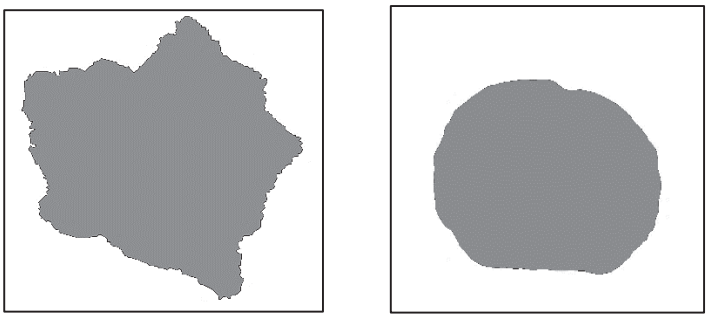

(a) (b)

Figure 2.13 Particle shape: (a) angular particle; (b) rounded particle.

2.6.1.3 Effective confining stress and effective stress path

Crushing increases as the confining stress increases. Compression and extension triaxial tests performed by Lade et al. (1996) on Cambria sand with different densities demonstrated that particle crushing increased the most for confining stress ranging from 5 to 30 MPa for dense Cambria sand, while at high confining stress, the amount of particle crushing taking place seemed to be constant. Particle damage increases not only with increases in confining stresses but also with increases in strain levels (Lade et al. 1996).

Particle damage is more pronounced during shearing than during isotropic compression (Sadrekarimi and Olson 2010). Mesri and Vardhanabhuti (2009) indicated based on 61 oedometer tests on 57 sands that the yield stress varies from 0.3 MPa for an angular biogenic carbonate sand to 30 MPa for a well-rounded quartz sand. Wang et al. (2002) performed a series of ring shear tests on soil samples from the Hiegaesi landslide and found that particle damage started for normal stresses as low as 40 kPa.

2.6.1.4 Void ratio

Figure 2.14 shows the distinct phases of a soil element describing the relationships between weights and volumes of the soil particles, voids and interstitial water. The void ratio *e* is the soil parameter that describes how dense or how loose is the soil, which is defined as the relationship of the volume of voids to the volume of solids, Figure 2.15 shows a schematic diagram with the definition of void ratio. At small void ratios, the number of particle contacts is greater than for high void ratios, allowing a better distribution of contact stresses and reducing particle damage. A series of triaxial compression and extension triaxial tests under drained and undrained conditions were carried out on Cambria sand by Lade et al. 1996; in their study it was found that the void ratio is directly related to the amount of particle crushing.

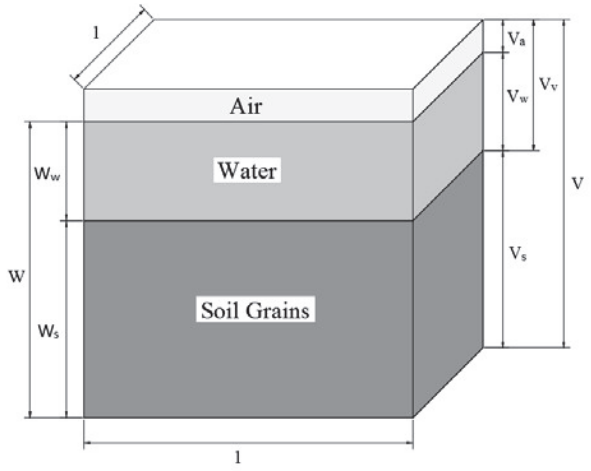

Figure 2.14 Phase diagram of the distinct phases separated by three layers (modified after Salgado 2008).

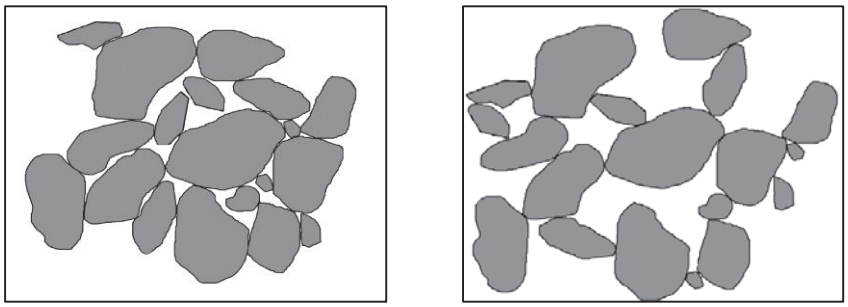

(a) (b)

Figure 2.15 Void ratio: (a) small void ratio (dense soil); (b) high void ratio (loose soil).

2.6.1.5 Particle hardness

Generally, stronger particles undergo less particle crushing for a given stress than weaker particles (Hardin 1985; Lade et al 1996). According to Feda (2002), quartz grains derived from an alluvial sand are stronger and less susceptible to particle crushing than feldspathic grains originated from weathering of granite. Under normal compression tests,

the yield stress in calcareous sands is lower than that in siliceous sands because calcareous grains are weaker and more brittle (McDowell and Bolton 1998).

Luzzani and Coop (2002) carried out a series of ring shear and direct shear tests on carbonate and quartz sands to investigate particle crushing during shearing. More particle crushing was observed for the carbonate sand than for the quartz sand.

2.6.2 Particle damage mechanisms

Nakata et al. (2001) defined five levels of particle damage by analyzing microscopic images of particles before and after testing. Type I is the level where no particle damage is observed; Type II is the level at which damage occurs by breakage of asperities; Type III is the level at which there is abrasion of asperities and particle fracture; Type IV is the level at which a particle is split into two or more particles; and Type V is the level at which a particle turns into powder.

Daouadji et al. (2001) classified particle breakage in three different modes: abrasion, when the particle-size distribution curve remains the same with a small increment of fine particles; attrition, when the particle breaks into one smaller particles with the creation of several smaller particles; and, fracture, when the particle breaks into smaller particles of equal sizes. Figure 2.16 shows the three levels of particle breakage defined by Daouadji et al. (2001).

Based on compression tests performed on granular materials, Mesri and Vardhanabhuti (2009) determined three levels of particle damage. In level I damage, there is abrasion or grinding of particle surface asperities. In level II damage, there is breaking

or crushing of particle surface asperities, while in level III damage, particles experience fracturing, splitting or shattering.

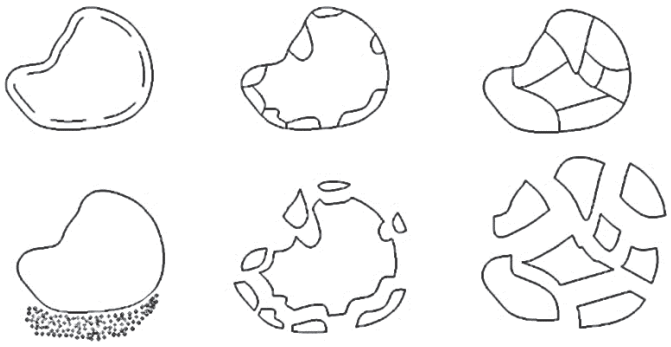

Figure 2.16 Levels of particle breakage (modified after Daouadji et al. 2009).

2.6.3 Particle crushing during compression

During one-dimensional compression, sand compresses due to particle rearrangement and particle crushing (during the rearrangement process, the stresses at inter-particle contacts may exceed their strength). Two mechanisms are operative during one-dimensional compression tests: (1) particle locking and (2) particle unlocking. The first mechanism is operative when the sand sample undergoes compression, resulting in an increase in its stiffness, while the second mechanism reflects inter-particle slippage and particle damage, with a resulting decrease in the stiffness of the sand sample. During compression of sandy soils, both mechanisms are operative simultaneously (Mesri and Vardhanabhuti 2009).

Particle crushing during one-dimensional compression tests starts at the yield point of the compression curve, which coincides with the maximum value of the compressibility

index. At very low stresses, where there are broad interparticle contact forces, the particle breakage begins, as the confining stresses become to be higher, the amount of fines increases because of the crushing of the particles. Consequently, the particle damage in one dimensional compression tests is a continuous process that depends on the stress applied (Mitchell and Soga 2005).

Nakata et al. (2001) performed a series of one-dimensional compression tests on silica sand and showed that particle damage depends on sand gradation; poorly-graded sands had compression curves with more marked yielding. Altuhafi and Coop (2011) found that well-graded sand has a lower compressibility index than poorly-graded sand (the yield point was not evident for the well-graded sand because of less particle breakage); this can be explained by the fact that the well-graded sand had a higher coordination number than the poorly-graded sand.

Poorly-graded sands may become well graded after one-dimensional compression tests because of particle damage. Hagerty et al. (1993) performed a series of one-dimensional compression tests on Ottawa sand at very high stresses (there was significant change in gradation as the confining stress increased). Figure 2.17 shows the grain size distribution curves for Ottawa sand before and after the 1D compression tests.

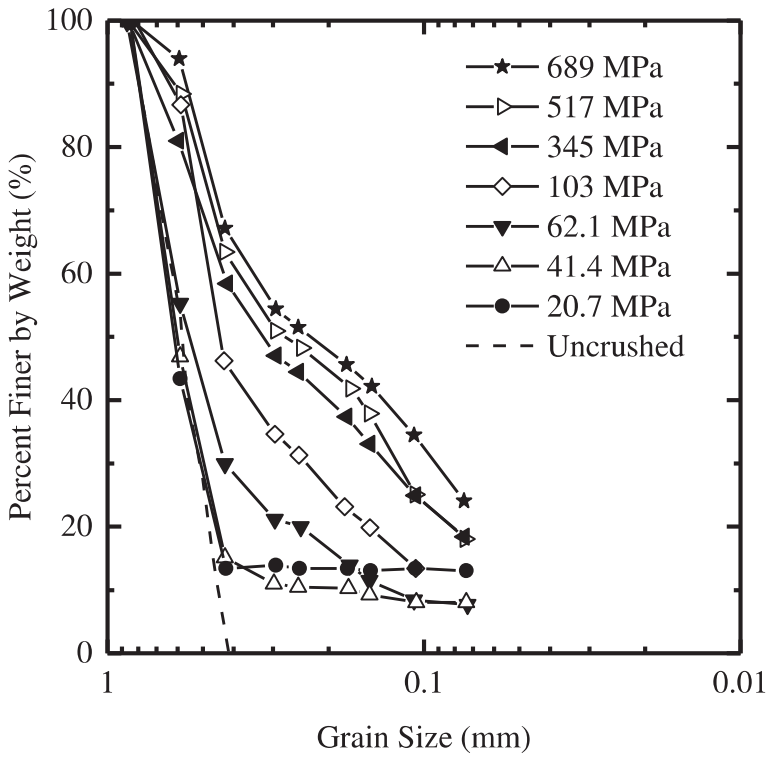

Figure 2.17 Grain size distribution curves for Ottawa sand before and after 1D compression tests (modified after Hagerty 1993).

Altuhafi and Coop (2011) carried out two one-dimensional compression tests (with normal stresses of 30 MPa and107 MPa) on Leighton Buzzard sand. Large particles did not exhibit any damage and there was almost no change in particle surface roughness for the sand tested with a 30 MPa normal stress. However, damage was intense with significant change in particle surface roughness for almost all particles for the sand sample subjected to a normal stress of 107 MPa. As expected, crushing depends on the normal stress applied in compression tests. According to their study, particle breakage processes end when a constant grading is achieved after the application of high stresses.

Karimpour and Lade (2010) carried out a series of triaxial compression tests on dense samples of Virginia Beach sand. In their study, a close relationship between time and particle crushing was observed in long-term creep tests performed with high confining stresses. Grain crushing was quantified by Hardin's relative breakage parameter, which was found to be proportional to the confining stress applied and amount of creep observed in each sand sample.

According to Mesri and Vardhanabhuti (2009), the term creep should not be used to refer to secondary compression during drained, laterally constrained or one-dimensional loading or drained. Which is due to the fact that time-dependent deformation because of creep may result a global failure, while the secondary compression does not.

According to Lade and Liu (1998) two conclusions were drawn from their studies: (1) the amount of secondary compression increases as the confining stresses become to be significant, and (2) loose sand and sand with brittle particles are more time-dependent deformation than dense sand or sands with stronger particles.

2.6.4 Particle crushing during shearing

To evaluate how much crushing is produced during shearing tests, the gradation of the shear band can be analyzed and compared with the gradation of the uncrushed sand. Sadrekarimi and Olson (2010) performed ring shear tests on three sands with different mineralogical compositions; these authors found that the degree of particle damage depends on the normal stress applied, shear displacement level, particle mineralogy, grain size distribution, drainage conditions and soil fabric. Sadrekarimi and Olson (2010) observed that particle damage was greater in drained tests than in constant volume tests.

Also, they found that at larger shear displacements, the fines content of the sand increased (the sand became well graded), but as shearing progressed further, the rate of particle damage decreased, with sliding and rolling of the particles predominating over particle damage. The critical state is achieved with a constant volume, constant shear stress and constant confining stress after very large shear displacements. Also, in their study, it was observed that the coarser particles remained almost intact, with just abrasion and shearing off of its asperities, and thereby increasing the amount of fines.

Coop et al. (2004) carried out a series of ring shear tests on Dog's Bay sand, a biogenic carbonate sand. They found that the particle breakage continues to very large strains, further than those achieved by triaxial tests, and concluded that the constant-volume state reached in triaxial tests is just an apparent critical state. The authors explained that the apparent critical state in triaxial tests is a result of the balance between the dilative strains due to particle rearrangement and compressive strains due to particle breakage. Dog's Bay sand achieved constant grading after very large shear displacements, with particle damage depending on both the normal stress and particle gradation.

2.6.4.1 Shear band formation

The thickness of shear bands is usually related to the mean grain size (D_{50}) of the sand (Viggiani et al. 2001). According to Finno (1997), during plane strain compression tests on loose sands, the shear band thickness ranges from $10D_{50}$ to $25D_{50}$. Sadrekarimi and Olson (2009) studied shear band formation in ring shear tests performed on three different sands using a solid confining ring-type ring shear device. The shear bands were determined

after the ring shear tests based on visible particle damage and change of sand color (the shear bands were formed at the base of the sample). Most of the tests showed a constant thickness equal to about 10 times D_{50}. Figure 2.18 shows the evolution of the shear band, as observed by Sadrekarimi and Olson (2009) in ring shear tests.

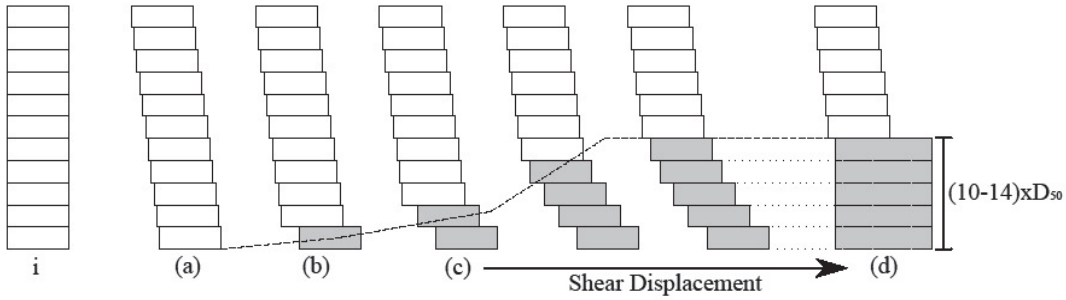

Figure 2.18 Shear band evolution on sand column during ring shear tests: (i) before the shear test; (a) before shear localization; (b) initiation of shear localization around 6 mm of shear displacement; (c) – (d) evolution of the shear band with shear displacement (modified after Sadrekarimi and Olson 2010).

According to Sadrekarimi and Olson (2010), the shear band evolves with shearing. Also, it was found that there are two shearing mechanisms within the shear band: (1) sand dilation within the shear band with an increase of the shear resistance, and (2) sand contraction due to particle damage and reduction of shear resistance (this was referred to as net "contraction"). The same behavior was confirmed by Ghafghazi et al. (2014) and Hyodo et al. (1999), who found that particle breakage increases after the peak in dilative response of the sand.

2.6.5 Quantification of particle crushing

Particle breakage is assessed through the grain-size distribution (GSD) curves before and after loading. To evaluate the degree of crushing, Hardin (1985) introduced three parameters, which are called breakage potential, total breakage, and relative breakage.

2.6.5.1 Breakage potential

Figure 2.19 shows that the breakage potential is defined as the area between the straight line at 0.075 mm and the initial grain size distribution curve before testing (D > 0.075 mm).

The potential for breakage b_p of a particle of diameter D (mm) is defined by:

$$b_p = \log_{10}\left[\frac{D}{0.075}\right] \qquad for \quad D \geq 0.075mm \tag{2.13}$$

$$b_p = 0 \qquad for \quad D < 0.075mm \tag{2.14}$$

The breakage potential B_p is represented by the integral:

$$B_p = \int_0^1 b_p dp \tag{2.15}$$

where:

b_p = potential for breakage of a given size portion

p = fraction passing a given sieve size as a number between 0 and 1

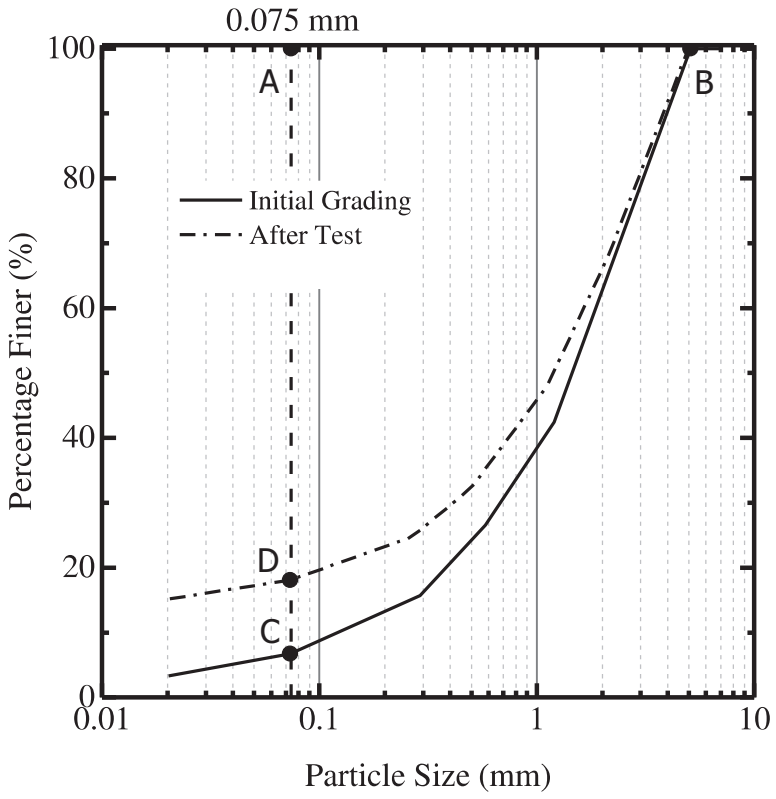

Figure 2.19 Area BCAB defined as breakage potential of the initial grading (modified after Hardin 1985).

In this study, the definition of b_p was extended to include particle diameters greater than 0.001 mm ($D > 0.001$ mm) to consider the larger percentage of fines produced during particle crushing in the ring shear tests. Hardin (1985) did not considered silt- and clay-sized particles because he argued that particle damage is more important in coarser particles and because of the larger stresses required to crush silt- and clay-sized particles (Sadrekarimi and Olson 2009).

2.6.5.2 Total breakage

Figure 2.20 shows the total breakage parameter, determined from the GSD curves of the soil before and after loading. Figure 2.21 shows the particle-size distribution curves before and after loading of crushed granite (Lee and Farhoomand 1967).

Total breakage is defined as:

$$B_t = \int_0^1 \left(b_{p0} - b_{pl} \right) dp \tag{2.16}$$

where

B_t = total breakage

b_{p0} = potential for breakage before crushing

b_{pl} =potential for breakage after crushing

dp = fraction passing a given sieve size as a number between 0 and 1

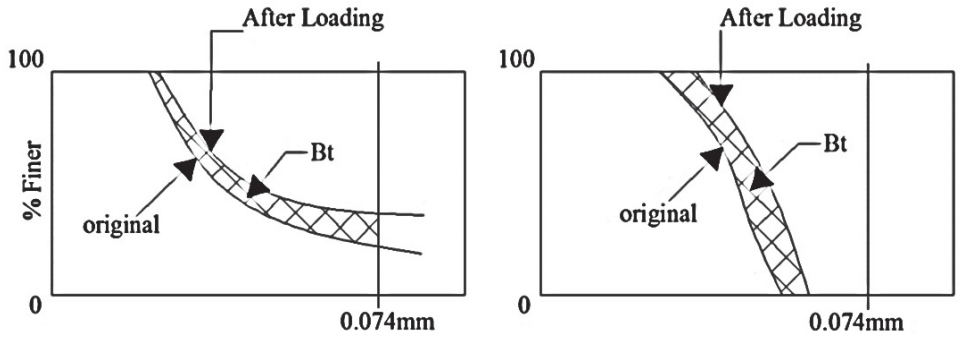

Figure 2.20 Description of total breakage (modified after Hardin 1993).

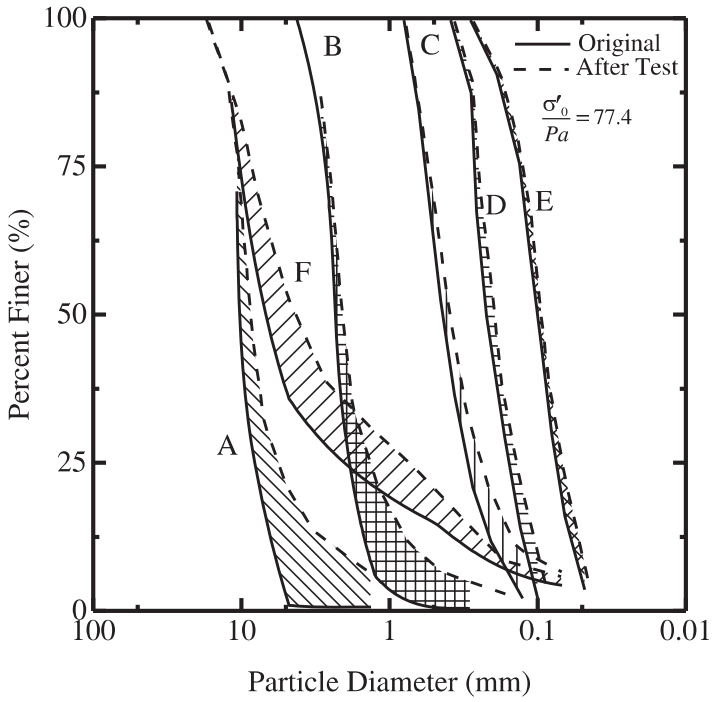

Figure 2.21 Total breakage (modified after Lee and Farhoomand 1967).

2.6.5.3 Relative breakage

Hardin (1985) indicated that if the grain size distribution is the only changeable parameter, the total breakage (B_t) is proportional to the breakage potential (B_p), calling it relative breakage:

$$B_r = \frac{B_t}{B_p} \tag{2.17}$$

K. L. Lee and Farhoomand (1967) performed isotropic compression tests on crushed granite with an effective stress of 80 kg/cm^2. The results of six tests are shown in Figure 2.21. Figure 2.22 shows the relative breakage obtained after each test as performed by Lee and Farhoomand (1967) and it clearly shows that the relative breakage does not depend on the grain-size distribution.

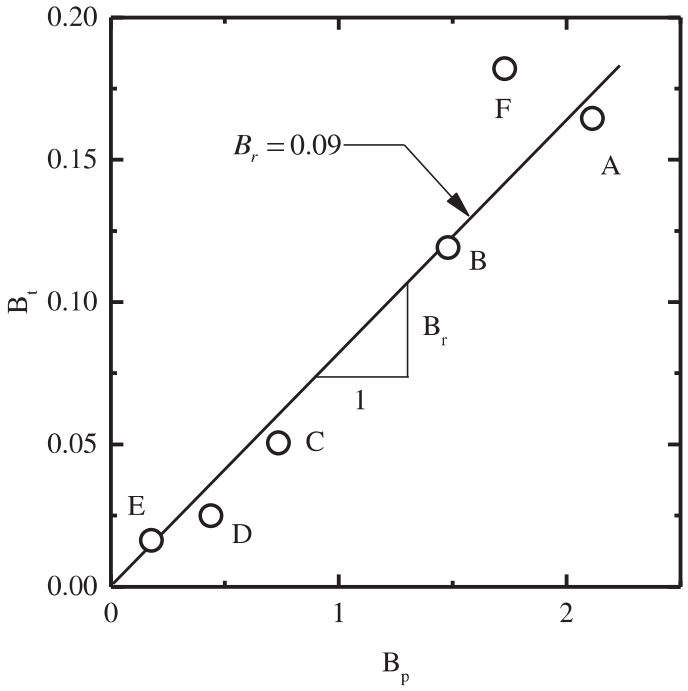

Figure 2.22 Relative breakage (modified after Lee and Farhoomand 1967).

Hardin (1985) showed that the breakage potential increases with the confining stress. Figure 2.23 shows the variation of the relative breakage parameter B_r for three samples of crushed granite angular soil with initial B_p=1.47. The samples were subjected to a stress path $R=\sigma'_1/\sigma'_3$, where σ'_1 is the major principal effective stress and σ'_3 is the minor principal stress. It can be seen in Figure 2.23 the effect of effective stress path on relative breakage, where B_r is normalized by the atmospheric pressure Pa and the minor principal effective stress was used to show the effective stress.

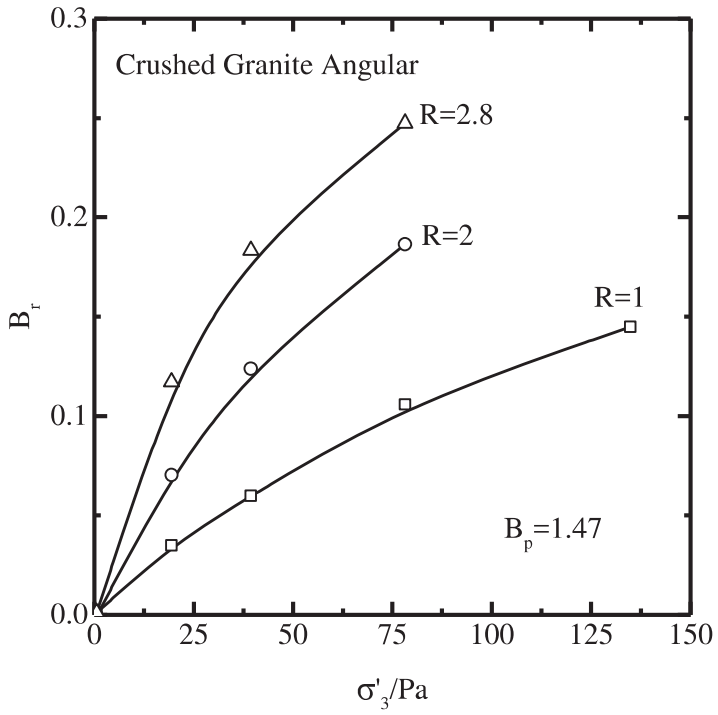

Figure 2.23 Levels of particle breakage (modified after Daouadji et al. 2009).

CHAPTER 3. EXPERIMENTAL PROGRAM

3.1 Index properties

3.1.1 Specific gravity test

The specific gravity is the relationship between the mass density of soil particles to the mass density of distilled water. The equation which relates these quantities is:

$$G_{s,t} = \frac{\rho_s}{\rho_{w,t}} \tag{3.1}$$

where:

G_{st}= specific gravity of soil solids at the test temperature (dimensionless)

ρ_s= mass density of solids (g/cm^3)

$\rho_{w,t}$= mass density of water (g/mL)

The standard used to determine the specific gravity of soils is the ASTM Standard D854-06, which uses the submersion technique. Due to the variations in temperature, the pycnometer must first be calibrated using:

$$V_p = \frac{M_{pw,c} - M_p}{\rho_{w,c}} \tag{3.2}$$

where:

V_p= pycnometer calibrated volume (mL)

$M_{pw,c}$= mass of the pycnometer and water at the calibration temperature (g)

M_p= average mass of the dry pycnometer at calibration temperature (g)

$\rho_{w,c}$ = mass density of water at the calibration temperature (g/mL) (which is provided in ASTM D854-06).

After calibration of the pycnometers was completed, the mass of the pycnometer plus water at the test temperature was calculated using the following equation:

$$M_{pw,t} = M_p + \left(V_p \cdot \rho_{w,t}\right) \tag{3.3}$$

where

$M_{pw,t}$= mass of the pycnometer and water at the test temperature (g)

M_p= average calibrated mass of the dry pycnometer (g)

V_p= average calibrated volume of the pycnometer (mL)

$\rho_{w,t}$= density of water at the test temperature (g/mL)

The specific gravity at the test temperature of the soil solids is calculated as:

$$G_{s,t} = \frac{\rho_s}{\rho_{w,t}} = \frac{M_s}{M_{pw,t} - \left(M_{pws,t} - M_s\right)} \tag{3.4}$$

where

$G_{s,t}$= specific gravity of soil solids at the test temperature (dimensionless)

ρ_s= density of the solids (g/cm^3)

$\rho_{w,t}$= density of water at the test temperature (from the standard tables) (g/mL)

M_s= mass of the oven dry soil solids (g)

$M_{pws,t}$= mass of pycnometer, water and soil solids at the test temperature (g)

Finally, the specific gravity of soil solids at 20°C was obtained from:

$$G_{20°C} = k.G_t \tag{3.5}$$

where

k= temperature coefficient from the standard tables (dimensionless)

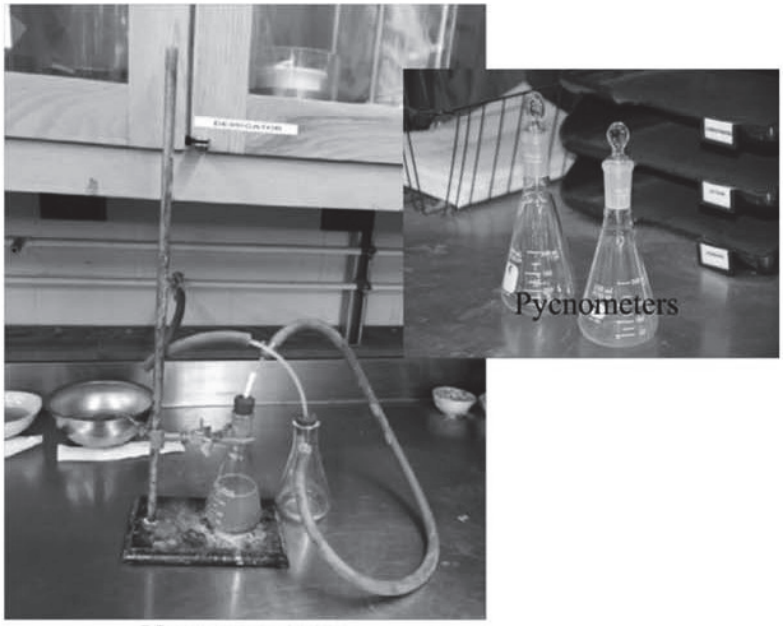

Vacuum system

Figure 3.1 Equipment used to obtain the specific gravity of Ohio Gold Frac sand.

3.1.1.1 Equipment

To carry out the specific gravity test, two pycnometers of 250 ml were employed. Figure 3.1 shows the equipment for the determination of the specific gravity of OGF sand. Additionally, the following instruments and devices were used: thermometer; beaker; vacuum system; and a cooler.

3.1.1.2 Sample preparation

For the sample preparation, 50 grams of dry sand was selected from the soil sample and mixed with 100 grams of distilled water.

3.1.1.3 Calibration of pycnometers

Initially, the mass of the pycnometers with caps was obtained (M_p). Then, the pycnometers were filled with distilled water up to the calibration level and the caps were placed. Then, the pycnometers were left in a cooler for about 3 hours for stabilization of the temperature; next, the mass of the pycnometers with water was measured ($M_{pw,c}$). The process was repeated three times at different temperatures.

3.1.1.4 Specific gravity test setup

At first, the sand sample was poured into the pycnometer, and vacuum was applied for one hour; then, the pycnometers were filled with distilled water above the calibration line and placed into the cooler. After temperature stabilization of the pycnometers with water and soil for about three hours, the process was repeated three times at different temperatures. The mass of the pycnometers with water and soil ($M_{pws,t}$) were measured. The specific gravity of Ohio Gold Frac sand was calculated using Equation (3.5).

3.1.2 Minimum and maximum relative density test

The relative density of a soil mass can be determined through the minimum and maximum density parameters. The relative density of sand can be expressed in two ways. In terms of density:

$$D_R = \frac{\rho_{\max}}{\rho_d} \cdot \frac{\rho_d - \rho_{\min}}{\rho_{\max} - \rho_{\min}} \cdot 100\% \tag{3.6}$$

where

D_R= relative density (dimensionless) (%)

ρ_d= dry mass density (g/cm^3)

ρ_{min}= minimum mass density (g/cm^3)

ρ_{max}= maximum mass density (g/cm^3)

And in terms of void ratio:

$$D_R = \frac{e_{\max} - e}{e_{\max} - e_{\min}} \cdot 100\% \tag{3.7}$$

where

e= void ratio (dimensionless)

e_{max}= maximum void ratio (dimensionless)

e_{min}= minimum void ratio (dimensionless)

ASTM Standard D4254-16 and ASTM Standard D4253-16 (2016) were used to obtain the minimum and maximum densities of OGF sand. The density of soil is calculated from the mass of soil divided by the volume:

$$\rho = \frac{M_s}{V} \tag{3.8}$$

where

M_s= mass of solids (g)

V= total volume (cm^3)

The phase relationships of the soils were used to obtain the mass of solids M_s. The total volume $_V$ is obtained from the volume of solids and the volume of voids:

$$V = V_v + V_s \tag{3.9}$$

where

V_v= volume of voids (cm^3)

V_s= volume of solids (cm^3)

and

$$V_s = \frac{M_s}{G_s \rho_w} \tag{3.10}$$

where

G_s= specific gravity (dimensionless) (previously determined in the specific gravity test)

ρ_w= density of the water (g/cm^3)

The maximum void ratio (e_{max}) and minimum void ratio (e_{min}) are determined from:

$$e_{\max} = \frac{G_s \gamma_w}{\rho_{\min}} - 1 \tag{3.11}$$

where

e_{max}= maximum void ratio (dimensionless)

G_s= specific gravity (dimensionless) (previously determined in the specific gravity test)

γ_w= specific weight of water (N/m^3)

$\rho_{\min}$ = minimum density (N/m^3)

$$e_{\min} = \frac{G_s \gamma_w}{\rho_{\max}} - 1 \tag{3.12}$$

where

e_{min}= minimum void ratio (dimensionless)

G_s= specific gravity (dimensionless) (previously determined in the specific gravity test)

γ_w= specific weight of water (N/m^3)

ρ_{max} = maximum density (N/m^3)

3.1.2.1 Equipment

To obtain the minimum and maximum densities, the standard compaction mold with collar was used. Figure 3.2(a) shows the funnel and mold used for the minimum density determination of OGF sand. Figure 3.2(b) shows the shaking table, rubber hammer and surcharge used for the maximum density determination of OGF sand.

3.1.2.2 Sample preparation

For sample preparation, 2,000 grams of dry sand were employed. The sand sample was very well mixed to obtain an equal distribution of particle sizes.

3.1.2.3 Minimum density test setup

First, the mass of the mold without the collar was obtained (M_m). Then, the dimensions of the mold, needed to compute the volume of the mold (V_m), were measured. With the help of a funnel, the soil was poured into the mold (following a spiral path); the free fall height was 0.5 inch. The collar was removed and the excess of the soil was trimmed off. The mass of the mold with soil (M_{ms_min}) was obtained. The process was repeated two more times to obtain a final average value.

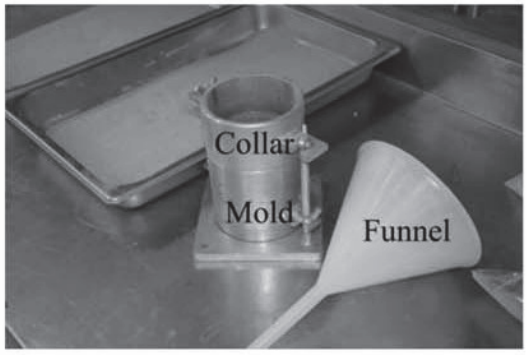

(a)

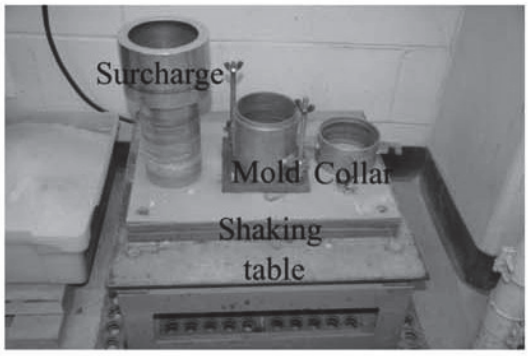

(b)

Figure 3.2 Equipment employed for the determination of: (a) minimum density and (b) maximum density for Ohio Gold Frac sand.

3.1.2.4 Maximum density test setup

First, the mass of the mold without the collar was obtained (M_m). Then, the dimensions of the mold, needed to compute the volume of the mold (V_m), were measured. The mold was filled with Ohio Gold Frac sand and struck by a rubber hammer to allow the settlement of the sand. Next, the mold was placed over the vibratory table and the surcharge was put over it. The vibratory table was on for 8 minutes at a frequency of 60 Hertz. The mold was detached from the vibratory table and the excess of soil was trimmed off. The

mass of the mold with sand (M_{ms_max}) was measured. The entire process was repeated two more times to obtain a final average value.

3.1.3 Grain size analysis

The grain size distribution of Ohio Gold Frac sand was determined before and after particle crushing. For the material retained on the sieve #200, the sieve technique was employed. For the soil that passed the sieve # 200, the sedimentation technique was used.

The sedimentation method is based on Stoke's Law. Stoke's law provides a hydrodynamic equation relating the gravitational and drag forces in a stationary fluid and the terminal velocity of spherical particles (Germaine and Germaine 2009). Stoke's law is expressed by:

$$\nu = \frac{\left(\rho_s - \rho_f\right) g D^2}{18\mu} \tag{3.13}$$

where

ρ_s= mass density of solids (g/cm^3)

ρ_f= mass density of fluid (g/cm^3)

g= acceleration of the gravity (cm/s^2)

μ= viscosity of fluid (MPa-s)

As can be seen in Equation (3.13), the terminal velocity ν (cm/s) is directly related to the square of the particle diameter D (mm).

ASTM D4253-16 and ASTM D422-63 provided the standard test procedure and necessary equipment required to perform mechanical sieve analyses and sedimentation of soils.

3.1.3.1 Equipment

The equipment used for the sieve analysis were: a) stack of sieves, b) a scale, c) shaker machine, and d) oven. For the sedimentation technique, the equipment used were: a) hydrometer type 151H or 152H, b) thermometer, c) scale, and d) de-aired water system. Figure 3.3(a) and Figure 3.3(b) show the equipment required for sieve and sedimentation analyses, respectively.

3.1.3.2 Sample preparation

Dry sand was used for the sieve analysis. For the original sand (uncrushed material), 2,000 grams of sand were quartered, and 500 grams were used for the grain size analysis. For the material obtained from one-dimensional compression the entire samples were collected to perform the sieve analysis and the sedimentation analysis of the material that passed the sieve #200. For the ring shear tests, the sand in the shear band was carefully collected with the help of a spatula to perform the sieve and the sedimentation analyses.

Due to the crushing of the sand, the fines content increased after testing; therefore, material passing the sieve #200 was collected for the hydrometer analysis. A solution of 40g/L of dispersing agent (sodium hexametaphostate) was prepared before the sedimentation process. Next, the collected material was mixed with 125mL of the solution. The mixture was left soaking for 24 hours.

(a)

(b)

Figure 3.3 Equipment employed for the grain size distribution: (a) sedimentation analysis (b) sieve analysis for Ohio Gold Frac sand.

3.1.3.3 Sieve analysis test setup

A stack of sieves was prepared as per ASTM D4253-16. Then, the mass of each clean empty sieve (M_{sieve}) was measured. Next, the stack of sieves was placed on the shaker machine and the sand sampler was poured into it. The shaker machine was turned on for

10 minutes. The mass of the sieves with the retained soil ($M_{sieve+sand}$) was recorded. The percentage of soil finer were calculated from:

$$M_{retsoil} = M_{sieve+sand} - M_{sieve} \tag{3.14}$$

$$\%S_{retained} = \frac{M_{sieve+sand} - M_{sieve}}{M_{sSA}} \times 100 \tag{3.15}$$

$$\%\mathrm{S}_{finer} = 100 - \sum_{n=1}^{n} \%S_{retained} \tag{3.16}$$

where

$M_{retsoil}$= mass of retained sand (g)

$M_{sieve+sand}$ = mass of the sieve with soil (g)

M_{sieve}= mass of the sieve (gr)

M_{sSA}= initial soil mass (gr)

$\%S_{retained}$= percentage of soil retained (%)

$\%S_{finer}$= percentage of soil finer (%)

The experimental error for sieving is analyzed as part of experimentation. The sieve analyses were the mechanisms used to obtain the gradation curves of Ohio Gold Frac sand after testing for particle sizes larger than 0.075 mm (D > 0.075 mm). The calibration of sieves is necessary to eliminate any source of error. The experimental error in sieving is related with some variables such as: 1) presence of a large amount of fines; 2) number of particles per sieve; 3) physical properties of the particles; 4) method of shaking the sieve; 5) duration of sieving; 6) variation of sieve aperture; 7) insufficient shaking time and

among others (Allen 2003). According to AASHTO T27-14, after sieving, the weights retained on each sieve and in the pan are added together to obtain a total after testing weight, which must not vary more than 0.5% from the initial weight of the sample (before sieving). In the case where the loss or gain of weight is more than 0.5%, the test is baseless and another sieve analysis has to be performed. The quantification of breakage parameters depends on the grain-size distribution curves obtained after testing, therefore it is necessary to obtain low experimental errors (less than 0.5%) to achieve reliable breakage parameter values.

3.1.3.4 Sedimentation analysis test setup

The soaked material was transferred to a 1,000 ml cylinder. Then, the cylinder was filled with distilled water until the 1,000 ml marked line. Another 1,000 ml cylinder was prepared with 125 ml of dispersing agent to control the change of the solution with temperature. A rubber stopper was placed at the top of the cylinder with the soaked material and shaken up and down for 1 minute.

The cylinder was placed in the upright position, and the readings were taken at the top of the meniscus formed by the hydrometer stem at 30, 60, 90 and 120 seconds. Again, the cylinder was shaken up and down and the readings were taken at 30, 60, 90 and 120 seconds. After the first two minutes, the readings of the hydrometer were recorded at 4, 8, 16 minutes. Also, the temperature of the mixture was recorded.

The zero correction (R_{ZC}) was recorded from the control cylinder. This reading was taken from the top of the meniscus formed by the hydrometer stem and the control solution;

also, the meniscus correction reading (R_{MC}) was recorded (it is the difference between the top of the meniscus and the level of the solution in the control cylinder).

The readings of the hydrometer R_H were recorded for at least 2 days or until the readings were stable. After the test was completed, the mixture was transferred to a large container and oven-dried in order to get the dry soil mass (M_{SH}). Next, the corrected hydrometer readings were obtained from:

$$R_{Corr} = R_H - R_{MC} \tag{3.17}$$

where

R_{Corr}= corrected hydrometer reading (dimensionless)

R_H= hydrometer reading (dimensionless)

R_{MC}= meniscus correction reading (dimensionless)

Table 2 of ASTM D422-63 was used to obtain the hydrometer depth L_H using the corrected reading (R_{Corr}). From Table 3 of ASTM D422-63, the value of k_H, which is a function of the test temperature and specific gravity of the sand, was obtained. Finally, the particle diameter (D) was calculated from:

$$D = k_H \sqrt{\frac{L_H}{t}} \tag{3.18}$$

where

D= particle diameter (mm)

k_H= constant for the particle diameter calculation (dimensionless)

L_H= hydrometer depth (cm)

t= time (min)

Due to temperature effects on readings, the temperature correction (C_T) was applied (from thermal-density tables provide in ASTM D422-63) to calculate the final corrected hydrometer reading:

$$R_{CorrF} = R_H - R_{MC} + C_T \tag{3.19}$$

where

R_{CorrF}= final corrected hydrometer reading (dimensionless)

C_T= temperature correction (dimensionless)

The correction factor a was obtained from Table 1 of ASTM D422-63, according the specific gravity of Ohio Gold Frac sand. The final percent finer was computed as:

$$P_{SH} = \frac{R_{CorrF} \times a}{M_{SH}} \times 100 \tag{3.20}$$

where

P_{SH} = percent finer (%)

a = correction factor for the percent finer calculation

M_{SH} = dry mass of the sand (gr)

3.2 Particle mineralogy study

3.2.1 X-Ray diffraction test

The X-Ray diffraction test on OGF sand was conducted in the Materials Laboratory of Purdue University's Civil Engineering Department. The American Society for Testing and Materials (ASTM) has a file of X-ray diffraction patterns published for different

materials that were compared with the obtained results for OGF sand. Mitchell and Soga (2005) presents a list of the most intense reflections for some common minerals.

3.2.1.1 Equipment

To carry out the X-Ray diffraction test, the equipment used was: 1) Siemens D500 diffractometer (voltage-50kV, current-30mA), 2) mortar and pestle, 3) sieve #200, and 4) sample holder. The diffractometer equipment used Cu-Kalpha radiation of wavelength equal to 1.54 Å. To collect and analyze the data, DataScan and Jade9 software were used, respectively. Figure 3.4 shows the employed equipment for the X-Ray diffraction test carried out on OGF sand.

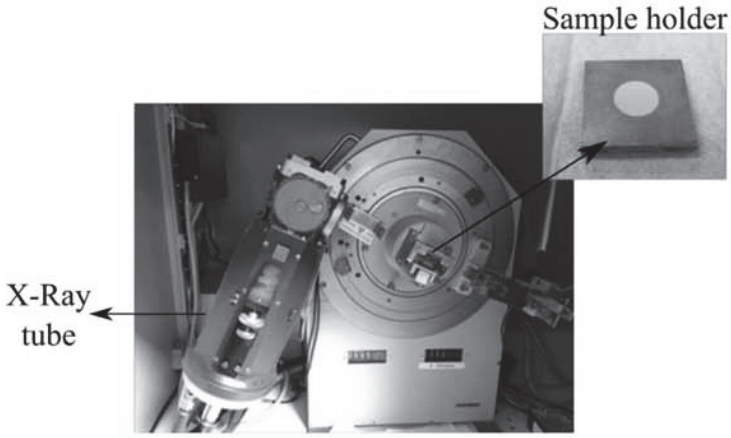

Figure 3.4 Equipment employed to perform the X-Ray diffraction test on Ohio Gold Frac sand.

3.2.1.2 Sample preparation

The sand sample was crushed using a ceramic mortar and a pestle. Then, the soil was passed through the sieve #200. Next, the sand that passed through the sieve # 200 was collected and placed inside of the sample holder. About 30 grams of OGF sand was used. Figure 3.4 shows the sand sample placed inside of the sample holder.

3.2.1.3 XRD test setup

The X-ray diffraction equipment was turned on and the Jade-9 software was initiated in the computer. The sample holder with the sand was placed inside of the diffractometer equipment and the X-ray beam was turn on. After 2 hours, the sand sample was removed from the diffractometer; The distancing (d) was calculated using Equation (2.3).

3.3 Particle morphology analysis

Particle morphology plays an important role on the mechanical behavior of soils. The morphology of the OGF sand was studied before and after the one-dimensional and ring shear tests. The morphology parameters determined for OGF sand before and after crushing are: circularity, roundness, aspect ratio and sphericity (these parameters were obtained using the image-processing tool "ImageJ").

3.3.1 Light microscope and image processing

3.3.1.1 Equipment

To perform the morphology analysis, the equipment used was: 1) AmScope light microscope, 2) charger-coupled camera, 3) light supplier, 4) sample holder, 5) ToupView software, 6) ImageJ processing tool software, and 7) computer. Figure 3.5 shows the equipment used for the morphology analysis performed on OGF sand. There are no standards for particle morphology analyses, but there are particle morphology charts and free software that can be used to obtain particle morphology parameters.

3.3.1.2 Sample preparation

Twenty particles were selected randomly from sieves #20, #40, #60 and #100. From sieve #200, the number of particles was variable because of the difficulty to visualize the small particles. At the end of each analysis, a range of 80 to 100 particles was studied. The morphology of the sand particles was analyzed before and after crushing. The morphology parameters of the uncrushed and crushed sand were compared to quantify the effects of different loading paths.

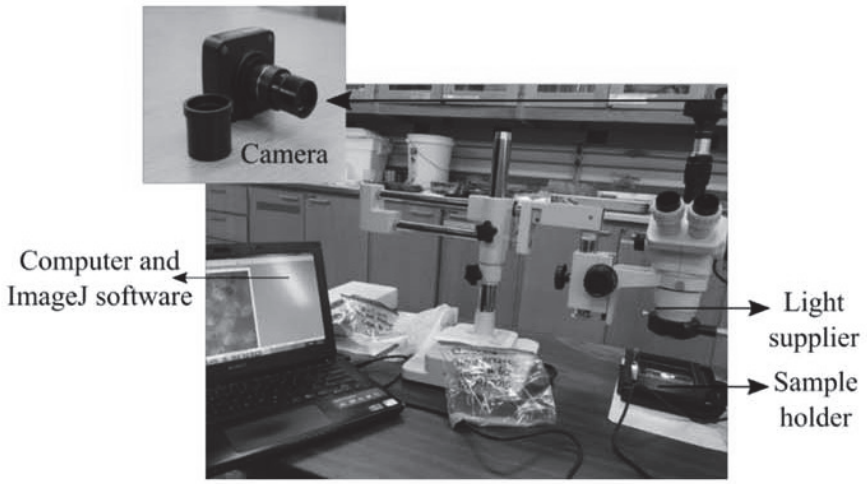

Figure 3.5 Equipment used to study the morphology of Ohio Gold Frac sand.

3.3.1.3 Microscope analysis setup

Twenty particles were placed in an orderly fashion under the microscope (see Figure 3.6.) Then, the couple-charge camera was connected to the computer and the light supply was turned on. The TopView software was initiated in the computer to visualize the image and the scale was set up to obtain the images with real dimensions. Finally, the images were captured.

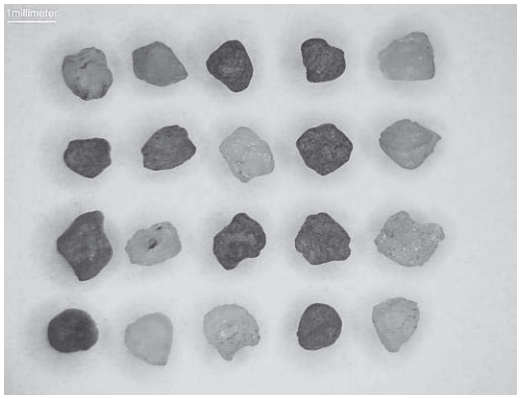

Figure 3.6 Arrangement of twenty particles under the microscope.

3.3.1.4 Image processing tool setup

The ImageJ software was initiated in the computer and the digital images were opened with the software. The scale was set up through the menu "Analyze" with the "set scale" command to obtain the results calibrated in units such as mm or μm. Next, using the sub-menu "Binary", the image was converted to black and white format. Generally, binary images in ImageJ are set to values of 0 and 255, representing images in black and white on an 8-bit scale. Before analyzing the particles profiles, in the menu "Process", the option "Fill Holes" is used to fill the holes of the particles due to the light. Before processing the images of particles, the measurements were adjusted in the command "Measure" in the menu "Analyze". Finally, the sub-menu "Analyze Particles" is used to define the edges of the particles. The results are shown in a summary table which can be exported to a notepad file. At the end, the results were exported to an excel spreadsheet and analyzed to obtain the morphology parameters.

3.4 Strength tests

3.4.1 Direct shear test

The direct shear tests were performed on OGF sand to determine the peak friction angle and critical-state friction angle. The testing procedure and equipment requirements were in accordance with ASTM D3080-D3080M. The sand samples were tested under three different normal stresses: 1) 25 kPa; 2) 50 kPa and 3) 100 kPa.

3.4.1.1 Equipment

The direct shear box is composed of upper and lower boxes. Horizontal displacement is applied to the upper box, shearing of the sand along the horizontal plane. The shear box has two porous stones which are placed below and above the sand sample. The diameter and height of the shear box is 63.3 mm and 30 mm, respectively. Figure 2.7 shows the set up for the direct shear test.

The tests were performed using the GeoTac direct shear machine located at the geotechnical laboratory at Purdue University (Figure 3.7). The system is composed of: 1) a shear box, 2) a vertical load cell (CF: -3564952.85 N/V/V) which measures the vertical force, 3) a horizontal load cell (CF: -768853.2 N/V/V) which measures the shear force, and 4) a vertical LVDT (CF: 76.537718 mm/V/V) which measures the vertical displacement during shearing. All three sensors were calibrated by the manufacturer. Additionally, the system has a GeoTac-DAQ to collect all the test data.

3.4.1.2 Sample preparation

The sand samples were prepared by air pluviation using a funnel. The mold was struck with a rubber hammer in order for the sample to achieve the desired density. Dense samples were prepared with an initial relative density of 85%.

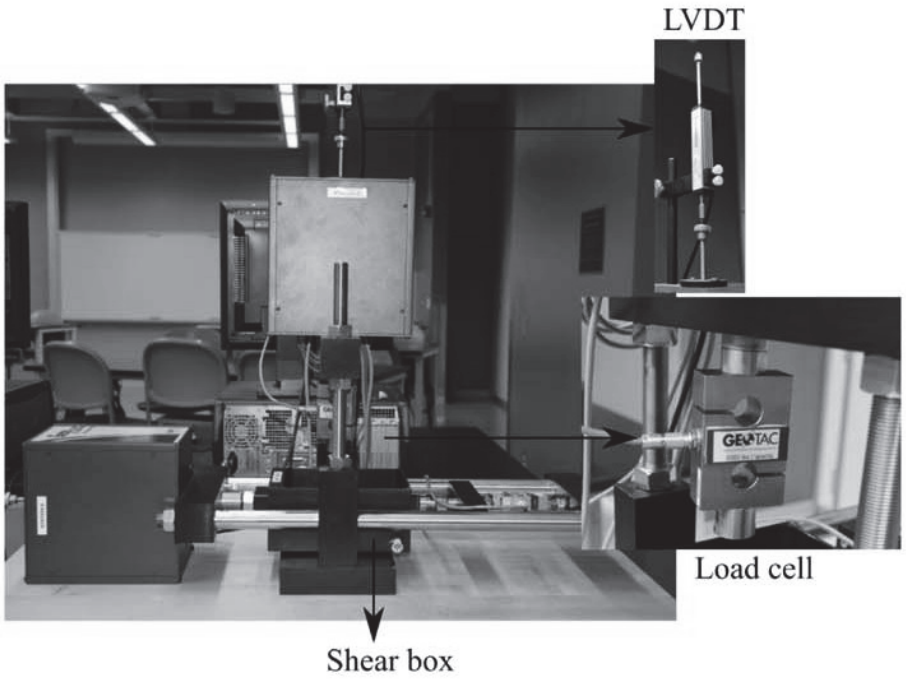

Figure 3.7 Direct shear equipment employed to obtain the peak and critical-state friction angles of Ohio Gold Frac sand.

3.4.1.3 Direct shear test setup

The dimensions of the shear box (height and diameter) were measured to obtain its volume:

$$V_{ST} = \pi \times \left(\frac{D_{ST}}{2} \right)^2 \times H_{ST} \tag{3.21}$$

where

V_{ST}= volume of the shear box container (cm^3)

H_{ST}= height of the shear box container (mm)

D_{ST}= diameter of the container (mm)

The sand sample was poured into the shear box using a funnel. The sides of the mold were slightly struck with a rubber hammer. The mass and volume of the sand sample were determined. The dry unit weight of the sample was calculated as:

$$\gamma_{dST} = \frac{M_{sST}}{V_{sST}} \tag{3.22}$$

where

γ_{dST}= dry unit weight of the sand sample used in the direct shear test (g/cm3)

M_{sST}= height of the shear box container (mm)

V_{sST}= diameter of the container (cm^3)

And the void ratio was obtained from:

$$e_{ST} = \frac{G_s \times \gamma_w}{\gamma_{dST}} - 1 \tag{3.23}$$

where

e_{ST}= void ratio of the sand sample (dimensionless)

G_s= specific gravity of OGF sand (dimensionless)

γ_w= unit weight of water (g/cm^3)

The relative density of the sand sample was calculated as:

$$D_{R_{ST}} = \frac{e_{\max} - e_{ST}}{e_{\max} - e_{\min}} \times 100 \tag{3.24}$$

where

D_{RST}= relative density of the sand sample (%)

e_{max}= maximum void ratio (dimensionless)

e_{min}= minimum void ratio (dimensionless)

To perform a test, the direct shear equipment was turned on and the software DigiShear-SI was initiated on the computer. The calibration factors and units of the sensors were configured and checked. Next, the shear box was placed onto the direct shear equipment and the top cap was positioned. Then, the steel ball and moment break connection were placed on top of the top cap. When the software was set up the vertical LVDT was zeroed; then, the piston was moved downwards to apply the vertical load. The direct shear tests were performed with a strain rate equal to 0.5 mm/ min.

The data collected by the DAQ was converted to engineering units by:

$$R_{ST} = \frac{R_{LVDT} - v_0}{v_i} \times Cal_{factor} \tag{3.25}$$

where

R_{ST}= reading in length units (mm)

R_{LVDT}= reading of the vertical LVDT (volts)

v_0= initial voltage at which the DAQ starts to record the data (volts)

v_i= input voltage at which the LVDT works (volts)

Cal_{factor}= calibration factor (mm/V/V)

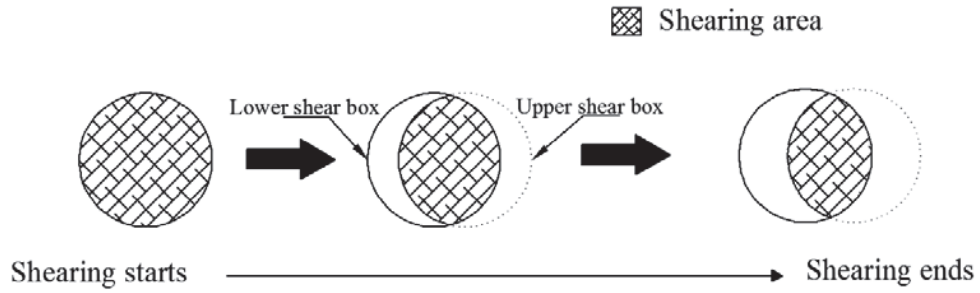

Figure 3.8 Illustration of the change of the area of the sample during shearing.

During shearing, the area of the sand sample changes. Figure 3.8 shows a schematic diagram of the change of the area during shearing. A correction factor F is applied to the initial area A_0 to obtain the corrected area:

$$A_{ST} = A_0 F \tag{3.26}$$

where

A_{ST}= corrected area (cm^2)

A_0= initial area (cm^2)

F= correction factor (dimensionless)

The correction factor is given by:

$$F = \frac{2}{\pi}\left[\cos^{-1}\left(\frac{\Delta h}{D_{ST}}\right) - \left(\frac{\Delta h}{D_{ST}}\right) \times \sqrt{1 - \left(\frac{\Delta h}{D_{ST}}\right)^2}\right] \tag{3.27}$$

where

Δh= horizontal displacement (mm)

D_{ST}= diameter of the shear box (mm)

3.4.2 Ring shear tests

Three ring shear tests were performed on OGF sand to obtain the peak friction angle and critical-state friction angle without crushing. The standard followed to perform the ring shear tests is ASTM D7608-10. The sand samples were subjected to three different normal stresses: 1) 25 kPa; 2) 50 kPa and 3) 100 kPa.

3.4.2.1 Equipment

The ring shear equipment is the GCTS SRS150 Residual Ring Shear Testing System available at the geotechnical laboratory at Purdue University. It consists of: 1) a ring shear container, 2) a ring shear disc, 3) a control console, 4) a computer, 5) an axial displacement sensor, 6) a strain gauge sensor, and 7) an angular displacement sensor (CF: 1,600,000 revolutions/radians). All the three sensors were calibrated previously by the manufacturer. Figure 3.9 shows the ring shear equipment used to test the OGF sand. A porous plate with small grooves is attached to the top cap to prevent slippage during shearing. The inner diameter, outer diameter and height of the ring shear box are equal to 96.46 mm, 152.38 mm and 32 mm, respectively. The software used to collect and analyze the data is the GCTS CATS Advanced.

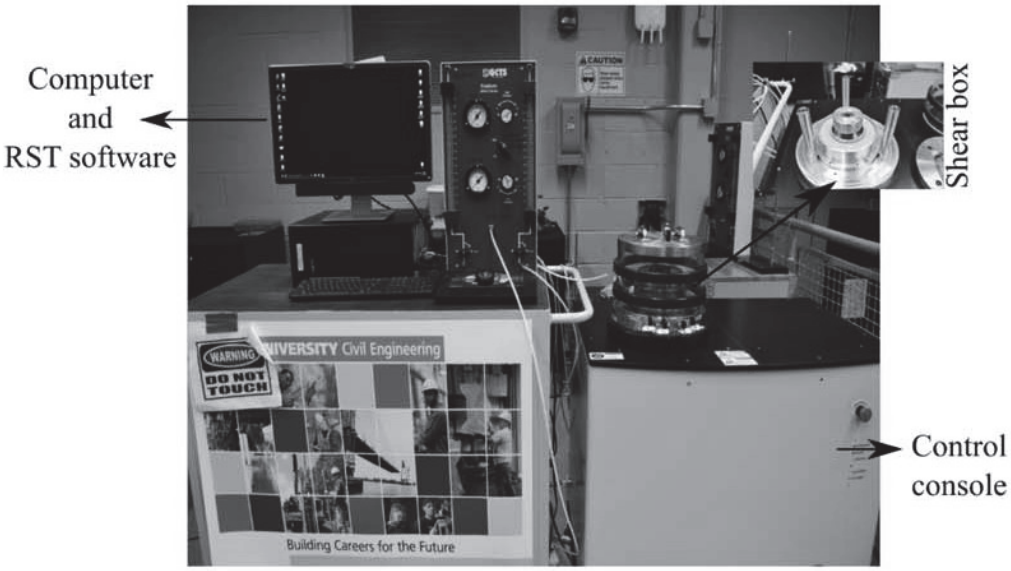

Figure 3.9 Ring shear equipment used to obtain the peak friction angle and critical-state friction angle of Ohio Gold Frac sand.

3.4.2.2 Sample preparation

Sand samples were prepared by air pluviation using a funnel and the mold was struck with a rubber hammer in order to achieve the desired sample density. Dense samples were prepared with an initial relative density of 85%. The relative density reported is the one after the consolidation stage.

3.4.2.3 Ring shear test setup

The dimensions (height, inner diameter, and outer diameter) of the ring shear box were determined to obtain its volume:

$$V_{RST} = \pi \times \left(\frac{D_{RSTo} - D_{RSTi}}{2} \right)^2 \times H_{RST} \tag{3.28}$$

where

V_{RST}= volume of the ring shear box (cm^3)

H_{RST}= height of the ring shear box (mm)

D_{RSTo}= outer diameter of the ring shear box (mm)

D_{RSTi}= inner diameter of the ring shear box (mm)

The sand sample was poured into the ring shear box using a funnel. The sides of the mold were slightly struck with a rubber hammer to increase the sample density. The mass (M_{sRST}) and the volume (V_{sRST}) of the sand samples were determined. The dry unit weight of the sand sample was calculated as:

$$\gamma_{dRST} = \frac{M_{sRST}}{V_{sRST}} \tag{3.29}$$

where

γ_{dRST}= dry unit weight of the sand sample used in the ring shear test (g/cm3)

M_{sRST}= height of the ring shear box container (mm)

V_{sRST}= diameter of the ring shear box container (cm^3)

The void ratio of the sand sample was obtained from:

$$e_{RST} = \frac{G_s \times \gamma_w}{\gamma_{dRST}} - 1 \tag{3.30}$$

where

e_{RST}= void ratio of the sand sample (dimensionless)

G_s= specific gravity of OGF sand (dimensionless)

γ_w= unit weight of water (g/cm^3)

Finally, the relative density of the sand sample was obtained from:

$$D_{R_{RST}} = \frac{e_{\max} - e_{ST}}{e_{\max} - e_{\min}} \times 100 \tag{3.31}$$

where

D_{RRST}= relative density of the sand sample (%)

e_{max}= maximum void ratio (dimensionless)

e_{min}= minimum void ratio (dimensionless)

Switch on the control button of the control console to start the ring shear equipment. Then, GCTS CATS Advanced software is initiated on the computer. Inside of the "Outputs function" menu, the shear actuator and axial actuator are turned on. In the "Views" menu, the screen layout is uploaded to visualize the "Normal Stress", "Shear Stress", "Axial Displacement", "Shear Angle", "Torque" and "Angular Rotation" values. In the "Outputs function" menu the piston is moved up. Next, in the "Inputs function" menu, the calibration factors and units of the sensors were configured and checked. The ring shear box with the soil was placed onto the ring shear equipment and the top cap was positioned on the piston and correctly tightened with the screws. Then, in the "Outputs function" menu the piston was moved downwards and a seating load of about 30 kPa was applied on the sample. Subsequently, the vertical axial actuator was zeroed in the "Inputs function" menu. Then,

the test was set up in the "Ring Shear Setup" menu in three stages: 1) consolidation, with the application of a normal stress to allow the stabilization of the sample height under loading; 2) shearing (the normal stress, and the shear displacement strain rate are inputted before starting the shearing test), and 3) Unconsolidation (when the test was completed, the piston was unloaded to 30 kPa of normal stress).

3.5 Particle characterization after loading

3.5.1 One-dimensional compression tests

One-dimensional compression tests were performed on OGF sand with a maximum load of 74 kN (24 MPa). The loading schedule was composed of 10 load increments. The tests were carried out with two time schedules: 10 hours and 10 days. A total of 4 tests were performed to study the effects of: 1) initial density and 2) time. The standard followed to perform the one-dimensional compression tests was ASTM D2435-D2435M. After the one-dimensional compression tests were completed, particle sieve and sedimentation analyses were done to obtain particle breakage parameters. In addition, particle morphology analyses were carried out to understand and quantify the evolution of particle gradation and morphology with crushing. Figure 3.10 shows the steps followed after the one-dimensional compression tests.

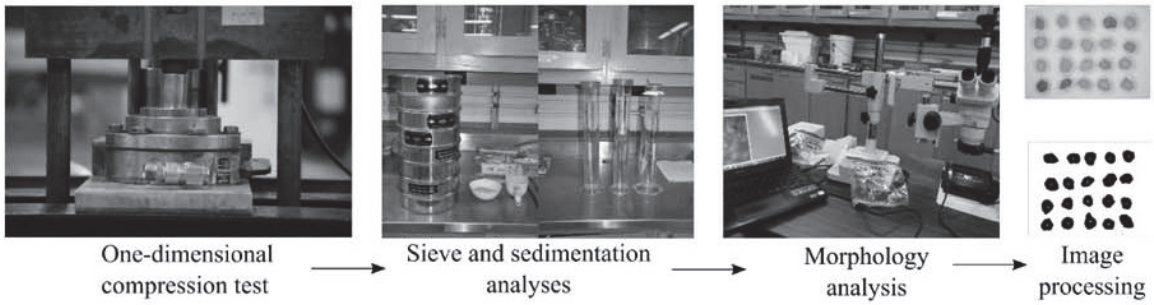

Figure 3.10 Steps followed to analyze particle crushing and morphology after performing one-dimensional compression tests on Ohio Gold Frac sand.

3.5.1.1 Equipment

The oedometer container has a diameter of 64 mm and a height of 26 mm. The tests were performed using a load frame machine located at the geotechnical laboratory at Purdue University. The system is designed such that the transmission of the load is 40 times the weight applied in the front arm and 10 times the weight applied in the back arm. To avoid inaccurate results, the load frame machine was first carefully calibrated. The calibration of the load frame machine was done using a calibrated load cell and a data acquisition system (DAQ) to collect all the data. To perform the tests, a linear variable differential transformer (LVDT) was coupled to the system to get the readings of the vertical displacement during loading. The Load cell and LVDT sensors were correctly calibrated; the calibration factors achieved are showed in section 3.5.1.2 and 3.5.1.3 respectively. The software used to collect the data is the TestNet-GP. Figure 3.11 shows the one-dimensional compression equipment used to test OGF sand, consisting of: 1) oedometer container, 2) load frame, 3) LVDT, and 4) weights.

3.5.1.2 Load cell calibration

The load cell was mounted on the one-dimensional compression device and connected to the DAQ. The TesNet-GP software was started to begin collecting the data. The loading schedule was set up on the TesNet-GP software to apply an increment of load in a fixed interval of time. A signal of an excitation voltage (5V or 10V) was sent before initiating the calibration. The process was repeated twice and the data were plot in Excel to obtain the calibration factor. The load cell calibration factor obtained was equal to 149500.55 Kg/V/V. In Appendix A (section a), the data and the calibration factor obtained is provided.

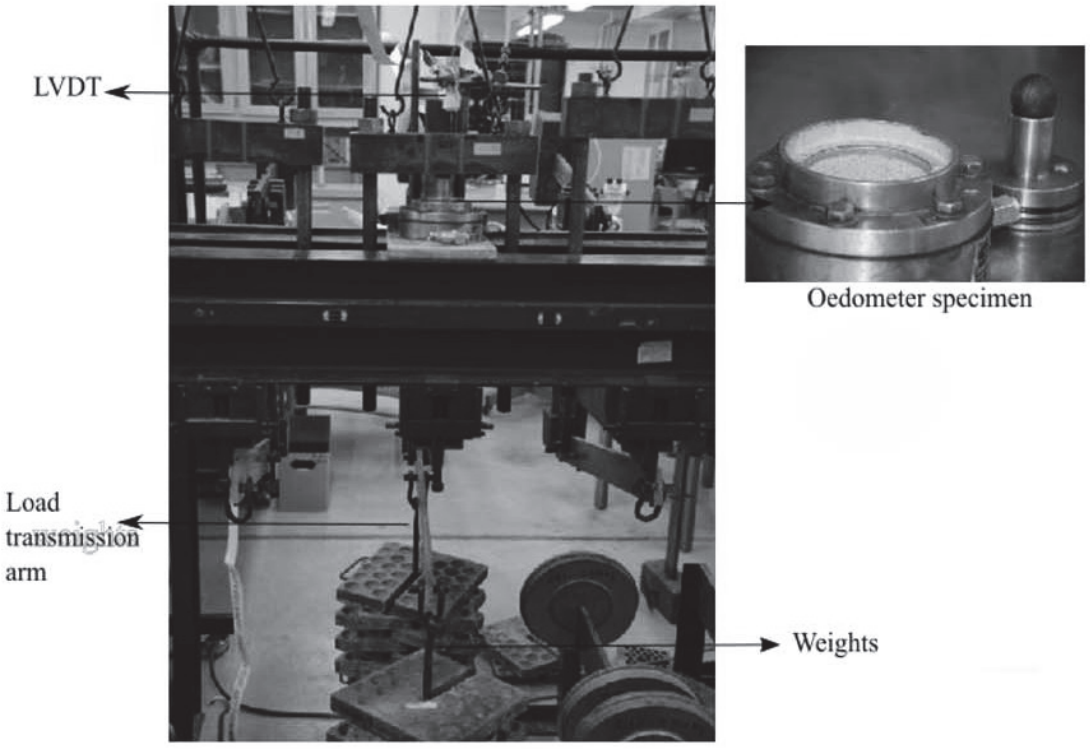

Figure 3.11 Load-frame system used to perform one-dimensional compression tests on Ohio Gold Frac sand.

3.5.1.3 LVDT calibration

Figure 3.12 shows the calibration device. The LVDT is first coupled onto the calibration device and connected to the DAQ. The TesNet-GP software is initiated to collect the data. When a zero voltage was located on the LVDT, then the calibration device was zeroed. A schedule was programmed on the TesNet-GP software to move the core of the LVDT. Before starting the calibration process, an excitation voltage signal (5V or 10V) was sent. The process was done twice to obtain accurate results. The calibration factor was calculated using the new data collected. The calibration factor acquired was equal to -20.738 mm/V/V. All the data and calculations done to obtain the calibration factor is shown in Appendix A, section b.

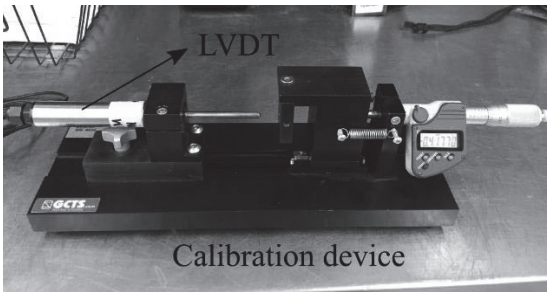

Figure 3.12 LVDT calibration device.

3.5.1.4 Calibration of the load frame

Figure 3.13 shows the load frame calibration set up. The calibrated load cell was placed below the load frame device and connected to the DAQ. A loading schedule was setup on the TesNet-GP software. The calibration factor of the load cell was applied before starting the load frame calibration. Once the test started, 8 weights of 16 kg each were

placed in the front and back arm following the loading schedule. The data obtained with this procedure indicated that the load in the front arm was increased by 40 times and 10 times the initial load in the front and back arms, respectively.

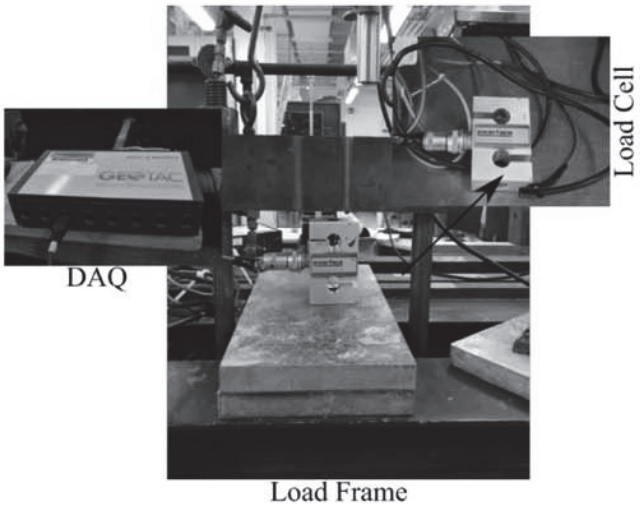

Figure 3.13 Load frame calibration before performing one-dimensional compression tests on Ohio Gold Frac sand.

3.5.1.5 Sample preparation

Dense sand samples were prepared by air pluviation using a funnel. The mold was struck with a rubber hammer to achieve the desired sample density. The initial relative density of the dense samples was 85%. Loose sand samples were prepared by carefully pouring sand into the mold using a funnel. The initial relative density of the loose samples was 35%.

3.5.1.6 One-dimensional compression test setup

The height and diameter of the oedometer container were determined to calculate the container volume as:

$$V_{1DC} = \pi \times \left(\frac{D_{1DC}}{2} \right)^2 \times H_{1DC} \tag{3.32}$$

where

V_{1DC}= volume of the oedometer container (cm^3)

H_{1DC}= height of the oedometer container (mm)

D_{1DC}= diameter of the oedometer container (mm)

The sand sample was poured into the oedometer container using a funnel. In the case of the dense sand samples, the sides of the mold were struck with a rubber hammer. In the case of the loose sand samples, the sand was poured in a circular manner and with an almost zero drop height. With the mass M_{s1DC} and the volume V_{s1DC} of the sand sample, the dry unit weight of the sand sample was calculated as:

$$\gamma_{d1DC} = \frac{M_{s1DC}}{V_{s1DC}} \tag{3.33}$$

where

γ_{d1DC}= dry unit weight of the sand sample used in one-dimensional compressional test (g/cm^3)

M_{s1DC}= height of the oedometer container (mm)

V_{s1DC}= diameter of the oedometer container (cm^3)

The void ratio of the sand sample was calculated as:

$$e_{1DC} = \frac{G_s \times \gamma_w}{\gamma_{1DC}} - 1 \tag{3.34}$$

where

e_{1DC}= void ratio of the sand sample (dimensionless)

G_s= specific gravity of OGF sand (dimensionless)

γ_w= unit weight of water (g/cm^3)

The relative density of the sand sample was obtained from:

$$D_{R_{1DC}} = \frac{e_{\max} - e_{ST}}{e_{\max} - e_{\min}} \times 100 \tag{3.35}$$

where

D_{R1DC}= relative density of the sand sample (%)

e_{max}= maximum void ratio (dimensionless)

e_{min}= minimum void ratio (dimensionless)

The sand sample surface was carefully leveled off and the top cap was positioned in place. Then, the sample was assembled in the oedometer load frame and the screws were tightened to put the load frame in contact with the top cap of the oedometer container. Next, the TesNet-GP software was initiated in the computer to record the data. The sensors were configured and the calibration factors and units were checked.

A data reading schedule was configured in the software to collect the readings during a determined time interval. The LVDT was then zeroed and the test started according to the prescribed loading schedule.

Once the one-dimensional compression test was completed, the entire sand sample was collected. Then, the mass of the collected sand sample was measured. Sieve and sedimentation analyses followed the procedures described in sections 3.1.3.3 and 3.1.3.4. Figure 3.14 shows the sand particles after the one-dimensional compression tests.

Figure 3.14 Ohio Gold Frac sand after one-dimensional compression test: left dish shows the material collected from sieve #200 and pan; and the right dish shows the material collected from sieve #20 to sieve #100.

The grain-size distribution curve of the sand after one-dimensional compression was compared with the grain-size distribution curve of the original sand to quantify particle crushing. Equations (2.15) (2.16) and (2.17) were used to obtain the breakage potential, total breakage and relative breakage respectively after one-dimensional compression tests. From each sieve, 20 particles were randomly selected to perform the morphology analyses, as described in sections 3.3.1.3 and 3.3.1.4.

3.5.2 Ring shear tests

Ring shear tests were performed to study particle crushing effects due to shearing. Particle gradation and morphology evolution were assessed for the sand recovered from the shear band after testing. The reference standard followed for the ring shear tests was ASTM D7608-10. The sand samples were tested under different normal stresses: 1) 100 kPa, 2) 200 kPa, 3) 300 kPa, and, 4) 400 kPa. Figure 3.15 shows the steps followed to analyze the crushability of Ohio Gold Frac sand after ring shear testing.

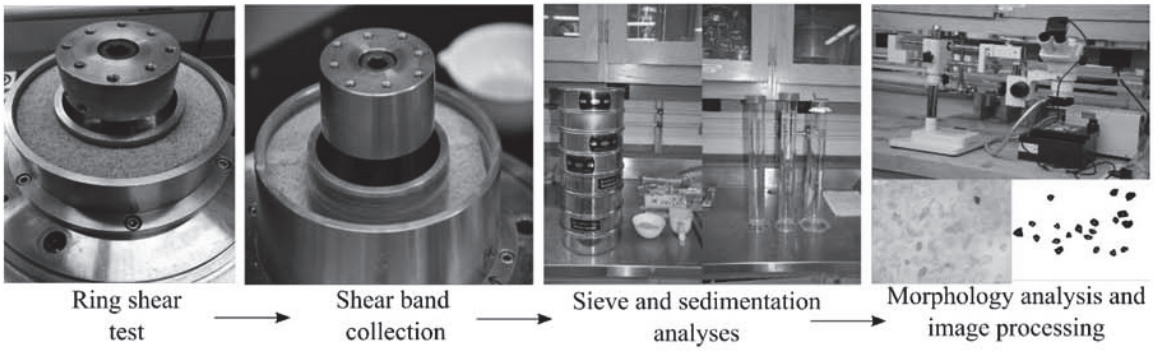

Figure 3.15 Steps followed to study particle crushing and morphology after performing ring shear tests on Ohio Gold Frac sand.

3.5.2.1 Equipment

The ring shear equipment is the GCTS SRS150 Residual Ring Shear Testing System, as described in the section 3.4.2.1.

3.5.2.2 Sand sample preparation

Dense sand samples were prepared by air pluviation using a funnel. The mold was struck with a rubber hammer in order to increase the density of the samples to the desired value. Dense samples were prepared with an initial relative density of 80 to 85%. The loose sand samples were prepared by pouring the sand through a funnel while keeping an almost zero drop height. Loose samples were prepared with an initial relative density of 35%.

3.5.2.3 Ring shear test setup

The ring procedure is described in section 3.4.2.3. In the"Ring Shear Setup" menu, the desired shear displacement is input for each test. The shear displacement for the tests performed on Ohio Gold Frac sand varied from 1 m to 20 m.

Once a ring shear test was completed, the top cap was carefully lifted. Then, a small amount of sand was removed from the top surface of the sand sample to allow measurement of the shear band thickness with a caliper. Then, the sand from the shear band was carefully collected using a spatula. Particle sieve analyses were done, as described in sections 3.1.3.3 and 3.1.3.4, to obtain the breakage potential, total breakage and relative breakage of Ohio Gold Frac sand. Additionally, particle morphology analyses were done for each sand sample collected from the shear band after testing, as explained in sections, 3.3.1.3 and 3.3.1.4.

CHAPTER 4. TEST RESULTS

4.1 Specific gravity

The specific gravity of Ohio Gold Frac, which was determined in accordance with ASTM D854-06, is 2.65. In section 3.1.1, the experimental method for the specific gravity test is explained. Two pycnometers were used to determine the specific gravity of Ohio Gold Frac sand. Table 4.1 and Table 4.2 show the results obtained for the specific gravity of Ohio Gold Frac sand for the two different pycnometers. Equations (3.4) and (3.5) were used to compute the specific gravity. The results of the calibration of the two pycnometers employed for these tests are provided in Appendix A.

Table 4.1 Specific gravity of Ohio Gold Frac sand (Pycnometer E).

Pycnometer E					
Description	Units	Symbol	1	2	3
Test Temperature	°C	t	10.4	24.2	32.0
Mass of the pycnometer and water at the test temperature	g	$M_{pw,t}$	421.93	421.19	420.55
Density of water at the test temperature	g/mL	$\rho_{w,t}$	1.000	0.997	0.995
Mass of pycnometer, eater and soil solids at the test temperature	g	$M_{pws,t}$	452.87	452.25	451.73
Mass of the oven dry of soil solids	g	M_S	49.88	49.88	49.87
Specific gravity of soil solids at the test temperature	-	G_t	2.63	2.65	2.67
Temperature coefficient	-	k	1.001	0.999	0.997
Specific gravity of soil solids at 20°C	-	$G_{20°C}$		2.65	

According to Salgado (2008), the value of the specific gravity for most silica-based soils fluctuates between 2.6 and 2.7. The specific gravity values obtained for Ohio Gold Frac sand are consistent with the average specific gravity of sands.

Table 4.2 Specific gravity of Ohio Gold Frac sand (Pycnometer H).

Pycnometer H					
Description	Units	Symbol	1	2	3
Test temperature	°C	t	10.4	24.2	32
Mass of the pycnometer and water at the test temperature	g	$M_{pw,t}$	403.92	403.2	402.54
Density of water at the test temperature	g/mL	$\rho_{w,t}$	1.000	0.997	0.995
Mass of pycnometer, eater and soil solids at the test temperature	g	$M_{pws,t}$	373.04	372.2	371.48
Mass of the oven dry of soil solids	g	M_S	49.77	49.76	49.77
Specific gravity of soil solids at the test temperature	-	G_t	2.63	2.65	2.66
Temperature coefficient	-	k	1.0015	0.999	0.9968
Specific gravity of soil solids at 20°C	-	$G_{20°C}$		2.65	

4.2 Minimum density

The minimum density test was used to determine the maximum void ratio e_{max} of Ohio Gold Frac sand. The standard followed to obtain the minimum density was ASTM D4254-16. In section 3.1.2.3, the experimental method for the minimum density test is provided in detail. The funnel method was selected to carry out this test. Equation (3.11) was used to calculate the e_{max} of Ohio Gold Frac sand. According to Salgado (2008), for clean silica sands, the range of e_{max} varies between 0.8 to 1.0. The maximum void ratio e_{max} obtained for Ohio Gold Frac is 0.81. Table 4.3 shows the results obtained for e_{max} of Ohio Gold Frac sand.

4.3 Maximum density

The maximum density test was used to determine the minimum void ratio e_{min} of Ohio Gold Frac. The standard used for the determination of the maximum density was ASTM D4253-16. In section 3.1.2.4, the test procedure for the determination of the minimum void ratio is explained. The vibratory table method was chosen to carry out the test. Equation (3.12) was used to calculate the e_{min} of Ohio Gold Frac sand. The minimum void ratio e_{min} obtained for Ohio Gold Frac sand is 0.59. Table 4.4 shows the results obtained for the e_{min} of Ohio Gold Frac sand.

Table 4.3 Minimum density of Ohio Gold Frac sand (funnel method).

Funnel method					
Description	Unit	Symbol	1	2	3
Mass of mold without collar	kg	M_m	4.13	4.13	4.13
Mass of mold with dry soil	kg	M_{ms_min}	5.5	5.51	5.51
Mass of dry soil	kg	M_s	1.370	1.380	1.380
Weight of dry soil	N	W_s	13.43	13.49	13.53
Volume of mold	m^3	V_m	0.00094	0.00094	0.00094
Minimum density	N/m^3	γ_{dmin}	14297.70	14360.36	14402.14
Specific gravity	-	G_s	2.65	2.65	2.65
Specific weight of water	N/m^3	γ_w	9810	9810	9810
Maximum void ratio	-	e_{max}		0.81	

Table 4.4 Maximum density of Ohio Gold Frac sand (vibratory table method).

Vibratory table					
Description	Unit	Symbol	1	2	3
Mass of mold without collar	kg	M_m	4.25	4.25	4.25
Mass of mold with dry soil	kg	M_{ms_max}	5.83	5.82	5.82
Mass of dry soil	kg	M_s	1.58	1.57	1.57
Weight of dry soil	N	W_s	15.50	15.35	15.40
Volume of soil	m^3	V_m	0.00094	0.00094	0.00094
Maximum density	N/m^3	γ_{dmax}	16448.40	16292.24	16344.30
Specific gravity	-	G_s	2.65	2.65	2.65
Specific weight of water	N/m^3	γ_w	9810	9810	9810
Minimum void ratio	-	e_{min}		0.59	

4.4 Grain-size distribution

Figure 4.1 shows the Ohio Gold Frac (OGF) sand particle-size distribution curve, which was determined in accordance with ASTM D4253-16. In section 3.1.3, the test procedure for obtaining a particle gradation curve is explained. The separation technique used for OGF sand was mechanical sieving. Figure 4.1 shows the relationship between the particle size (horizontal axis) and the percentage finer (vertical axis). The particle-size distribution curve in Figure 4.1 is used as reference when comparing gradation changes due to particle crushing during one-dimensional compression tests and ring shear tests. Table 4.5 provides the data used to obtain the GSD curve of OGF sand.

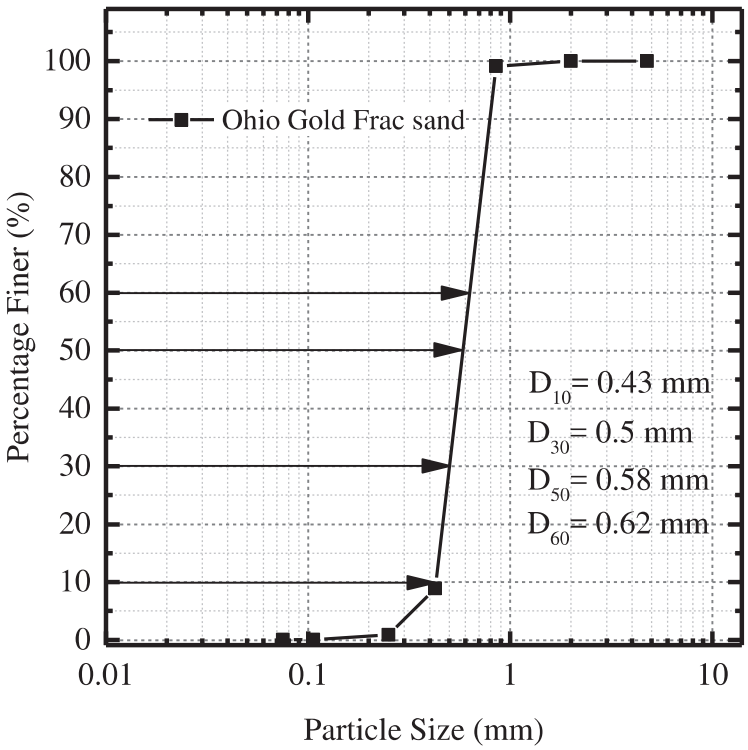

Figure 4.1 Particle size distribution of Ohio Gold Frac sand.

Table 4.5 Particle size distribution data for Ohio Gold Frac sand.

Sieve No.	Sieve opening (mm)	Mass of empty sieve (g)	Percentage of soil retained (%)	Cumulative percentage of soil retained (%)	Percentage finer (%)
4	4.75	784.08	0.00	0.00	100.00
10	2	396.18	0.00	0.00	100.00
20	0.85	378.29	0.83	0.83	99.17
40	0.425	358.23	90.26	91.09	8.91
60	0.25	544.07	8.05	99.15	0.85
100	0.106	325.71	0.82	99.96	0.04
200	0.075	279.95	0.02	99.98	0.02
PAN	-	497.66	-	100.00	0.00

4.4.1 Soil classification

In accordance with the Unified Classification System (USCS), soils can be classified with reference to their plasticity properties and particle-size distribution (Salgado 2008). Ohio Gold Frac sand was classified in accordance with ASTM D2487-16. The coefficient of uniformity C_u and the coefficient of curvature C_c, which are defined by Equations (2.1) and (2.2), are necessary for soil classification. Table 4.6 shows the composition of Ohio Gold Franc sand, where it can be seen that 99.98 % of the particles are in the sand-size range, and the content of fines is clearly null.

Table 4.6 Soil composition of Ohio Gold Frac sand.

Soil name	Particle size range (mm)	Composition (%)
Gravel	> 4.75	0.00
Sand	0.075 to 4.75	99.98
Coarse sand	2 to 4.75	0.00
Medium sand	0.425 to 2	91.09
Fine sand	0.075 to 0.425	8.89
Fines content	<0.075	0.02

Table 4.7 Particle parameters of Ohio Gold Frac sand.

Soil Parameters	Units	Values
D_{10}	mm	0.43
D_{30}	mm	0.5
D_{50}	mm	0.58
D_{60}	mm	0.62
(C_u)	-	1.44
(C_c)	-	0.94

Table 4.6 shows that more than 50% of the OGF sand particles are smaller than 4.75 mm, with negligible fines content. Therefore, the size composition of OGF sand is between 0.075 and 4.74mm. Also, in Table 4.7, C_u and C_c values are reported for the sand classification. According to ASTM Standard D2487-06, Ohio Gold Frac sand is classified with the group symbol "SP" and group name "Poorly-Graded Sand". Well-graded sands have at the same time C_u values larger than 6 and C_c values between 1 and 3.

4.5 Mineralogy results

Figure 4.2 shows the results obtained from the X-ray diffraction tests. The test pattern obtained for Ohio Gold Frac (OGF) sand was compared with known X-ray diffraction patterns published by the American Society for Testing and Materials (ASTM), indicating that almost 99% of the minerals present in OGF sand are quartz. Table 4.8 shows the results for the interplanar spacing for the first eight peaks. Equation (2.3) was used to obtain the values of the interplanar spacing.

Table 4.8 Interplanar spacing for the first eight peaks of the X-ray diffraction test on Ohio Gold Frac sand.

θ	Intensity	Interplanar spacing (Å)
20.8	2769	4.264
26.6	10277	3.349
36.4	753	2.46
37.6	731	2.285
40.6	360	2.24
42.4	493	2.131
45.6	316	1.98
50	1323	1.82

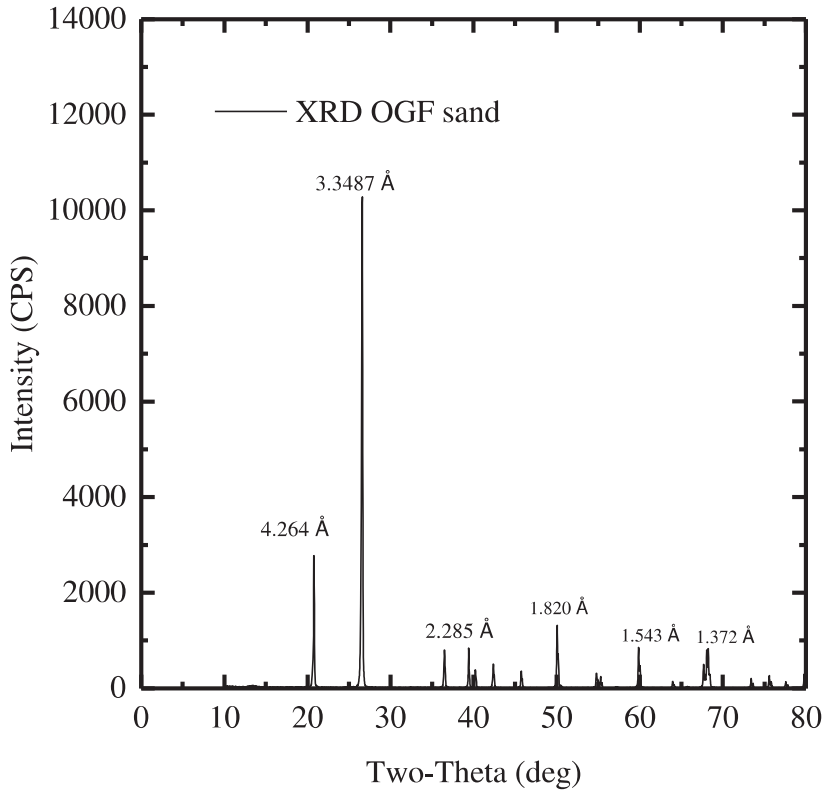

Figure 4.2 X-ray diffraction pattern for Ohio Gold Frac sand.

4.6 Morphology analyses

The particle morphology of OGF sand was assessed before and after one-dimensional compression tests and ring shear tests. As mentioned in Chapter 2, there is no standardized technique for particle morphology assessment, therefore image-processing software and tools were used to determine morphology parameters of the OGF sand before and after testing. Sand particles were separated by sieving, and about 20 particles per each sieve were randomly selected. The sand particles were placed under the microscope and, with a charge-couple camera, images were taken and stored in a computer. Figure 4.3

shows images of the particles of the original sand selected per each sieve. The entire particle morphology assessment process is detailed in section 3.4.1.

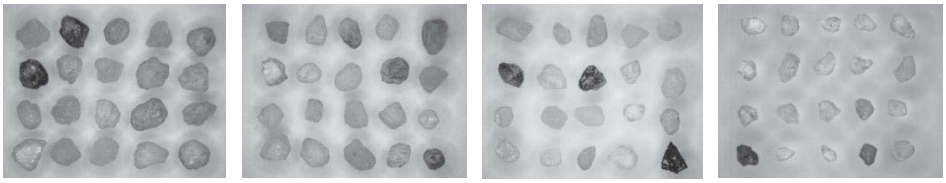

(a) (b) (c) (d)

Figure 4.3 Random selection of Ohio Gold Frac sand particles from various gradations: (a) Sieve #20 (mesh opening size = 0.841 mm); (b) Sieve #40 (mesh opening size = 0.420 mm); (c) Sieve #60 (mesh opening size= 0.250 mm); and (d) Sieve #100 (mesh opening size = 0.149 mm).

The digital images were processed with the image-processing tool ImageJ to obtain the morphology parameters, such as particle area, perimeter, circularity, aspect ratio (*AR*), roundness and sphericity. The sphericity was calculated using Equation (2.8). Figure 4.4 shows an example of an image processed with the ImajeJ software. Figure 4.5 shows that the larger particles from sieve #20 have a higher value of sphericity (equal to 0.96) than the smaller particles from sieve #100 (equal to 0.59). According to the results obtained in Figure 4.5, the particles of Ohio Gold Frac have sub-angular to sub-rounded shape. As the particle size decreases, the shape of the particle becomes more angular.

Figure 4.4 Digital image of OGF sand processed by the ImajeJ software.

Table 4.9 Parameters obtained after the processing of a digital image of OGF sand.

No.	Area	Perimeter	Circularity	Aspect Ratio	Roundness	Sphericity
1	0.85	3.97	0.68	1.14	0.88	0.92
2	0.91	3.96	0.73	1.17	0.86	0.91
3	0.86	3.88	0.72	1.39	0.72	0.85
4	0.63	3.25	0.75	1.22	0.82	0.90
5	0.82	3.91	0.68	1.44	0.70	0.84
6	0.88	3.87	0.74	1.24	0.81	0.88
7	0.94	4.06	0.72	1.33	0.75	0.86
8	0.97	4.49	0.60	1.24	0.81	0.90
9	0.91	4.24	0.64	1.48	0.67	0.84
10	0.79	3.81	0.69	1.11	0.90	0.94
11	0.92	4.33	0.61	1.36	0.74	0.88
12	0.72	3.41	0.78	1.13	0.88	0.93
13	0.85	3.85	0.72	1.35	0.74	0.87
14	0.81	3.92	0.66	1.08	0.93	0.93
15	0.87	3.89	0.72	1.18	0.85	0.91
16	0.79	3.73	0.72	1.15	0.87	0.93
17	0.90	3.80	0.78	1.18	0.85	0.92
18	0.85	4.13	0.63	1.10	0.91	0.95
19	0.80	3.64	0.75	1.10	0.91	0.94
20	0.70	3.55	0.69	1.06	0.95	0.96

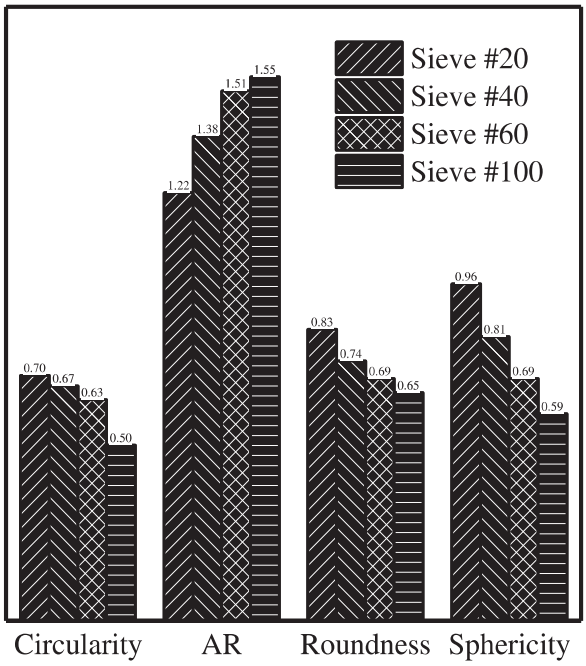

(a)

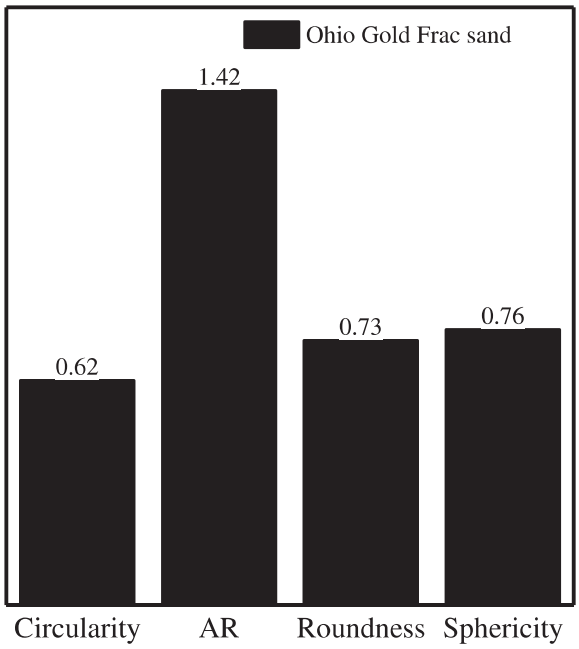

(b)

Figure 4.5 Results obtained after the processing of the OGF sand digital images: (a) morphology parameters obtained per each sieve; (b) average of the morphology parameters for all the sieves.

4.7 Direct shear peak and critical-state friction angles

Direct shear tests were performed in accordance with ASTM D3080. The tests were carried out on dense samples of Ohio Gold Frac sand prepared using the air pluviation method. OGF sand was poured through a funnel in such a way as to maintain a constant drop height; once the shear box was filled with sand, a rubber hammer was used to strike the sides of the container to densify the sample. Figure 4.6 and Figure 4.7 show the relationship between the shear stress and vertical displacement with respect to the shear displacement for direct shear tests performed with normal stresses σ_N of 25 kPa, 50 kPa and 100 kPa. The OGF sand response shown in these tests is typical of dilative sands. The peak strength in the shear stress versus shear displacement curve reduces as the confining stress increases. The critical-state strength is reached after 4 to 6 mm of shear displacement, where the vertical displacement stabilizes.

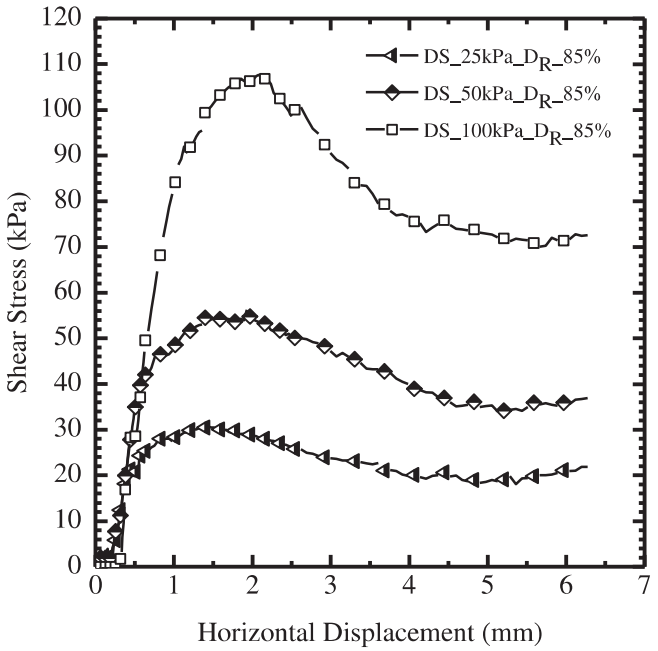

Figure 4.6 Shear stress versus horizontal displacement curves (direct shear test, σ_N= 25 kPa, 50 kPa, and 100 kPa, D_R=85%).

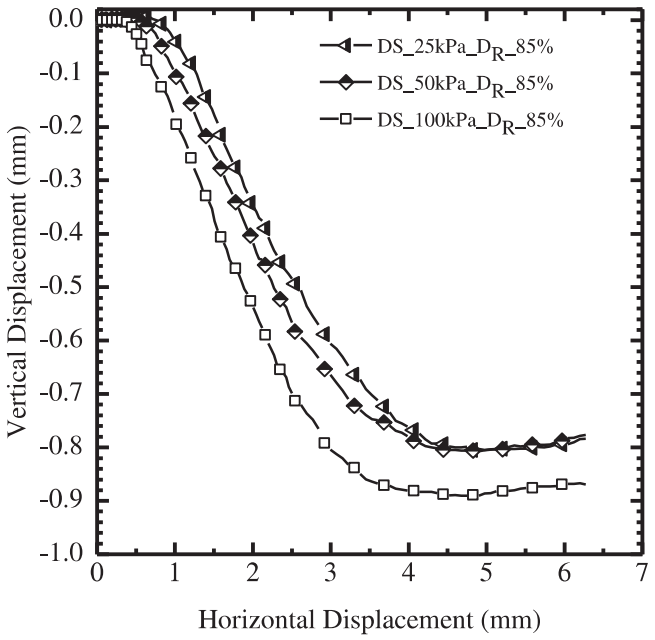

Figure 4.7 Vertical displacement versus horizontal displacement curves (direct shear test, σ_N= 25 kPa, 50 kPa, and 100 kPa, D_R=85%).

Figure 4.8 shows the critical-state friction angle obtained from the three direct shear tests performed on dense samples of OGF sand at different normal stresses of 25 kPa, 50 kPa and 100 kPa. Also, the different peaks observed in Figure 4.8, corresponds to the peak friction angles reached in each test. The peak friction angle depends on the sample density and normal stress applied. As the normal stress increases, the peak friction angle decreases, as can be seen in Figure 4.8. For example, for the test performed with a normal stress equal to 25 kPa, the peak friction angle ($\phi_{p,DS}$= 49°) is greater than the peak friction angle ($\phi_{p,DS}$= 45°) for the test performed with a normal stress equal to 100 kPa.

Figure 4.9 shows the direct-shear critical-state strength envelope for Ohio Gold Frac sand obtained from the three tests performed on dense samples (D_R= 85%). The direct shear test critical-state friction angle $\phi_{c,DS}$ is 35º.

Grain size distribution curves were obtained for the entire sand samples after the direct shear tests and compared with the original grain size distribution curve of Ohio Gold Frac sand. In Figure 4.10, it can be seen that these grain size distribution curves overlap, indicating minimal overall particle crushing (although particle crushing likely occurred within the shear zone).

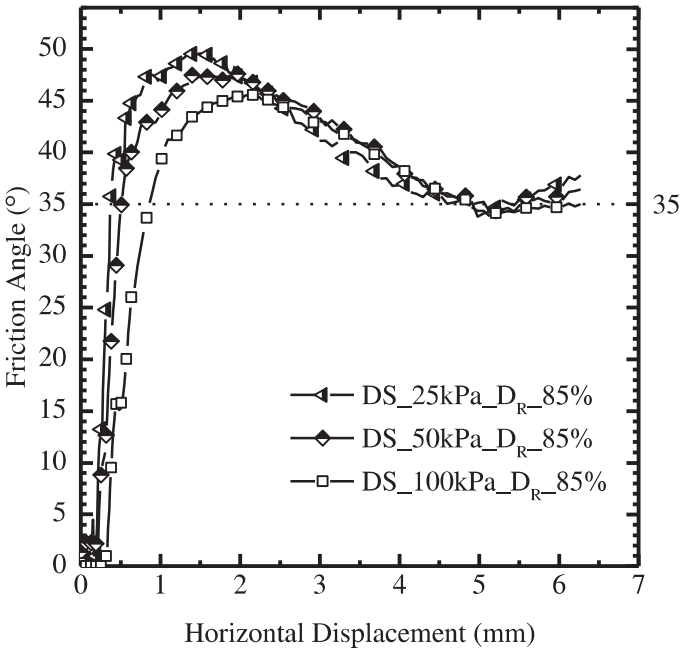

Figure 4.8 Direct-shear peak and critical-state friction angles for tests performed with normal stresses of 25 kPa, 50 kPa and 100 kPa in dense OGF sand samples (D_R= 85%).

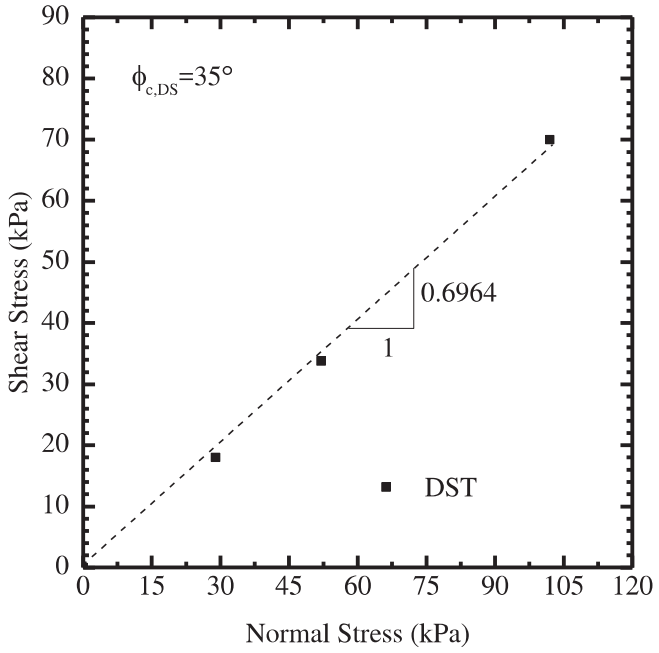

Figure 4.9 Direct shear critical-state envelope for Ohio Gold Frac sand.

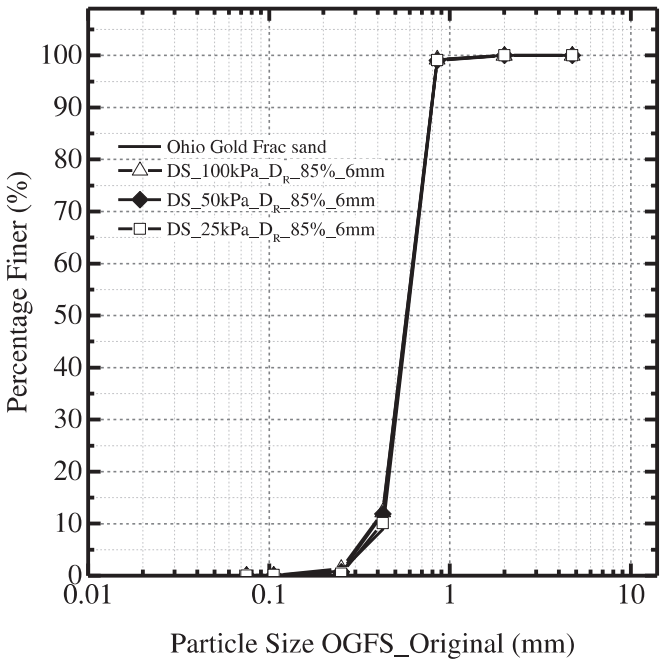

Figure 4.10 Grain size distribution curves of Ohio Gold Frac sand before and after performing direct shear tests on dense samples (D_R= 85%) with normal stresses of 25 kPa, 50 kPa and 100 kPa.

4.8 Ring shear peak and critical-state friction angles

Figure 4.11 and Figure 4.12 show the relationship between the shear stress and vertical displacement with respect to the shear displacement for ring shear tests performed with normal stresses of 25 kPa, 50 kPa and 100 kPa. These tests were carried out on dense samples of Ohio Gold Frac sand. Dense sand samples were prepared by air pluviation using a funnel, followed by vibration densification (using the same method described earlier in the direct shear test sample preparation). The larger the normal stress is, the greater the shear stress is. After the peak, all the three samples reached a plateau after 15 to 20 mm of displacement, where the vertical displacement and the shear strength stabilized.

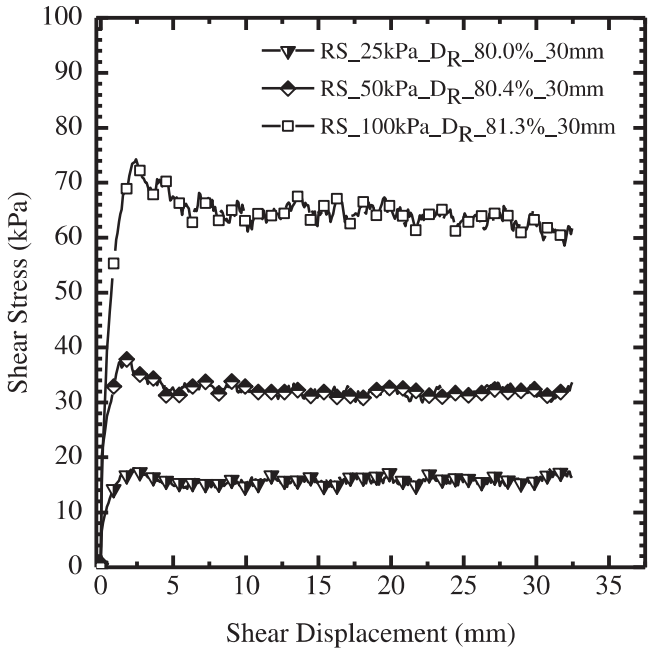

Figure 4.11. Shear stress versus shear displacement curves (ring shear test, σ_N= 25 kPa, 50 kPa, and 100 kPa, D_R=80%, 80.4% and 81.3%).

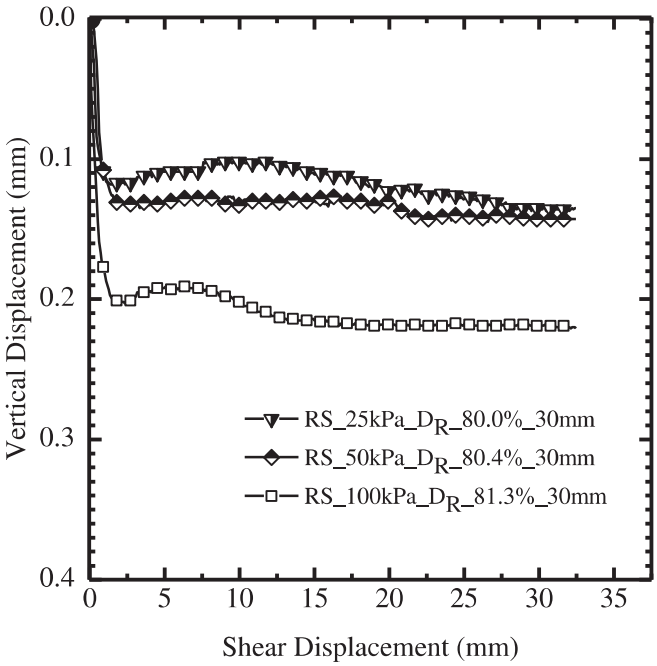

Figure 4.12. Vertical displacement versus shear displacement (ring shear test, σ_N= 25 kPa, 50 kPa, and 100 kPa; D_R=80%, 80.4% and 81.3% respectively).

Figure 4.13 shows the critical-state friction angle obtained from the three tests performed on dense samples of OGF sand with normal stresses of 25 kPa, 50 kPa and 100 kPa. As is shown in Figure 4.12, the critical-state friction angle fluctuates between 31 and 33 º, if the lower bound of the three curves is considered the critical-state friction angle (lower bound) $\phi_{c,RS}$ is equal to 31.3º obtained at the end of the test at about 25 to 30 mm, where a plateau is observed in the vertical displacement versus shear displacement curves. Also, the different peaks in Figure 4.13 correspond to the peak friction angles, which are slightly different because they depend on the normal stress and sample density. The sample tested with a normal stress equal to 100 kPa shows a peak friction angle slightly lower ($\phi_{p,RS}$= 34°) than that of the sample tested with a normal stress equal to 25 kPa ($\phi_{p,RS}$= 36°). Figure 4.14 shows the ring shear critical-state strength envelope for Ohio Gold Frac obtained from the three tests performed on dense samples in the ring shear equipment.

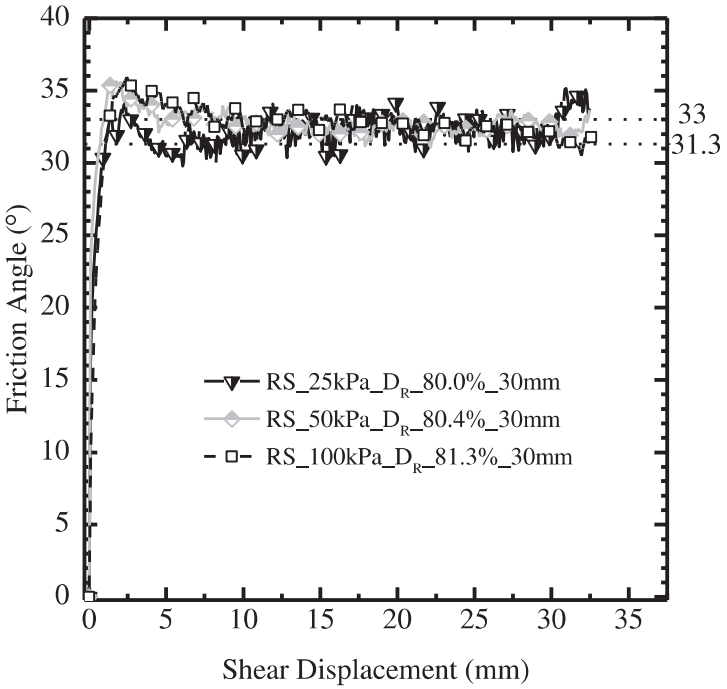

Figure 4.13 Ring shear peak and critical-state friction angle for different confining stresses of 25 kPa, 50 kPa and 100 kPa in dense samples (D_R=80%, 80.4% and 81.3%).

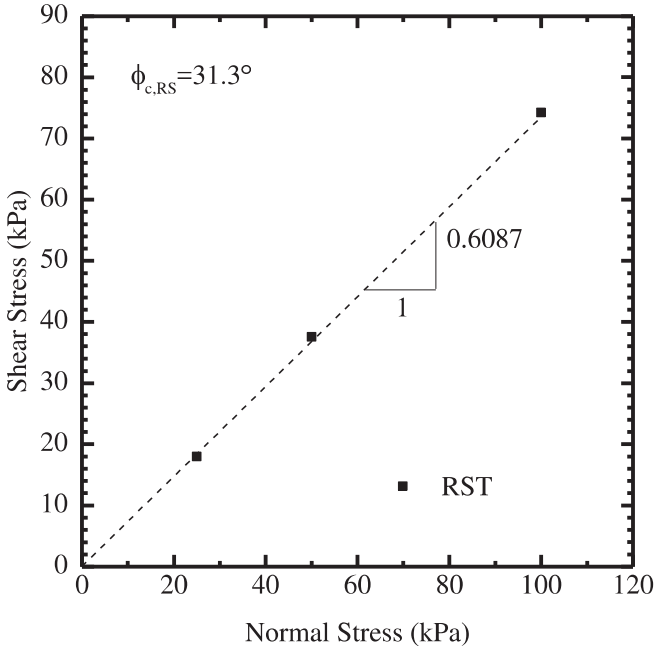

Figure 4.14 Ring shear critical-state strength envelope for Ohio Gold Frac sand.

After performing the ring shear tests, the grain size distribution curves for the entire sand samples were determined and compared with the original grain size distribution curve of Ohio Gold Frac sand. In Figure 4.15, it can be seen that the GSD curves overlap for particle sizes ranging from 4.75 mm to 0.85 mm and from 0.25 mm to 0.075 mm and tend to deviate slightly for particle sizes ranging from 0.42 mm to 0.25 mm, indicating minimal particle crushing (GSD curves were not determined for the sand from the shear bands formed in these ring shear tests).

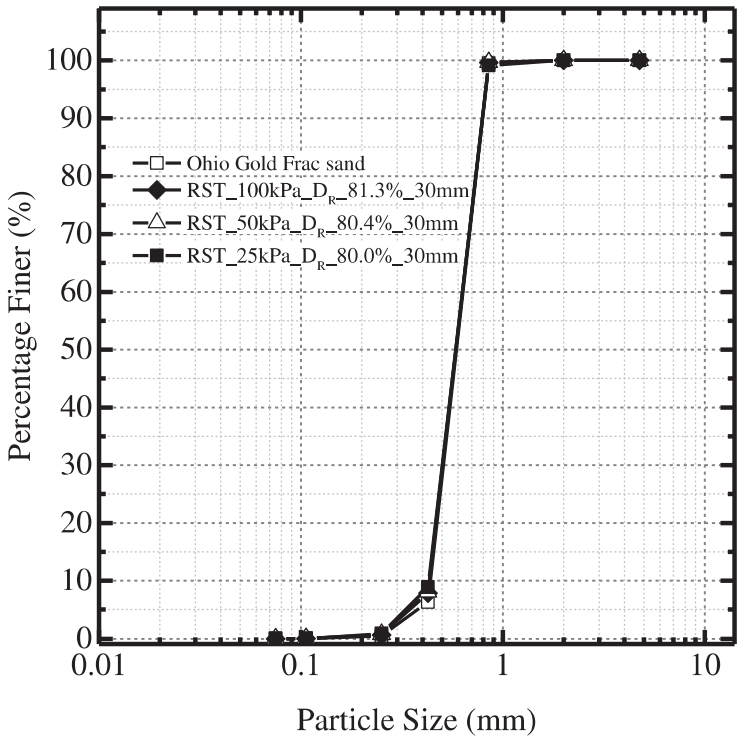

Figure 4.15. Grain size distribution curves of Ohio Gold Frac sand before and after performing ring shear tests on dense samples (D_R=80%, 80.4% and 81.3%) of Ohio Gold Frac sand with normal stresses of 25 kPa, 50 kPa and 100 kPa.

4.9 One-dimensional compression test results

One-dimensional (1D) compression tests were performed on Ohio Gold Frac sand to study particle crushing. The maximum load applied on the 1D compression tests was equal to 74kN, which in terms of stress is equal to 24 MPa. Table 4.10 shows the load increment schedule for the 1D compression tests. The 1D compression tests performed on Ohio Gold Frac sands are summarized in Table 4.11. After completing the 1D compression tests, particle size and morphology analyses were performed on the samples tested.

Table 4.10 Load schedule for one-dimensional compression tests performed on Ohio Gold Frac sand.

No.	Load		Stress
	(Kg)	(kN)	(MPa)
1	40	0.4	0.125
2	80	1	0.25
3	160	2	0.5
4	320	3	1
5	640	6	2
6	1280	13	4
7	2560	25	8
8	5760	56	16
9	7520	74	24

Table 4.11 Matrix test table for one-dimensional compression tests performed on Ohio Gold Frac sand.

No.	Test	Duration	Density	Nomination
1	1D compression	10 hours	35	1DC_10h_D_R_35%
2	1D compression	10 hours	85	1DC_10h_D_R_85%
3	1D compression	5 days	35	1DC_5d_D_R_35%
4	1D compression	5 days	85	1DC_5d_D_R_85%
5	1D compression	10 days	35	1DC_10d_D_R_35%
6	1D compression	10 days	85	1DC_10d_D_R_85%

Figure 4.16 shows the void ratio versus normal stress curves for two samples with different densities compressed with normal stresses of up to 24 MPa for 10 hours. Crushing intensified for the dense and loose samples at normal stresses of 10 MPa and 9 MPa, respectively. Some particle crushing of Ohio Gold Frac sand was also observed in one-dimensional compression tests carried out on dense samples ($D_R \approx 85\%$) with normal stresses of up to 10 MPa by Arshad et al. (2014). Table 4.12 shows the initial void ratio e_0 (before 1D compression) and final void ratio e_f after (1D compression). It can be observed that the loose (D_R= 35%) sand sample was more compressible that the dense sample (D_R=85%), as expected.

Table 4.12 Void ratio change with normal stress for one-dimensional compression tests performed for 10 hours.

No.	Test Code	e_0	e_f
1	1DC_10h_D_R_35%	0.733	0.524
2	1DC_10h_D_R_85%	0.623	0.504

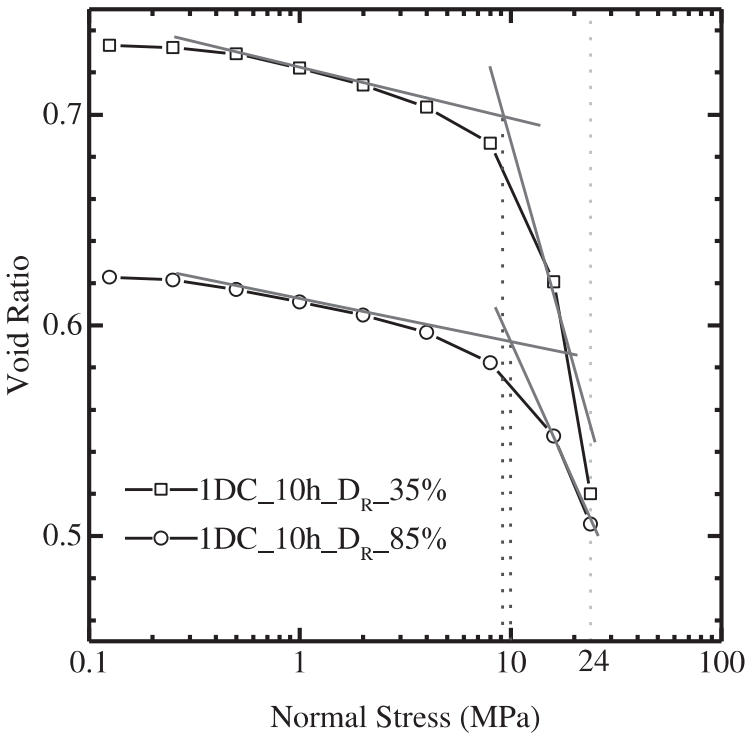

Figure 4.16 Void ratio versus normal stress (log scale) curves for one-dimensional compression tests performed on Ohio Gold Frac sand for 10 hours (maximum σ_N = 24 MPa).

Figure 4.17 shows the compression curves in void ratio versus normal stress space for the dense and loose sample compressed up to 24 MPa during 10 hours with the horizontal axis in linear scale to better understand particle crushing processes in one-dimensional compression tests. It can be observed from Figure 4.17 that particle crushing is an ongoing process for both the loose and dense samples. Three stages of compression can be identified for the loose sample (D_R= 35%), as shown in Figure 4.17; these results are similar to what was observed by Mesri and Vardhanabhuti (2009) from 1D compression tests performed on Ottawa sand. According to Mesri and Vardhanabhuti (2009) the compression behavior of Ottawa sand corresponds to what they referred to as type A

compression behavior, which is mostly observed in clean well-rounded quartz sands, but not exclusively. Also, in their study, type B compression behavior corresponds to a transition between type A and type C, and type C is observed for angular weak particles such as those of carbonate sands.

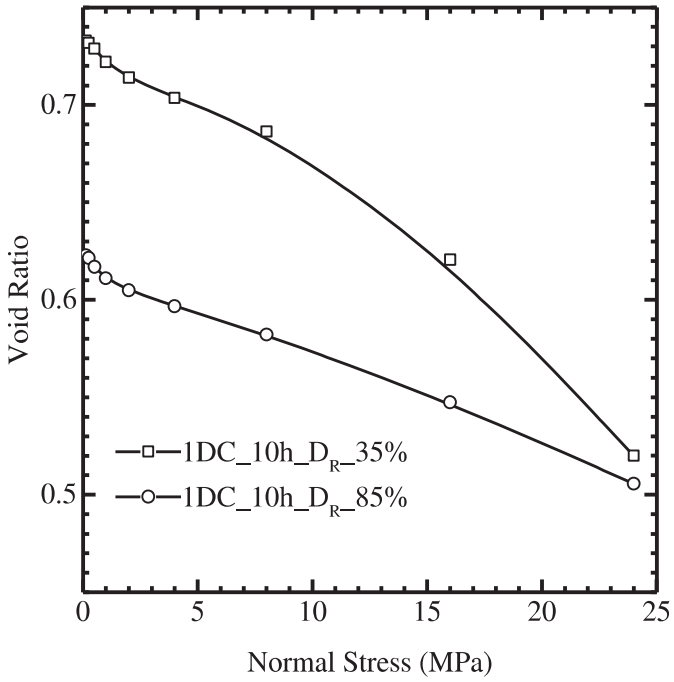

Figure 4.17 Void ratio versus normal (linear scale) stress curves for one-dimensional compression tests performed on Ohio Gold Frac sand for 10 hours (maximum σ_N = 24 MPa).

Figure 4.18 shows the void ratio versus normal stress curves for two samples (loose and dense) compressed with normal stresses of up to 24 MPa for 5 days. It was observed that the stresses at which crushing intensifies for the loose sample and dense samples are about 9 MPa and 10 MPa, respectively. Table 4.13 shows the initial void ratio e_0 (before 1D compression) and final void ratio e_f (after 1D compression).

Table 4.13 Void ratio change with normal stress for one-dimensional compression tests performed for 5 days.

No.	Test Code	e_0	e_f
1	1DC_5d_D_R_35%	0.733	0.501
2	1DC_5d_D_R_85%	0.623	0.508

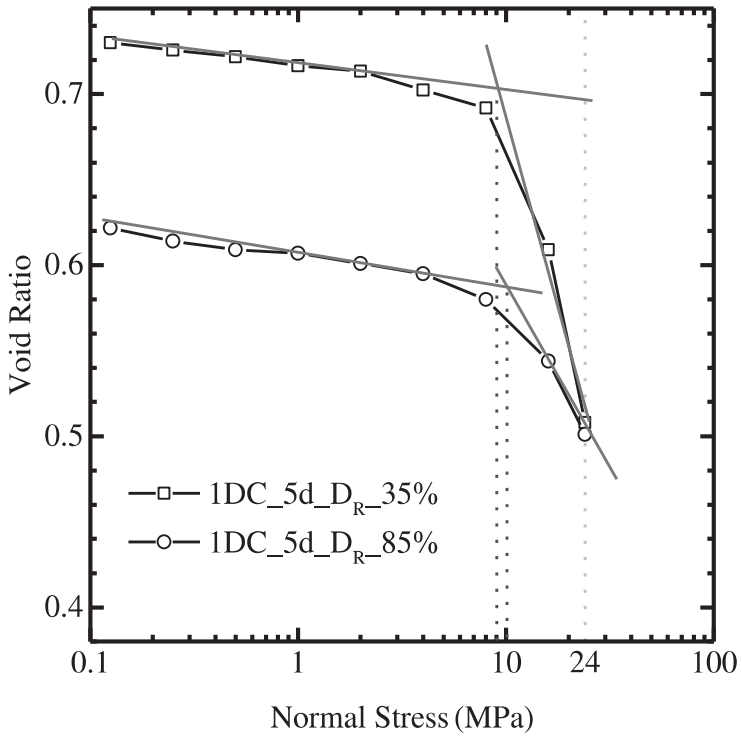

Figure 4.18 Void ratio versus normal stress (log scale) curves for one-dimensional compression tests performed on Ohio Gold Frac sand for 5 days (maximum σ_N = 24 MPa).

Figure 4.19 shows the compression curves in void ratio versus normal stress space for the one-dimensional compression tests performed on dense (D_R= 85%) and loose (D_R= 35%) samples for 5 days with normal stresses of up to 24 MPa (the horizontal axis is in linear scale). Following the same reasoning explained previously for the samples

compressed for 10 hours, the loose and dense samples continued to compress due to particle crushing during the 5 days of load application.

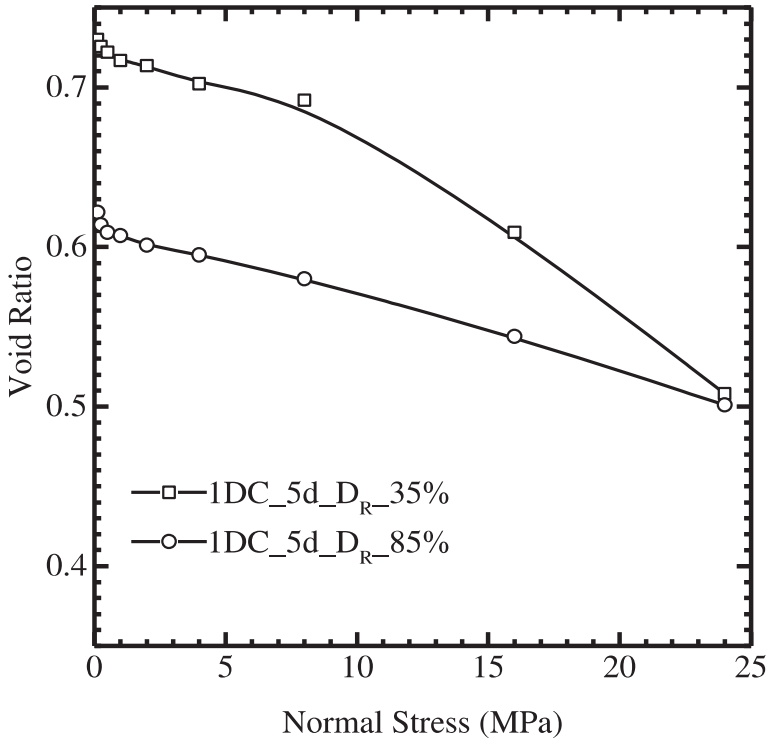

Figure 4.19 Void ratio versus normal stress (linear scale) curves for one-dimensional compression tests performed on Ohio Gold Frac sand for 5 days (maximum σ_N = 24 MPa).

Figure 4.20 shows the compression curves for two sand samples with different initial densities compressed up to 24 MPa for a period of 10 days. Crushing intensified for the dense and loose samples at normal stresses of 10 MPa and 9 MPa, respectively (these results are similar to the results obtained for the 1D compression tests performed for 10 hours). Table 4.14 shows the change in void ratio as the 1D compression tests progressed

for a period of 10 days. The loose sand sample compressed more than the dense sand sample, as expected.

Table 4.14 Void ratio change with normal stress for one-dimensional compression tests performed for a period of 10 days.

No.	Test Code	e_0	e_f
1	1DC_10d_D_R_35%	0.733	0.434
2	1DC_10d_D_R_85%	0.623	0.496

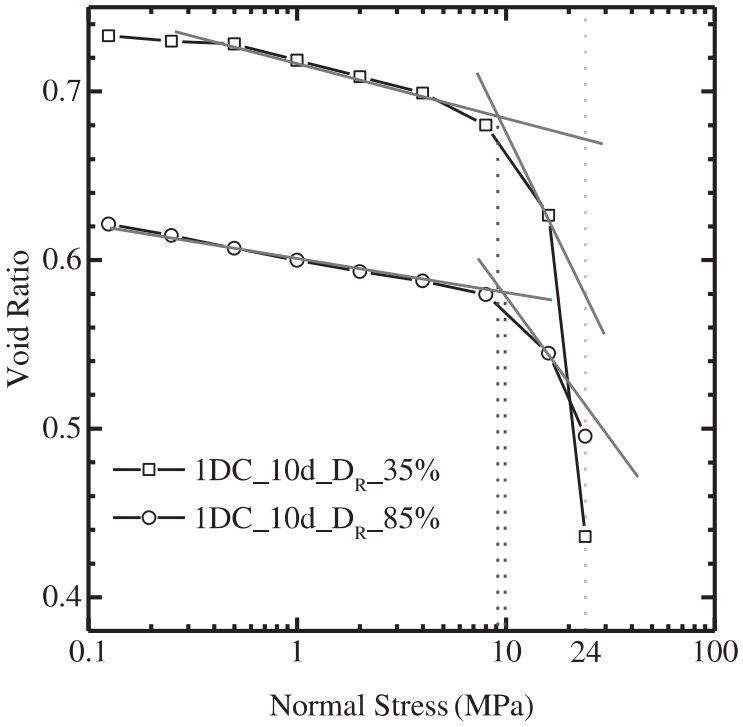

Figure 4.20. Void ratio versus normal stress (log scale) curves for one-dimensional compression tests performed on Ohio Gold Frac sand during 10 days (σ_N= 24 MPa).

Figure 4.21 shows the compression curves for the loose and dense samples in void ratio versus normal stress space obtained from the one-dimensional compression tests

performed with stresses of up to 24 MPa for 10 days (the horizontal axis is in linear scale). Particle crushing is ongoing during the 10 days of load application. As shown in Figure 4.21, particle crushing not only occurs for normal stresses greater than 9 MPa for loose samples and 10 MPa for dense samples. Particle crushing is occurring even at very small loads.

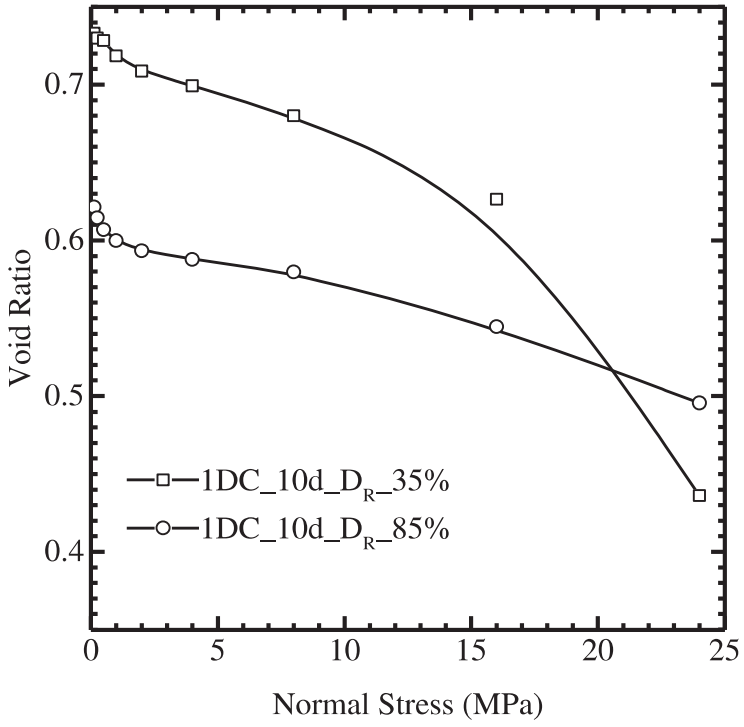

Figure 4.21 Void ratio versus normal (linear scale) stress curves for one-dimensional compression tests performed on Ohio Gold Frac sand for 10 days (maximum σ_N = 24 MPa).

4.9.1 Particle breakage parameters of Ohio Gold Frac sand after one-dimensional compression tests

Equations (2.15), (2.16) and (2.17) were used to calculate the initial and final breakage potential (B_{p0} and B_{pf}), the total breakage (B_t) and the relative breakage (B_r) to evaluate the crushability of the sand after the one-dimensional compression tests. The gradation curves were obtained after the one-dimensional compression tests to compare with the original gradation curve of Ohio Gold Frac sand and to obtain the breakage parameters. Figure 4.22, Figure 4.23, and Figure 4.24 show the gradation curves after the one-dimensional compression tests performed during 10 hours, 5 days and 10 days, respectively, together with the original gradation curve for OGF sand.

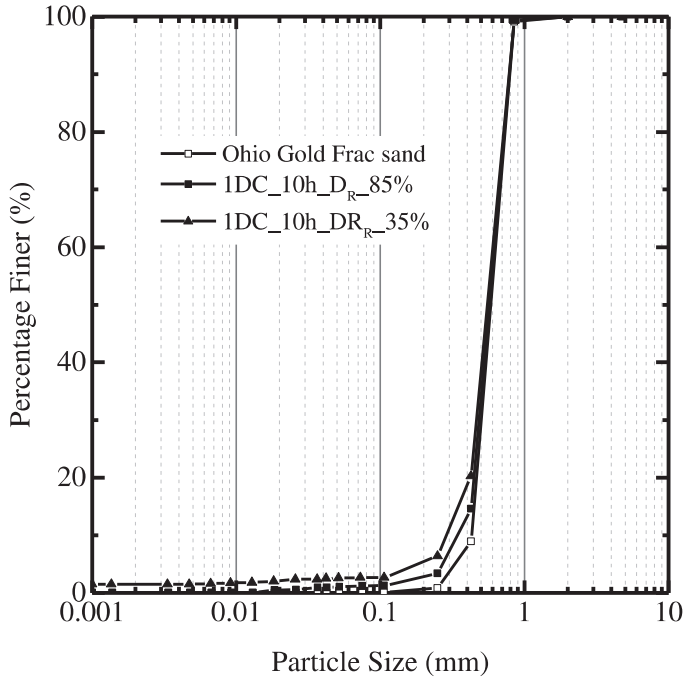

Figure 4.22. Grain size distribution curves for Ohio Gold Frac sand before and after performing one-dimensional compression tests for a period of 10 hours with normal stresses of up to 24 MPa.

Table 4.15 shows the breakage parameters obtained for the Ohio Gold Frac sand samples subjected to one-dimensional compression tests for a period of 10 hours, 5 days and 10 days taking into account particles with D> 0.001 mm [considering the particle size extension suggested by Sadrekarimi and Olson (2010) and Table 4.16 shows the breakage parameters considering particles with D> 0.075 mm [as proposed by Hardin (1985)]. Figure 4.25 shows the initial breakage potential B_{p0} for Ohio Gold Frac sand, which is equal to 2.76.

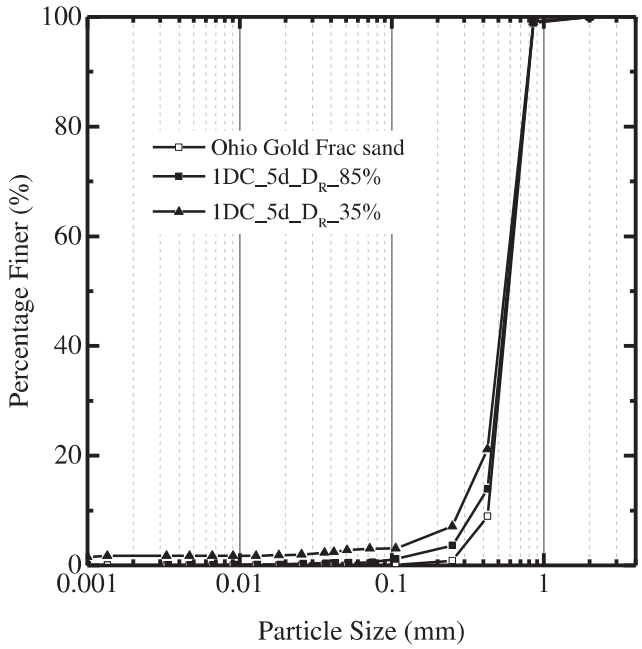

Figure 4.23. Grain size distribution curves for Ohio Gold Frac sand before and after performing one-dimensional compression tests for a period of 5 days with normal stresses of up to 24 MPa.

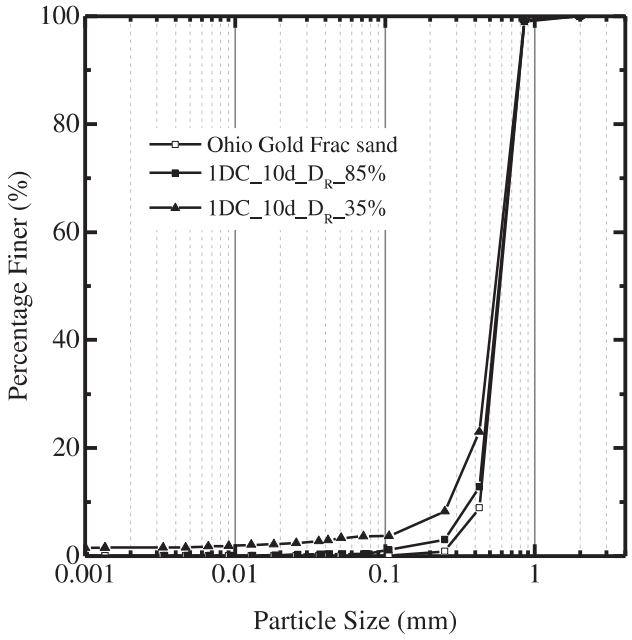

Figure 4.24. Grain size distribution curves for Ohio Gold Frac sand before and after performing one-dimensional compression tests for a period of 10 days with normal stresses of up to 24 MPa.

It is observed that the breakage parameters from Table 4.15 (D> 0.001mm) differ from the breakage parameters from Table 4.16 (D> 0.075mm). After the one-dimensional compression tests, there is an increase in the percentages of silt- and clay-sized particles; therefore, it is necessary to take into account the particles smaller than 0.075mm when calculating the breakage parameters. The breakage parameters in Table 4.15 are used to analyze the results of the one-dimensional compression tests

Table 4.15 Initial breakage potential B_{p0}, final breakage potential B_{pf}, total breakage B_t, and relative breakage B_r obtained after one-dimensional compression tests on Ohio Gold Frac sand (D> 0.001 mm).

Test Code	B_{p0}	B_{pf}	B_t	B_r
1DC_10h_D_R_35%	2.755	2.515	0.240	0.081
1DC_10h_D_R_85%	2.755	2.593	0.162	0.063
1DC_5d_D_R_35%	2.755	2.533	0.222	0.082
1DC_5d_D_R_85%	2.755	2.582	0.173	0.061
1DC_10d_D_R_35%	2.755	2.533	0.222	0.087
1DC_10d_D_R_85%	2.755	2.582	0.173	0.059

Table 4.16 Initial breakage potential B_{p0}, final breakage potential B_{pf}, total breakage B_t, and relative breakage B_r obtained after one-dimensional compression tests on Ohio Gold Frac sand (D> 0.075 mm).

Test Code	B_{p0}	B_{pf}	B_t	B_r
1DC_10h_D_R_35%	0.880	0.824	0.056	0.064
1DC_10h_D_R_85%	0.880	0.853	0.028	0.031
1DC_5d_D_R_35%	0.880	0.819	0.061	0.070
1DC_5d_D_R_85%	0.880	0.856	0.024	0.027
1DC_10d_D_R_35%	0.880	0.808	0.072	0.082
1DC_10d_D_R_85%	0.880	0.861	0.019	0.022

In Figure 4.26 to Figure 4.31, the breakage parameters are shown for the six samples subjected to one-dimensional compression tests. As indicated in these figures, particle crushing increases the percentage of fines without any change in the maximum particle size of the sand. It can also be seen in these figures that the loose samples experienced more particle crushing than the dense samples.

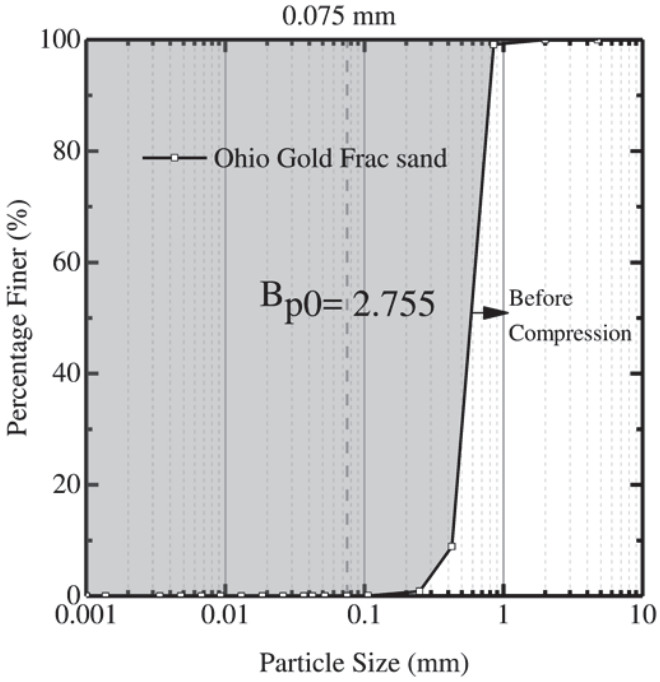

Figure 4.25. Initial breakage potential B_{p0} for Ohio Gold Frac sand.

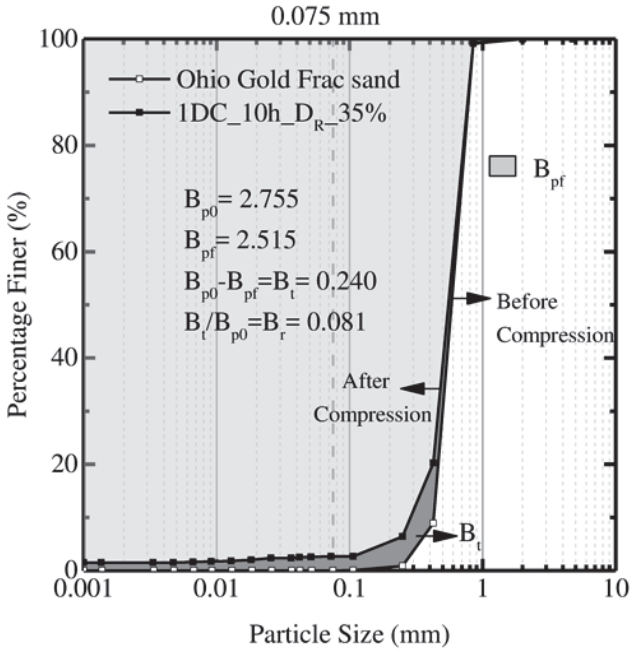

Figure 4.26. Breakage parameters for the test performed on a loose sample (D_R=35%) of Ohio Gold Frac during 10 hours with normal stresses of up to 24 MPa.

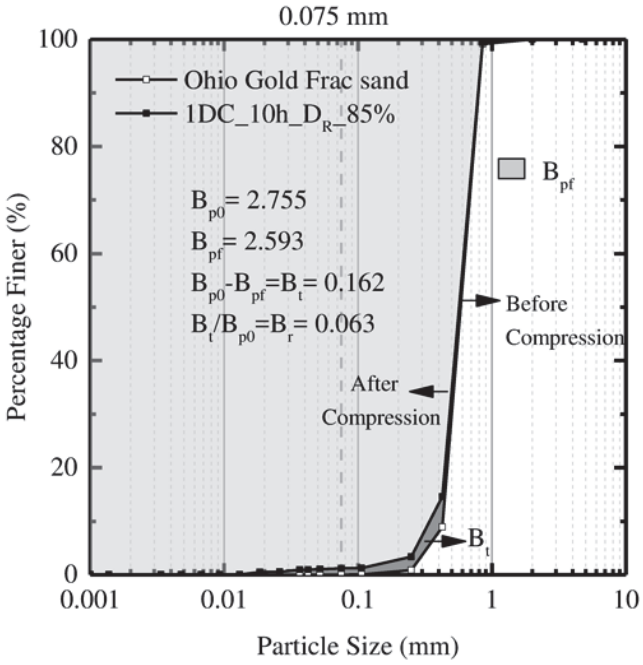

Figure 4.27. Breakage parameters for the test performed on a dense sample (D_R=85%) of Ohio Gold Frac during 10 hours with normal stresses of up to 24 MPa.

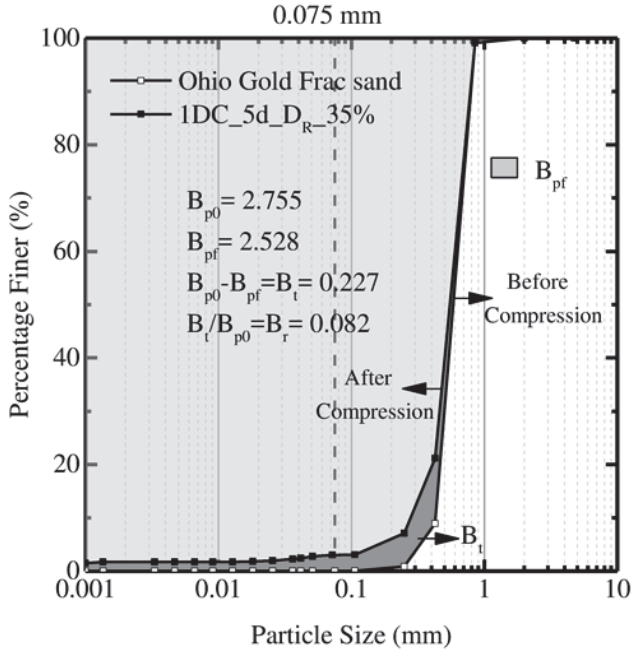

Figure 4.28. Breakage parameter values for the test performed on a loose sample (D_R=35%) of Ohio Gold Frac during 5 days with normal stresses of up to 24 MPa.

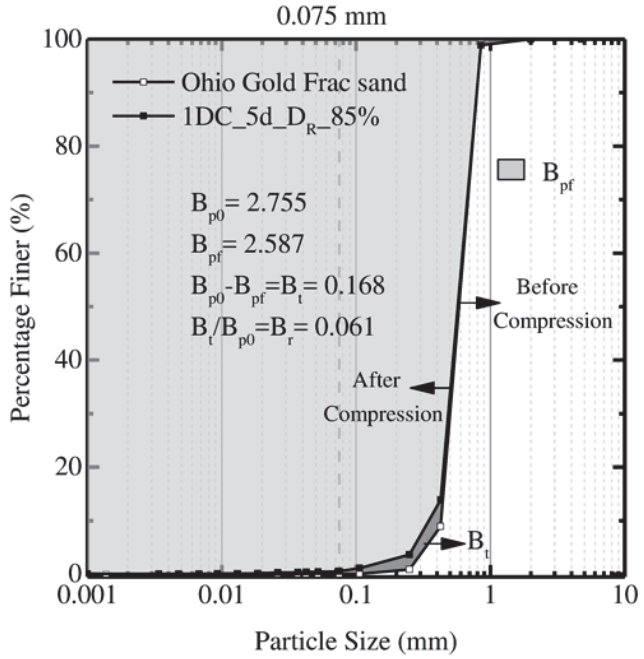

Figure 4.29. Breakage parameter values for the test performed on a dense sample (D_R=85%) of Ohio Gold Frac during 5 days with normal stresses of up to 24 MPa.

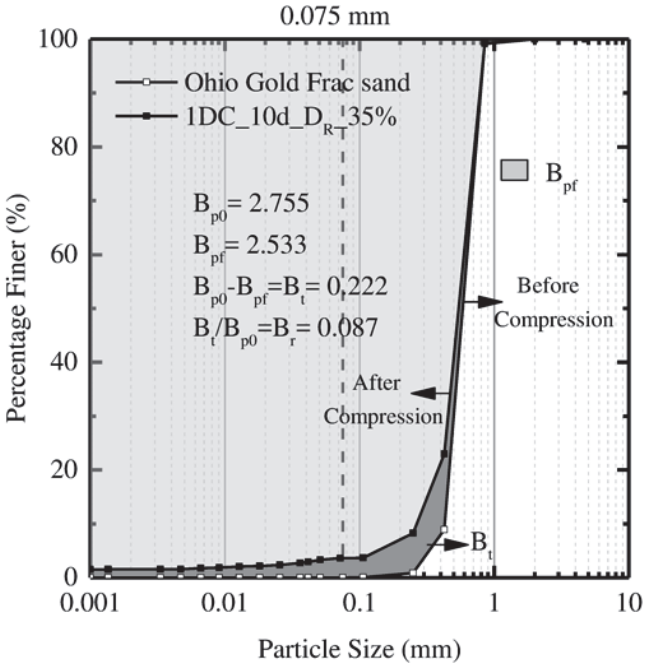

Figure 4.30. Breakage parameter values for the test performed on a loose sample (D_R=35%) of Ohio Gold Frac during 10 days with normal stresses of up to 24 MPa.

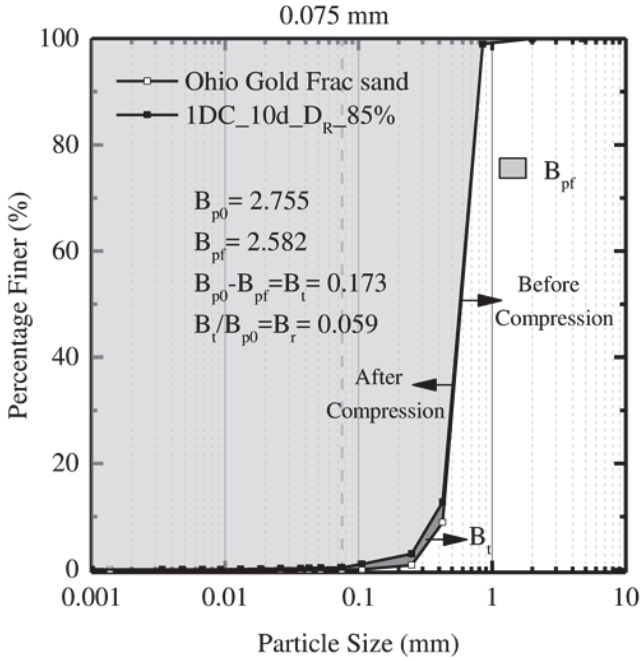

Figure 4.31. Breakage parameter values for the test performed on a dense sample (D_R=85%) of Ohio Gold Frac during 10 days with normal stresses of up to 24 MPa.

According to Table 4.15 and Figure 4.26 to Figure 4.31, the sand sample that experienced the most particle crushing is the loose sand sample (D_R=35%) tested during 10 days. Figure 4.32 shows the evolution of the relative breakage parameter B_r with time, where it can be seen that it is almost constant for dense samples, but for loose samples may increase slightly, which indicates that there is no time-dependence.

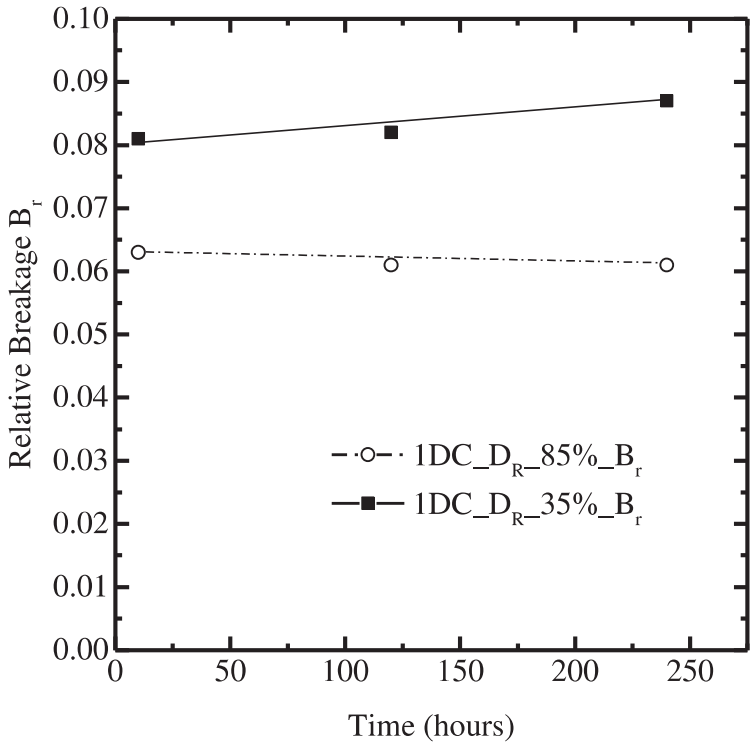

Figure 4.32. Relative breakage evolution for the Ohio Gold Frac sand after performing one-dimensional compression tests for 10 hours and 10 days.

4.9.2 Particle size evolution after one-dimensional compression tests

During one-dimensional compression tests, particle crushing is accompanied by particle rearrangement as the test progresses. Particle gradation changes are caused by abrasion of the edges and asperities of the particles and by splitting and breaking of the particles into progressively smaller sizes. With these gradation changes, a sand initially classified as poorly graded, may be classified as well graded after testing. According to Table 4.17, the gradation parameters that changed the most are the coefficient of uniformity C_u and the particle size diameter D_{10}. The particle size diameter D_{10} of the original sand changed from 0.43 to 0.27, thereby affecting the value of the coefficient of uniformity C_u, which changed from 1.44 to 2.22 after performing the one-dimensional compression test

for 10 days in a loose sample. However, according to the USCS, despite the gradation changes, none of the four sand samples subjected to the one-dimensional compression tests would meet the requirements to be re-classified as well-graded sand. All the four sand samples after the 1D compression tests are still designated as poorly-graded sands "SP" according to ASTM 2487.

Figure 4.33 and Figure 4.34 show the particle diameter evolution with respect to time for the loose and dense samples tested under one-dimensional compression. Figure 4.35 and Figure 4.36 show the evolution of the coefficient of uniformity and coefficient of curvature as a function of time for the loose and dense samples. It can be observed that there is not significant evolution of the gradation parameters with respect to time. The difference between the samples tested during 10 hours and during 10 days is almost negligible, which indicates no time-dependence

Table 4.17 Gradation parameters of Ohio Gold Frac sand before and after performing one-dimensional compression tests.

Test Code	D_{10}	D_{30}	D_{50}	D_{60}	C_u	C_c
Original Sand	0.43	0.5	0.58	0.62	1.44	0.94
1DC_10h_D_R_85%	0.35	0.49	0.58	0.61	1.74	1.12
1DC_10h_D_R_35%	0.28	0.47	0.55	0.6	2.14	1.31
1DC_5d_D_R_85%	0.35	0.49	0.59	0.62	1.771	1.13
1DC_5d_D_R_35%	0.27	0.46	0.55	0.6	2.22	1.32
1DC_10d_D_R_85%	0.33	0.49	0.56	0.6	1.82	1.21
1DC_10d_D_R_35%	0.27	0.47	0.53	0.61	2.26	1.34

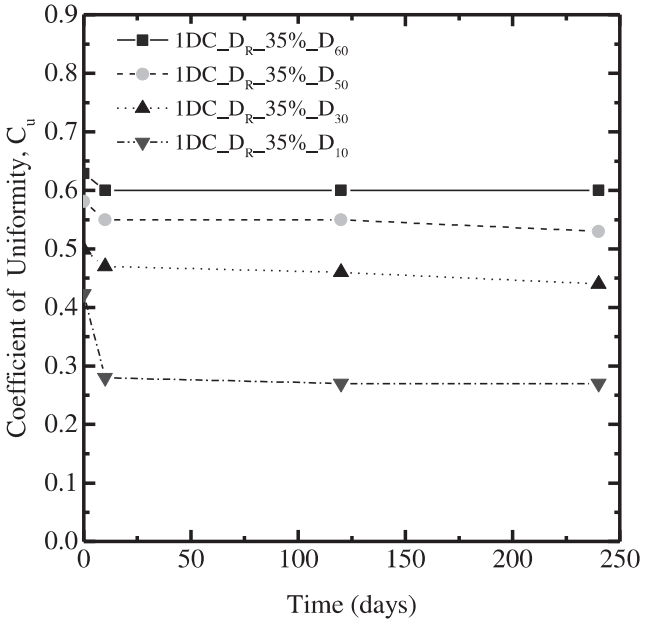

Figure 4.33 Particle diameter evolution after performing one-dimensional compression tests on loose samples (D_R=35%) of Ohio Gold Frac sand during 10 hours, 5 days and 10 days.

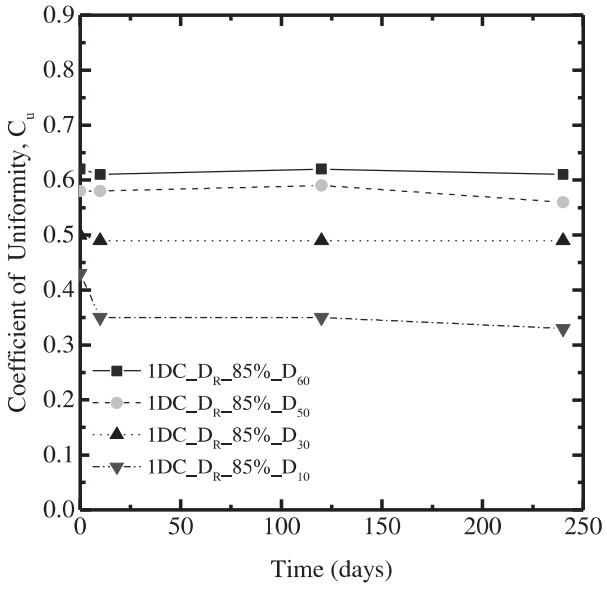

Figure 4.34 Particle diameter evolution after performing one-dimensional compression tests on dense samples (D_R=85%) of Ohio Gold Frac sand during 10 hours, 5 days and 10 days.

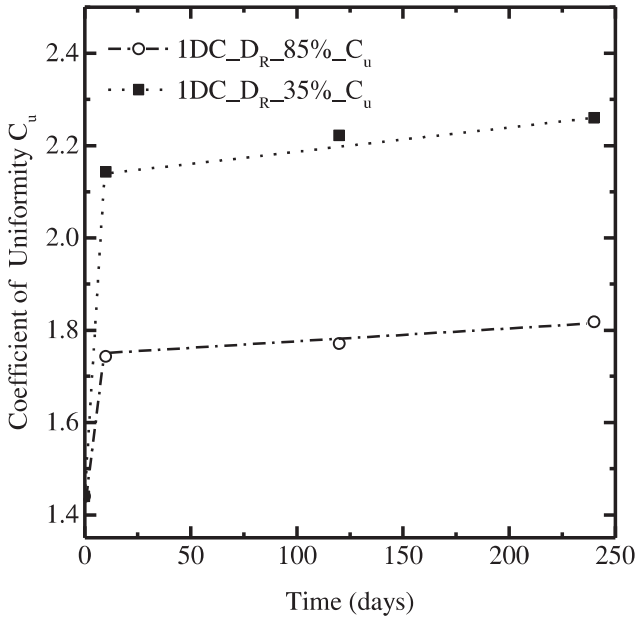

Figure 4.35 Coefficient of uniformity evolution after performing one-dimensional compression tests on dense samples (D_R=85%) of Ohio Gold Frac sand during 10 hours, 5 days and 10 days.

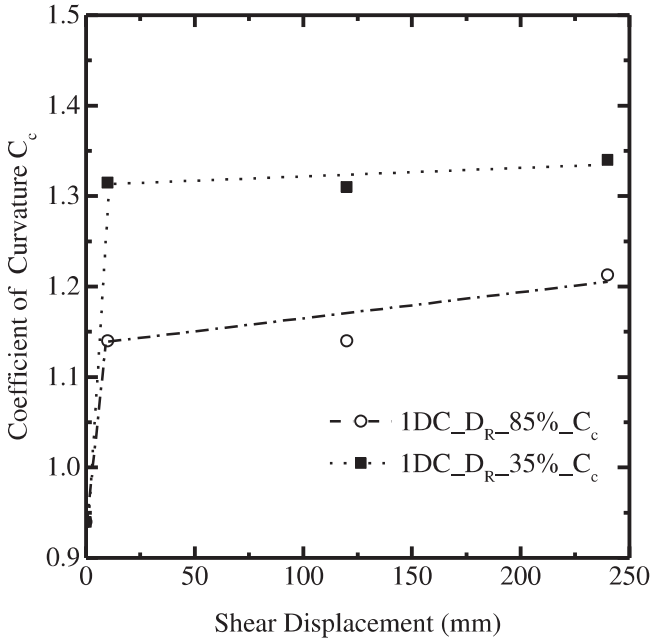

Figure 4.36 Coefficient of curvature evolution after performing one-dimensional compression tests on dense samples (D_R=85%) of Ohio Gold Frac sand during 10 hours, 5 days and 10 days.

4.9.3 Particle morphology evaluation after one-dimensional compression tests

By using a light microscope, visual characterization of the sand particles was done after the one-dimensional compression tests were performed. The typical arrangement of the particles and the images taken after the tests are shown in Figure 4.37. A total of 20 particles per each sieve were selected randomly and analyzed under the microscope. Digital images were captured by a camera connected to a computer and processed by the image processing tool ImageJ. All the raw images and processed images are shown in Appendix C.

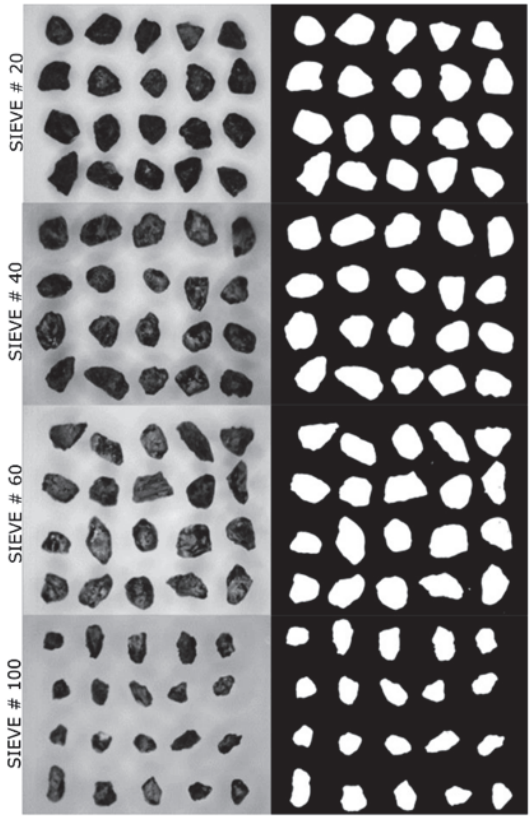

Figure 4.37 Microscope image of the particles retained on sieves # 20, # 40, # 60 and #100 after performing one-dimensional compression tests on Ohio Gold Frac sand.

Table 4.18 Global particle morphology parameters after one-dimensional compression tests.

Test Code	*Circularity*	*AR*	*Roundness*	*Sphericity*
Original Sand	0.62	1.42	0.73	0.76
1DC_10h_35%	0.63	1.39	0.74	0.86
1DC_10h_85%	0.60	1.48	0.71	0.84
1DC_5d_35%	0.60	1.41	0.74	0.85
1DC_5d_85%	0.60	1.40	0.74	0.85
1DC_10d_35%	0.63	1.42	0.73	0.85
1DC_10d_85%	0.67	1.43	0.73	0.84

Table 4.18 summarizes the global particle morphology parameters determined after the one-dimensional compression tests that were performed on Ohio Gold Frac sand. The average values for these parameters show that they do not change significantly in comparison with the average values of the original Gold Frac sand. It is worth to emphasize that the fines are created by particle crushing; therefore, the morphology analyses after 1D compression tests also include the particle morphology parameters of the particles retained over the sieve #200.

As shown in Figure 4.38, Figure 4.40, Figure 4.42, Figure 4.44, Figure 4.46, and Figure 4.48, the sand particles became more spherical (the sphericity parameter increased for all sieves). The range of particles that experienced most change in the sphericity parameter are those that were retained in the sieve #60 (0.250 mm) and in the sieve #100 (0.149 mm). The sphericity parameter for the original sand from sieve #60 (Figure 4.5) is equal to 0.69, and it increased to 0.8 after testing for all the samples from one-dimensional compression tests. Similarly, for sieve #100, the sphericity parameter increment to 0.8; It can be inferred from the changes in these parameters that abrasion of the angularities and shearing-off of asperities of the particles from sieves #20,#40 and #60 occurred.

Figures 4.35 and 4.36 (which provide the sand particle morphology parameters after 1D compression of a loose sample with D_R= 35% to normal stresses of up to 24 MPa during 10 days) show that the crushed particles from sieve #200 have lower values of circularity and roundness, which are equal to 0.5 and 0.6, respectively, than the larger particles from sieve #20 (circularity=0.62; sphericity=0.82) and sieve #100 (circularity=0.68; sphericity=0.7). This shows that the crushed particles from sieve #200 are more elongated. It can also be observed that the values of the aspect ratio morphology parameter (the relationship between the largest diameter to the smaller diameter of the particle) for this test has its highest value (=1.6) for sieve #200, confirming that the newly formed crushed particles from sieve #200 are more elongated than the crushed particles retained on sieves #20, #40, #60 and #100.

With respect to the larger particles from sieve #20, it can be noticed that the values of the sphericity (=0.86) and roundness (ranging from 0.71 to 0.74) parameters are similar for the four 1D compression tests. This indicates that the mechanisms that produced most particle damage during 1D compression tests are the shearing-off of the asperities and edges of the large particles.

Figure 4.39 to Figure 4.49 show a comparison between the global particle morphology parameters (the values provided in these figures are averages) after and before 1D compression tests. It can be noticed that the most affected global morphology parameter after the 1D compression tests is the sphericity parameter, with values ranging from 0.76 to 0.86.

Figure 4.50 and Figure 4.51 show the global sand particle morphology parameters (the values provided in these figures are averages) versus time for the sand samples analyzed after the one-dimensional compression tests performed for 10 hours, 5 days and 10 days. It can be observed from these figures that there is no change in the morphology parameters with time (from 10 hours to 10 days) for the loose and dense samples after the 1D compression tests, therefore the response of Ohio Gold Frac sand after one-dimensional compression tests does not evolve with time.

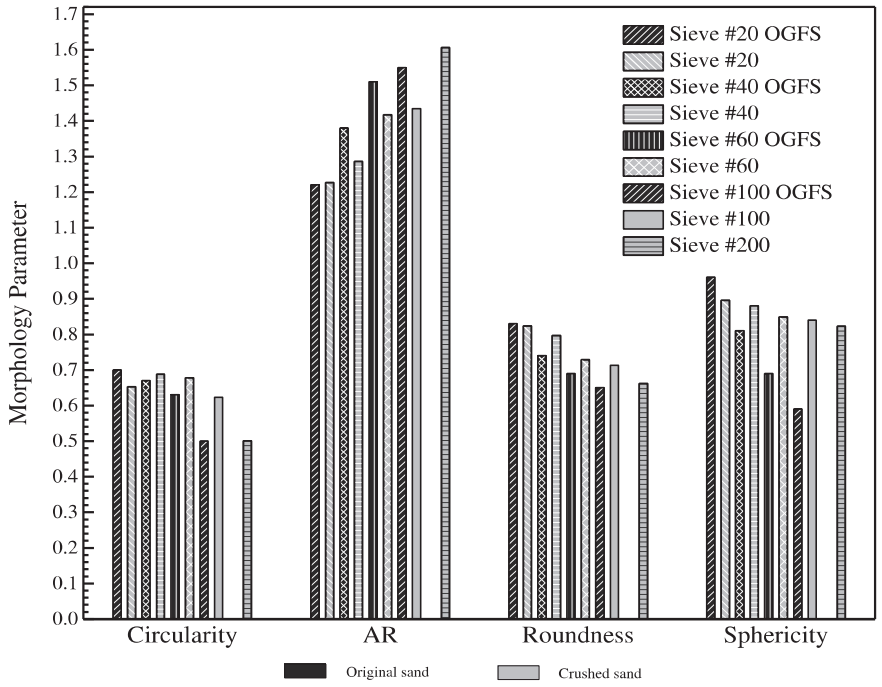

Figure 4.38 Sand particle morphology parameters after 1D compression test of a loose sample (D_R= 35%) to normal stresses of up to 24 MPa during 10 hours.

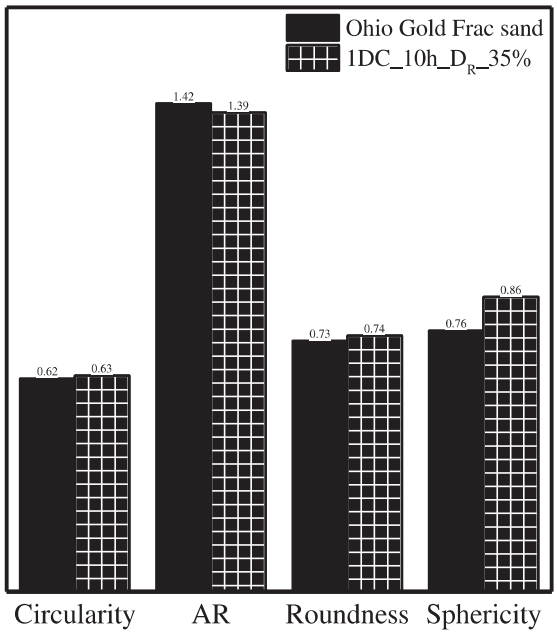

Figure 4.39 Comparison between the global particle morphology parameters obtained before and after a one-dimensional compression test on a loose (DR=35%) sand sample tested with normal stresses of up to 24 MPa during 10 hours.

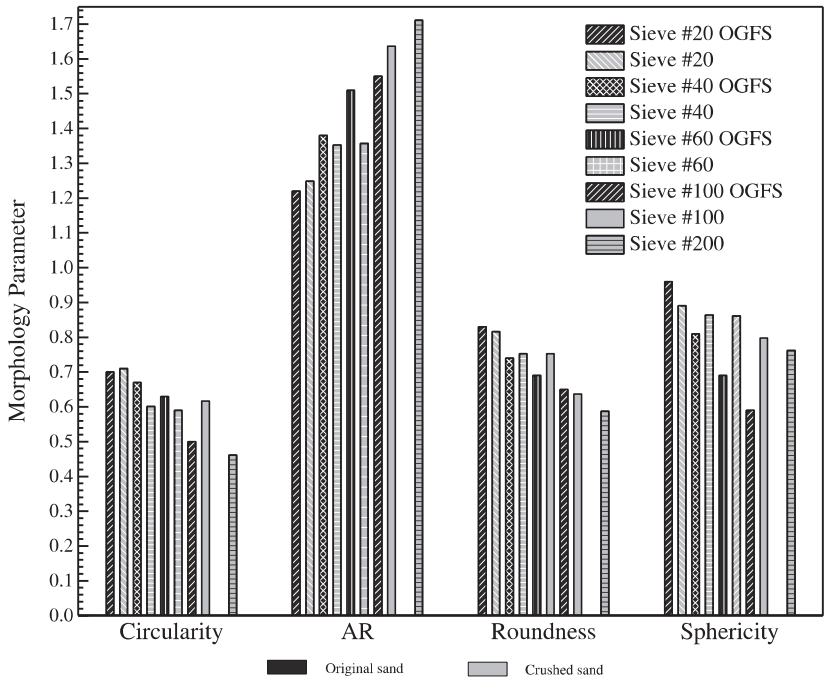

Figure 4.40 Sand particle morphology parameters after 1D compression test of a dense sample (D_R= 85%) to normal stresses of up to 24 MPa during 10 hours.

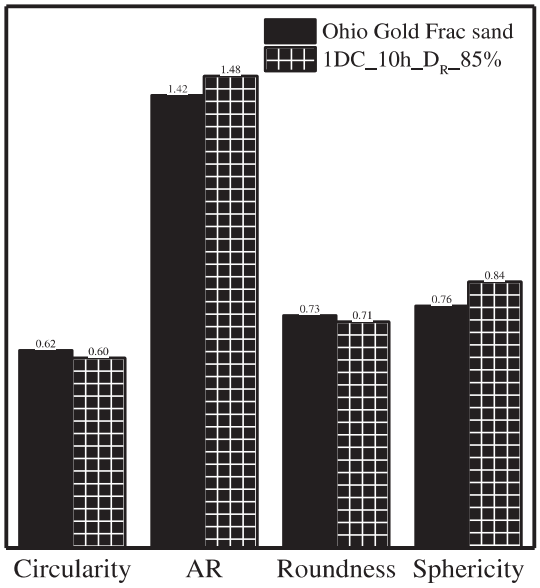

Figure 4.41 Comparison between the global particle morphology parameters obtained before and after a one-dimensional compression test on a dense (D_R= 85%) sand sample tested with normal stresses of up to 24 MPa during 10 hours.

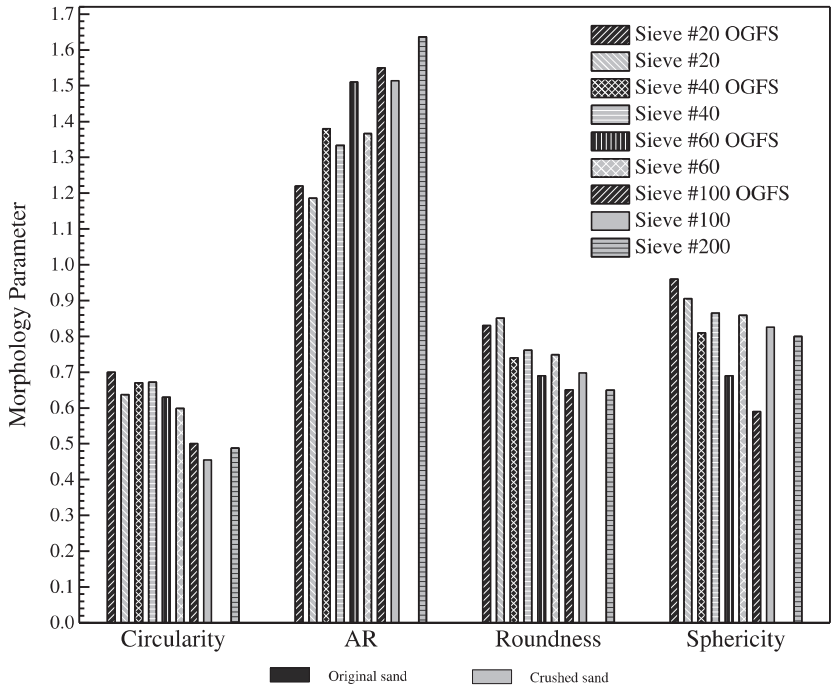

Figure 4.42 Sand particle morphology parameters after 1D compression test of a loose sample (D_R= 35%) to normal stresses of up to 24 MPa during 5 days.

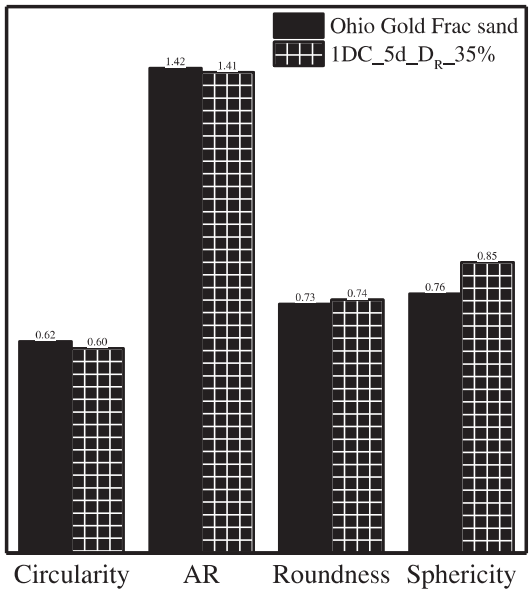

Figure 4.43 Comparison between the global particle morphology parameters obtained before and after a one-dimensional compression test on a loose (D_R=35%) sand sample tested with normal stresses of up to 24 MPa during 10 days.

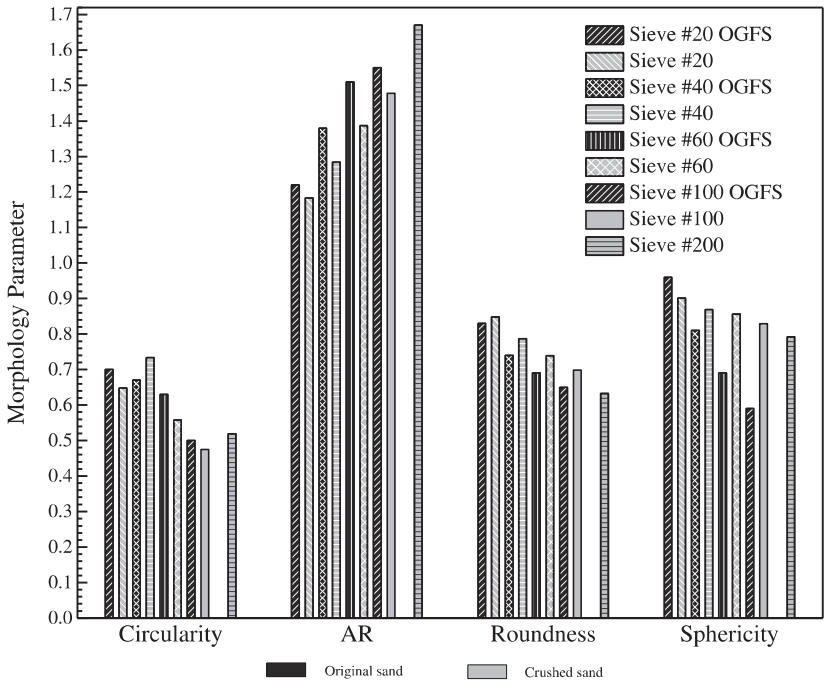

Figure 4.44 Sand particle morphology parameters after 1D compression test of a dense sample (D_R= 85%) to normal stresses of up to 24 MPa during 5 days.

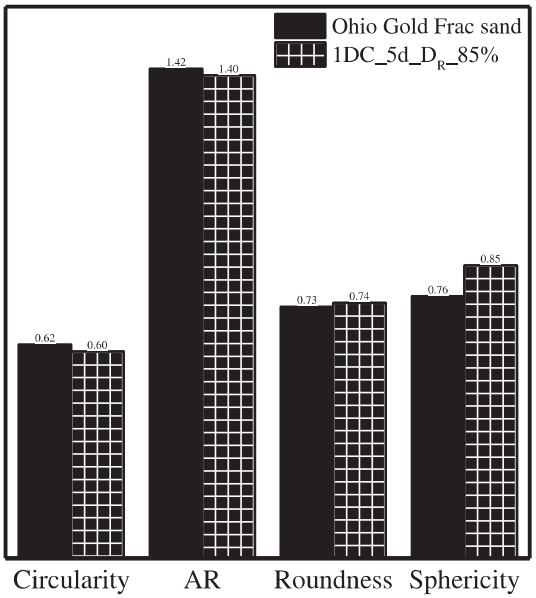

Figure 4.45 Comparison between the global particle morphology parameters obtained before and after a one-dimensional compression test on a dense (D_R=85%) sand sample tested with normal stresses of up to 24 MPa during 10 days.

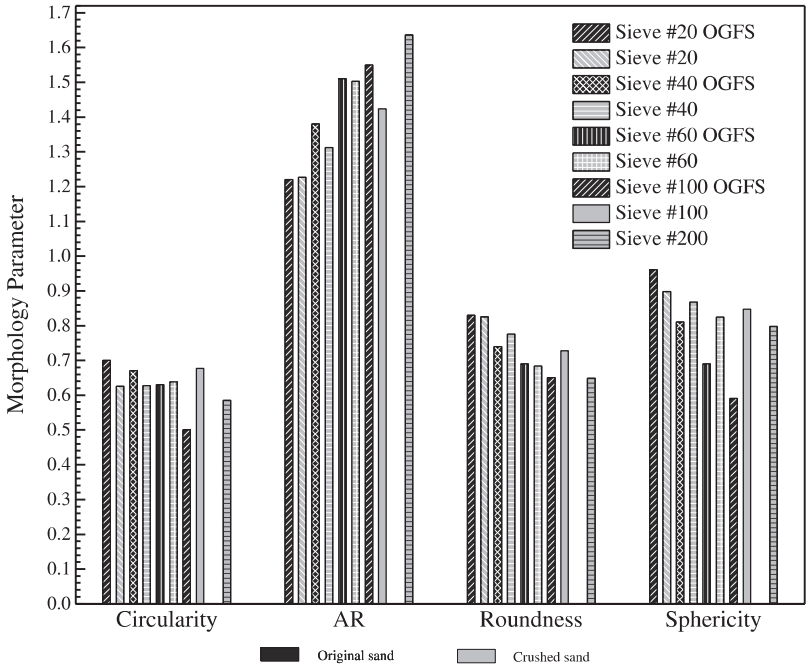

Figure 4.46 Sand particle morphology parameters after 1D compression test of a loose sample (D_R= 35%) to normal stresses of up to 24 MPa during 10 days.

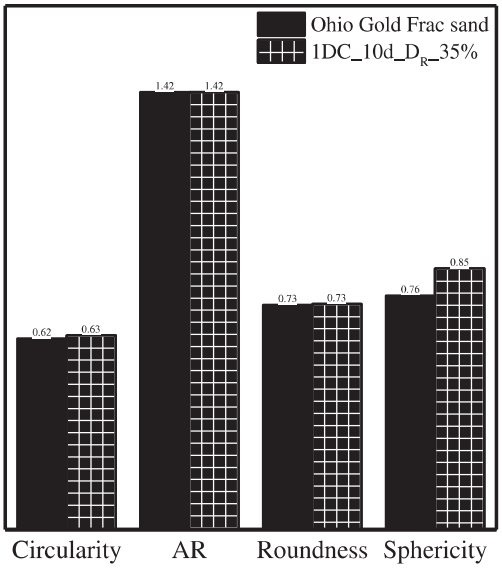

Figure 4.47 Comparison between the global particle morphology parameters obtained before and after a one-dimensional compression test on a loose (D_R=35%) sand sample tested with normal stresses of up to 24 MPa during 10 days.

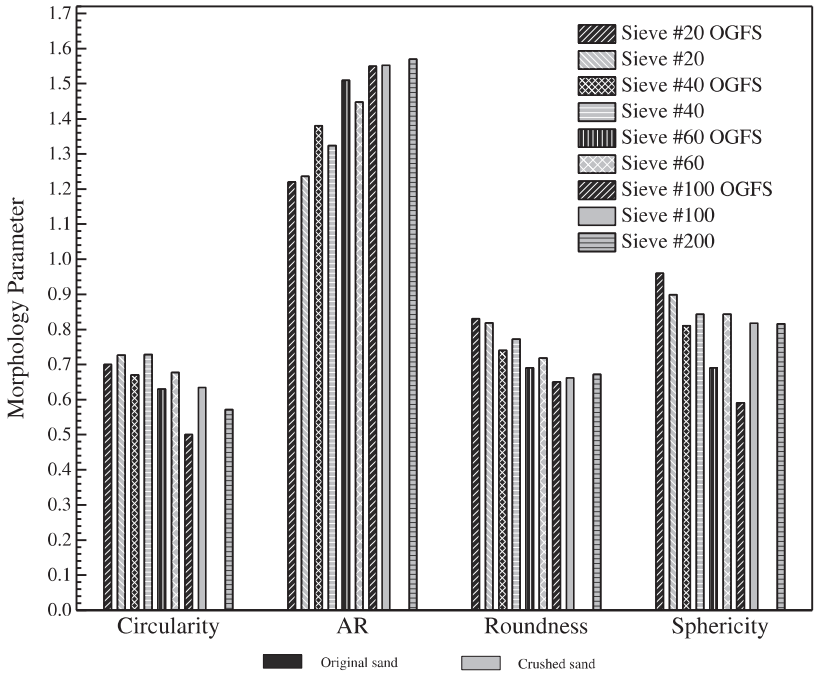

Figure 4.48 Sand particle morphology parameters after 1D compression test of a dense sample (D_R= 85%) to normal stresses of up to 24 MPa during 10 days.

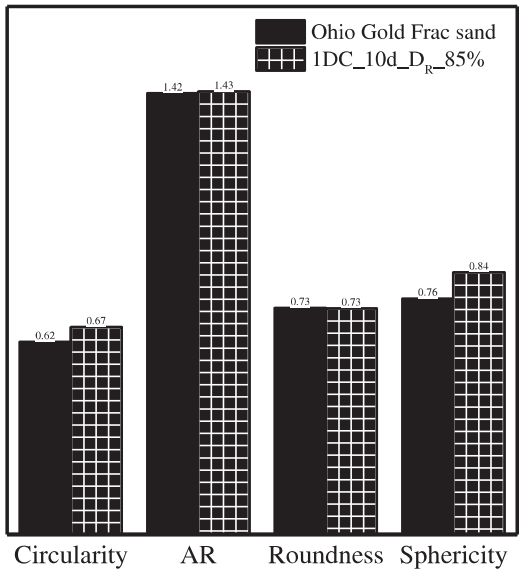

Figure 4.49 Comparison between the global particle morphology parameters obtained before and after a one-dimensional compression test on a dense (D_R=85%) sand sample tested with normal stresses of up to 24 MPa during 10 days.

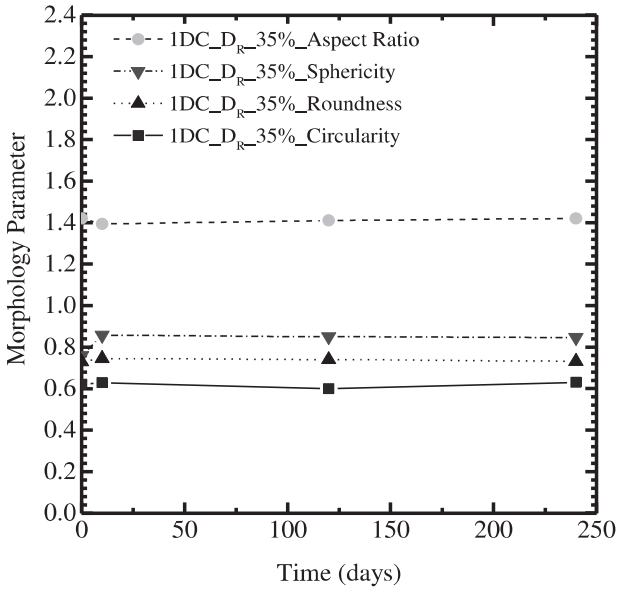

Figure 4.50 Global sand particle morphology parameters versus time after performing one-dimensional compressional tests on loose samples (D_R=35%) with normal stresses of up to 24 MPa during 10 hours, 5 days and 10 days.

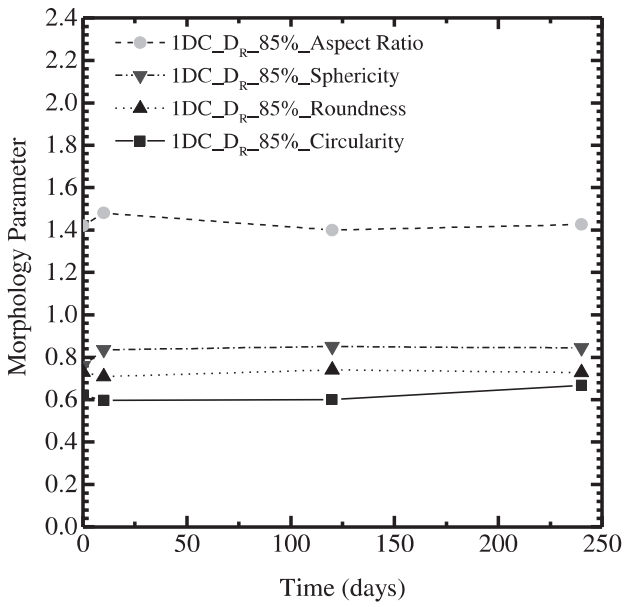

Figure 4.51 Global sand particle morphology parameters versus time after performing one-dimensional compressional tests on dense samples (D_R=85%) with normal stresses of up to 24 MPa during 10 hours, 5 days and 10 days.

4.10 Ring shear test results

A series of drained ring shear tests were carried out to evaluate the crushability of Ohio Gold Frac sand subjected to different normal stresses and shear displacement levels. The ring shear tests were performed at a rate of shear equal to 30 degrees per minute or 32.6 mm/min and 11 degrees per minute or 11.95 mm/min (top platen rotation). After each ring shear test was performed, sand particles in the shear band were carefully collected for particle gradation analyses. The grain size distribution curves of the sand collected from the shear band after testing were compared with the grain size distribution curve of the original Ohio Gold Frac sand (prior to shearing). After performing the gradation analyses of the sand collected from the shear band, twenty particles per each sieve were randomly chosen and placed under the AmScope light microscope to get digital images, which were

then processed and analyzed using the image-processing tool ImageJ to determine particle morphology parameters. Table 4.19 summarizes the tests performed in the ring shear equipment.

Table 4.19 Ring shear tests performed on Ohio Gold Frac sand.

Test	Normal stress (kPa)	D_R[a] (%)	D_{Rc}[b] (%)	Displacement (mm)	Test Code
Ring shear	100	85	86	20000	RS_100kPa_D_R_86%_20m
Ring shear	200	35	36	20000	RS_200kPa_D_R_36%_20m
Ring shear	300	85	87.4	2000	RS_300kPa_D_R_87.4%_2m
Ring shear	400	85	85.7	1000	RS_400kPa_D_R_85.7%_1m
Ring shear	400	85	86.1	2000	RS_400kPa_D_R_86.1%_2m
Ring shear	400	80	81.4	4000	RS_400kPa_D_R_81.4%_4m
Ring shear	400	80	80.8	6000	RS_400kPa_D_R_80.8%_6m
Ring shear	400	85	86.1	7000	RS_400kPa_D_R_86.1%_7m

[a] Initial relative density
[b] Relative density after compression

4.10.1 Shear band formation in the ring shear tests

In the ring shear test, particle crushing is observed within the shear band. The thickness of the shear band depends on the normal stress applied and the shear displacement traveled during testing. The shear band thickness evolves with shear displacement until it reaches an approximately constant thickness. According to the ring shear tests performed by Sadrekarimi and Olson 2009, the shear band stabilized at smaller shear displacements in drained tests than in constant volume tests (for instance, the thickness of the shear band for Ottawa sand was 5 mm and it stabilized at 10 cm of shear displacement in drained tests). For Ohio Gold Frac sand, the thickness of the shear band was about 6 mm at the end of the ring shear tests (it is about 10 times the mean particle diameter size D_{50} of the uncrushed sand). Figure 4.52 shows the shear band formed in a

ring shear test performed in a dense sample (D_R= 80 %) with a normal stress (σ_N) of 400 kPa and shear displacement of 4 meters. Table 4.20 shows the shear band thickness measured after every ring shear test performed on Ohio Gold Frac sand; additionally, D_{10} and D_{50} from the original and crushed sand are indicated to evaluate the evolution of the particle size with respect the shear band thickness. The particle size D_{50} does not show a significant change in comparison with D_{10}.

Table 4.20 Shear band thickness obtained after the ring shear tests performed on Ohio Gold Frac sand.

Test Code	D_{10}[a] mm	D_{10}[b] mm	D_{50}[a] mm	D_{50}[b] mm	Shear Band Thickness mm
RS_100kPa_DR_86%_20m	0.43	0.41	0.58	0.58	6
RS_200kPa_DR_36%_20m	0.43	0.35	0.58	0.58	6
RS_300kPa_DR_87.4%_2m	0.43	0.38	0.58	0.58	5.5
RS_400kPa_DR_85.7%_1m	0.43	0.37	0.58	0.58	5.6
RS_400kPa_DR_86.1%_2m	0.43	0.37	0.58	0.58	5.8
RS_400kPa_DR_81.4%_4m	0.43	0.30	0.58	0.57	5.9
RS_400kPa_DR_80.8%_6m	0.43	0.28	0.58	0.55	6
RS_400kPa_DR_86.1%_7m	0.43	0.26	0.58	0.55	6

[a] D_{10} and D_{50} of the original sand
[b] D_{10} and D_{50} of the crushed sand

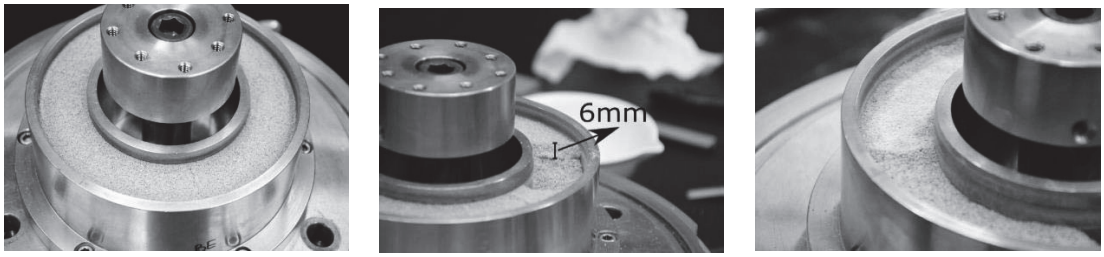

(a) (b) (c)

Figure 4.52 Shear band formation in Ohio Gold Frac sand after performing a ring shear test on a dense sample (D_R= 81.4%) with a normal stress of 400 kPa and shear displacement of 4 meters: (a) uniform shear band; (b) shear band thickness; and (c) particle damage within the shear band.

4.10.2 Stress-displacement response

As shown in Table 4.19, ring shear tests were performed on Ohio Gold Frac sand for normal stresses of 100 kPa, 200 kPa, 300 kPa and 400 kPa and shear displacements ranging from 1m to 20m. These ring shear tests were performed to understand the impact of crushing and particle gradation and morphology evolution on sand response. The results of these tests are provided in sections 4.10.2.1 to 4.10.2.4.

4.10.2.1 Ring shear tests performed on a dense (D_R=86%) sample with a normal stress of 100 kPa and shear displacement of 20 meters.

Figure 4.53 shows the shear stress and vertical displacement versus the shear displacement curves for the ring shear test performed with a normal stress equal to 100 kPa and sheared to a displacement equal to 20 m. The sand sample was prepared using the preparation method described in section 3.5.2.2. The initial relative density D_R of the dense sand sample was equal to 85% and, after compression to a normal stress of 100 kPa, the sample density increased to 86%. The shear rate was equal to 30 degrees per minute. It can be seen that there is no final stabilization of the shear stress and vertical displacement with respect to the shear displacement during these tests; only temporary plateaus for the shear stress and vertical displacement are observed. This indicates that the sand as a material evolves throughout the tests because of particle crushing within the shear band. Figure 4.54 shows the mobilized friction angle [$\phi_{RS}= \tan^{-1}(\tau/\sigma_N)$, where τ is the shear stress and σ_N is the normal stress] and the vertical displacement versus shear displacement curves for the dense sample (D_R= 86%) of Ohio Gold Frac sand tested with a normal stress of 100 kPa and sheared to a displacement of 20m.

Figure 4.55 (a) and Figure 4.55 (b) show the mobilized friction angle and vertical displacement versus shear displacement curves of the dense sample (D_R= 86%) sheared with a normal stress of 100 kPa for shear displacements ranging from 0 to 0.1m (at the beginning of the test) and from 18 to 20m (at the end of the test). It can be observed initially, at a small shear displacement of 3 mm, that the dense sample shows a peak friction angle of 35º. At the first plateau observed for shear displacement ranging from 6 to 9 mm, the mobilized friction angle has a value of 32.5°, as can be seen in Figure 4.55(a). The second plateau observed in Figure 4.55(a) is at about 40 to 50 mm of shear displacement, corresponding to a mobilized friction angle of 33°. Figure 4.55(b) shows that the mobilized friction angle fluctuates between 30 and 33° during the last 2 m of shearing. A lower bound of the mobilized friction angle can be used to obtain values of the critical-state friction angles (values of the friction angle greater than the smallest values measured are only due to attempts of the sand to dilate which is suppressed when particle crushing starts). In Figure 4.54, the lower mobilized friction is equal to about 30 °

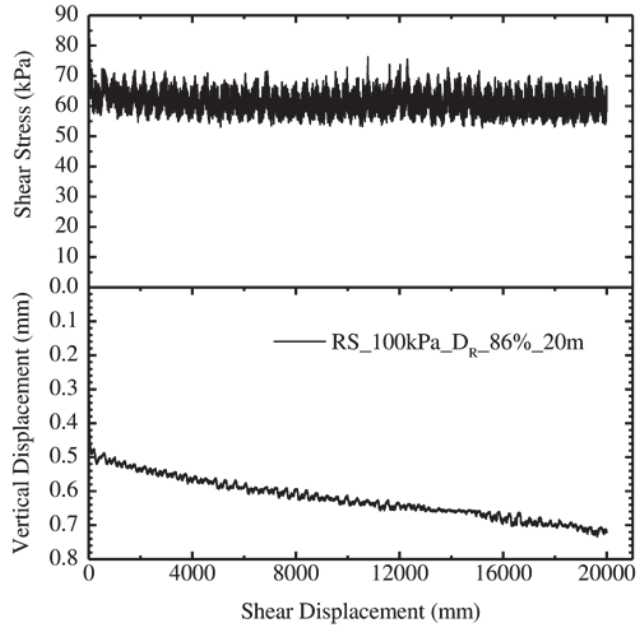

Figure 4.53 Shear stress and vertical displacement versus shear displacement curves for a ring shear test performed on a dense sample (D_R= 86%) of Ohio Gold Frac with a normal stress of 100 kPa and shear displacement of 20 m.

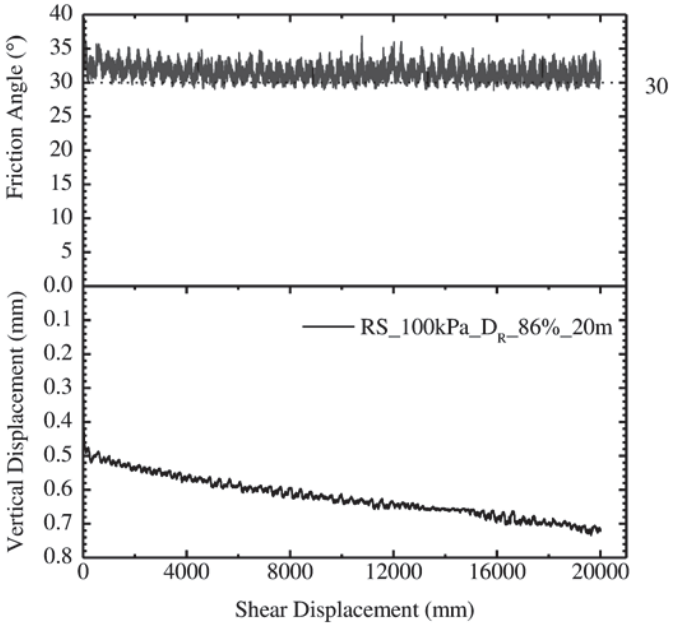

Figure 4.54 Mobilized friction angle for a ring shear test performed on a dense sample (D_R= 86%) of Ohio Gold Frac with a normal stress of 100 kPa and shear displacement of 20 m.

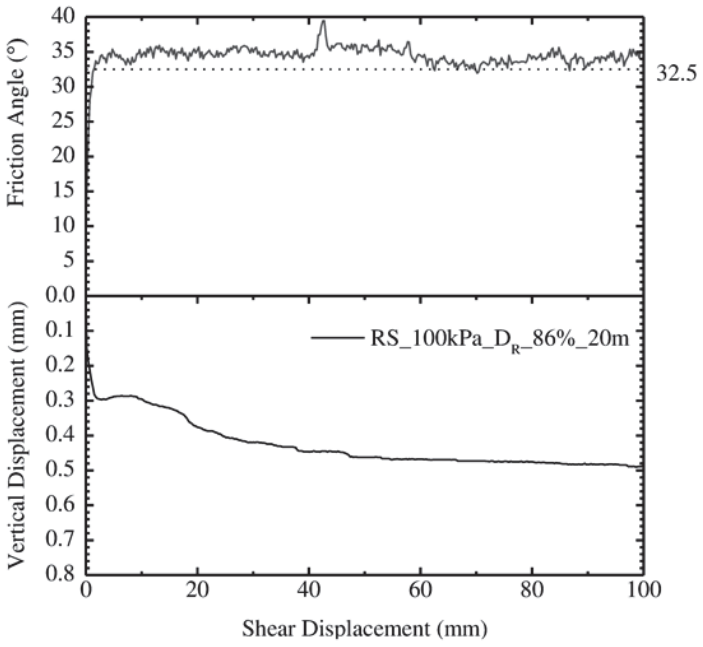

(a)

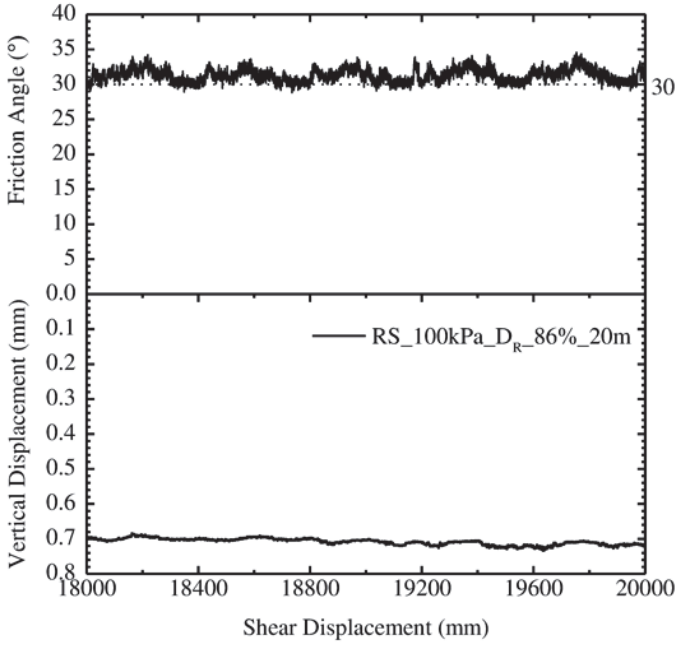

(b)

Figure 4.55 Mobilized friction angle and vertical displacement versus shear displacement curves for a ring shear test performed on a dense sample (D_R=86%) of OGF sand with a normal stress of 100 kPa and shear displacement of 20 m: (a) shear displacement from 0 to 0.1 m; (b) shear displacement from 18 to 2 m.

4.10.2.2 Ring shear test performed on a loose sample (D_R=36%) with a normal stress of 200 kPa and shear displacement of 20 meters.

Figure 4.56 shows the shear stress and vertical displacement versus the shear displacement for a loose sample (D_R=36%) compressed to a normal stress equal to 200 kPa and sheared to a displacement equal to 20 m. The sand sample was prepared with an initial density equal to 35% using the air pluviation method, as explained in section 3.5.2.2. The shear rate was equal to 30 degrees per minute. Again, during this test, there is no final stabilization of the shear stress and vertical displacement with respect to the shear displacement, indicating that the gradation of the sand continues to evolve due to particle crushing. Figure 4.57 shows the mobilized friction angle and the vertical displacement versus the shear displacement curves. The typical cycles with peaks and valleys due to particle crushing and particle rearrangement can be observed in these figures as well.

Figure 4.58(a) and Figure 4.58(b) show the mobilized friction angle (ϕ_{RS}) and vertical displacement versus shear displacement curves of the loose sample (D_R= 36%) sheared with a normal stress of 200 kPa to shear displacements ranging from 0 to 0.1m (in the beginning of the test) and from 18 to 20m (at the end of the test). In Figure 4.58(a), the first plateau in vertical displacement occurs for shear displacement between 3 and 6 mm; the mobilized friction angle in this shearing range is equal to 30º. A second plateau is observed at about 25 mm of shear displacement, corresponding to the same mobilized friction angle of 30º as in the first plateau. Figure 4.58(b) shows the mobilized friction angle for shear displacement between 18 and 20 m; a slight increase of the mobilized friction angle due to particle crushing is observed in this shearing range with the creation

of smaller particles (due to abrasion and shearing-off of the asperities of larger particles) that progressively fill up the small voids in the sand matrix. The smallest values of the mobilized friction angle in Figure 4.57 are equal to 30 °.

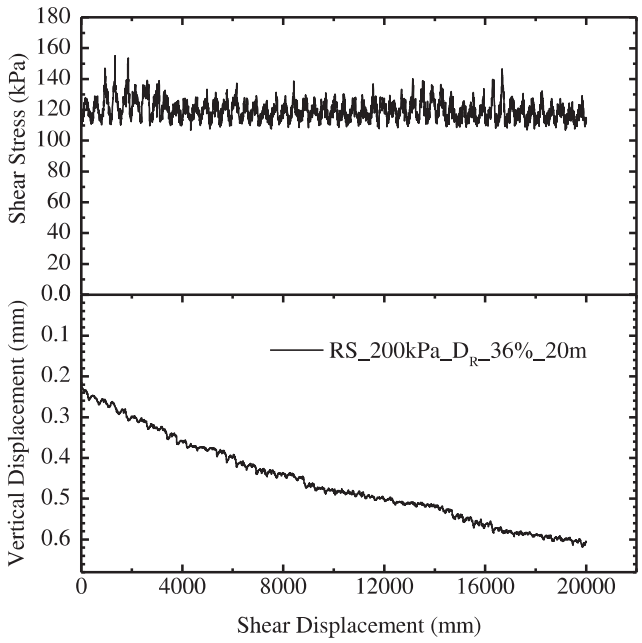

Figure 4.56 Shear stress and vertical displacement versus shear displacement curves for a ring shear test performed on a loose sample (D_R=36%) of Ohio Gold Frac with a normal stress of 200 kPa and shear displacement of 20 m.

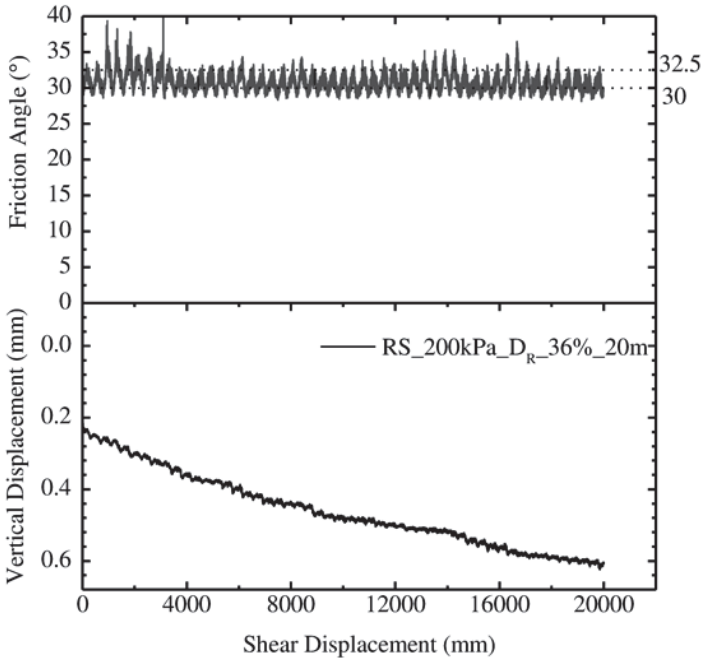

Figure 4.57 Mobilized friction angle for a ring shear test performed on a loose sample (D_R=36%) of Ohio Gold Frac with a normal stress of 200 kPa and shear displacement of 20 m.

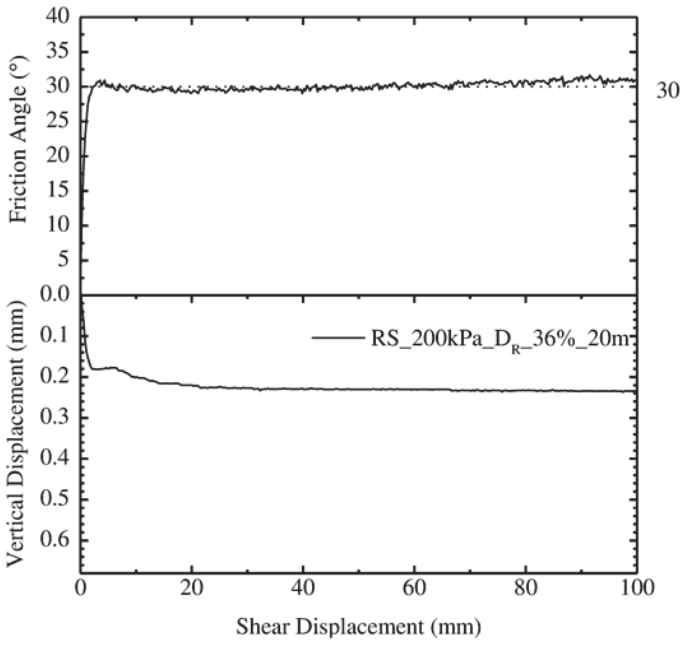

(a)

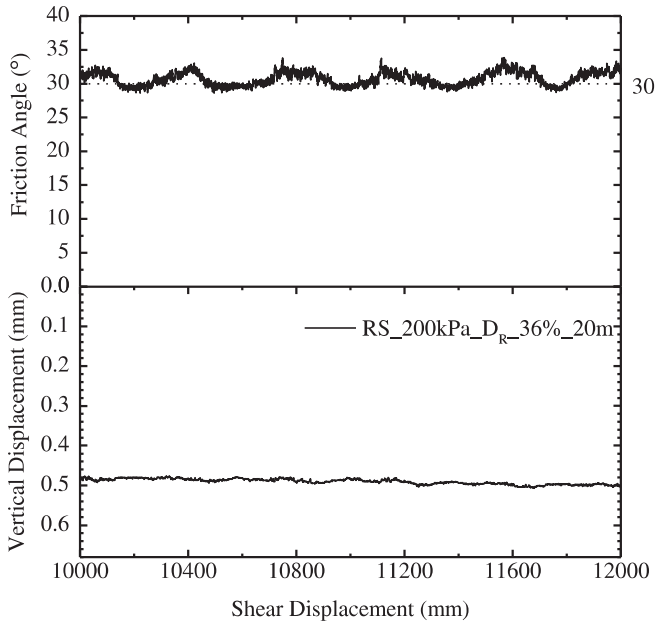

(b)

Figure 4.58 Mobilized friction angle and vertical displacement versus shear displacement curves for a ring shear test performed on a dense sample (D_R=86%) of OGF sand with a normal stress of 200 kPa and shear displacement of 20 m: (a) shear displacement from 0 to 0.1 m; (b) shear displacement from 10 to 12 m.

4.10.2.3 Ring shear test performed on a dense sample (D_R=87.4%) with a normal stress of 300 kPa and shear displacement of 2 meters.

Figure 4.59(a) shows the shear stress and vertical displacement versus the shear displacement curves for the ring shear test performed with a normal stress of 300 kPa and shear displacement equal to 2 m. The dense (D_R= 85%) sand sample was prepared with the air pluviation method (after application of the normal stress equal to 300 kPa, D_R increased to 87.4%). In this test the shear rate applied was about 30 degrees per minute. The cyclic pattern in Figure 4.59(a) indicates that the sample undergoes contraction cycles followed

by dilation cycles and temporary plateaus of shear stress and vertical displacement. However, there is an overall decrease in sample volume with increasing shearing.

Close-up views of the mobilized friction angle and vertical displacement versus shear displacement are shown in Figure 4.60(a) and Figure 4.60(b), where it can be observed that the peak friction angle is equal to 35º and is reached at 5mm of shear displacement. The first plateau is observed at about 7 to 10 mm of shear displacement; in this range, the critical-state friction angle is equal to 30º. The mobilized friction angle fluctuates between 30º and 32.5º and is in synchrony with the shear stresses, as expected, indicating that there is ongoing particle crushing and rearrangement throughout the test, as is shown in Figure 4.60(b). The lower bound value for the mobilized friction angle according to the valleys observed in Figure 4.60(a) and Figure 4.60(b) is about 30°.

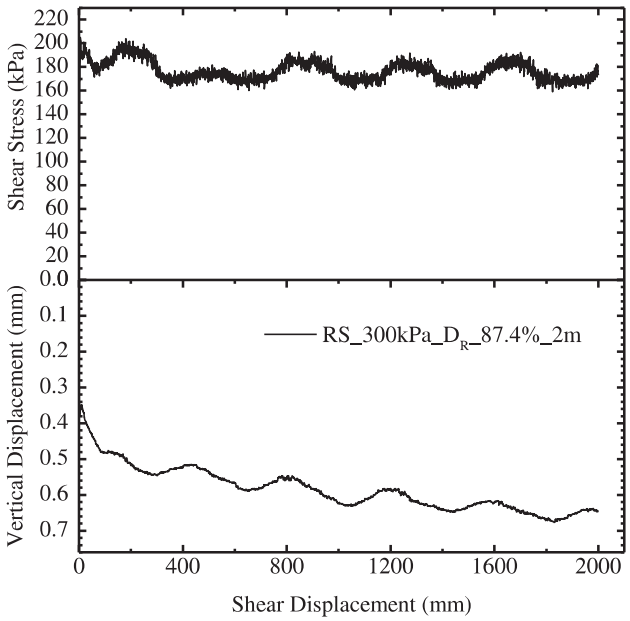

Figure 4.59 Shear stress and vertical displacement versus shear displacement curves for a ring shear test performed on a dense sample (D_R=87.4%) of Ohio Gold Frac with a normal stress of 300 kPa and shear displacement of 2 m.

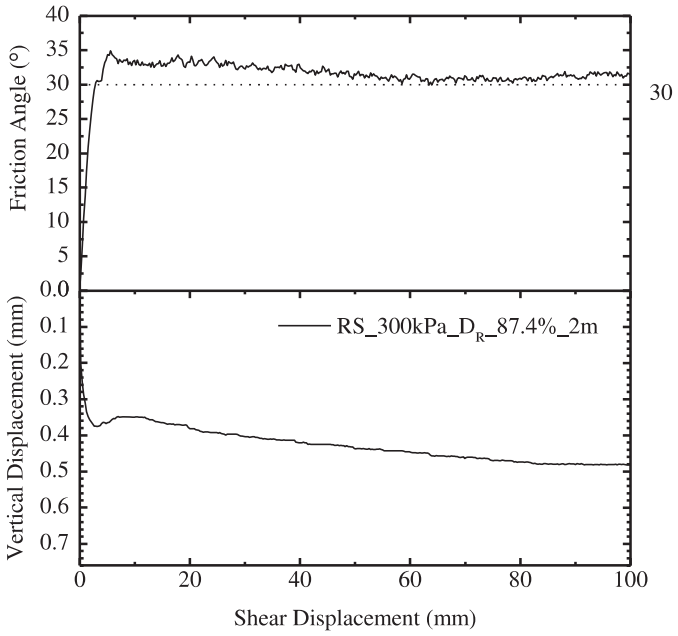

(a)

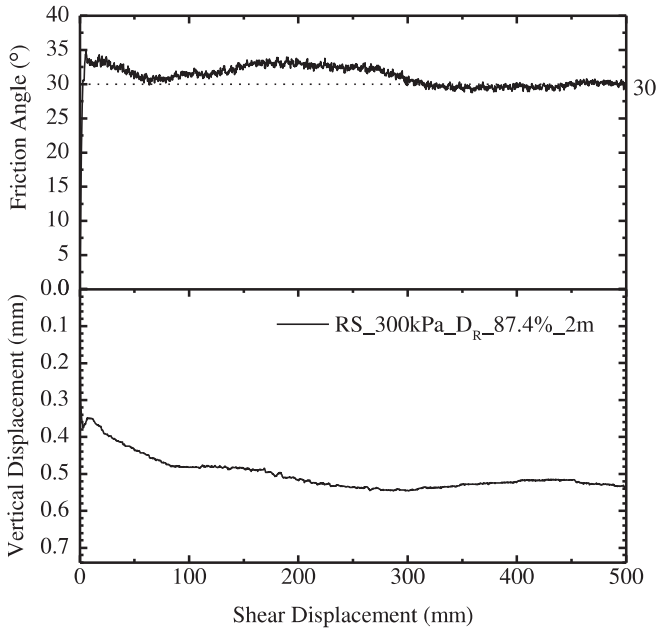

(b)

Figure 4.60 Mobilized friction angle and vertical displacement versus shear displacement curves for a ring shear test performed on a dense sample (D_R= 87.4%) of OGF sand with a normal stress of 300 kPa and shear displacement of 2 m: (a) shear displacement from 0 to 0.1 m; (b) shear displacement from 0 to 0.5 m.

4.10.2.4 Ring shear tests performed on dense samples (relative density ranging from 80.8 to 86.1%) with a normal stress of 400 kPa and shear displacement of 1, 2, 4, 6 and 7 meters.

The results of the tests presented in this section were performed with a normal stress of 400 kPa (a higher normal stress than used in the previous tests) to evaluate the crushing response of Ohio Gold Frac sand during shearing. Figure 4.61 shows the shear stress and vertical displacement versus the shear displacement curves for the ring shear tests performed with a normal stress of 400 kPa and shear displacements of 1, 2 and 7 m (the sand samples were prepared with an initial relative of 85%). A shear rate equal to 30 dpm was used for the samples sheared to 1 and 7 m, while a shear rate equal to 11 dpm for the sample sheared to 2 m. The three samples were subjected to a normal stress of 400 kPa. The relative density after application of the normal stress increased to 85.7% for one of the samples and to 86.1% for the other two samples. As shearing increased, there is an overall decrease in sample volume due to vertical compression. The typical response, with contraction phases followed by dilation and stabilization phases, is also observed for these three samples. In addition, the shear stress versus shear displacement curves for these three tests overlap. Figure 4.61 shows the first 2.5 m of the sample sheared to 7 m for better visualization of the test results.

Figure 4.62 shows the mobilized friction angle (ϕ_{RS}) and vertical displacement versus shear displacement curves for the dense samples compressed to a normal stress of 400 kPa and sheared to displacements of 1, 2 and 7m. The mobilized friction angle fluctuates between 31 and 33 º. Figure 4.63 shows the mobilized friction angle in the first 100 mm of shear displacement for these three tests. The first plateau in vertical

displacement is reached at about 3 to 5 mm of shear displacement, where the mobilized friction angle is equal to 31.5 º.

According to Figure 4.62, the smallest values of the mobilized friction angle are equal to 31 º for the samples sheared to 1 and 2 m. For the sample sheared to a shear displacement of up to 7 m, the lower bound value of the mobilized friction angle is 31.5 º (it increased slightly with increasing shear displacement).

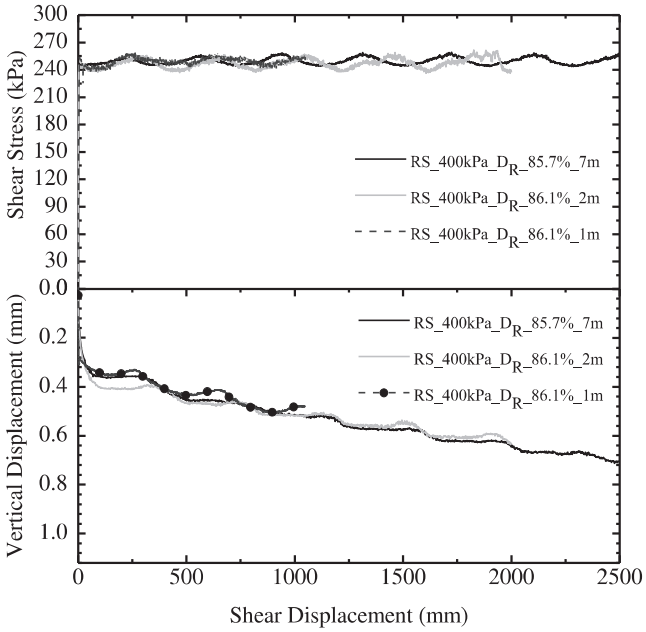

Figure 4.61 Shear stress and vertical displacement versus shear displacement curves for ring shear tests performed on three dense samples (D_R=85.7% and 86.1%) of Ohio Gold Frac with a normal stress of 400 kPa and shear displacements of 1, 2 and 7 m.

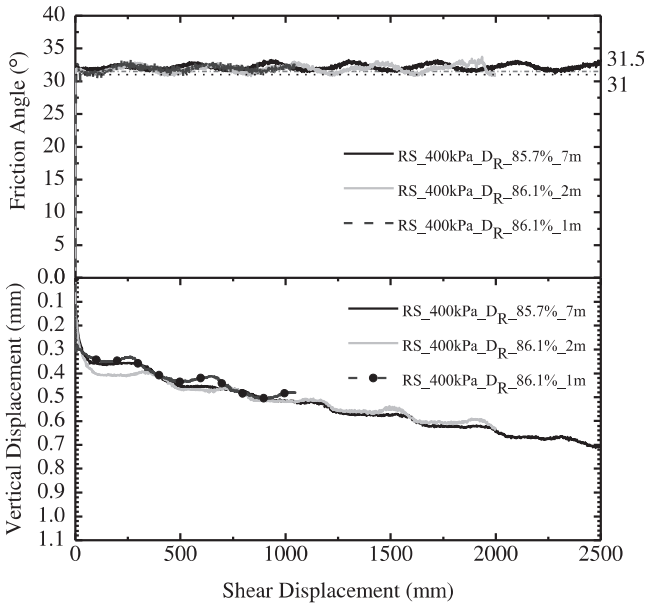

Figure 4.62 Mobilized friction angle and vertical displacement versus shear displacement curves for ring shear tests performed on three dense samples (D_R=85.7% and 86.1%) of Ohio Gold Frac with a normal stress of 400 kPa and shear displacements of 1, 2 and 7 m.

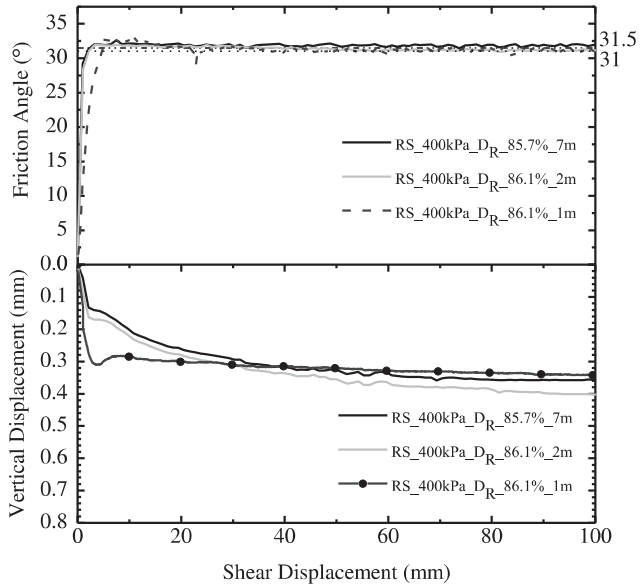

Figure 4.63 Mobilized friction angle and vertical displacement versus shear displacement curves (for the first 100mm of shear displacement) for ring shear tests performed on three dense samples (D_R=85.7% and 86.1%) of Ohio Gold Frac with a normal stress of 400 kPa and shear displacements of 1, 2 and 7 m.

Figure 4.64 provides the shear stress and vertical displacement versus the shear displacement curves for the ring shear tests carried out with a normal stress of 400 kPa and shear displacements of 4 and 6 m. The initial density of the samples was 80%. After application of the normal stress, the relative density of the sand samples increased to 80.8 and 81.4%. The samples were sheared with a shear rate equal to 30 degrees per minute. The overall trend observed during the 4 m and 6 m of shear displacement in these tests is of progressive sample contraction due to particle crushing. The typical response of sample contraction followed by dilation and temporary stabilization of the vertical displacement is also observed in these tests. Also, the shear stress versus shear displacement curves overlap almost perfectly.

Figure 4.65 shows the mobilized friction angle and vertical displacement versus shear displacement curves for the two samples compressed to a normal stress of 400 kPa and sheared to shear displacements of 4 and 6 m. The mobilized friction angle fluctuates between 32 and 33º. Figure 4.66 shows the mobilized friction angle for shear displacement ranging from 0 to 100 mm, in the beginning of these tests. The first plateau in vertical displacement is observed at about 5 to 10 mm of shear displacement, where the mobilized friction angle is equal to 32 º. Also, it can be observed from the valleys shown in Figure 4.65 that the lower bound value for the mobilized friction angle is 32 º for the sample sheared to 6 m and about 33 º for the sample sheared to 4 m. The peak values correspond to mobilized friction angles that reflect the attempts of the sand sample to dilate, which is inhibited by particle crushing.

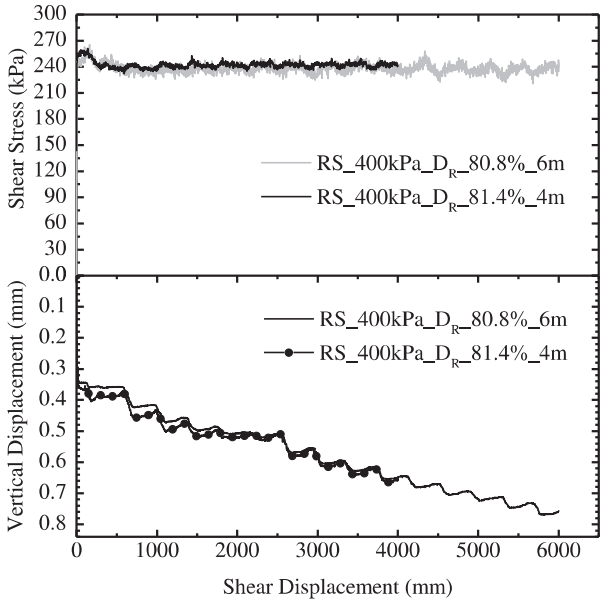

Figure 4.64 Shear stress and vertical displacement versus shear displacement curves for ring shear tests performed on dense samples (D_R=80.8% and 81.4%) of Ohio Gold Frac with a normal stress of 400 kPa and shear displacements of 4 and 6 m.

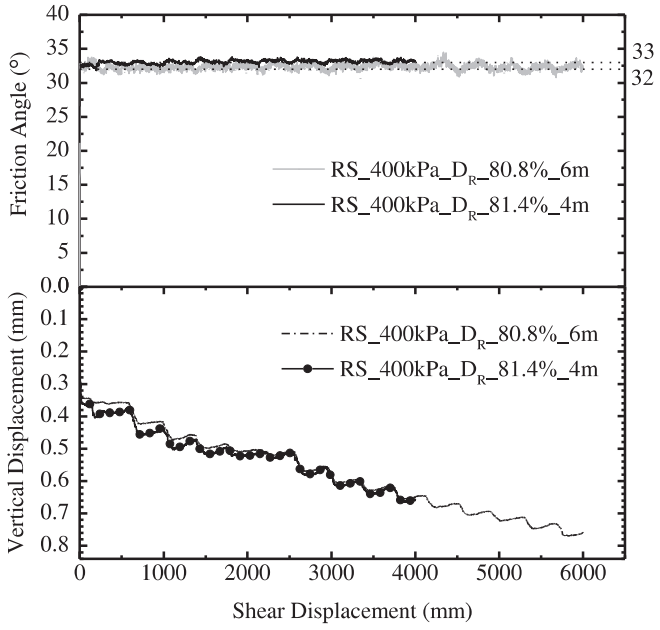

Figure 4.65 Mobilized friction angle and vertical displacement versus shear displacement curves for ring shear tests performed on dense samples (D_R=80.8% and 81.4%) of Ohio Gold Frac with a normal stress of 400 kPa and shear displacements of 4 and 6 m.

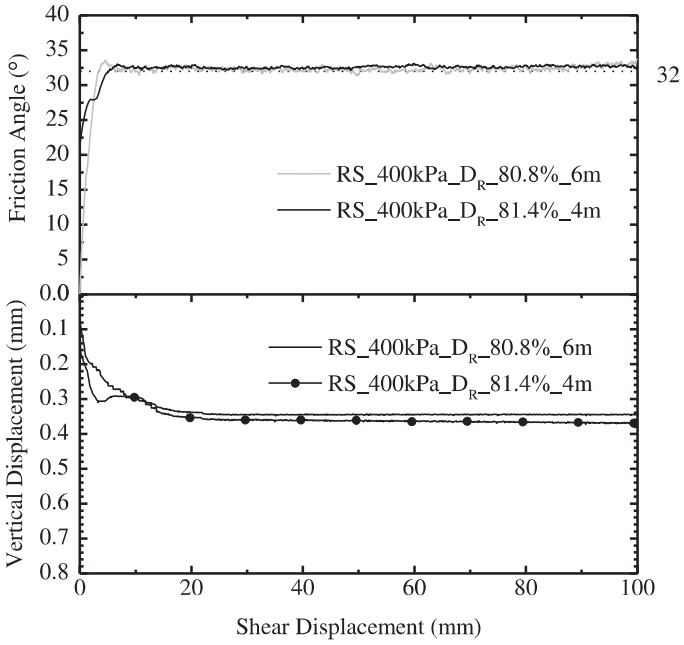

Figure 4.66 Mobilized friction angle and vertical displacement versus shear displacement curves (during the first 100mm) for ring shear tests performed on dense samples (D_R=80.8% and 81.4%) of Ohio Gold Frac with a normal stress of 400 kPa and shear displacements of 4 and 6 m.

4.10.3 Breakage parameters for Ohio Gold Frac sand after the ring shear tests

Breakage parameters were obtained for Ohio Gold Frac sand after ring shear testing. Equations (2.8), (2.9) and (2.10) were used to obtain the initial and final breakage potential (B_{p0} and B_{pf}), the total breakage (B_t) and the relative breakage (B_r) parameters. Figure 4.67 shows the original OGF particle size distribution curve and the particle size distribution curves obtained for the sand collected from the shear bands formed in the nine samples tested in the ring shear equipment.

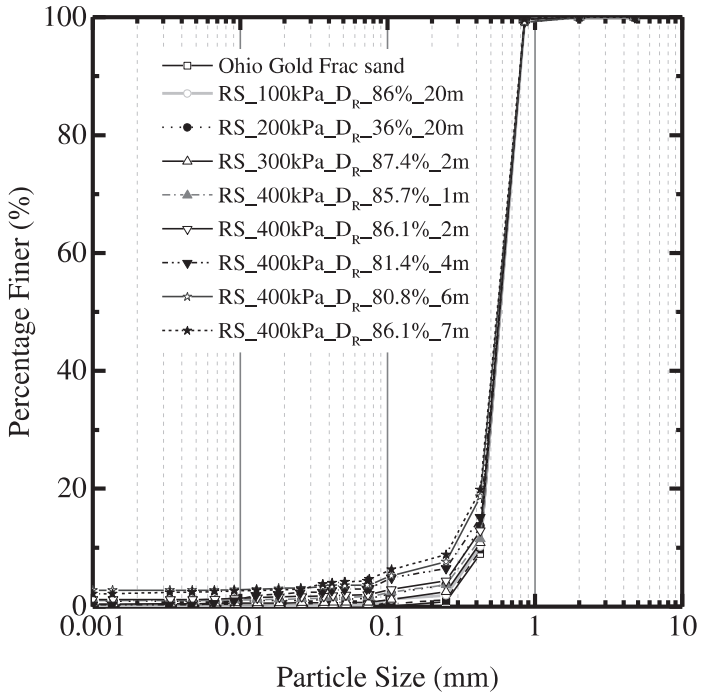

Figure 4.67 Particle size distribution curves obtained for Ohio Gold Frac sand before and after performing ring shear tests with different normal stresses and shear displacements.

Table 4.21 summarizes the breakage parameters for Ohio Gold Frac sand obtained before and after the ring shear tests for D> 0.001 mm. The breakage parameters are: B_{p0} (initial breakage potential before shearing), B_{pf} (final breakage potential after shearing), B_t (total breakage), and B_r (relative breakage = B_t/B_{p0}).

Table 4.22 shows the breakage parameters obtained for Ohio Gold Frac sand before and after the ring shear tests considering particle diameter D>0.075mm, where the contribution from the silt- and clay-sized particles are not considered. The breakage parameters shown in Table 4.21 are higher than the breakage parameters in Table 4.22. Therefore, it is necessary to consider particle sizes greater than 0.001 mm (D> 0.001 mm) to properly quantify also particle damage of very small particles.

Table 4.21 Breakage parameters for Ohio Gold Frac sand before and after ring shear tests (D> 0.001mm).

Test Code	B_{p0}	B_{pf}	B_t	B_r
RS_100kPa_D_R_86%_20m	2.755	2.744	0.012	0.004
RS_200kPa_D_R_36%_20m	2.755	2.708	0.048	0.017
RS_300kPa_D_R_87.4%_2m	2.755	2.729	0.026	0.010
RS_400kPa_D_R_85.7%_1m	2.755	2.705	0.050	0.018
RS_400kPa_D_R_86.1%_2m	2.755	2.696	0.059	0.022
RS_400kPa_D_R_81.4%_4m	2.755	2.682	0.074	0.027
RS_400kPa_D_R_80.8%_6m	2.755	2.636	0.119	0.043
RS_400kPa_D_R_86.1%_7m	2.755	2.496	0.259	0.047

Table 4.22 Breakage parameters for Ohio Gold Frac sand before and after ring shear tests (D> 0.075mm).

Test Code	B_{p0}	B_{pf}	B_t	B_r
RS_100kPa_DR85%_20m	0.880	0.878	0.002	0.002
RS_200kPa_DR35%_20m	0.880	0.869	0.011	0.013
RS_300kPa_DR85%_2m	0.880	0.873	0.007	0.008
RS_400kPa_DR85%_1m	0.880	0.869	0.011	0.012
RS_400kPa_DR85%_2m	0.880	0.867	0.013	0.015
RS_400kPa_DR80%_4m	0.880	0.858	0.022	0.025
RS_400kPa_DR80%_6m	0.880	0.853	0.027	0.031
RS_400kPa_DR85%_7m	0.880	0.805	0.075	0.035

The results shown in Table 4.21 show that the test that produces the greatest particle breakage is the test that was carried out with a normal stress of 400 kPa and a shear displacement of 7 m. This is expected since particle crushing increases as the confining stress and shear displacement increase (Hardin 1985; Sadrekarimi and Olson 2010).

The sand samples tested with a normal stress equal to 100 kPa have lower relative breakage (B_r) than those samples tested with larger normal stresses of 200 kPa, 300 kPa

and 400 kPa. Therefore, these test results are in agreement with results in the literature showing that the relative breakage parameter increases with the normal stress applied (Hardin 1985). Figure 4.68 shows the initial breakage potential (B_{p0}) for Ohio Gold Frac sand before shearing. Figure 4.69 to Figure 4.76 show the total breakage for the tests performed in the ring shear equipment; the particle-size distribution curve of the original (uncrushed) Ohio Gold Frac sand is plotted together with the particle-size distribution curves of the crushed Ohio Gold Frac sand present in the shear bands formed during the ring shear tests.

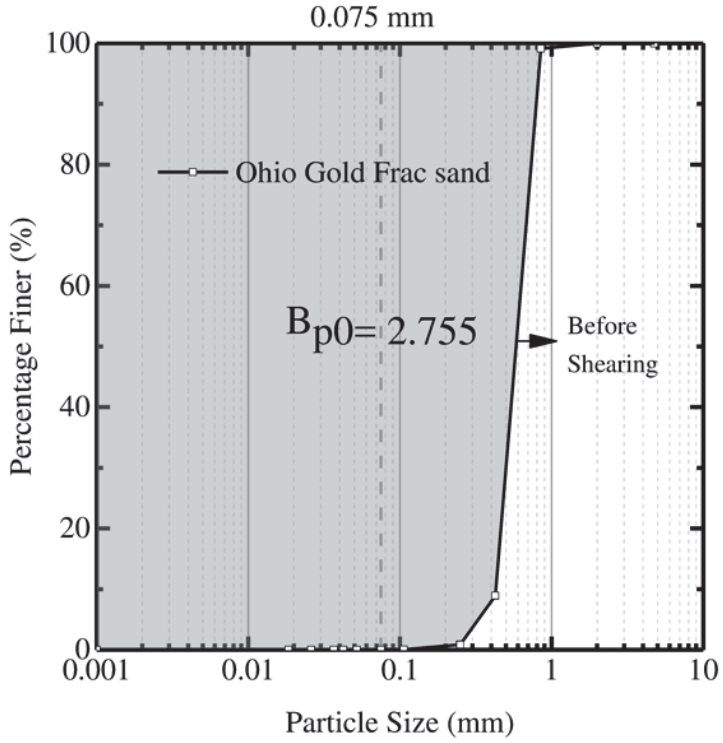

Figure 4.68 Initial breakage potential (B_{p0}) of Ohio Gold Frac sand before the ring shear tests.

Figure 4.69 shows the PSD curve for the original OGF sand and for the sand from the shear band formed in the ring shear test carried out in a dense sample (D_R=86%) with

a normal stress of 100 kPa and shear displacement of 20 meters. The PSD curves overlap for particle sizes ranging from 0.85 mm to 4.75 mm and deviate for particle sizes ranging from 0.150 mm to 0.42 mm.

Figure 4.70 shows the original OGF PSD and the PSD curve obtained for the crushed sand from the shear band of the ring shear test performed on a loose sample (D_R=36%) with a normal stress of 200 kPa and shear displacement of 20 m. The original and crushed PSD curves overlap for particle sizes ranging from 0.85 mm to 4.75 mm and deviate for particle sizes ranging from less than 0.075 mm to 0.42 mm.

Figure 4.71 to Figure 4.74 show the original GSD for OGF sand and the GSD curves obtained for the sand collected from the shear band formed in the ring shear tests performed on dense samples (D_R ranging from 80.8% to 86.1%) with normal stresses of 300 kPa and 400 kPa and shear displacement ranging from 1 to 4m. The GSD curves overlap for particle sizes ranging from 0.85 mm to 4.75 mm and deviate for particle sizes ranging from less than 0.075 mm to 0.42 mm.

Figure 4.75 and Figure 4.76 show that the original OGF GSD curve and the GSD curves obtained for the sand from the shear band formed in the ring shear tests performed with a normal stress of 400 kPa and shear displacements of 6 m and 7 m overlap for particle sizes ranging from 2 mm to 4.75 mm and deviate for particle sizes ranging from less than 0.075 mm to 0.841 mm, indicating a higher degree of particle crushing than observed in the previous results.

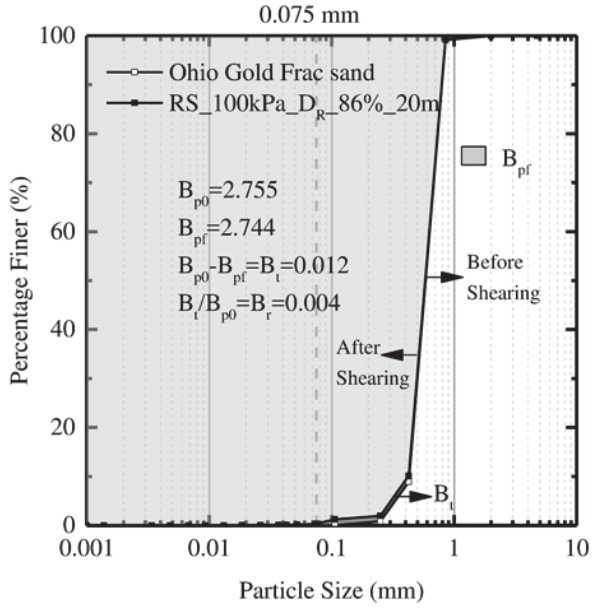

Figure 4.69 Total breakage (B_t) for the test performed on a dense sample (D_R=86%) of Ohio Gold Frac sand with a normal stress of 100 kPa and shear displacement of 20 m.

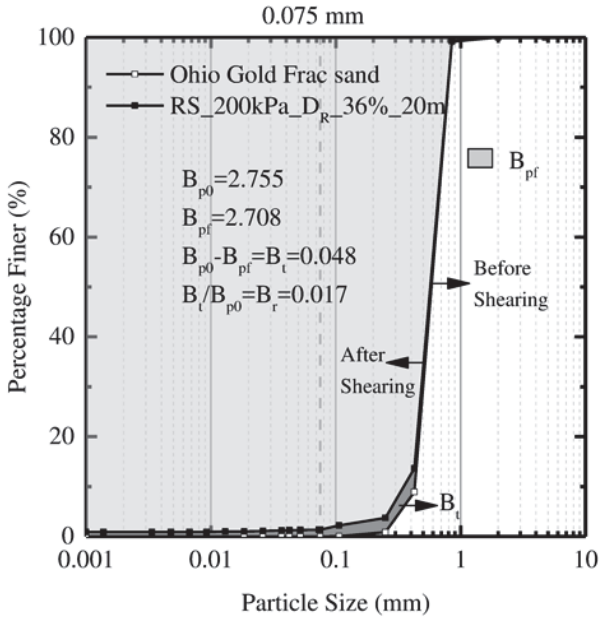

Figure 4.70 Total breakage (B_t) for the test performed on a loose sample (D_R=36%) of Ohio Gold Frac sand with a normal stress of 200 kPa and shear displacement of 20 m.

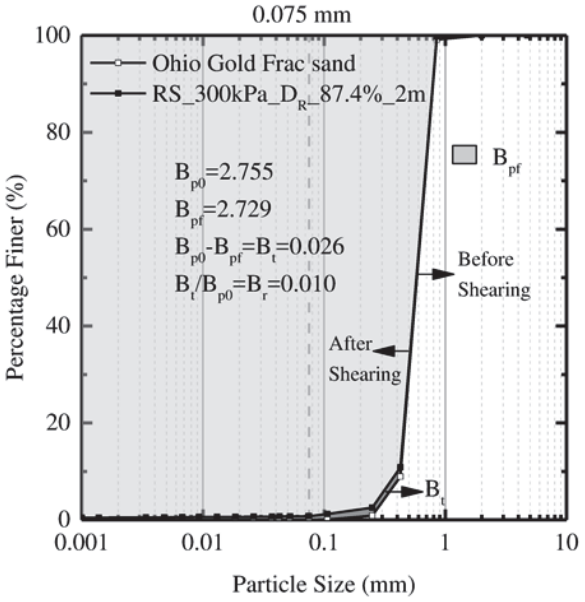

Figure 4.71 Total breakage (B_t) for the test performed on a dense sample (D_R=87.4%) of Ohio Gold Frac sand with a normal stress of 300 kPa and shear displacement of 2 m.

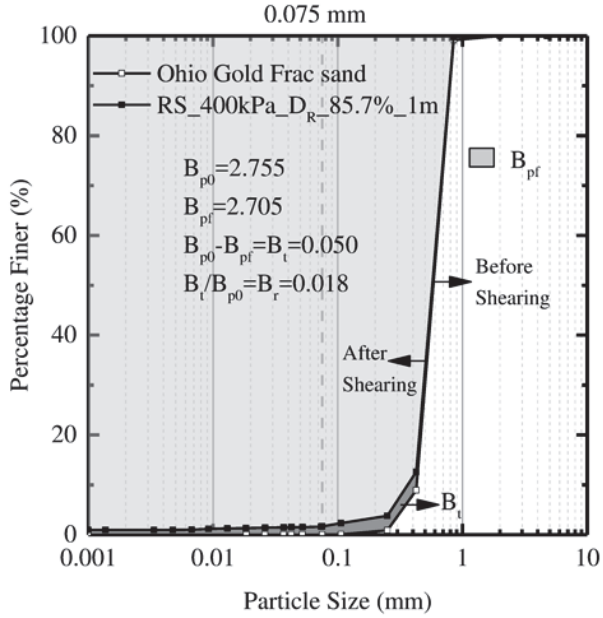

Figure 4.72 Total breakage (B_t) for the test performed on a dense sample (D_R=85.7%) of Ohio Gold Frac sand with a normal stress of 400 kPa and shear displacement of 1m.

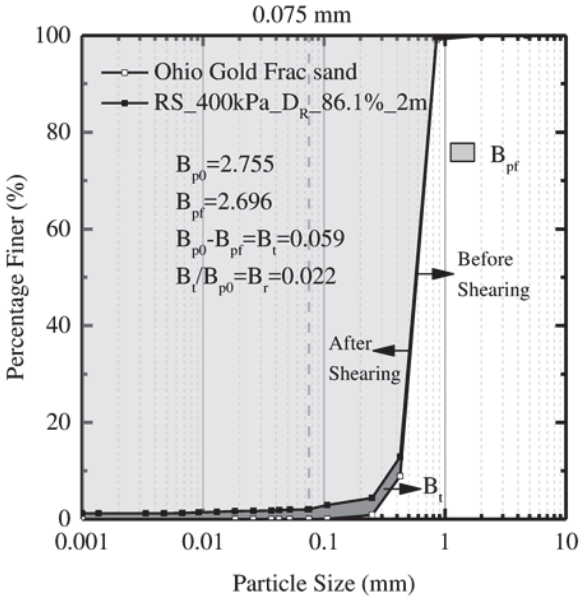

Figure 4.73 Total breakage (B_t) for the test performed on a dense sample (D_R=86.1%) of Ohio Gold Frac sand with a normal stress of 400 kPa and shear displacement of 2m.

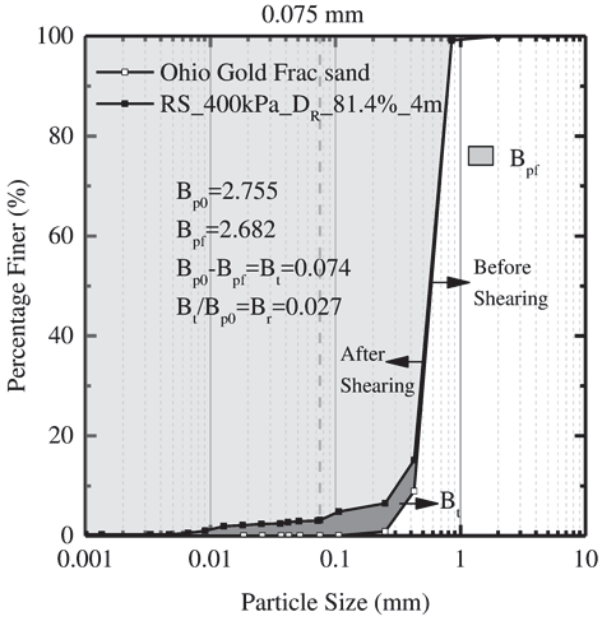

Figure 4.74 Total breakage (B_t) for the test performed on a dense sample (D_R=81.4%) of Ohio Gold Frac sand with a normal stress of 400 kPa and shear displacement of 4 m.

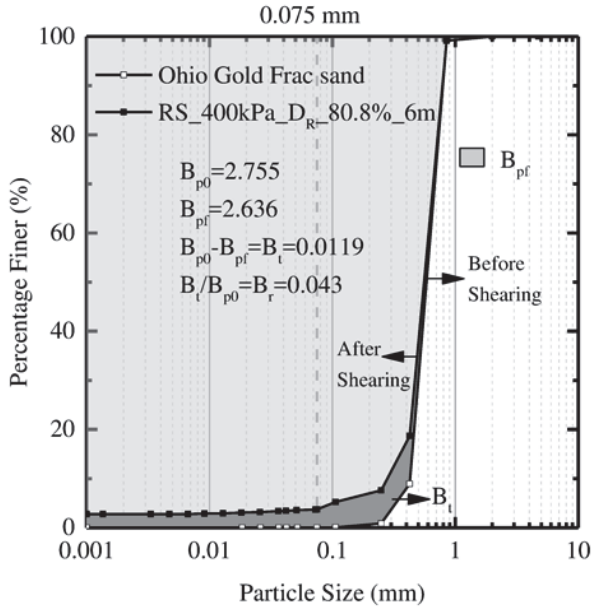

Figure 4.75 Total breakage (B_t) for the test performed on a dense sample (D_R=80.8%) of Ohio Gold Frac sand with a normal stress of 400 kPa and shear displacement of 6 m.

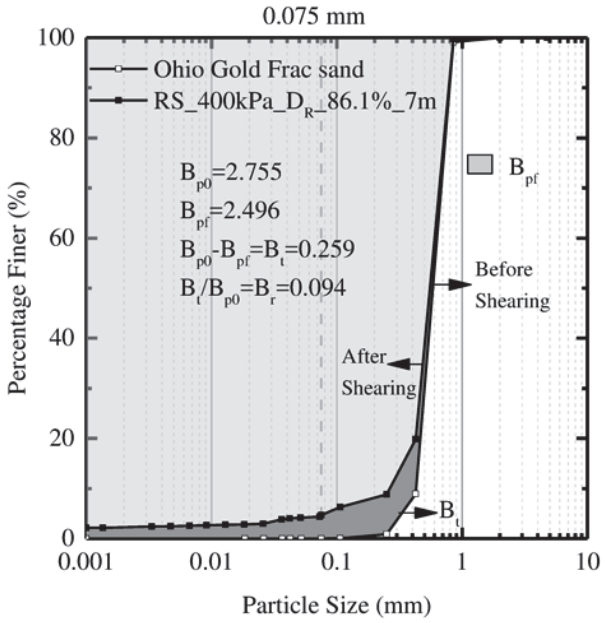

Figure 4.76 Total breakage (B_t) for the test performed on a dense sample (D_R=86.1%) of Ohio Gold Frac sand with a normal stress of 400 kPa and shear displacement of 7 m.

Figure 4.77 shows the evolution of the relative breakage parameter for the OGF sand collected from the shear bands formed in the ring shear tests performed with a normal stress of 400 kPa and shear displacements of 1, 2, 4, 6 and 7 meters. No stabilization of the breakage parameter is observed in this shearing range.

The rate of crushing for the ring shear tests performed with a normal stress of 400 kPa and shear displacements equal to 1, 2, 4, 6 and 7 m was evaluated to better understand how fast Ohio Gold Frac sand particles breaks when shearing increases. The rates of crushing for the different shear displacements are equal to: 0.0013 for the shear displacements from 1 m and 2m; 0.005 for shear displacements from 2 to 4 m; 0.004 for the shear displacements from 4 to 6 m, and finally 0.054 for the shear displacements from 6 to 7 m.

Table 4.23 and Table 4.24 show the rate of crushing after ring shear tests performed with normal stress equal to 400 kPa and shear displacements of 1, 2, 4, 6, and 7 m. Table 4.23 considers the particle diameter greater than 0.001 mm (D> 0.001mm), whereas Table 4.24 shows the values obtained for the particle diameter greater than 0.075 mm (D> 0.075 mm). It can be observed from Table 4.23 and Table 4.24 that the rate of crushing R_c has a similar value for 1, 2, 4, 6 and 7 m of shear displacement.

Table 4.23 Rate of crushing of Ohio Gold Frac for ring shear test performed with normal stress of 400 kPa (D> 0.001 mm).

Breakage Parameters			Shear Displacement (m)			
Initial	Final	ΔB_r (Final-Initial)	u_1	u_2	Δ_u (u_2-u_1)	R_c=ΔB_r / Δ_u
0.018	0.022	0.004	1	2	1	0.004
0.022	0.027	0.005	2	4	2	0.003
0.027	0.043	0.016	4	6	2	0.008
0.043	0.047	0.004	6	7	1	0.004

Table 4.24 Rate of crushing of Ohio Gold Frac for ring shear test performed with normal stress of 400 kPa (D> 0.075mm).

Breakage Parameters			Shear Displacement (m)			
Initial	Final	ΔB_r (Final-Initial)	u_1	u_2	Δ_u (u_2-u_1)	R_c=ΔB_r / Δ_u
0.012	0.015	0.003	1	2	1	0.003
0.015	0.025	0.01	2	4	2	0.005
0.025	0.031	0.006	4	6	2	0.003
0.031	0.035	0.02	6	7	1	0.04

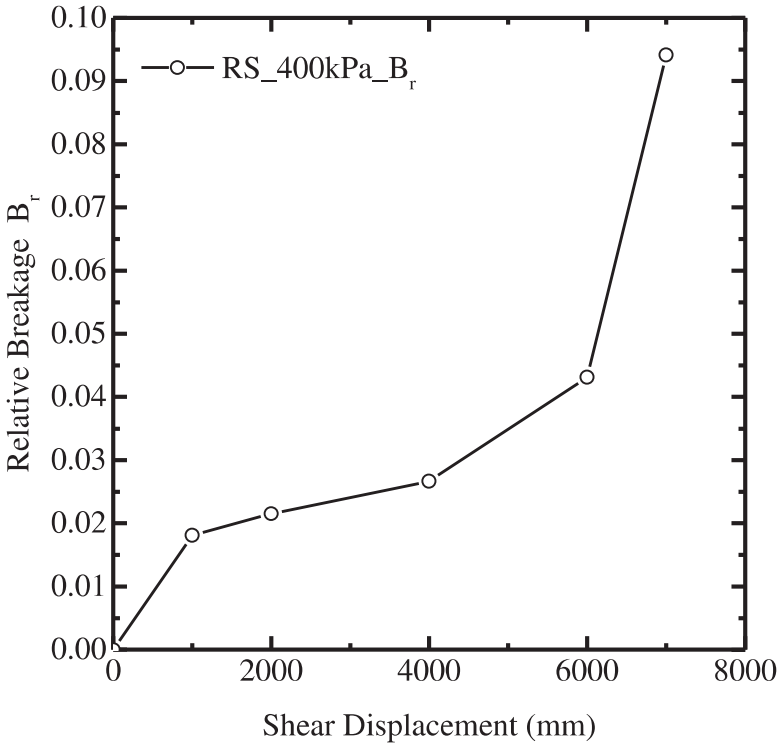

Figure 4.77 Relative breakage parameter evolution for the ring shear tests performed on Ohio Gold Frac sand with a normal stress of 400 kPa and with shear displacements of 1, 2, 4, 6, and 7 m.

4.10.4 Particle size evolution in ring shear tests

Ohio Gold Frac sand is classified as a "poorly-graded sand" according to ASTM 2487. As shearing progresses in a ring shear test, the particle-size distribution evolves.

Therefore, poorly-graded sands may be re-classified as well-graded sands after large shear displacements. Table 4.25 summarizes the OGF sand particle diameters and gradation coefficients before and after ring shear testing (note that the gradation considered after testing is that for the sand present in the shear band).

Table 4.25 Gradation parameters for Ohio Gold Frac sand before and after ring shear testing.

Test Code	D_{10}	D_{30}	D_{50}	D_{60}	C_u	C_c
Original Sand	0.43	0.5	0.58	0.62	1.44	0.94
RS_100kPa_D_R_86%_20m	0.41	0.49	0.58	0.62	1.51	0.94
RS_200kPa_D_R_36%_20m	0.35	0.49	0.58	0.62	1.77	1.11
RS_300kPa_D_R_87.4%_2m	0.38	0.49	0.58	0.62	1.63	1.02
RS_400kPa_D_R_85.7%_1m	0.37	0.49	0.58	0.62	1.68	1.05
RS_400kPa_D_R_86.1%_2m	0.37	0.49	0.58	0.62	1.68	1.05
RS_400kPa_D_R_81.4%_4m	0.3	0.48	0.57	0.61	2.03	1.26
RS_400kPa_D_R_80.8%_6m	0.28	0.46	0.55	0.6	2.14	1.26
RS_400kPa_D_R_86.1%_7m	0.26	0.46	0.55	0.6	2.31	1.36

Figure 4.78 shows the particle diameter evolution in the shear zone for the ring shear tests performed with a normal stress of 400 kPa. The particle diameters become progressively smaller with increasing shear displacement. The effective particle size D_{10} decreases from 0.43 to 0.26 with increasing shearing. In addition, for particle sizes larger than 0.45 mm, there is only a slight decrease in size (almost negligible) with increasing shearing. These results provide evidence to the fact that the dominant particle damage mechanisms observed in these tests are particle breakage (prevailing for particle size smaller than 0.150 mm) and abrasion and shearing off of the asperities of particles (prevailing for particle size ranging from 0.25 to 0.84 mm).

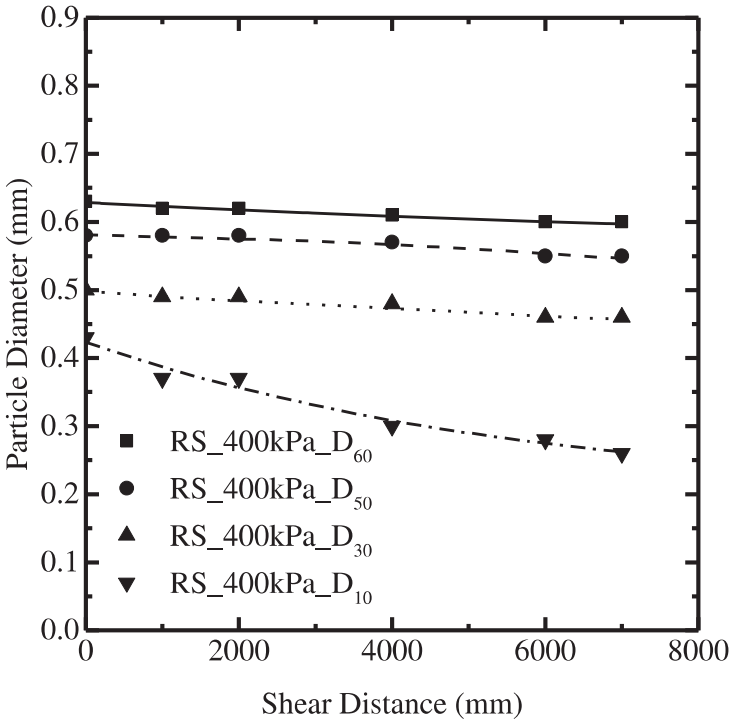

Figure 4.78 Particle diameter evolution in the shear band for ring shear tests performed on Ohio Gold Frac sand with a normal stress of 400 kPa and shear displacements of 1, 2, 4, 6 and 7 m.

The coefficient of uniformity C_u indicates whether a soil is well or poorly graded. Figure 4.79 shows the evolution of the coefficient of uniformity with increasing shear displacement (it increases from 1.42 to approximately 2.3). However, according to ASTM 2487, a sand is classified as a well-graded sand when the coefficient of uniformity exceeds a value of 6. The coefficient of uniformity is equal to 2.3 for the sand from the shear band formed in the sample subjected to a normal stress of 400 kPa and sheared to a shear displacement of 7 m; therefore, it does not satisfy the criteria for it to be classified as a well-graded sand.

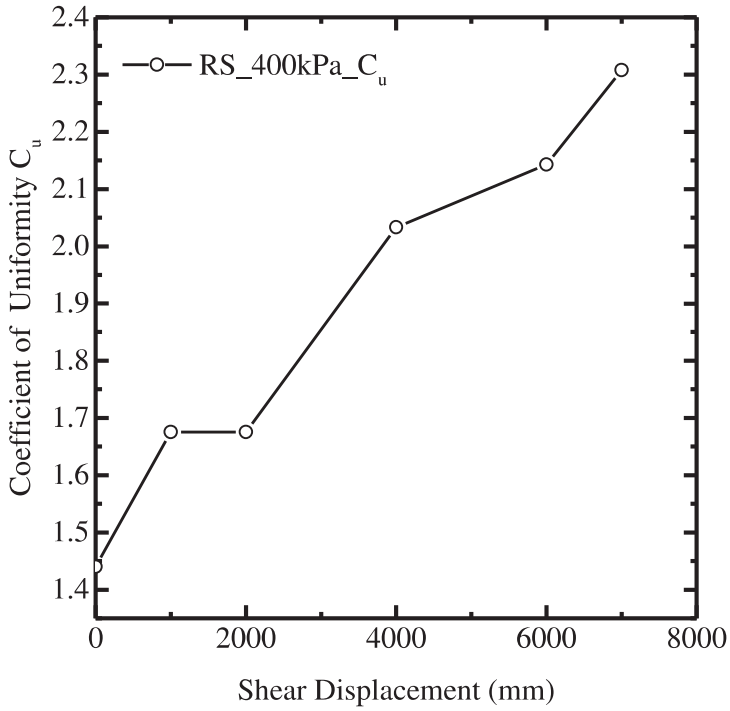

Figure 4.79 Coefficient of uniformity evolution in the shear band for the ring shear tests performed on Ohio Gold Frac sand with a normal stress of 400 kPa and with shear displacements of 1, 2, 4, 6, and 7m.

Another parameter that is used for soil classification is the coefficient of curvature (C_c). A sand is considered a well-graded sand if the coefficient of curvature is in the 1-to-3 range and the coefficient of uniformity C_u is greater than 6. According to Figure 4.80, the coefficient of curvature increases with shear displacement, reaching a value equal to 1.36 at a shear displacement of 7m. However, the coefficient of uniformity criterion was never satisfied for the sand crushed in the ring shear. Therefore, all the sand samples from the shear band formed in the ring shear tests are still classified as poorly-graded sands (SP).

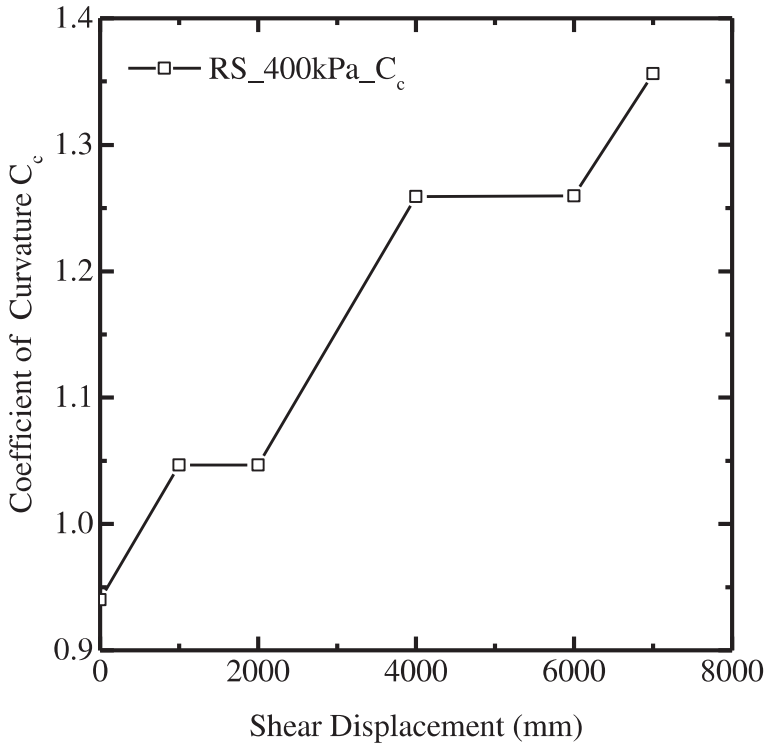

Figure 4.80 Coefficient of curvature evolution for the ring shear tests performed on Ohio Gold Frac sand with a normal stress of 400 kPa and shear displacements of 1, 2, 4, 6, and 7 meters.

4.10.5 Minimum and maximum void ratios of the crushed sand in the shear band formed in the ring shear tests.

The addition of non-plastic silt to clean sands (for silt contents from 2 to 20% by weight) decreases the minimum and maximum void ratios of mixtures of sand and non-plastic fines (Salgado et al. 2000). As described in section 4.4, the original Ohio Gold Frac sand has 0.02% of fines content. However, the sand samples from the shear band formed in the ring shear tests have silt contents of up to 5%. Therefore, minimum and maximum void ratios were determined for OGF sand with the same gradations as those of the sand from the shear bands formed during shearing to shear displacements of up to 7m in the ring shear (these tests were performed with a normal stress of 400 kPa). To reconstitute the

gradation of the sand from the shear bands, OGF sand was crushed manually with a tamper (this was done because the amount of sand collected from each shear band was less than 200g). Knowing the percentage of sand retained in each sieve for the sand samples collected from the shear band after each ring shear test, the required amounts of sand for each particle size range was calculated such that a sand mixture with approximately 2,000 grams would be produced (the GSD curve of each sand mixture reconstituted in this manner was determined three times to make sure that the actual gradation of the sand from the shear band matched the one of the reconstituted sand mixture).

ASTM D4253 was used to determine the maximum void ratio (e_{max}) of the reconstituted sand mixtures. The Yamamuro and Lade (1997) procedure was used to determine the minimum void ratio (e_{min}) of the reconstituted sand mixtures in order to prevent segregation of fines in the mixtures during testing. According to the Yamamuro and Lade (1997) procedure, about 50 g of sand is placed into a graduated glass cylinder and tapped twice in each of the four sides; this was repeated until the glass cylinder contained about 800 g of the reconstituted sand mixtures. Table 4.26 shows the results obtained for the minimum void ratio and maximum ratio for the reconstituted sand mixtures matching the gradation of the sand from the shear bands formed in the ring shear tests performed with a normal stress of 400 kPa and shear displacements equal to 1, 2, 4, 6 and 7 meters.

Table 4.26 Minimum and maximum void ratios of the sand from the shear band after ring shear tests (these ratios were determined using reconstituted sand mixtures).

Test Code	e_{min}	e_{max}
Original Sand	0.59	0.81
RS_400kPa_D_R_85.7%_1m	0.54	0.78
RS_400kPa_D_R_86.1%_2m	0.52	0.77
RS_400kPa_D_R_81.4%_4m	0.50	0.74
RS_400kPa_D_R_80.8%_6m	0.49	0.71
RS_400kPa_D_R_86.1%_7m	0.49	0.70

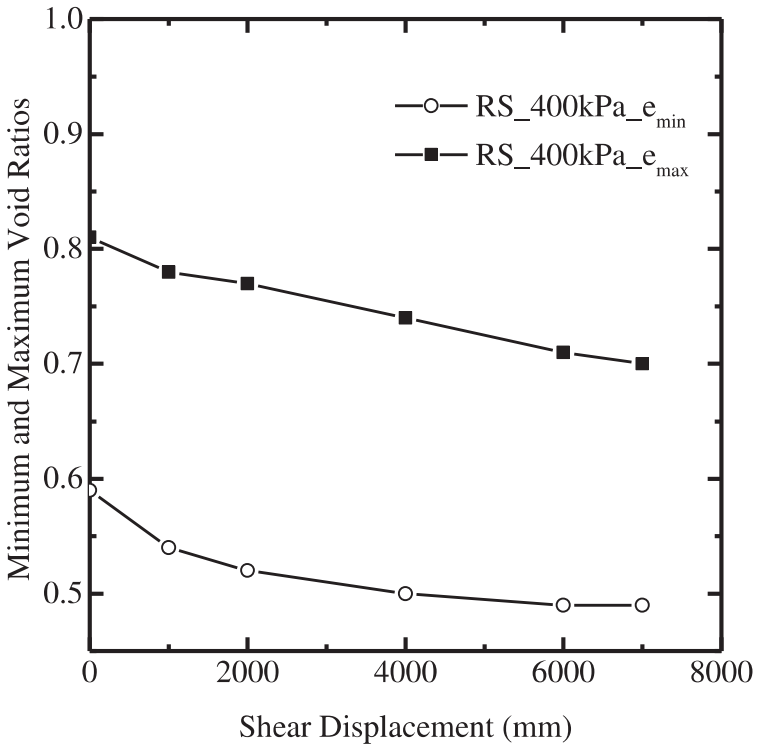

Figure 4.81 Minimum and maximum void ratio evolution for the Ohio Gold Frac sand in the shear band formed in ring shear tests performed with a normal stress of 400 kPa and shear displacements of 1, 2, 4, 6, and 7 meters.

Figure 4.81 shows the evolution of the minimum and maximum void ratios with increasing shearing (and increasing particle crushing) for the sand from the shear bands. Determination of the minimum and maximum ratios is important because the content and type of fines present in sand not only affects its strength and stiffness, but also its static liquefaction potential (Lade, Liggio, and Yamamuro 1998).

4.10.6 Particle morphology evolution after the ring shear tests performed on Ohio Gold Frac sand.

The evolution of particle morphology with crushing was studied using the AmScope light microscope, a digital camera and the image-processing tool ImageJ. Table 4.27 summarizes the morphology parameters for the original OGF sand and for the sand collected from the shear band after ring shear testing.

Table 4.27 Morphology parameters of the original and crushed Ohio Gold Frac sand.

Test Code	Circularity	AR	Roundness	Sphericity
Original Sand	0.62	1.42	0.73	0.76
RS_100kPa_D_R_86%_20m	0.65	1.41	0.73	0.72
RS_200kPa_D_R_36%_20m	0.68	1.32	0.77	0.72
RS_300kPa_D_R_87.4%_2m	0.59	1.36	0.75	0.86
RS_400kPa_D_R_85.7%_1m	0.61	1.38	0.75	0.86
RS_400kPa_D_R_86.1%_2m	0.58	1.33	0.77	0.87
RS_400kPa_D_R_81.4%_4m	0.59	1.29	0.79	0.88
RS_400kPa_D_R_80.8%_6m	0.65	1.39	0.74	0.86
RS_400kPa_D_R_86.1%_7m	0.61	1.36	0.75	0.86

In section 3.3, the processes followed to analyze the particle images and to determine the morphology parameters were described in detail. All the digital images and

processed images of the particles analyzed before and after the ring shear tests are provided in Appendix C. In Figure 4.82 to Figure 4.97, the values of the morphology parameters are provided for the particles retained in each of the sieves. Sieves #20, #40, #60, #100, and #200, which have mesh openings equal to 0.841 mm, 0.420 mm, 0.250 mm, 0.149 mm and 0.074mm, respectively. Global morphology parameters, which were calculated as the average of the individual values obtained for each particle size ranging from 0.074 to 0.841 mm, are compared in Figure 4.82 to Figure 4.97 (the global morphology parameters for both the original OGF sand (OGFS) crushed sand are shown in these figures).

As shown in Figure 4.82 and Figure 4.84, the newly formed particles from sieve #200 (produced during ring shear tests performed with normal stresses of 100 kPa and 200 kPa and shear displacements of 20 m) are less spherical (0.49) than the particles from the sieves #20, #40, #60 and #100. This is because these new, small particles are the product of the shearing-off of the asperities of the large particles with large shear displacements.

The shearing off of the asperities and the abrasion of the large particles occur as particles rotate and translate during shearing. The sand particles from the shear band became more rounded and spherical as the shear displacement increased (as compared with the original, uncrushed sand), particularly for the sand collected from the shear band formed in the ring shear tests performed with a normal stress of 400 kPa and shear displacements of 7 m. For instance, for this case, the global sphericity parameter of the original sand changes from 0.76 to 0.86 for the crushed sand, and the corresponding roundness global parameter changes from 0.73 to 0.75.

It can be observed in Figure 4.88, Figure 4.90, Figure 4.92, Figure 4.94 and Figure 4.96 that all the particles from sieves #20, #40, #60, #100 and #200, have similar values of

sphericity parameter, which is about 0.86 to 0.88. Also, it is shown in Figure 4.89, Figure 4.91, Figure 4.93, Figure 4.95 and Figure 4.97 that the global aspect ratio parameter decreased (as expected, since the sphericity and roundness parameters increased), changing from 1.42 (OGF sand) to 1.29 (crushed material). It can be concluded that the evolution of the sand particle sizes depends on the normal stress and shear displacement used in these tests. Additionally, during these tests (ring shear tests performed with normal stress equal to 400 kPa and shear displacement up to 7m) it can be observed that the global circularity slightly decreased from 0.62 (original sand) to 0.59 (newly formed particles) in most of the cases. Which indicates that the particles are less circular after shearing than the uncrushed material (OGFS).

Figure 4.98 shows the evolution of the global sand particle morphology parameters with shear displacement (for shear displacements of 1, 2, 4, 6, 7 m) for the ring shear tests performed with a normal stress of 400 kPa. The increase in particle roundness and particle sphericity as shear displacement increases indicates that the angular edges of the particles become more rounded as a result of the abrasion of the particles.

According to Sadrekarimi and Olson (2010), since the critical-state friction angle depends on particle size distribution and particle shape, it evolves during ring shear testing because these two parameters also evolve during shearing. The particle gradation and morphology of the sand from the shear band formed in the ring shear tests performed on OGF sand also evolved. Particles in the shear band became more rounded with shearing because of the abrasion of the edges of the particles and shearing-off of the asperities and irregularities due to particle rotation and translation, and, in addition, the gradation of the sand in the shear band became broader. These are two factors that affected the values of

the critical-state friction angle of the test sand. It is known that the more rounded the particles are, the smaller the critical-state friction angle is. On the other hand, the more well-graded the sand is, the greater the critical-state friction angle is3. These two factors seemed to have compensated each other, and, as a result, the mobilized friction angle only increased slightly (by less than 1 degree) with increasing shearing in the ring shear tests performed in OGF sand.

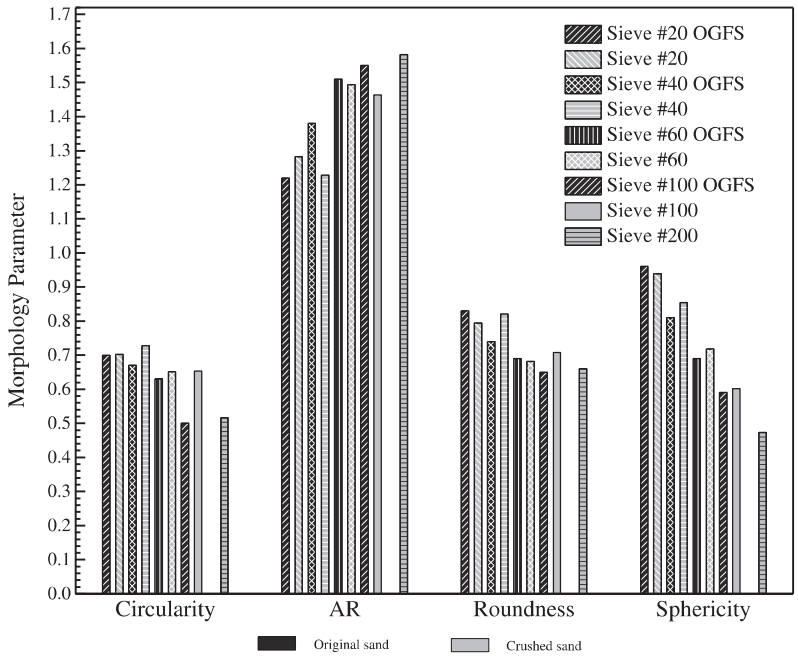

Figure 4.82 Sand particle morphology parameters before and after performing a ring shear test on a dense sample (D_R=86%) with a normal stress of 100 kPa and shear displacement of 20 m.

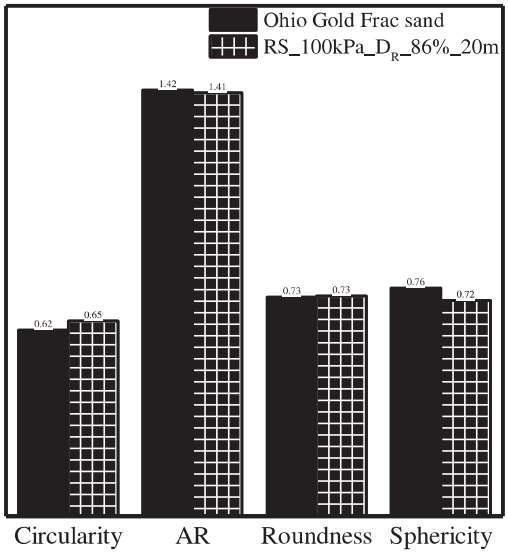

Figure 4.83 Comparison between the global particle morphology parameters obtained before and after performing a ring shear test on a dense sand sample (D_R=86%) with a normal stress of 100 kPa and shear displacement of 20 m.

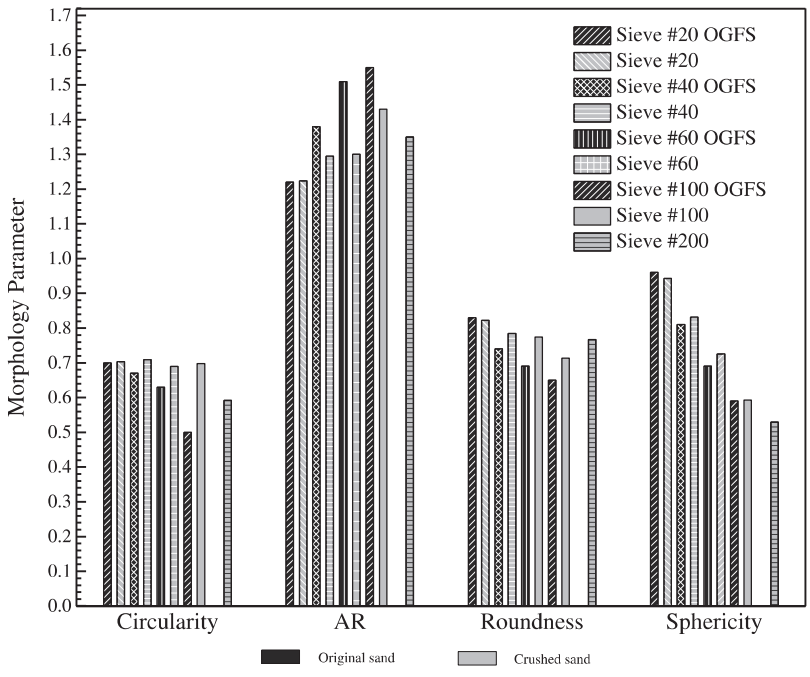

Figure 4.84 Sand particle morphology parameters before and after performing a ring shear test on a loose sample (D_R=36%) with a normal stress of 200 kPa and shear displacement of 20 m.

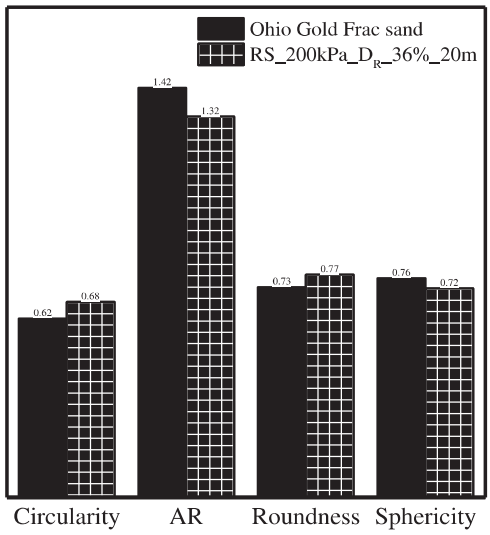

Figure 4.85 Comparison between the global particle morphology parameters obtained before and after performing a ring shear test on a loose sand sample (D_R=36%) with a normal stress of 200 kPa and shear displacement of 20 m.

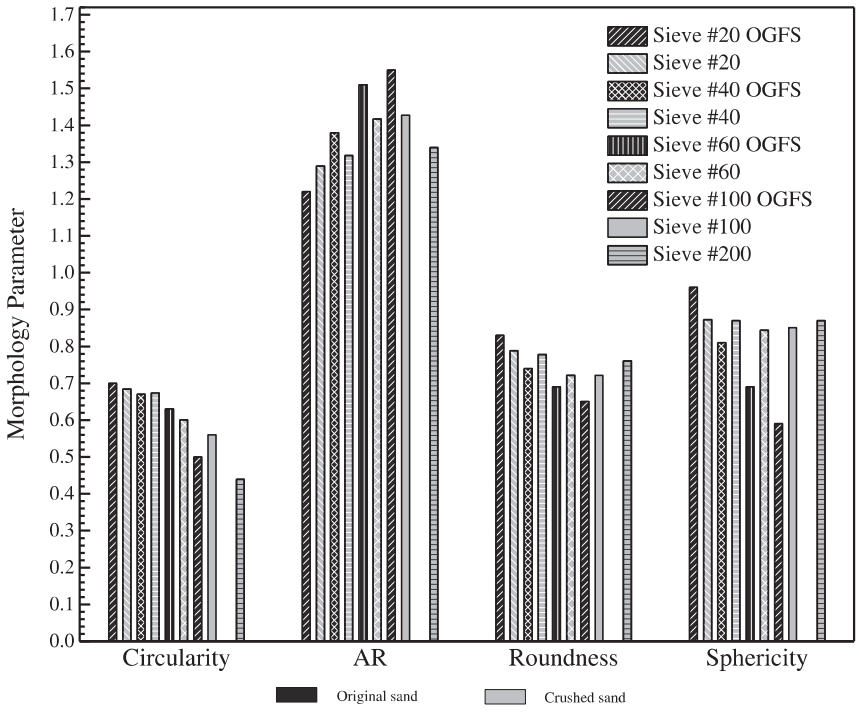

Figure 4.86 Sand particle morphology parameters before and after performing a ring shear test on a dense sample (D_R=87.4%) with a normal stress of 300 kPa and shear displacement of 2 m.

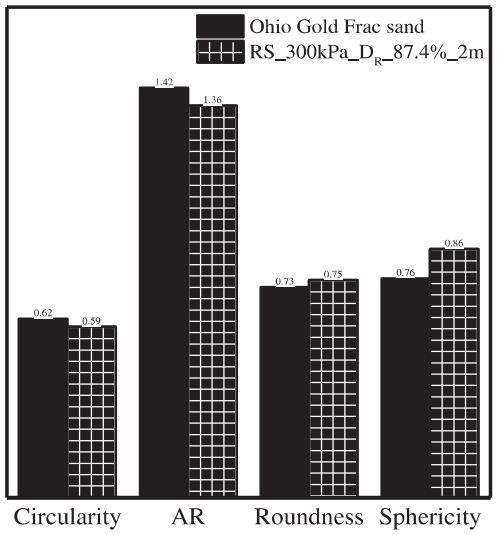

Figure 4.87 Comparison between the global particle morphology parameters obtained before and after performing a ring shear test on a dense sand sample (D_R=87.4%) with a normal stress of 300 kPa and shear displacement of 2 m.

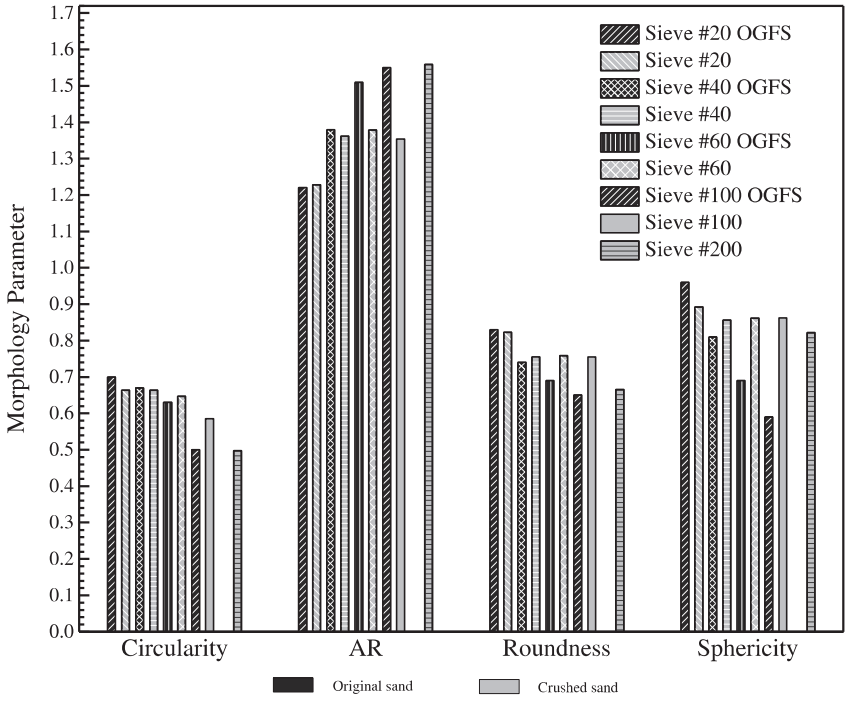

Figure 4.88 Sand particle morphology parameters before and after performing a ring shear test on a dense sample (D_R=85.7%) with a normal stress of 400 kPa and shear displacement of 1 m.

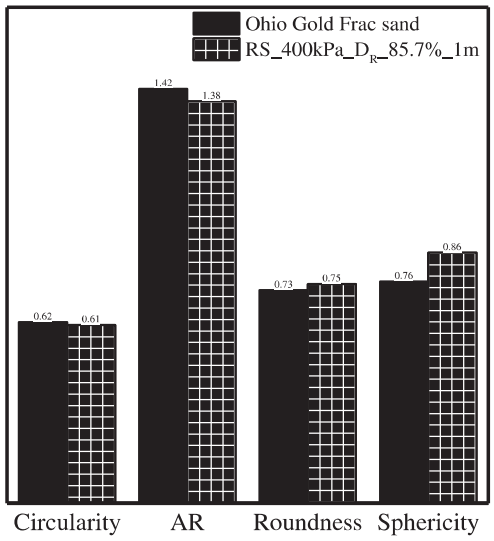

Figure 4.89 Comparison between the global particle morphology parameters obtained before and after performing a ring shear test on a dense sand sample (D_R=85.7%) with a normal stress of 400 kPa and shear displacement of 1 m.

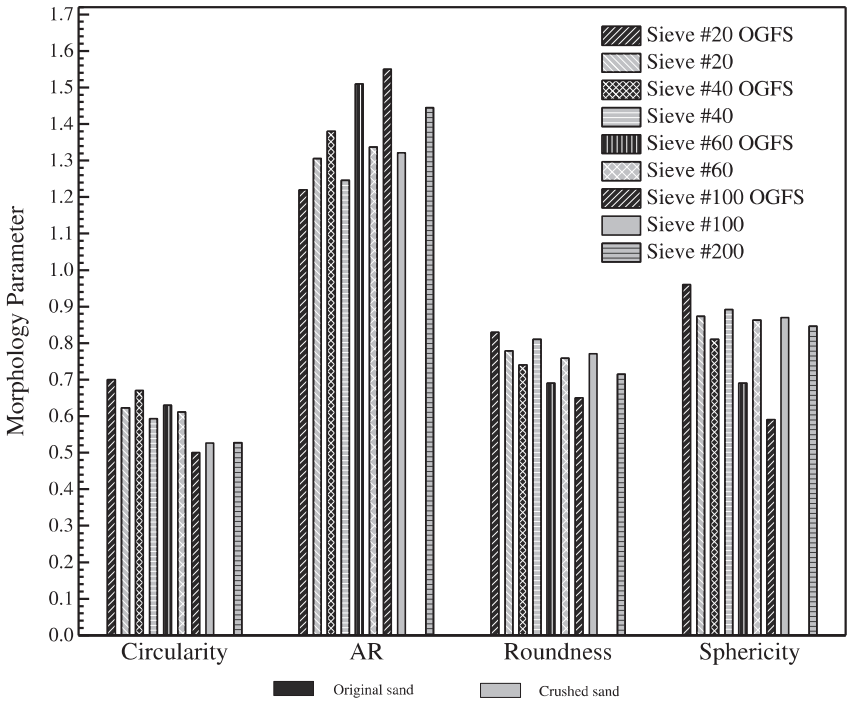

Figure 4.90 Sand particle morphology parameters before and after performing a ring shear test of a dense sample (D_R=86.1%) with a normal stress of 400 kPa and shear displacement of 2 m.

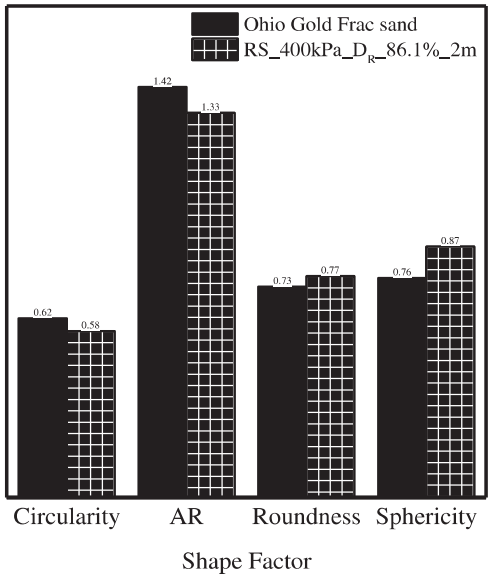

Figure 4.91 Comparison between the global particle morphology parameters obtained before and after performing a ring shear test on a dense sand sample (D_R=86.1%) with a normal stress of 400 kPa and shear displacement of 2 m.

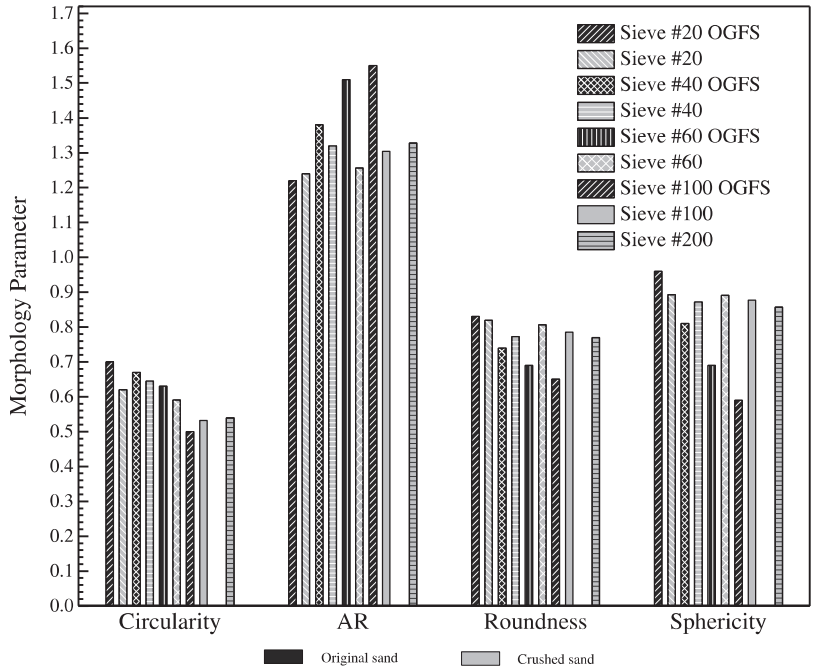

Figure 4.92 Sand particle morphology parameters before and after performing a ring shear test of a dense sample (D_R=81.4%) with a normal stress of 400 kPa and shear displacement of 4 m.

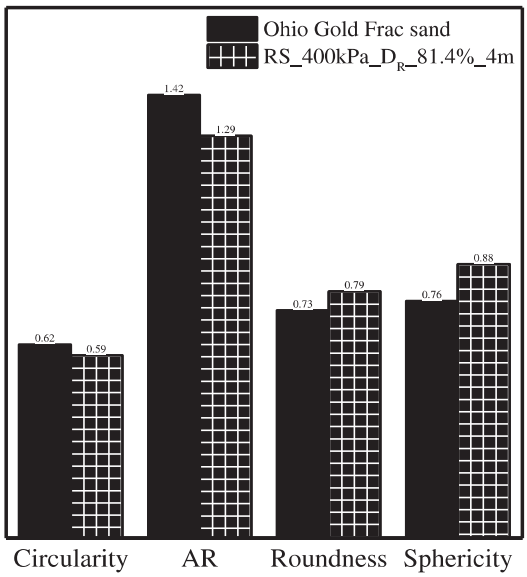

Figure 4.93 Comparison between the global particle morphology parameters obtained before and after performing a ring shear test on a dense sand sample (D_R=81.4%) with a normal stress of 400 kPa and shear displacement of 4 m.

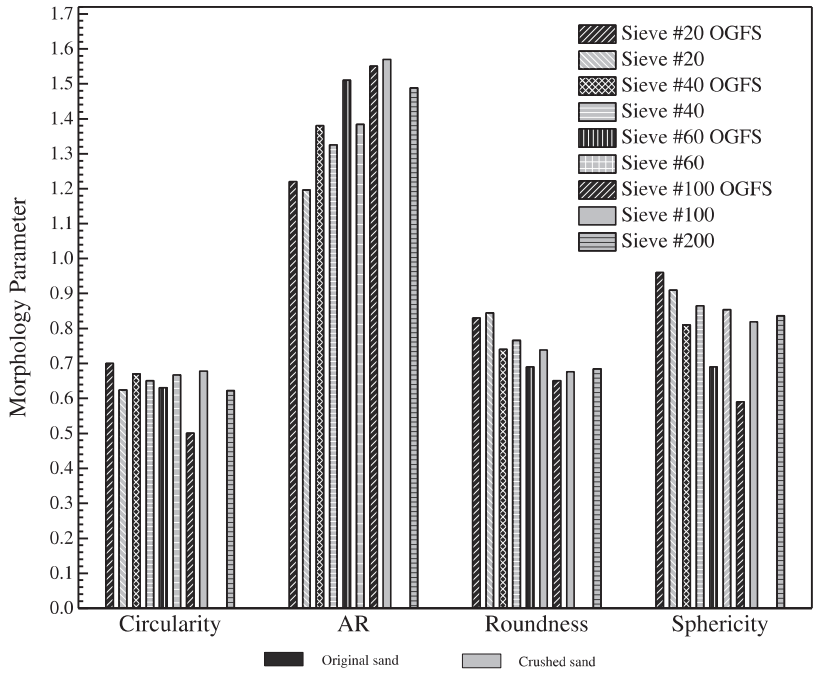

Figure 4.94 Sand particle morphology parameters before and after performing a ring shear test of a dense sample (D_R=80.8%) with a normal stress of 400 kPa and shear displacement of 6 m.

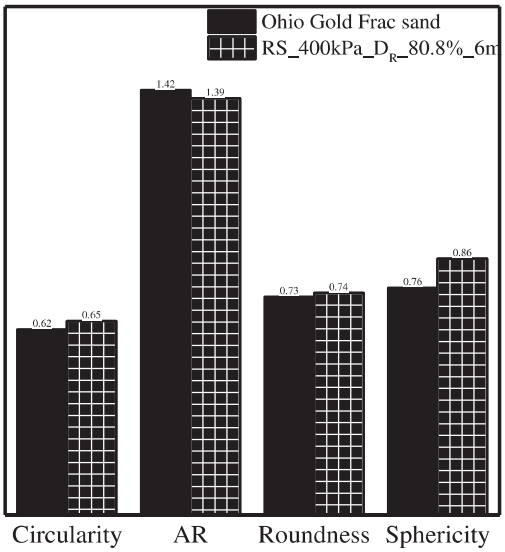

Figure 4.95 Comparison between the global particle morphology parameters obtained before and after performing a ring shear test on a dense sand sample (D_R=80.8%) with a normal stress of 400 kPa and shear displacement of 6 m.

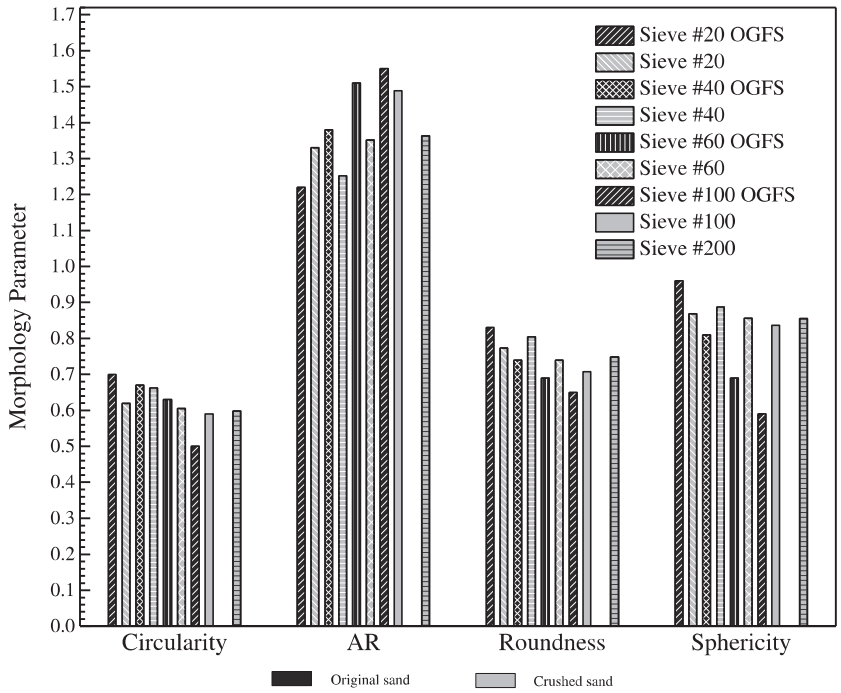

Figure 4.96 Sand particle morphology parameters before and after performing a ring shear test of a dense sample (D_R=86.1%) with a normal stress of 400 kPa and shear displacement of 7 m.

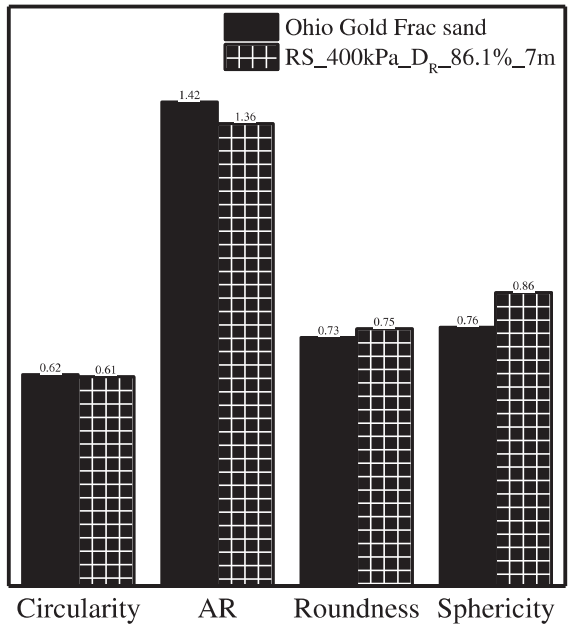

Figure 4.97 Comparison between the global particle morphology parameters obtained before and after performing a ring shear test on a dense sand sample (D_R=85%) with a normal stress of 400 kPa and shear displacement of 7 m.

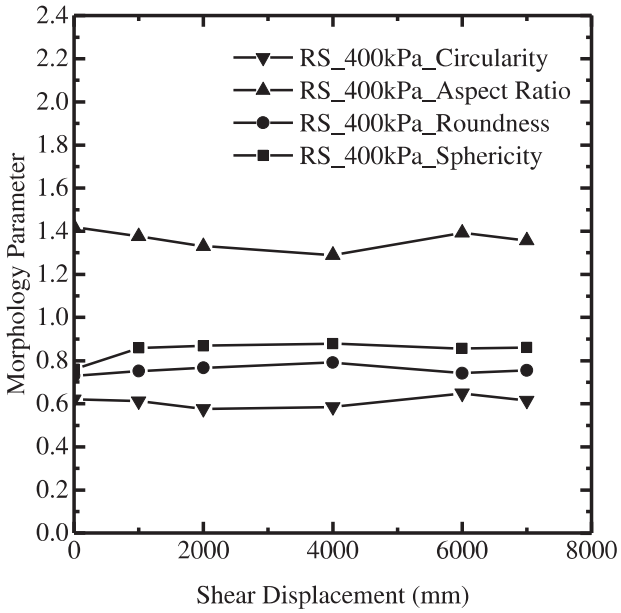

Figure 4.98 Global sand particle morphology parameters versus shear displacement curves for the ring sheart tests performed with a normal stress equal to 400 kPa and shear displacement equal to 1, 2, 4, 6 and 7 m.

CHAPTER 5. CONCLUSIONS

From the results of the present study, the following conclusions are drawn:

5.1 Index properties of Ohio Gold Frac sand

The index properties of Ohio Gold Frac sand were researched as a first base for the consecutive studies of particle crushing. The specific gravity obtained after performing two tests was found to be equal to 2.65. This value is consistent with the average specific gravity of sands.

The ASTM D4254-16 was used to determine the minimum density of Ohio Gold Frac sand. The minimum and maximum density parameters are useful to determine the maximum void ratio e_{max} and minimum void ratio e_{min} of soils. The maximum void ratio e_{max} obtained for Ohio Gold Frac sand was found to be equal to 0.81 and the minimum void ratio e_{min} determined for Ohio Gold Frac sand was found to be equal to 0.59.

The soil composition after the sieve analysis of Ohio Gold Frac sand consisted of: medium sand (91.09%), fine sand (8.89%) and fines content (0.02%). The gradation parameters obtained for Ohio Gold Frac sand are: D_{10}=0.43, D_{30}=0.5, D_{50}=0.58, and, D_{60}=0.62, C_u=1.44 and C_c=0.94. According to ASTM D2487-16, Ohio Gold Frac sand is classified as a poorly graded sand “SP”. The particle-size distribution of the uncrushed

material was used to quantify the particle damage after one-dimensional compression and ring shear tests through the breakage parameters.

5.2 Mineralogy and morphology properties of Ohio Gold Frac sand

The X-ray diffraction test was performed on Ohio Gold Frac sand to determine the particle mineralogy. The test pattern obtained for Ohio Gold Frac (OGF) sand was compared with known X-ray diffraction patterns published by the American Society for Testing and Materials (ASTM), indicating that almost 99% of the minerals present in OGF sand are quartz.

The morphology analyses were performed on the uncrushed Ohio Gold Frac sand through the use of a light microscope, couple-charged camera and the image-processing tool ImageJ. It was found that the larger particles sieve #20 (0.841 mm) have a sphericity value equal to 0.96, and the smaller particles sieve #100 (0.150 mm) have a sphericity value of 0.59. The morphology analyses showed that Ohio Gold Frac sand particles become more angular, less rounded and less circular as the particle size decreased.

5.3 Shear strength response

The shear strength response of Ohio Gold Frac sand before particle crushing was evaluated by direct shear and ring shear tests performed at low normal stresses.

The critical-state friction angle obtained from direct shear tests was found to be equal to 35° at 4 to 6 mm of horizontal displacement. To obtain the critical-state strength envelope for Ohio Gold Frac sand, three dense ($D_R \approx$ 85%) samples were tested under normal stresses equal to 25 kPa, 50 kPa and 100 kPa.

Three tests were performed on dense samples (relative density ranging from 80 to 81.8%) of Ohio Gold Frac sand under different normal stresses equal to 25 kPa, 50 kPa, and 100 kPa in the ring shear equipment to obtain the critical-state strength envelope. No significant particle crushing was observed during these tests. The critical-state friction angle obtained from the ring shear test was found to be equal to 31.3º where the first plateau was observed at 20 to 30 mm of shear displacement.

5.4 Particle crushing analyses during one-dimensional compression tests

During one-dimensional compression tests, the soil become to be more packed due to particle rearrangement and interparticle slip and consequent particle damage; therefore, the stiffness response of the soil is diminished. Also, the particle crushing is greater in uniformly graded soils than in well graded soils, and particle crushing increases as the confining stress increases in one-dimensional compression tests.

One-dimensional compression tests were performed on Ohio Gold Frac sand with a maximum load applied equal to 74kN, which in terms of stress is equal to 24 MPa. The one dimensional compression tests were carried out during 10 hours, 5 days and 10 days. It was observed that the stress at which the sand starts to crush (coincides with the maximum compression index) was found to be equal to 9 MPa for loose samples (D_R=35%) and 10 MPa for dense samples (D_R=85%).

Significant particle crushing was found on the loose sample (D_R=35%) compressed during 10 days up to maximum load equal to 74 kN. The relative breakage parameter B_r obtained was about 0.087. It was observed in the GSD curve of the tested material after 10 days of load application that the particle sizes between 0.85mm and 4.75 mm overlaps the

original GSD curve of OGF sand and deviates for particle sizes ranging from less than 0.075 mm to 0.42 mm.

It was found that the particle damage during one-dimensional compression tests can be classified according the shape and mineralogy. The compression behavior of Ohio Gold Frac sand was compared with the compression behavior (loose and dense samples) of Ottawa sand indicated by Mesri and Vardhanabhuti (2009).The first compression stage about 0 to 2 MPa corresponds to a slight particle motion where the roughness is mostly affected; the second compression stage between 2 and 10 MPa corresponds to the fracture or crushing of particles while in the third compression stage about 10 to 24 MPa the particle damage is diminished as a consequence of the reduction of the void ratio due to the previous particle fragmentation.

5.4.1 Morphology evolution after one-dimensional compression tests

The morphology analyses were carried out on the loose and dense samples after one-dimensional compressions tests to evaluate the morphology evolution of the particles due to compression loading. It can be concluded that the particles from sieves #20, #40, #60 and #100 become to be more spherical due to the abrasion and shearing-off of the asperities, but the particles retained on the sieve #200 (smaller particles) have low values of sphericity and roundness because they are product of the fracture of the angularities and shearing-off of asperities, indicating that the sand become to be more angular as the particle size decreases. These observations were determined for the four one-dimensional compression tests performed on Ohio Gold Frac sand.

5.5 Particle crushing analyses after ring shear tests

The two mechanisms that the soil experiments to overcome the volume change during loading is the particle damage and particle rearrangement. Particle damage was observed within the shear band after the ring shear tests performed on OGF sand without any significant damage in the soil below of the shear band.

A series of ring shear tests were performed in drained conditions on Ohio Gold Frac sand to analyze the shear-strain response during large shear displacement tests. One of the features observed during these tests was the formation of the shear band with a thickness equal to 6mm (10 times D_{50} of the original sand). The ring shear tests on Ohio Gold Frac sand were performed with normal stresses equal to 100 kPa, 200 kPa, 300 kPa and 400 kPa at different shear displacements ranging from 1 to 20 m. The results indicating that the particle damage increased with higher confining stresses and larger shear displacements. Therefore, the higher values of breakage parameters were obtained from the tests performed with confining stresses equal to 400 kPa.

The global behavior of Ohio Gold Frac sand tested during drained ring shear tests showed a contractive behavior for both loose and dense sand samples. For instance, in dense it was observed that initially the particle rearrangement dominated the soil response, afterwards, the dilation controlled the behavior until the particle damaged started reaching the critical-state.

It was observed that in most of the tests that the critical-state friction angle reached around 30º at few millimeters of shear displacements. The fluctuation of the mobilized friction angle was found to be about 30 to 33º. Additionally, some dilative samples showed

the peak friction angle around 35 º at 3 to 5 mm of shear displacement. Generally, the lower bound mobilized friction angle is about 31º.

5.5.1 Particle breakage quantification after large shear displacement tests

With the increment of the damage, the grain-size distribution curves (GSD) evolved. The evolution of the particle size with respect the shear displacement was evident for samples tests performed with confining stress equal to 400 kPa. The particle diameter with size higher than 0.45 mm did not evolve during shearing, but for the particles smaller than 0.45 mm the evolution was noticeable. From the GSD curves of the shear bands collected after the ring shear tests, it is evident that there is no change in the maximum particle diameter. It can be concluded that as the particle damage increases the coordination number increases, therefore at very large shear displacements the particle damage capacity reduces.

The abrasion and shearing-off of the asperities were the particle damage mechanisms that most affected the coarser particles of Ohio gold Frac sand during shearing tests. As the content of fines increased, the coordination number for larger particles increased as well; but, the coordination number was small for the smallest particles, therefore the particle damage mechanism response on the smallest particles was particle splitting.

The biggest relative breakage obtained from the eight ring shear tests performed was about 0.094, which was obtained from the GSD curve of the ring shear test carried out in a dense sand sample (D_R= 86.1%) with confining stress equal to 400 kPa and shear displacement equal to 7 m. For the ring shear test performed on a dense sand sample (D_R= 86%) during 20 m of shear displacement and confining stress equal to 100 kPa the relative

breakage obtained was 0.004. It can be concluded from these tests that the particle damage mostly depended on confining stresses.

Additionally, it was found that more particle crushing occurred during shear loading than during one-dimensional compression loading. It was observed that during one-dimensional compression tests, that the loose sand sample underwent more particle damage at 24 MPa during 10 days, while for shearing, significant crushing was observed in sand sample with confining stress equal to 400 kPa sheared at a displacement equal to 7 m.

5.5.2 Minimum and maximum void ratio after ring shear tests

The sand samples from the shear band formed in the ring shear tests have silt contents of up to 5%. Therefore, minimum and maximum void ratios were determined for OGF sand with the same gradations as those of the sand from the shear bands formed during shearing to shear displacements of up to 7m in the ring shear (these tests were performed with a normal stress of 400 kPa). To reconstitute the gradation of the sand from the shear bands, OGF sand was crushed manually with a tamper (this was done because the amount of sand collected from each shear band was less than 200g). Knowing the percentage of sand retained in each sieve for the sand samples collected from the shear band after each ring shear test, the required amounts of sand for each particle size range was calculated such that a sand mixture with approximately 2,000 grams would be produced (the GSD curve of each sand mixture reconstituted in this manner was determined three times to make sure that the actual gradation of the sand from the shear band matched the one of the reconstituted sand mixture). The evolution of the minimum void and maximum void ratios

after the ring shear test performed with normal stress equal to 400 kPa and shear displacement of 7 m was found to range between 0.59 to 0.49 and 0.81 to 0.70 respectively.

5.5.3 Particle morphology evolution after large shear displacements tests

The shearing-off of the asperities and the abrasion of the large particles occur as particles rotate and translate during shearing. The sand particles from the shear band became more rounded and spherical as the shear displacement increased (as compared with the original, uncrushed sand), particularly for the sand collected from the shear band formed in the ring shear tests performed with a normal stress of 400 kPa and shear displacements of 7 m. For instance, for this case, the global sphericity parameter of the original sand changes from 0.76 to 0.86 for the crushed sand, and the corresponding roundness global parameter changes from 0.73 to 0.75.

It can be observed in Figure 4.85, Figure 4.87, Figure 4.89, Figure 4.91 and Figure 4.93 that all the particles from sieves #20, #40, #60, #100 and #200, have similar values of sphericity parameter, which is about 0.86 to 0.88. Also, it is shown in Figure 4.86, Figure 4.88, Figure 4.90, Figure 4.92 and Figure 4.94 that the global aspect ratio parameter decreased (as expected, since the sphericity and roundness parameters increased), changing from 1.42 (OGF sand) to 1.29 (crushed material). It can be concluded that the evolution of the sand particle sizes depends on the normal stress and shear displacement used in these tests. Additionally, during these tests (ring shear tests performed with normal stress equal to 400 kPa and shear displacement up to 7m) it can be observed that the global circularity slightly decreased from 0.62 (original sand) to 0.59 (newly formed particles) in most of the

cases. Which indicates that the particles are less circular after shearing than the uncrushed material (OGFS).

It was observed that in the ring shear tests performed on OGF sand, the sand particles become more rounded with shearing because of the abrasion of the edges of the particles and shearing-off of the asperities and irregularities. Which explains the small evolution of the mobilized friction angle after the ring shear tests. The lower bound of the mobilized friction angle was calculated taken into account the lower values of the friction angle versus shear displacement curves; also, the higher values correspond to the attempts of the soil to dilate, whose effect is diminished through the particle crushing.

LIST OF REFERENCES

LIST OF REFERENCES

Agung, M. W., Sassa, K., Fukuoka, H., & Wang, G. (2004). Evolution of shear-zone structure in undrained ring-shear tests. *Landslides*, *1*(2), 101–112.

Altuhafi, F., & Coop, M. R. (2011). Changes to particle characteristics associated with the compression of sands. *Geotechnique*, *61*(6), 459–471.

Allen, T. (2003). Powder sampling and particle size determination. Elsevier.

Arshad, M., Tehrani, F., Prezzi, M., & Salgado, R. (2014). Experimental study of cone penetration in silica sand using digital image correlation. Geotechnique, 64(7), 551–569.

AASHTO T27-14. (2014). *Standard method of test for sieve analysis of fine and coarse aggregates.*

ASTM Standard D2435-D2435M. (2011). Standard test methods for one-dimensional consolidation properties of soils using incremental loading. doi: 10.1520/D2435-D2435M-11

ASTM Standard D2487-06. (2006). *Standard practice for classification of soils for engineering purposes (unified soil classification system).*

ASTM Standard D2488-09a. (2009). *Standard practice for description and identification of soils*. doi: 10.1520/D2488-09A

ASTM Standard D422-63. (2007). *Standard test method for particle-size analysis of soils*. doi: 10.1520/D0422-63R07E02

ASTM Standard D4253-16. (2004). *Standard test methods for particle-size distribution (gradation) of soils using sieve analysis*. doi: 10.1520/D6913- 04R09E01

ASTM Standard D4253-16. (2016). *Standard test methods for maximum index density and unit weight of soil using a vibratory table*. doi: 10.1520/D4253-16

ASTM Standard D4254-16. (2016). *Standard test methods for minimum index density and unit weight of soils and calculation of relative density*. doi: 10.1520/D4254-16

ASTM Standard D7608-10. (2010). *Standard test method for torsional ring shear test to determine drained fully softened shear strength and nonlinear strength envelope of cohesive soils (using normally consolidated specimen) for slopes with no preexisting shear surfaces*. doi: 10.1520/D760810.

ASTM Standard D854. (2014). *Standard test methods for specific gravity of soil solids by water pycnometer*. doi: 10.1520/D0854-14

Billam, J. (1971). Some aspects of the behaviour of granular materials at high pressures. In *Proceeding of the roscoe memorial symposium, Cambridge* (pp. 69–80).

Bishop, A. W. (1966). The strength of soils as engineering materials. *Geotechnique*.

Cavarretta, I., Coop, M., & O'sullivan, C. (2010). The influence of particle characteristics on the behaviour of coarse grained soils. *Geotechnique*, *60*(6), 413–423.

Charpentier, I., Sarocchi, D., & Sedano, L. A. R. (2013). Particle shape analysis of volcanic clast samples with the matlab tool morpheo. *Computers & Geosciences*, *51*, 172–181.

Chester, J. S., Lenz, S. C., Chester, F. M., & Lang, R. (2004). Mechanisms of compaction of quartz sand at diagenetic conditions. *Earth and Planetary Science Letters*, *220*(3), 435–451.

Cho, G. C., Dodds, J., & Santamarina, J. C. (2006). Particle shape effects on packing density, stiffness, and strength: natural and crushed sands. Journal of geotechnical and geoenvironmental engineering, 132(5), 591-602

Coop, M., Sorensen, K., Freitas, T. B., & Georgoutsos, G. (2004). Particle breakage during shearing of a carbonate sand. *Geotechnique*, *54*(3), 157–164.

Cox, M. R., & Budhu, M. (2008). A practical approach to grain shape quantification. *Engineering Geology*, *96*(1), 1–16.

Daouadji, A., Hicher, P.-Y., & Rahma, A. (2001). An elastoplastic model for granular materials taking into account grain breakage. *European Journal of Mechanics-A/Solids*, *20*(1), 113–137.

Das, B. M. (2013). *Advanced soil mechanics*. CRC Press.

Feda, J. (2002). Notes on the effect of grain crushing on the granular soil behaviour. *Engineering geology*, *63*(1), 93–98.

Finno, R., Harris, W., Mooney, M. A., & Viggiani, G. (1997). Shear bands in plane strain compression of loose sand. *Geotechnique*, *47*(1), 149–165.

Germaine, J. T., & Germaine, A. V. (2009). *Geotechnical laboratory measurements for engineers*. John Wiley & Sons.

Ghafghazi, M., Shuttle, D., & DeJong, J. (2014). Particle breakage and the critical state of sand. *Soils and Foundations*, *54*(3), 451–461.

Hagerty, M., Hite, D., Ullrich, C., & Hagerty, D. (1993). One-dimensional high-pressure compression of granular media. *Journal of Geotechnical Engineering*, *119*(1), 1–18.

Hall, E., & Gordon, B. (1964). Triax1al testing with large-scale high pressure equipment. In *Laboratory shear testing of soils.* ASTM International.

Hardin, B. O. (1985). Crushing of soil particles. *Journal of Geotechnical Engineering*, *111*(10), 1177–1192.

Hyodo, M., Aramaki, N., Nakata, Y., Inoue, S., Hyde, A. F., et al. (1999). Particle crushing and undrained shear behaviour of sand. In *The ninth international offshore and polar engineering conference.*

Karimpour, H., & Lade, P. V. (2010). Time effects relate to crushing in sand. *Journal of Geotechnical and Geoenvironmental Engineering*, *136*(9), 1209–1219.

Krumbein, W., & Sloss, L. (1963). Properties of sedimentary rocks. *Stratigraphy and Sedimentation*, 106–113.

Lade, P. V., Yamamuro, J. A., & Bopp, P. A. (1996). Significance of particle crushing in granular materials. *Journal of Geotechnical Engineering*, *122*(4), 309–316.

Lade, P. V., & Liu, C. T. (1998). Experimental study of drained creep behavior of sand. Journal of Engineering Mechanics, 124(8), 912-920.

Lade, P. V., Liggio, C. D., & Yamamuro, J. A. (1998). Effects of non-plastic fines on minimum and maximum void ratios of sand

Lee, D.-M. (1992). *Angles of friction of granular fills.* (Unpublished doctoral dissertation). University of Cambridge.

Lee, K. L., & Farhoomand, I. (1967). Compressibility and crushing of granular soil in anisotropic triaxial compression. *Canadian Geotechnical Journal*, *4*(1), 68–86.

Leung, C., Lee, F., & Yet, N. (1997). The role of particle breakage in pile creep in sand. Canadian Geotechnical Journal, 33(6), 888–898.

Lobo-Guerrero, S. (2006). *Evaluation of crushing in granular materials using the discrete element method and fractal theory* (Unpublished doctoral dissertation). University of Pittsburgh.

Lobo-Guerrero, S., & Vallejo, L. (2005). Crushing a weak granular material: experimental numerical analyses. *Geeotechnique*, *55*(3)

Luzzani, L., & Coop, M. (2002). On the relationship between particle breakage and the critical state of sands. *Soils and Foundations*, *42*(2), 71–82.

Marsal, R. J. (1967). Large-scale testing of rockfill materials. *Journal of the Soil Mechanics and Foundations Division*, *93*(2), 27–43.

McDowell, G., & Bolton, M. (1998). On the micromechanics of crushable aggregates. *Geotechnique*, *48*(5), 667–679.

McDowell, G., Bolton, M., & Robertson, D. (1996). The fractal crushing of granular materials. *Journal of the Mechanics and Physics of Solids*, *44*(12), 2079–2101.

McDowell, G., & Khan, J. (2003). Creep of granular materials. *Granular Matter*, *5*(3), 115–120.

Mesri, G., & Vardhanabhuti, B. (2009). Compression of granular materials. *Canadian Geotechnical Journal*, *46*(4), 369–392.

Mitchell, J., & Soga, K. (2005). *Fundamentals of soil behavior* (Third Edition ed.; I. Wiley & Sons, Ed.). Wiley & Sons, Inc.

Müller, G. (1967). Methods in sedimentary petrology.

Muszynski, M. R., & Vitton, S. J. (2012). Particle shape estimates of uniform sands: visual and automated methods comparison. J. Mater. Civ. Eng., 24(2), 194-206.

Nakata, Y., Bolton, M. D., & Cheng, Y. P. (2005). Relating particle characteristics to macro behavior of dem crushable material. *Powders and grains. Taylor & Francis Group, London*, 1387–1391.

Nakata, Y., Hyodo, M., Hyde, A. F., Kato, Y., & Murata, H. (2001). Microscopic particle crushing of sand subjected to high pressure one-dimensional compression. *Soils and foundations*, *41*(1), 69–82.

Nakata, Y., Hyodo, M., Murata, H., Hyde, A., & Ham, T. (2003). Effect of water on particle breakage for decomposed granite soils. *Deformation characteristics of geomaterials. Edited by H. Di Benedetto, T. Doanh, H. Geoffroy, and C. Sauze´at. Taylor & Francis, London*, 701–705.

Rasband, W. S. (2004). ImageJ; US National Institutes of Health: Bethesda, MD, 1997-2006. There is no corresponding record for this reference

Saada, A., & Townsend, F. (1981). State of the art: laboratory strength testing of soils. In *Laboratory shear strength of soil.* ASTM International.

Sadrekarimi, A., & Olson, S. M. (2009). Shear band formation observed in ring shear tests on sandy soils. *Journal of geotechnical and geoenvironmental engineering*, *136*(2), 366–375.

Sadrekarimi, A., & Olson, S. M. (2010). Particle damage observed in ring shear tests on sands. *Canadian Geotechnical Journal*, *47*(5), 497–515.

Salgado, R. (2008). *The engineering of foundations*. McGraw Hill New York.

Santamarina, J. C., Klein, K., & Fam, M. (2001). Soils and waves: particulate materials behavior, characterization and process monitoring, j. *England: John Wiley and Sons Ltd.*

Sassa, K., et al. (2000). Mechanism of flows in granular soils. In *Isrm international symposium.*

Takei, M., Kusakabe, O., & Hayashi, T. (2001). Time-dependent behavior of crushable materials in one-dimensional compression tests. *Soils and foundations*, *41*(1), 97–121.

Terzaghi, K. (1925). Principles of soil mechanics, settlement and consolidation of clay. *Engineering News-Record*, *95*(3), 874–878.

Terzaghi, K., Peck, R. B., & Mesri, G. (1996). *Soil mechanics in engineering practice*. John Wiley & Sons.

Vallejo, L. E. (1995). Fractal analysis of granular materials. In *International journal of rock mechanics and mining sciences and geomechanics abstracts* (Vol. 8, p. 371A)

Viggiani, G., Ku¨ntz, M., & Desrues, J. (2001). An experimental investigation of the relationships between grain size distribution and shear banding in sand. In *Continuous and discontinuous modelling of cohesive-frictional materials* (pp. 111–127). Springer.

Wadell, H. (1932). Volume, shape, and roundness of rock particles. The Journal of Geology, 443-451.

Wadell, H. (1935). Volume, shape, and roundness of quartz particles. *The Journal of Geology*, 250–280.

Wang, F., Sassa, K., & Wang, G. (2002). Mechanism of a long-runout landslide triggered by the august 1998 heavy rainfall in fukushima prefecture, japan. *Engineering Geology*, *63*(1), 169–185.

Wood, D. M., & Maeda, K. (2008). Changing grading of soil: effect on critical states. Acta Geotechnica, 3(1), 3–14.

Yamamuro, J. A., & Lade, P. V. (1997). Static liquefaction of very loose sands. *Canadian Geotechnical Journal*, *34*(6), 905–917.

APPENDICES

Appendix A Calibrations

a. Load cell calibration

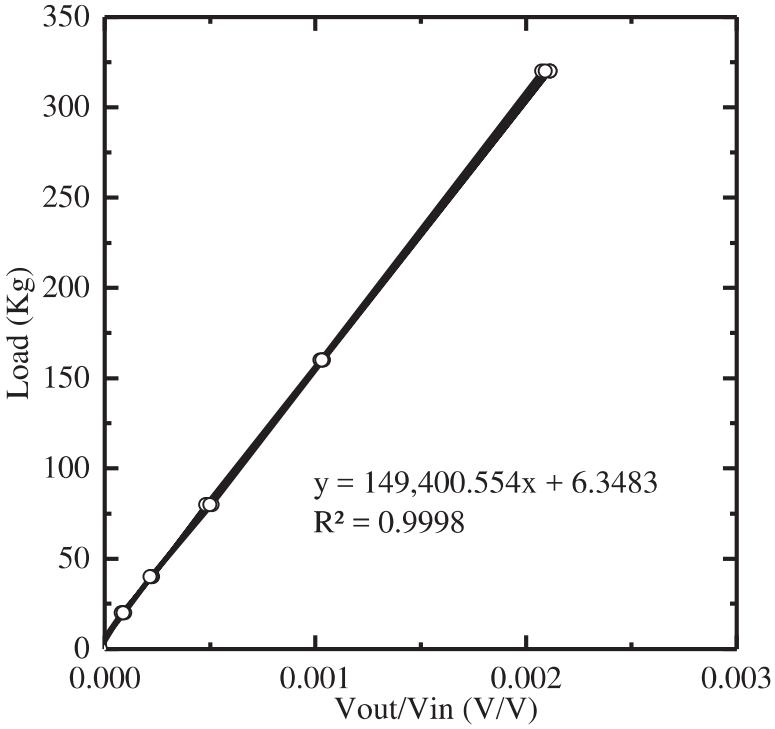

Load cell calibration					
Zero	0.02052	Volts			
Excitacion	10.08040	Volts			
AD-IO Module	#2642				
Cycles	Load [Kg]	Load [N] (Kg *g*10)	Vout	Vout-Zero	V/V
Cycle 1 load	0	0	0.02033	-0.00019	-0.00002
	2	196	0.02136	0.00084	0.00008
	4	392	0.02274	0.00222	0.00022
	8	784	0.02539	0.00487	0.00048
	16	1568	0.03094	0.01042	0.00103
	32	3136	0.04183	0.02131	0.00211
Cycle 1 Unload	32	3136	0.04143	0.02091	0.00207
	16	1568	0.03082	0.01030	0.00102
	8	784	0.02535	0.00483	0.00048
	4	392	0.02281	0.00229	0.00023
	2	196	0.02131	0.00079	0.00008
	0	0	0.02011	-0.00041	-0.00004
Cycle 2 Load	0	0	0.02012	-0.00040	-0.00004
	2	196	0.02148	0.00096	0.00010
	4	392	0.02276	0.00224	0.00022
	8	784	0.02565	0.00513	0.00051
	16	1568	0.03100	0.01048	0.00104
	32	3136	0.04183	0.02131	0.00211
Cycle 2 Unload	32	3136	0.04160	0.02108	0.00209
	16	1568	0.03091	0.01039	0.00103
	8	784	0.02556	0.00504	0.00050
	4	392	0.02268	0.00216	0.00021
	2	196	0.02140	0.00088	0.00009
	0	0	0.02012	-0.00040	-0.00004

b. LVDT calibration

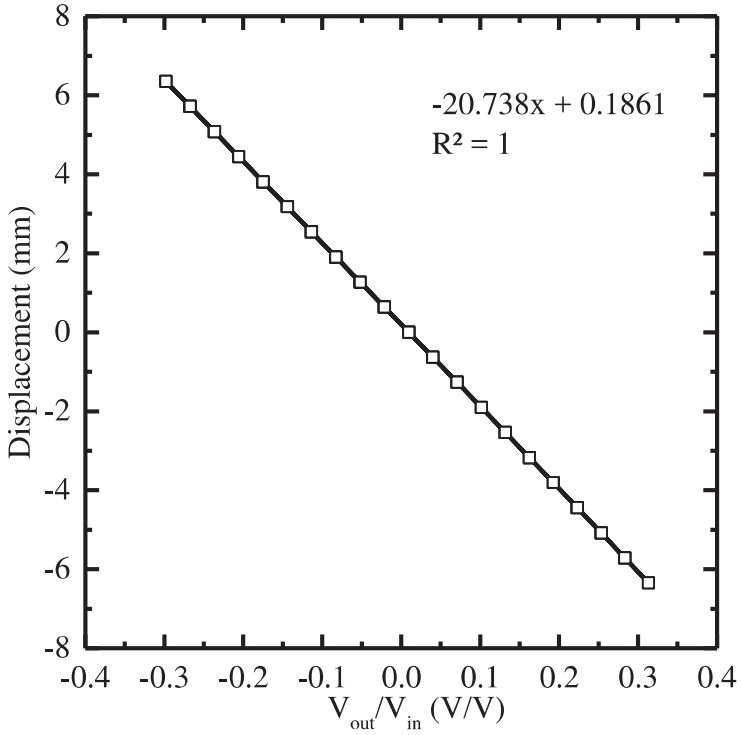

LVDT Calibration				
AD-IO Module	#2642			
Channel	3			
Unit	mm			
Cal. Factor	1			
Excitation	10.0804			
Zero	0.096			
Min. Reading	-100			
Max. Reading	100			
Time	LVDT Cal	[in]	Vout/Vin	[mm]
7/2/2015 17:42	0.096	0.000	0.010	0.000
7/2/2015 17:42	-0.215	0.025	-0.021	0.635
7/2/2015 17:42	-0.523	0.050	-0.052	1.270
7/2/2015 17:43	-0.834	0.075	-0.083	1.905
7/2/2015 17:43	-1.144	0.100	-0.113	2.540
7/2/2015 17:43	-1.453	0.125	-0.144	3.175
7/2/2015 17:43	-1.763	0.150	-0.175	3.810
7/2/2015 17:44	-2.073	0.175	-0.206	4.445
7/2/2015 17:44	-2.383	0.200	-0.236	5.080
7/2/2015 17:44	-2.693	0.225	-0.267	5.715
7/2/2015 17:44	-3.002	0.250	-0.298	6.350
7/2/2015 17:45	-2.694	0.225	-0.267	5.715
7/2/2015 17:45	-2.385	0.200	-0.237	5.080
7/2/2015 17:45	-2.074	0.175	-0.206	4.445
7/2/2015 17:45	-1.764	0.150	-0.175	3.810
7/2/2015 17:46	-1.455	0.125	-0.144	3.175
7/2/2015 17:46	-1.145	0.100	-0.114	2.540
7/2/2015 17:46	-0.835	0.075	-0.083	1.905
7/2/2015 17:46	-0.524	0.050	-0.052	1.270
7/2/2015 17:47	-0.215	0.025	-0.021	0.635
7/2/2015 17:47	0.096	0.000	0.009	0.000
7/2/2015 17:47	0.405	-0.025	0.040	-0.635
7/2/2015 17:47	0.714	-0.050	0.071	-1.270
7/2/2015 17:48	1.022	-0.075	0.101	-1.905
7/2/2015 17:48	1.330	-0.100	0.132	-2.540
7/2/2015 17:48	1.636	-0.125	0.162	-3.175
7/2/2015 17:48	1.942	-0.150	0.193	-3.810
7/2/2015 17:49	2.249	-0.175	0.223	-4.445

Time	LVDT Cal	[in]	Vout/Vin	[mm]
7/2/2015 17:49	2.552	-0.200	0.253	-5.080
7/2/2015 17:49	2.856	-0.225	0.283	-5.715
7/2/2015 17:49	3.157	-0.250	0.313	-6.350
7/2/2015 17:50	2.857	-0.225	0.283	-5.715
7/2/2015 17:50	2.553	-0.200	0.253	-5.080
7/2/2015 17:50	2.249	-0.175	0.223	-4.445
7/2/2015 17:50	1.944	-0.150	0.193	-3.810
7/2/2015 17:51	1.638	-0.125	0.162	-3.175
7/2/2015 17:51	1.331	-0.100	0.132	-2.540
7/2/2015 17:51	1.024	-0.075	0.102	-1.905
7/2/2015 17:51	0.715	-0.050	0.071	-1.270
7/2/2015 17:52	0.406	-0.025	0.040	-0.635
7/2/2015 17:52	0.097	0.000	0.010	0.000
7/2/2015 17:52	-0.213	0.025	-0.021	0.635
7/2/2015 17:52	-0.523	0.050	-0.052	1.270
7/2/2015 17:53	-0.833	0.075	-0.083	1.905
7/2/2015 17:53	-1.142	0.100	-0.113	2.540
7/2/2015 17:53	-1.452	0.125	-0.144	3.175
7/2/2015 17:53	-1.763	0.150	-0.175	3.810
7/2/2015 17:54	-2.072	0.175	-0.206	4.445
7/2/2015 17:54	-2.383	0.200	-0.236	5.080
7/2/2015 17:54	-2.693	0.225	-0.267	5.715
7/2/2015 17:54	-3.003	0.250	-0.298	6.350
7/2/2015 17:55	-2.694	0.225	-0.267	5.715
7/2/2015 17:55	-2.384	0.200	-0.236	5.080
7/2/2015 17:55	-2.073	0.175	-0.206	4.445
7/2/2015 17:55	-1.764	0.150	-0.175	3.810
7/2/2015 17:56	-1.454	0.125	-0.144	3.175
7/2/2015 17:56	-1.144	0.100	-0.114	2.540
7/2/2015 17:56	-0.835	0.075	-0.083	1.905
7/2/2015 17:56	-0.525	0.050	-0.052	1.270
7/2/2015 17:57	-0.213	0.025	-0.021	0.635
7/2/2015 17:57	0.097	0.000	0.010	0.000
7/2/2015 17:57	0.405	-0.025	0.040	-0.635
7/2/2015 17:57	0.714	-0.050	0.071	-1.270
7/2/2015 17:58	1.023	-0.075	0.102	-1.905
7/2/2015 17:58	1.330	-0.100	0.132	-2.540

Time	LVDT Cal	[in]	Vout/Vin	[mm]
7/2/2015 17:58	1.638	-0.125	0.162	-3.175
7/2/2015 17:58	1.943	-0.150	0.193	-3.810
7/2/2015 17:59	2.249	-0.175	0.223	-4.445
7/2/2015 17:59	2.554	-0.200	0.253	-5.080
7/2/2015 17:59	2.858	-0.225	0.284	-5.715
7/2/2015 17:59	3.158	-0.250	0.313	-6.350
7/2/2015 18:00	2.858	-0.225	0.284	-5.715
7/2/2015 18:00	2.555	-0.200	0.253	-5.080
7/2/2015 18:00	2.250	-0.175	0.223	-4.445
7/2/2015 18:00	1.945	-0.150	0.193	-3.810
7/2/2015 18:01	1.639	-0.125	0.163	-3.175
7/2/2015 18:01	1.331	-0.100	0.132	-2.540
7/2/2015 18:01	1.025	-0.075	0.102	-1.905
7/2/2015 18:01	0.716	-0.050	0.071	-1.270
7/2/2015 18:02	0.407	-0.025	0.040	-0.635
7/2/2015 18:02	0.098	0.000	0.010	0.000
7/2/2015 18:02	-0.212	0.025	-0.021	0.635
7/2/2015 18:02	-0.522	0.050	-0.052	1.270
7/2/2015 18:03	-0.833	0.075	-0.083	1.905
7/2/2015 18:03	-1.142	0.100	-0.113	2.540
7/2/2015 18:03	-1.452	0.125	-0.144	3.175
7/2/2015 18:03	-1.762	0.150	-0.175	3.810
7/2/2015 18:04	-2.072	0.175	-0.206	4.445
7/2/2015 18:04	-2.382	0.200	-0.236	5.080
7/2/2015 18:04	-2.692	0.225	-0.267	5.715
7/2/2015 18:04	-3.002	0.250	-0.298	6.350

c. Pycnometer calibration

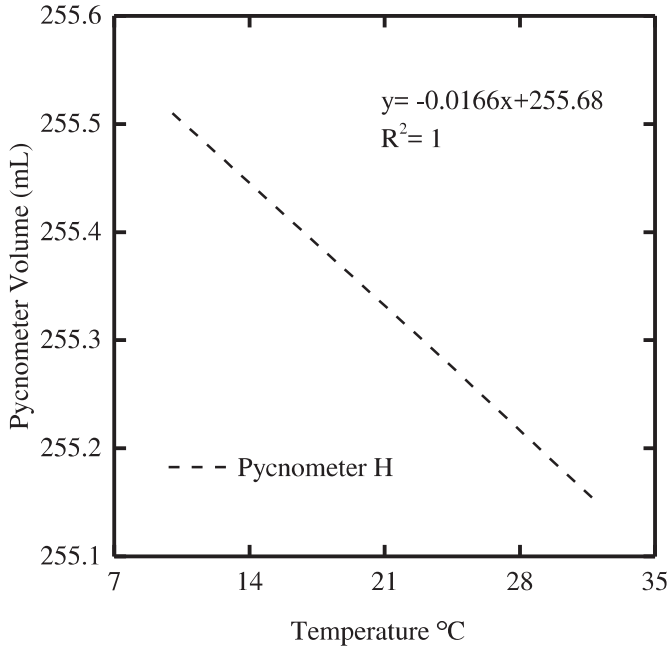

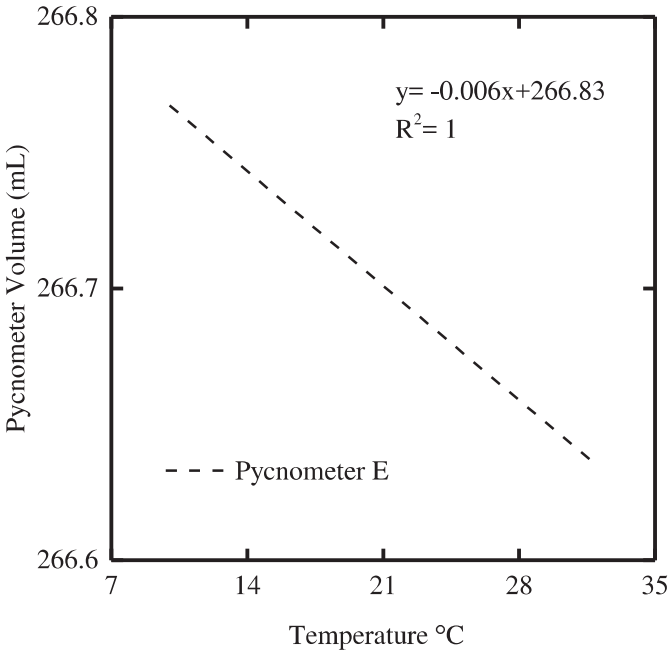

Calibration						
	Pycnometer H			Pycnometer E		
Test No	1	2	3	1	2	3
Temperature (°C)	24.20	32.00	10.00	24.20	32.00	10.00
$(M_B + M_W)_T$ (g)	372.18	371.48	373.04	421.19	420.55	421.93
M_B (g)	117.60	117.60	117.60	155.24	155.24	155.24
γ_{WT} (g/mL)	1.00	1.00	1.00	1.00	1.00	1.00
V_B (mL)	255.28	255.15	255.51	266.68	266.64	266.77

Appendix B Calculations

a. Minimum and maximum void ratios

Mold dimensions						
Description	Unit	Symbol	1	2	3	Average
Height	m	H	0.117	0.116	0.117	0.117
Internal diameter	m	D	0.101	0.101	0.101	0.101
Volume	m3	V	0.00094	0.00094	0.00094	0.00094

Vibratory table					
Description	Unit	Symbol	1	2	3
Mass of mold without collar	kg	M_m	4.25	4.25	4.25
Mass of mold with dry soil	kg	M_{ms_max}	5.83	5.82	5.82
Mass of dry soil	kg	M_s	1.58	1.57	1.57
Weight of dry soil	N	W_s	15.50	15.35	15.40
Volume of soil	m^3	V_m	0.00094	0.00094	0.00094
Maximum density	N/m^3	Y_{dmax}	16448.40	16292.24	16344.30
Specific gravity	-	G_s	2.65	2.65	2.65
Specific weight of water	N/m^3	Y_w	9810	9810	9810
Minimum void ratio	-	e_{min}		0.59	

b. Direct shear test

Information of the shear box		
Douter	63.3	mm
Height	28.999	mm
AREA	31.470	cm2
VOLUME	91.26	cm3

Information of the soil		
G_s	2.65	
e_{max}	0.81	
e_{min}	0.59	
γ_w	1	g/cm3
h soil	28.999	mm
Vol sample	91.260	cm3
Mass	149.012	gr
Vol sand	56.231	cm3
e	0.623	
D_R	85.03	%

c. Ring shear test

Characteristics of the test		
Load	25	kPa
Speed	10	DPM
Revolution	30	Degrees
Unloading	10	kPa

Dimensions of the mold		
Dinner	96.46	mm
Douter	152.377	mm
Height	31.807	mm
AREA	109.281	cm2
VOLUME	347.59	cm3

Information of the soil		
G_s	2.65	
e_{max}	0.81	
e_{min}	0.59	
γ_w	1	g/cm3
h soil	24.976	mm
Vol sample	272.941	cm3
Mass	443.080	gr
Vol sand	167.200	cm3
e	0.632	
D_R	80.72	%

d. One-dimensional compression test

Dimesnions of the mold		
Douter	63.19	mm
Height	25.74	mm
AREA	31.360761	cm2
VOLUME	80.72	cm3

Information of the soil		
G_s	2.65	
e_{max}	0.81	
e_{min}	0.59	
γ_w	1	g/cm3
h soil	22	mm
Vol sample	68.994	cm3
Mass	85%	
Vol sand	0.623	
e	1.633	g/cm3
D_R	112.651	g

Void Ratio check		
Vol(sample)	68.994	cm3
Vol (sand)	42.510	cm3
e	0.623	
D_R	85%	
Checking h	0.374	cm

e. Hydrometer

Sieve analysis original sand	
Sieve opening (mm)	Percentage finer (%)
4.75	100
2	100
0.85	99.166
0.425	8.908
0.25	0.854
0.106	0.036
0.075	0.016

Sieve analysis and Hydrometer analysis	
Sieve opening (mm)	Percentage finer (%)
4.75	100
2	100
0.85	99.318
0.425	9.684
0.25	1.179
0.106	0.520
0.075	0.318
0.074568746	0.266
0.052745039	0.171
0.043079999	0.123
0.037308373	0.123
0.026389485	0.076
0.018576506	0.076
0.013135573	0.076
0.009291237	0.028
0.00678536	0.028
0.004797974	0.028
0.00339268	0.028

f. Breakage potential

Sieve analysis and B_{p0} Original sand		
Sieve opening (mm)	Percentage finer (%)	B_{p0}
2	100	3.301
0.85	99.166	2.929
0.425	8.908	2.628
0.25	0.854	2.398
0.106	0.036	2.025
0.075	0.016	1.875
0.001	0	0

Sieve analysis B_{p0} after test		
Sieve opening (mm)	Percentage finer (%)	B_{p0}
2	100	3.301
0.85	98.969	2.929
0.425	12.782	2.628
0.25	3.004	2.398
0.106	1.093	2.025
0.074	0.417	1.867
0.052	0.365	1.717
0.043	0.330	1.629
0.037	0.278	1.567
0.026	0.243	1.417
0.019	0.139	1.268
0.013	0.104	1.117
0.009	0.069	0.967
0.007	0.035	0.831
0.005	0.035	0.680
0.003	0.035	0.530
0.001	0.035	0.141

Appendix C Morphology parameters

a. One-dimensional compression test

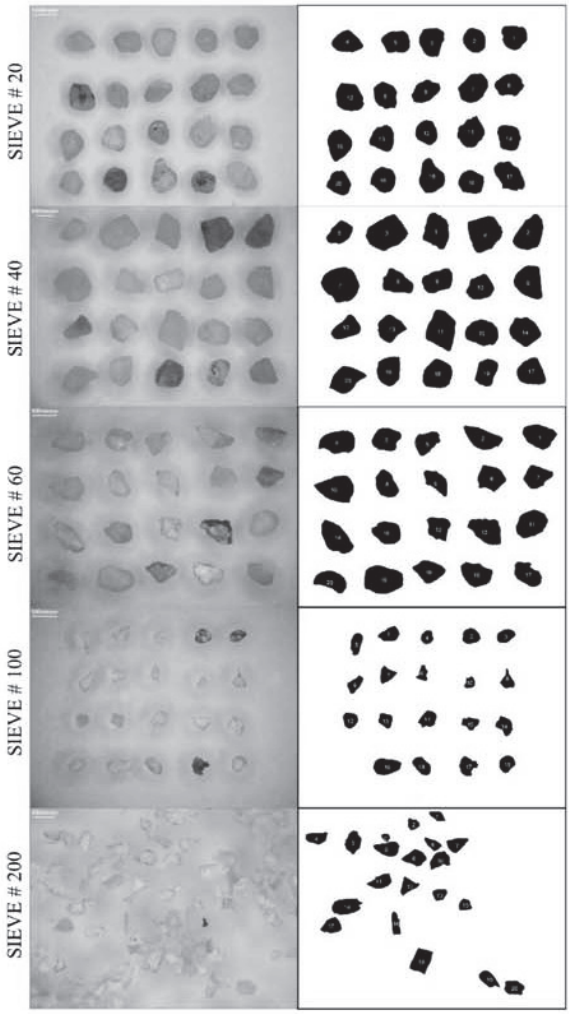

1DC_10d_D_R_35%

Parameter	Sieve #20	Sieve #40	Sieve #60	Sieve #100	Sieve #200	Total Average
Circularity	0.76 ± 0.04	0.73 ± 0.07	0.64 ± 0.09	0.68 ± 0.1	0.58 ± 0.08	0.68 ± 0.06
AR	1.24 ± 0.14	1.31 ± 0.17	1.5 ± 0.25	1.42 ± 0.28	1.64 ± 0.45	1.42 ± 0.14
Roundness	0.82 ± 0.09	0.77 ± 0.1	0.68 ± 0.11	0.73 ± 0.13	0.65 ± 0.14	0.73 ± 0.06
Sphericity	0.89 ± 0.04	0.87 ± 0.05	0.82 ± 0.05	0.85 ± 0.06	0.8 ± 0.08	0.85 ± 0.03

Note: A value ± standard deviation

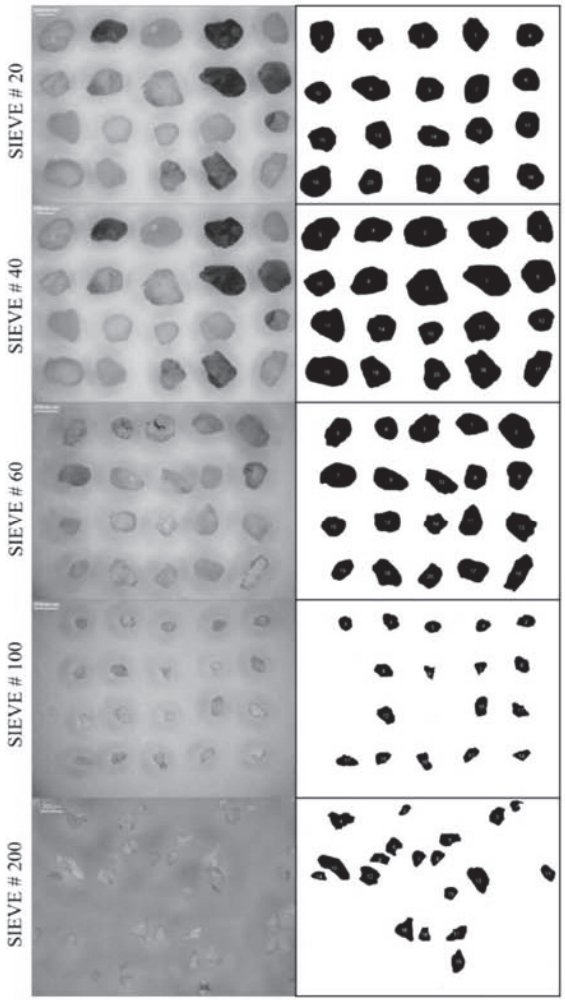

1DC_10d_D_R_85%

Parameter	Sieve #20	Sieve #40	Sieve #60	Sieve #100	Sieve #200	Total Average
Circularity	0.73 ± 0.07	0.73 ± 0.06	0.68 ± 0.09	0.63 ± 0.11	0.57 ± 0.09	0.67 ± 0.06
AR	1.24 ± 0.15	1.32 ± 0.2	1.45 ± 0.32	1.55 ± 0.26	1.57 ± 0.38	1.43 ± 0.13
Roundness	0.82 ± 0.08	0.77 ± 0.11	0.72 ± 0.13	0.66 ± 0.11	0.67 ± 0.15	0.73 ± 0.06
Sphericity	0.9 ± 0.04	0.84 ± 0.05	0.84 ± 0.06	0.82 ± 0.05	0.82 ± 0.07	0.84 ± 0.03

Note: Mean value ± standard deviation

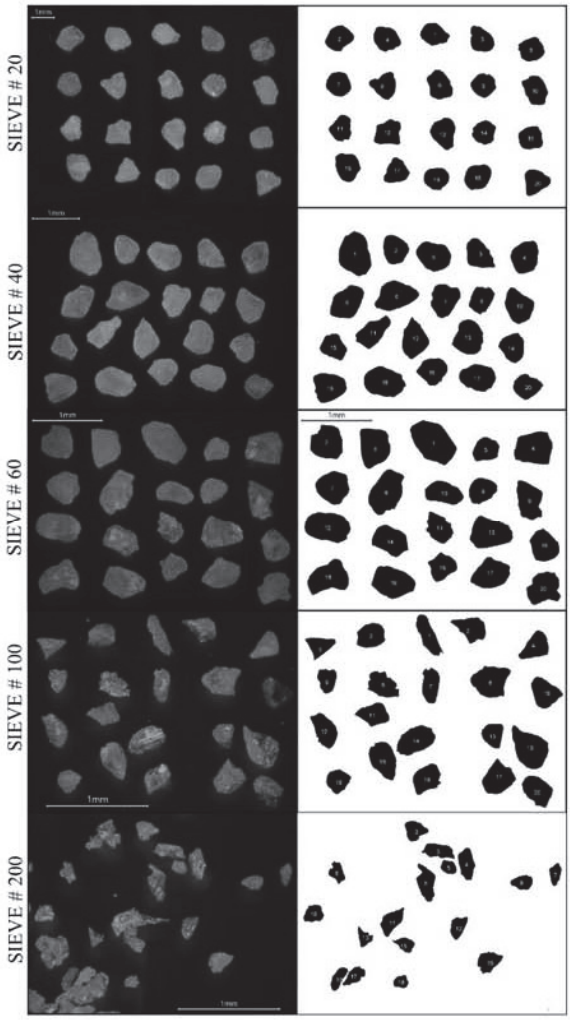

1DC_5d_D_R_35%

Parameter	Sieve #20	Sieve #40	Sieve #60	Sieve #100	Sieve #200	Total Average
Circularity	0.64 ± 0.04	0.67 ± 0.05	0.6 ± 0.06	0.45 ± 0.07	0.47 ± 0.08	0.57 ± 0.09
AR	1.19 ± 0.11	1.33 ± 0.18	1.37 ± 0.21	1.51 ± 0.43	1.68 ± 0.41	1.42 ± 0.17
Roundness	0.85 ± 0.08	0.76 ± 0.09	0.75 ± 0.11	0.7 ± 0.14	0.63 ± 0.15	0.74 ± 0.07
Sphericity	0.91 ± 0.03	0.87 ± 0.05	0.86 ± 0.05	0.83 ± 0.07	0.79 ± 0.08	0.85 ± 0.04

Note: Mean value ± standard deviation

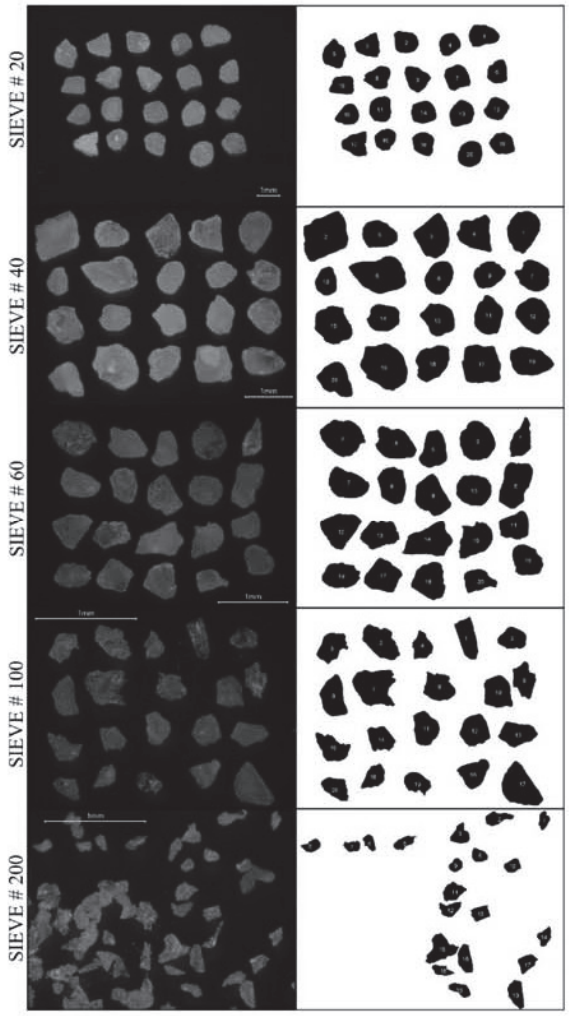

1DC_5d_D_R_85%

Parameter	Sieve #20	Sieve #40	Sieve #60	Sieve #100	Sieve #200	Total Average
Circularity	0.65 ± 0.03	0.73 ± 0.05	0.56 ± 0.08	0.47 ± 0.05	0.52 ± 0.09	0.59 ± 0.09
AR	1.18 ± 0.08	1.28 ± 0.13	1.39 ± 0.23	1.48 ± 0.28	1.67 ± 0.41	1.4 ± 0.17
Roundness	0.85 ± 0.05	0.79 ± 0.08	0.74 ± 0.11	0.7 ± 0.12	0.63 ± 0.14	0.74 ± 0.07
Sphericity	0.9 ± 0.02	0.87 ± 0.04	0.86 ± 0.06	0.83 ± 0.05	0.79 ± 0.07	0.85 ± 0.04

Note: Mean value ± standard deviation

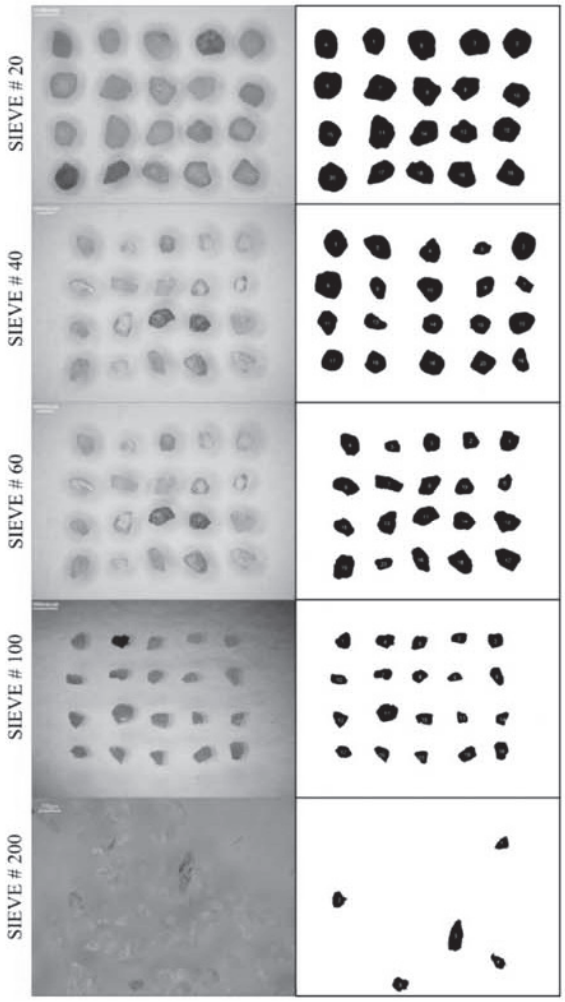

1DC_10h_D_R_35%

Parameter	Sieve #20	Sieve #40	Sieve #60	Sieve #100	Sieve #200	Total Average
Circularity	0.65 ± 0.09	0.69 ± 0.1	0.68 ± 0.06	0.62 ± 0.11	0.5 ± 0.12	0.63 ± 0.07
AR	1.23 ± 0.13	1.29 ± 0.21	1.42 ± 0.28	1.43 ± 0.22	1.61 ± 0.38	1.39 ± 0.13
Roundness	0.82 ± 0.08	0.8 ± 0.12	0.73 ± 0.12	0.71 ± 0.11	0.66 ± 0.14	0.74 ± 0.06
Sphericity	0.9 ± 0.04	0.88 ± 0.05	0.85 ± 0.06	0.84 ± 0.05	0.82 ± 0.08	0.86 ± 0.03

Note: Mean value ± standard deviation

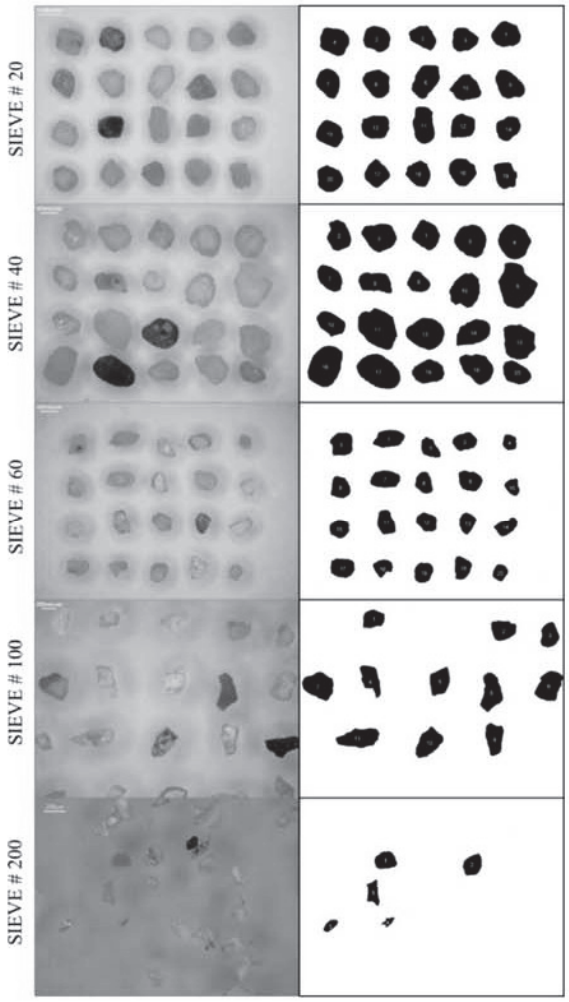

1DC_10h_D_R_85%

Parameter	Sieve #20	Sieve #40	Sieve #60	Sieve #100	Sieve #200	Total Average
Circularity	0.71 ± 0.06	0.6 ± 0.09	0.59 ± 0.06	0.62 ± 0.12	0.46 ± 0.22	0.6 ± 0.08
AR	1.25 ± 0.19	1.35 ± 0.18	1.36 ± 0.21	1.64 ± 0.35	1.81 ± 0.42	1.48 ± 0.21
Roundness	0.82 ± 0.1	0.75 ± 0.1	0.75 ± 0.11	0.64 ± 0.12	0.59 ± 0.15	0.71 ± 0.08
Sphericity	0.89 ± 0.05	0.86 ± 0.05	0.86 ± 0.06	0.8 ± 0.06	0.76 ± 0.09	0.84 ± 0.05

Note: Mean value ± standard deviation

b. Ring shear tests

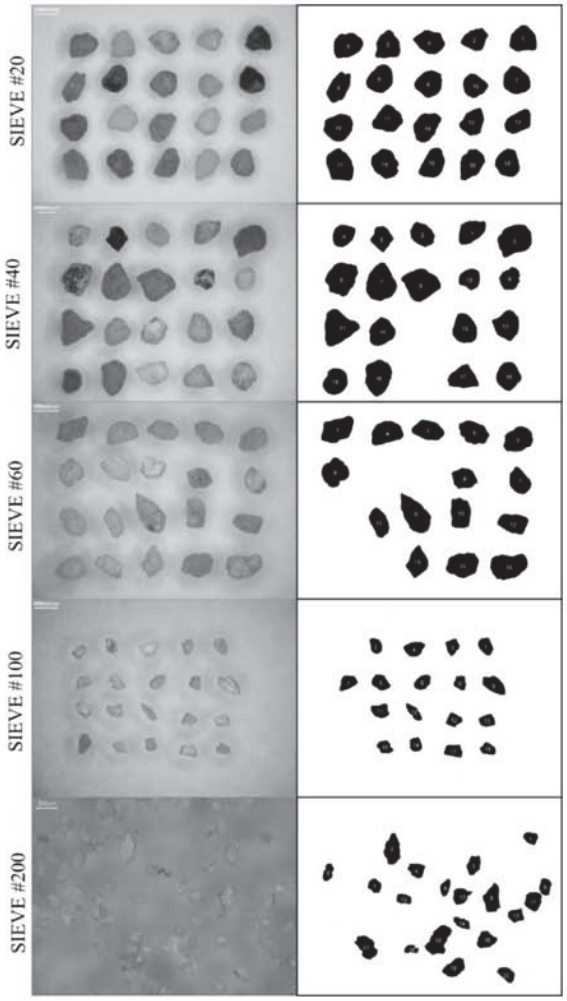

RS_100kPa_D_R_86%_20m

Parameter	Sieve #20	Sieve #40	Sieve #60	Sieve #100	Sieve #200	Total Average
Circularity	0.7 ± 0.09	0.73 ± 0.07	0.65 ± 0.08	0.65 ± 0.08	0.52 ± 0.1	0.65 ± 0.07
AR	1.28 ± 0.18	1.23 ± 0.11	1.49 ± 0.2	1.46 ± 0.35	1.58 ± 0.32	1.41 ± 0.13
Roundness	0.79 ± 0.1	0.82 ± 0.07	0.68 ± 0.09	0.71 ± 0.11	0.66 ± 0.14	0.73 ± 0.06
Sphericity	0.94 ± 0.04	0.85 ± 0.05	0.72 ± 0.03	0.6 ± 0.03	0.47 ± 0.04	0.72 ± 0.17

Note: Mean value ± standard deviation

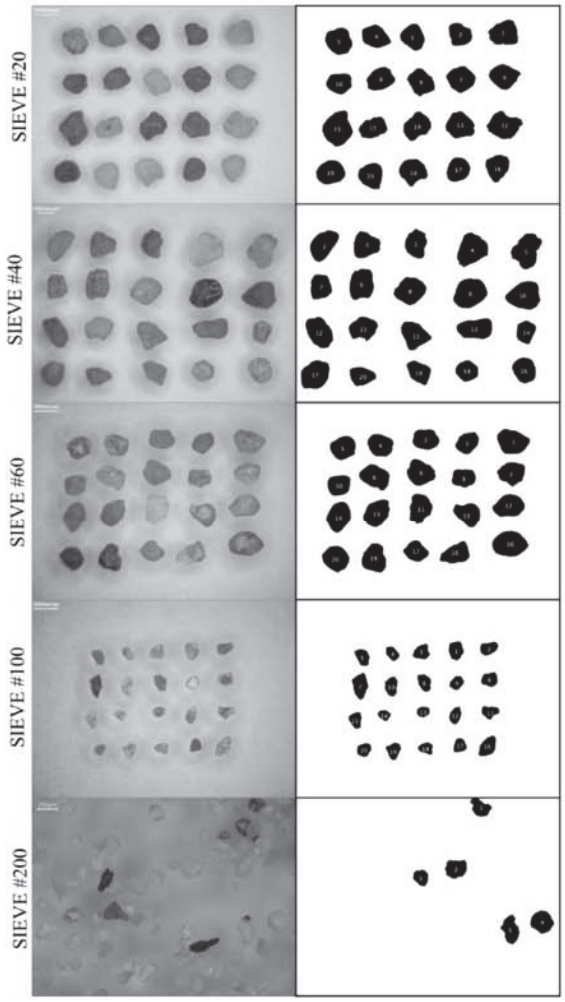

RS_200kPa_D_R_36%_20m

Parameter	Sieve #20	Sieve #40	Sieve #60	Sieve #100	Sieve #200	Total Average
Circularity	0.7 ± 0.11	0.71 ± 0.07	0.69 ± 0.07	0.7 ± 0.07	0.59 ± 0.12	0.68 ± 0.04
AR	1.22 ± 0.1	1.29 ± 0.18	1.3 ± 0.1	1.43 ± 0.21	1.35 ± 0.26	1.32 ± 0.07
Roundness	0.82 ± 0.06	0.78 ± 0.09	0.77 ± 0.06	0.71 ± 0.1	0.77 ± 0.14	0.77 ± 0.03
Sphericity	0.94 ± 0.03	0.83 ± 0.04	0.73 ± 0.02	0.59 ± 0.02	0.53 ± 0.03	0.72 ± 0.15

Note: Mean value ± standard deviation

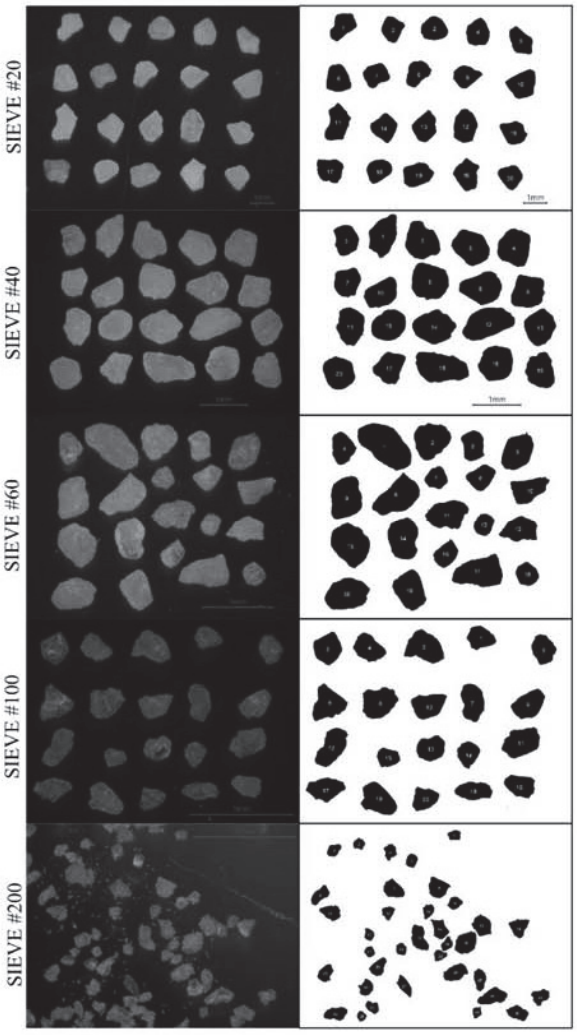

RS_300kPa_D_R_87.4%_2m

Parameter	Sieve #20	Sieve #40	Sieve #60	Sieve #100	Sieve #200	Total Average
Circularity	0.68 ± 0.05	0.67 ± 0.04	0.6 ± 0.07	0.56 ± 0.06	0.6 ± 0.07	0.62 ± 0.05
AR	1.29 ± 0.17	1.32 ± 0.23	1.42 ± 0.21	1.43 ± 0.26	1.44 ± 0.31	1.38 ± 0.06
Roundness	0.79 ± 0.1	0.78 ± 0.11	0.72 ± 0.11	0.72 ± 0.12	0.72 ± 0.13	0.75 ± 0.03
Sphericity	0.87 ± 0.04	0.87 ± 0.06	0.84 ± 0.05	0.85 ± 0.06	0.85 ± 0.07	0.86 ± 0.01

Note: Mean value ± standard deviation

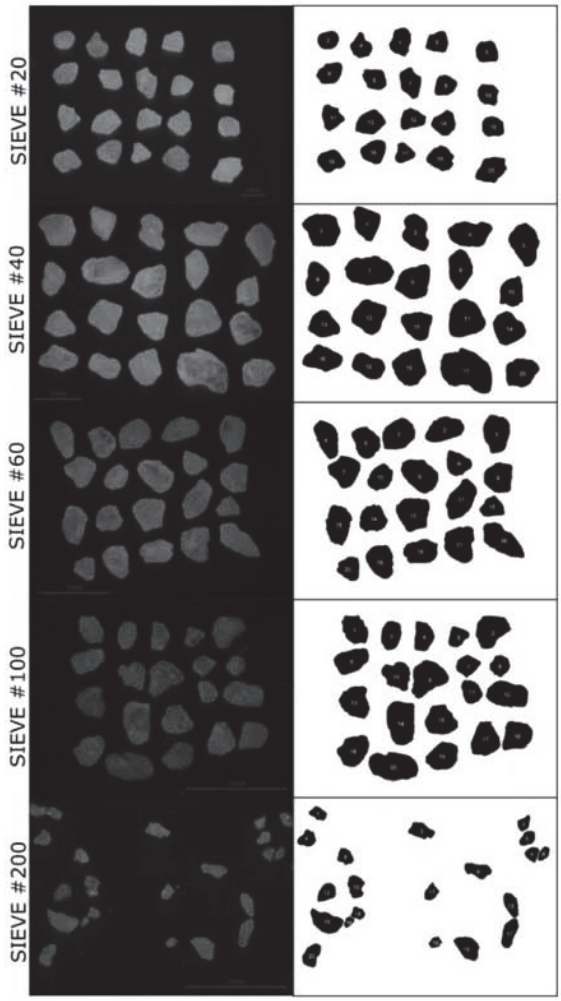

RS_400kPa_D_R_85.7%_1m

Parameter	Sieve #20	Sieve #40	Sieve #60	Sieve #100	Sieve #200	Total Average
Circularity	0.66 ± 0.04	0.66 ± 0.05	0.65 ± 0.05	0.59 ± 0.05	0.5 ± 0.06	0.61 ± 0.06
AR	1.23 ± 0.12	1.36 ± 0.23	1.38 ± 0.31	1.35 ± 0.21	1.56 ± 0.31	1.38 ± 0.11
Roundness	0.82 ± 0.08	0.76 ± 0.13	0.76 ± 0.15	0.75 ± 0.11	0.67 ± 0.12	0.75 ± 0.05
Sphericity	0.89 ± 0.04	0.86 ± 0.06	0.86 ± 0.07	0.86 ± 0.05	0.82 ± 0.06	0.86 ± 0.02

Note: Mean value ± standard deviation

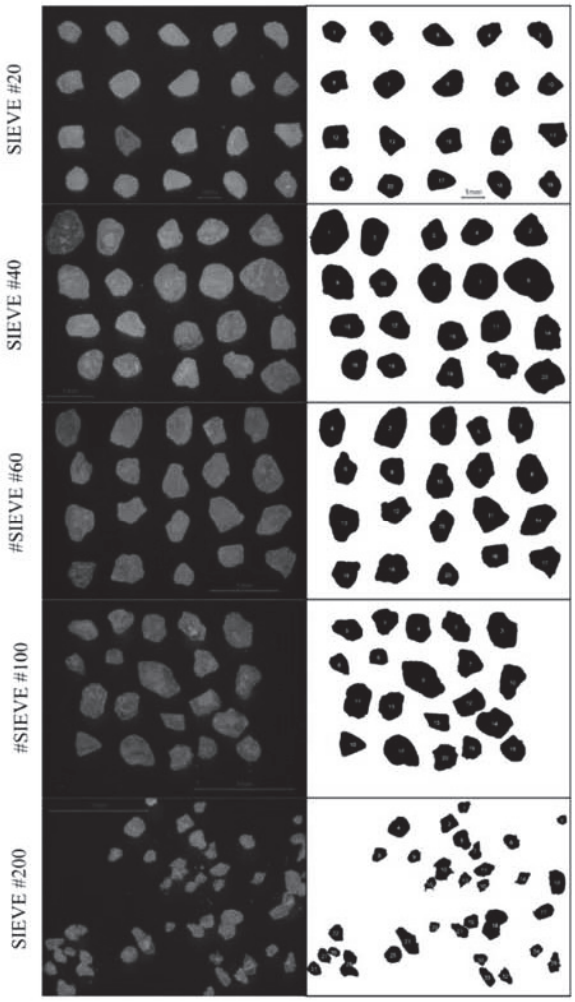

RS_400kPa_DR86.1%_2m

Parameter	Sieve #20	Sieve #40	Sieve #60	Sieve #100	Sieve #200	Total Average
Circularity	0.62 ± 0.04	0.59 ± 0.09	0.61 ± 0.06	0.53 ± 0.05	0.63 ± 0.07	0.6 ± 0.04
AR	1.31 ± 0.17	1.25 ± 0.12	1.34 ± 0.16	1.32 ± 0.18	1.44 ± 0.28	1.33 ± 0.06
Roundness	0.78 ± 0.1	0.81 ± 0.08	0.76 ± 0.09	0.77 ± 0.1	0.72 ± 0.12	0.77 ± 0.03
Sphericity	0.87 ± 0.04	0.89 ± 0.03	0.86 ± 0.04	0.87 ± 0.05	0.85 ± 0.06	0.87 ± 0.01

Note: Mean value ± standard deviation

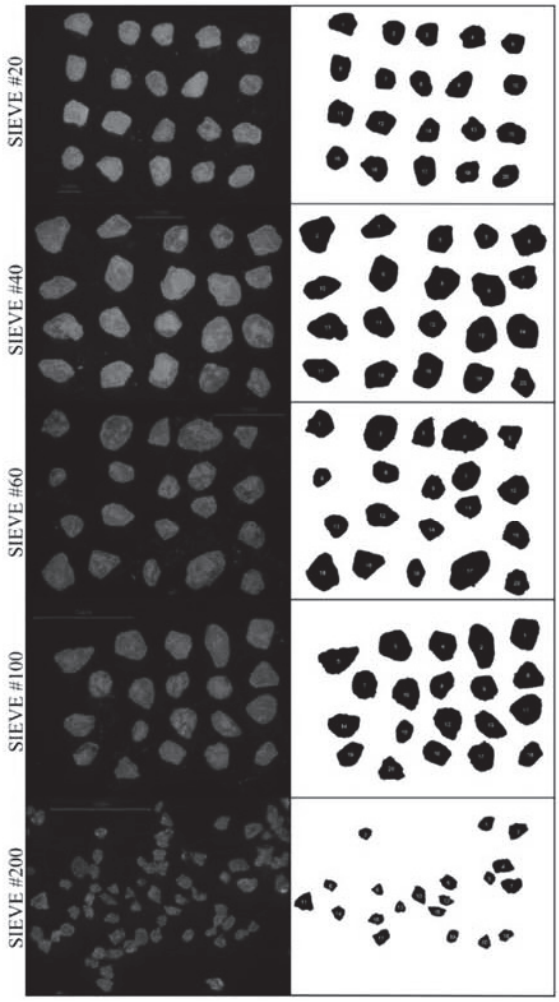

RS_400kPa_D_R_81.4%_4m

Parameter	Sieve #20	Sieve #40	Sieve #60	Sieve #100	Sieve #200	Total Average
Circularity	0.62 ± 0.04	0.65 ± 0.07	0.59 ± 0.05	0.53 ± 0.04	0.54 ± 0.07	0.59 ± 0.04
AR	1.24 ± 0.16	1.32 ± 0.19	1.26 ± 0.15	1.3 ± 0.22	1.33 ± 0.2	1.29 ± 0.04
Roundness	0.82 ± 0.1	0.77 ± 0.1	0.81 ± 0.09	0.79 ± 0.11	0.77 ± 0.11	0.79 ± 0.02
Sphericity	0.89 ± 0.04	0.87 ± 0.05	0.89 ± 0.04	0.88 ± 0.05	0.86 ± 0.06	0.88 ± 0.01

Note: Mean value ± standard deviation

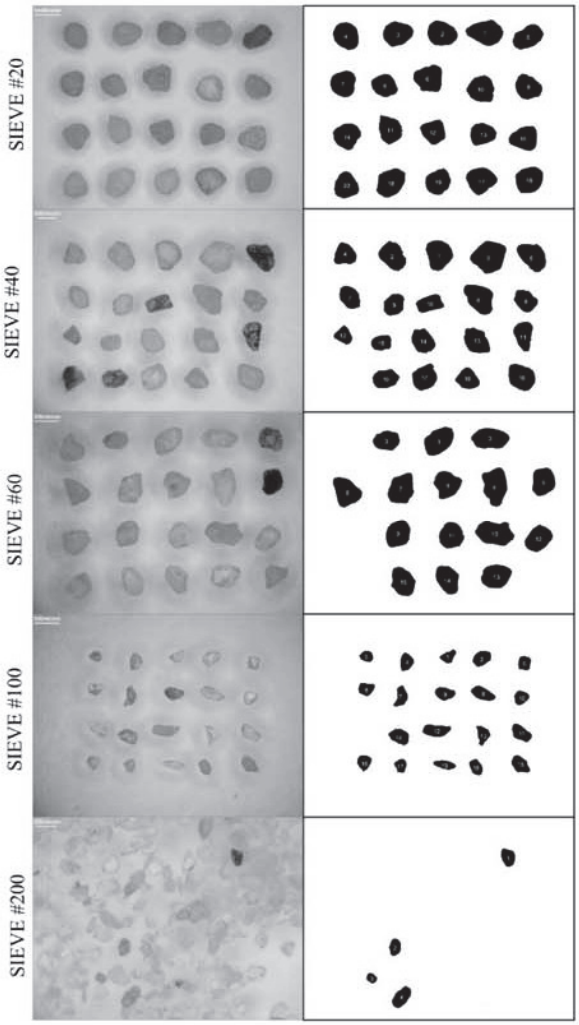

RS_400kPa_D_R_80.8%_6m

Parameter	Sieve #20	Sieve #40	Sieve #60	Sieve #100	Sieve #200	Total Average
Circularity	0.71 ± 0.09	0.71 ± 0.06	0.67 ± 0.06	0.68 ± 0.1	0.62 ± 0.03	0.68 ± 0.03
AR	1.21 ± 0.14	1.33 ± 0.17	1.38 ± 0.2	1.57 ± 0.42	1.49 ± 0.21	1.4 ± 0.13
Roundness	0.84 ± 0.09	0.76 ± 0.1	0.74 ± 0.11	0.68 ± 0.15	0.68 ± 0.09	0.74 ± 0.06
Sphericity	0.91 ± 0.04	0.86 ± 0.04	0.85 ± 0.08	0.82 ± 0.08	0.84 ± 0.05	0.86 ± 0.03

Note: Mean value ± standard deviation

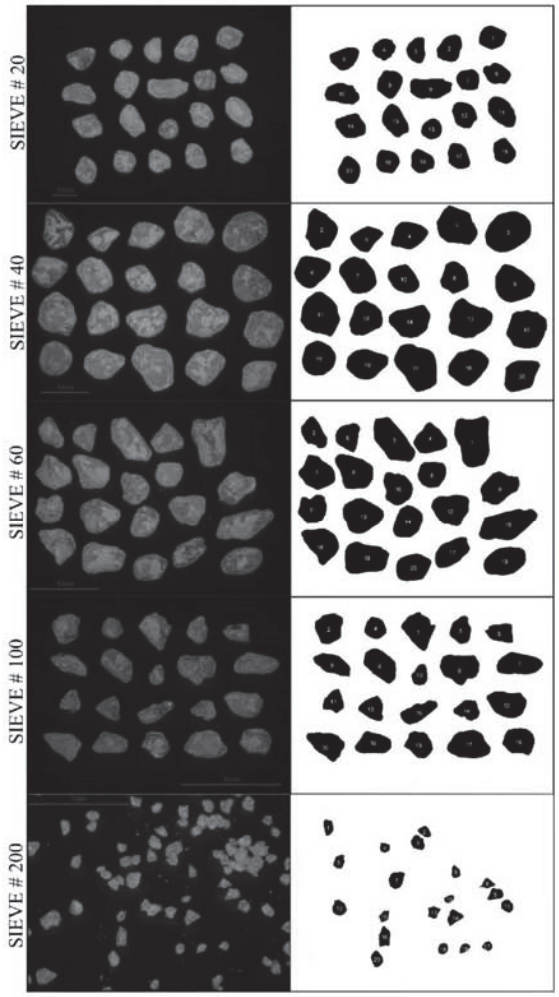

RS_400kPa_DR86.1%_7m

Parameter	Sieve #20	Sieve #40	Sieve #60	Sieve #100	Sieve #200	Total Average
Circularity	0.62 ± 0.05	0.66 ± 0.06	0.61 ± 0.07	0.59 ± 0.05	0.7 ± 0.06	0.64 ± 0.04
AR	1.33 ± 0.25	1.25 ± 0.11	1.35 ± 0.28	1.49 ± 0.37	1.36 ± 0.19	1.36 ± 0.08
Roundness	0.77 ± 0.12	0.8 ± 0.07	0.74 ± 0.13	0.71 ± 0.15	0.75 ± 0.1	0.75 ± 0.03
Sphericity	0.87 ± 0.06	0.89 ± 0.04	0.86 ± 0.07	0.84 ± 0.08	0.85 ± 0.05	0.86 ± 0.02

Note: Mean value ± standard deviation